

Study of hybrid III-V/Si photonic crystal lasers

Halioua Yacine



Université Paris 7 - Denis diderot
Ghent University
Faculteit Ingenieurswetenschappen
Vakgroep Informatietechnologie

Prof. Dr. Ir. Jeroen BEECKMAN	(Reviewer)
Prof. Dr. Philippe BOUCAUD	(Invited)
Prof. Dr. Richard DE LA RUE	(Reviewer)
Prof. Dr. Yannick DUMEIGE	
Prof. Dr. Ir. Geert MORTIER	(Reviewer)
Prof. Dr. Bert OFFREIN	
Prof. Rama RAJ	(PhD supervisor)
Prof. Dr. Ir. Gunther ROELKENS	(PhD supervisor)
Prof. Dr. Pierre VIKTOROVITCH	(Reviewer)
Chairman)	

University of Paris 7 - Denis Diderot
DEVU - Batiment Grands Moulins
75205 PARIS CEDEX 13

Universiteit Gent
Faculteit Ingenieurswetenschappen
Vakgroep Informatietechnologie
Gaston Crommenlaan 8 bus 201, B-9050 Gent, België

Tel.: +32-9-331.49.00
Fax.: +32-9-331.48.99

Remerciements

dankwoord...

Paris, printemps 2011
Yacine Halioua

Table of Contents

Remerciements	i
Resumé en français	xxi
References	xxviii
English summary	xxxix
References	xxxvii
Nederlandstalige samenvatting	xxxix
References	xlii
1 Introduction	1-1
1.1 Context	1-3
1.1.1 Photonic integration	1-3
1.1.2 Silicon photonics	1-4
1.1.3 III-V photonics	1-5
1.1.4 III-V/Si hybrid structures	1-6
1.1.5 Photonic crystals	1-7
1.2 Objectives	1-8
1.3 Conclusion	1-10
References	1-12
2 III-V photonic structures on SOI wires: general considerations and discussion	2-1
2.1 General scheme of the structure	2-1
2.2 Passive layer : SOI waveguide layer	2-1
2.3 Active level : III-V Photonic Crystal layer	2-3
2.4 Evanescent coupling	2-3
2.5 Conclusion	2-9
References	2-11
3 Hybrid III-V photonic crystal on silicon wire technology	3-1
3.1 Silicon layer processing	3-1
3.2 Bonding technologies	3-3
3.2.1 Molecular bonding technique	3-3
3.2.2 Adhesive bonding technique	3-4

3.3	Alignment technology	3-8
3.4	III-V Photonic crystal etching	3-9
3.5	Characterization and discussion	3-12
3.5.1	Characterization	3-12
3.5.2	Discussion on the importance of alignment accuracy . . .	3-14
3.6	Conclusion	3-16
	References	3-18
4	Photonic crystals	4-1
4.1	Underlying physics and properties	4-2
4.1.1	Maxwell's equations for a photonic crystal	4-2
4.1.2	Bloch-Floquet theorem	4-3
4.1.3	Band structure and photonic band gap	4-5
4.2	2D and 2.5D photonic crystals	4-10
4.2.1	2D photonic crystals	4-10
4.2.2	2.5D Photonic crystals	4-13
4.3	Photonic crystal cavities	4-15
4.3.1	Generalities	4-15
4.3.2	Q-factor and losses	4-16
4.4	Photonic crystal waveguides	4-20
4.5	Conclusion	4-21
	References	4-24
5	Numerical methods	5-1
5.1	Frequency domain methods	5-1
5.1.1	Scattering-matrix technique	5-2
5.1.2	Plane wave expansion	5-3
5.1.3	Application to hybrid systems	5-3
5.2	Finite-Difference Time-Domain	5-4
5.2.1	Introduction	5-4
5.2.2	Definition of the grid	5-6
5.2.3	Inclusion of the material	5-7
5.2.4	Initiation of the calculation	5-7
5.2.5	Simulation time	5-8
5.2.6	Processing of the data	5-8
5.3	Conclusion	5-9
	References	5-10
6	Experimental setup : general scheme	6-1
6.1	Coupling to the passive layer	6-2
6.2	III-V level addressing	6-3
6.3	Imaging	6-4
6.4	Conclusion	6-5
	References	6-6

7	Photonic crystal waveguide laser integrated on SOI	7-1
7.1	W1 photonic crystal waveguides	7-1
7.1.1	Modelling : III-V semiconductors PhC waveguide	7-3
7.1.2	Modelling : hybrid structure	7-4
7.1.3	Experimental studies	7-7
7.1.3.1	Experimental setup	7-7
7.1.3.2	Low group velocity modes of the PhC waveguides	7-8
7.1.3.3	PhC waveguides modes and coupling to the Si wire	7-10
7.1.3.4	Lasing operation	7-11
7.2	W0.65 photonic crystal waveguides	7-12
7.2.1	Modelling	7-12
7.2.2	Experimental studies	7-13
7.2.2.1	Experimental setup	7-13
7.2.2.2	Lasing operation	7-14
7.3	Conclusion	7-16
	References	7-18
8	Wire cavity laser integrated on SOI	8-1
8.1	Wire cavity : history and principle	8-1
8.2	Adaptation of an existing design	8-4
8.3	InP based wire cavity on silicon substrate	8-7
8.3.1	Numerical studies	8-7
8.3.1.1	Wavelength behaviour	8-8
8.3.1.2	Q factor against wavelength	8-10
8.3.1.3	Modal volume and confinement factor	8-12
8.3.2	Experimental study	8-13
8.4	Wire cavity coupled to a silicon wire	8-17
8.4.1	Modelling of the hybrid system	8-17
8.4.1.1	Mode profiles	8-18
8.4.1.2	Coupling strength and length of coupling	8-19
8.4.1.3	Silicon wires influence on the Q factor	8-21
8.4.2	Laser emission coupled to the wire	8-22
8.4.2.1	Multi wavelength operation	8-24
8.4.3	Study of the coupling	8-25
8.4.3.1	Theoretical model : a cavity coupled to a wire	8-25
8.4.3.2	Experimental study of the coupling	8-27
8.5	Continuous wave laser operation	8-31
8.6	Conclusion	8-32
	References	8-34

9	Conclusion and perspectives	9-1
9.1	Conclusions	9-2
9.1.1	Results Review	9-2
9.1.1.1	Fabrication of the hybrid structures	9-2
9.1.1.2	Modelling confronted to experimental results	9-2
9.1.1.3	Summary	9-3
9.1.2	Bistability	9-3
9.2	Perspectives	9-5
9.2.1	Present system improvement	9-6
9.2.1.1	Design and material	9-6
9.2.1.2	Electrical pumping	9-7
9.2.2	Cascaded cavities	9-7
9.2.3	Flip-flop operation	9-8
	References	9-10
A	Publications and conferences	A-1
A.1	Publications	A-1
A.1.1	Related to the studies on hybrid structures	A-1
A.1.2	Collaborations	A-2
A.2	Conferences concerning Hybrid III-V semiconductors/silicon structures	A-2

List of Figures

1	Image d'une aile de papillon réalisé à l'aide d'un microscope électronique à balayage. [Université d'Exeter]	xxii
2	Vue schématique de la structure hybride étudiée. Le niveau inférieur (bleu/gris) consiste en un guide silicium pour le guide de la lumière. A l'extrémité du guide de silicium sont gravés des réseaux permettant le couplage à une fibre optique pour l'injection et l'extraction de lumière dans le système. Le niveau supérieur (vert) est un cristal photonique en semiconducteurs III-V à la source des effets non-linéaire étudiés.	xxiii
3	Image obtenu au microscope électronique d'un échantillon fini. Le guide en cristal photonique, de 10 microns de long, apparaît parfaitement aligné sur le guide silicium visible par transparence sous le BCB. La grossissement faisant clairement apparaître la structure à deux niveaux.	xxv
4	SEM image of a butterfly wing. [Exeter University]	xxxii
5	Schematic view of the hybrid structure studied. The lower level (blue/grey) consist in a SOI wire for the guiding of light. At the extremity of this wire grating couplers are etched for coupling to a single mode fiber allowing the extraction and injection of light in the system. The upper level (green) is a III-V semiconductor photonic crystal achieving in which all the non-linear effects and stimulated emission arise.	xxxiii
6	SEM image of a processed sample. The 10 micron long PhC waveguide appears perfectly aligned with the silicon wire underneath, visible through the transparency of the BCB layer. The inset clearly shows the two level structuring.	xxxiv
7	Image d'une aile de papillon réalisé à l'aide d'un microscope électronique à balayage. [Université d'Exeter]	xli
1.1	Possible scheme for optical integration. The top level consist in optical elements electrically connected to the bottom level composed of silicon electronic transistors. [Courtesy of Ghent University-Intec]	1-4

1.2	Possible configurations for hybrid InP/SOI structures. a) Hybrid silicon evanescent device, from [28] - b) III-V photonic device coupled evanescently to an SOI wire, from [31]	1-6
1.3	Example of photonic crystal structures. From left to right : 1D Bragg mirror of alterned AlOx/AlGaAs layers (LPN), InP photonic crystal with a line of holes removed to form a waveguide (LPN), 3D TiO ₂ inverse opal [38]	1-7
1.4	Schematic representation of the hybrid structures studied in the present work. The upper level consist in a III-V semiconductor layer photonic crystal structure (green). The lower level consist in a silicon wire on insulator (grey correspond to silicon, deep blue to silicon oxide). Bonding is achieved via the use of an intermediate BCB layer (yellow layer). Those two structures are evanescently coupled. For typical sizes please refer to fig. 2.1	1-9
2.1	Top view (a) and vertical view (b) of the hybrid structure. Typical scales are reported on the figure : $h=600$ nm, $a=300$, $w=500$ nm . .	2-2
2.2	Left - Energy levels in the InP/InGaAsP/InGaAs quantum wells (black line): 1- InP around 60 nm thick (gap around 900 nm), 2- InGaAsP around 16 nm thick (gap around 1200 nm), 3- InGaAs around 13.5 nm (gap around 1698 nm); The red line represent a possible quantified state in the well. Right - Photoluminescence spectra of the composite layer	2-4
2.3	Scheme of two parallel waveguides of index and width respectively n_1, w_1 and n_2, w_2 separated by a distance d and embedded in a material of index n_s	2-5
2.4	Energy transfer between two similar waveguides against wavelength for initial parameter $a_1=1$ and $a_2=0$, the line correspond to waveguide 1 and the dashed line to waveguide 2, for two different detuning - blue correspond to zero detuning and then a maximum transfer of 100 percent, - green correspond to a detuning of 3 percent with a maximum energy transfer around 96 percent	2-8
2.5	Index of the 2 first modes of the coupled InP wire of variable width (height=255nm) with a silicon wire (500×220 nm) separated by a 465 nm thick BCB intermediate layer. Dashed line corresponds to the index of an uncoupled wire. Field profiles of points A-F are plotted on fig. 8.17.	2-9
3.1	SEM image of grating couplers etched in the LETI fab. The periodicity of the gratings is of the order of 610 nm and the etch depth around 50 nm. The coupling efficiency with a single mode fiber is around 30% over a bandwidth of approximatively 40 nm.	3-2

-
- 3.2 Main processing steps for bonding, a) Starting materials consist of the III-V semiconductor layer and a prepatterned silicon substrate, b) after spin coating of BCB on the silicon layer the InP is gently placed on the sample, c) entire structure obtained after a curing step and the substrate removal. 3-4
- 3.3 Thickness of BCB against the fraction of added mesytilene. Data from [11] 3-5
- 3.4 Relative planarization of a 300 nm thick layer of BCB with (blue dotted line) and without oxygen plasma exposure (blue line) on the $220 \text{ nm} \times 1 \text{ }\mu\text{m}$ height surrounded but trenches of 5 or 10 μm SOI cross-section (red and green line). Two different patterns are etched in the SOI layer : Zone A (red line) - 300 nm width silicon wire inserted in 5 microns trenches separated by 15 microns of silicon, Zone B (green line) - 300 nm width silicon wire inserted in 10 microns trenches separated by 10 microns of silicon. Inset correspond to a photography of the sample. 3-6
- 3.5 Photograph of a bonded InP layer (blue zone on the right) above a SOI chip patterned with waveguides (left part of the picture) . . . 3-7
- 3.6 Alignment technique : red cross represents the marks defining the basis (blue lines) used for silicon waveguide definition in the CMOS line against the basis of the e-beam writer (blue dotted lines). Green square represent the PhC location. 3-8
- 3.7 SEM picture of an InP PhC waveguide, of 50 microns long, etched on top of silicon wire, clear alignment between the two levels is visible 3-10
- 3.8 PhC etching process (vertical view), a) PC pattern transferred through the PMMA positive resist (in pink) in the hard mask (in green), b) etched PC in the InP (grey zone) after removing of the masks, c) MAN, negative electron resist, cap layer (orange) after a second alignment step and development of the latter resist, d) PhC after removing of the surrounding InP 3-10
- 3.9 Picture of the sample at different process step : a) picture of the PMMA after e-beam insolation, b) etched Si_3N_4 hard mask picture, c) SEM of the etched hard mask, d) picture etched InP below the hard mask, e) picture of the etched InP, f) final result after the surround InP removal, note the visible silicon layer below and waveguides in pink which attest for the accuracy of the alignement method. 3-11
- 3.10 AFM profile (left) and top view (right) of first generation hybrid PhC waveguides 3-12

-
- 3.11 Fitted data showing the located hole centers (+ crosses) and the fitted lattice (* asterisks joined by continuous zig-zagging line). The cross (\times at 2.669,1.324) shows the predicted end of the PhC waveguide. The waveguide center is shown as a noisy line and the linear fit (overlaid) predicts the intersection between the center of the waveguide and the PhC facet at the position marked by the darker cross (+ at 2.669,1.338). 3-14
 - 3.12 The fitted alignment offset tolerances for nine $90\ \mu\text{m}$ PhC long waveguides, along with the error in determining the waveguide position, WG error. 3-15
 - 3.13 The variation in coupling length of an InP-based ($255\times 360\ \text{nm}^2$) wire phase matched to a ($220\times 360\ \text{nm}^2$) Si wire as a function of the (a) vertical and (b) lateral offset between the guides at a constant vertical offset of 400 nm for $\lambda = 1.55\ \mu\text{m}$ 3-15
 - 3.14 Energy transfer between two similar waveguides against wavelength for initial parameter $a_1=1$ and $a_2=0$, the line correspond to waveguide 1 and the dashed line to waveguide 2, for two different detuning - blue correspond to zero detuning and then a maximum transfer of 100 percent, - green correspond to a detuning of 3 percent with a maximum energy transfer around 96 percent 3-16

 - 4.1 Example of photonic crystal structure, from left to right : 1D Bragg mirror of alterned AlOx/AlGaAs layers (LPN), InP photonic crystal with a line of holes removed to form a waveguide (LPN), 3D TiO₂ inverse opal [3] 4-2
 - 4.2 The multilayer film, a one-dimensional photonic crystal. The term “one-dimensional” is used because the dielectric function $\epsilon(z)$ varies along one direction (z) only. The system consists of alternating layers of materials (blue and green) with different dielectric constants, with a spatial period a in the z direction. We imagine that each layer is uniform and extends to infinity along the x and y directions. 4-6
 - 4.3 The photonic band structures for on-axis propagation, as computed for three different multilayer films. In all three cases, each layer has a width $0.5a$. *Left* : every layer has the same dielectric constant $n = 3$. *Center* : layers alternate between n of 3.3 and 2.5. *Right* : layers alternate between n of 3.3 and 1. The yellow shaded zone correspond to the bandgap. Modelled with FDTD. . . 4-7
 - 4.4 Low group velocity and balance between forward and backward propagating modes intensity (respectively left and right vertical axis) against a “detuning parameter” $\delta \propto (1 - \frac{\omega_B}{\omega})/M$, where ω_B is inversely proportional to the periodicity of the structure and M is the reflectivity strength at the interfaces. Moreover, δ allows the discrimination between the evanescent modes, when $\delta^2 < 1$, and the propagating modes, when $\delta^2 > 1$ 4-8

-
- 4.5 Intensity corresponding to the band edge modes in fig. 4.3 right. (a) correspond to the mode at the lowest band edge (point B) and (c) to the mode at the upper band edge (point A). (b) is the index profile of the structure, blue zone correspond to index equal to 1, and brown to index equal to 3.3. The distinction, via intensity localisation, between valence and conduction band modes appears clearly. Modelled with FDTD. 4-9
- 4.6 The triangular lattice in real space (left pannel), the corresponding reciprocal space (middle panel) with possible basis axis and the related Brillouin zone (right panel). From [7] 4-10
- 4.7 The photonic band structure for the modes of a triangular array of air columns drilled in a dielectric substrate ($n=2.8$). The blue lines represent TE bands and the red lines represent TM bands. The shaded regions, blue and red, represents the bandgaps of respectively TE and TM modes). Superposition of the shaded regions correspond to a full bandgap. The inset represent the symmetry axis followed in drawing the band diagram encapsulating the irreducible Brillouin zone. Modelled with FDTD. 4-11
- 4.8 Profile of the modes corresponding to point A-D of band structure plotted on fig. 4.7. Modelled with FDTD. 4-12
- 4.9 Gap map for a triangular lattice of air holes in a dielectric ($\epsilon=11.4$). From [7] 4-13
- 4.10 Harmonic mode frequencies for a plane of material of dielectric constant $\epsilon=11.4$ and thickness a surrounded by air. The shaded blue region is a continuum of states that extend into both the high index material and air around it. The red line is the light line $\omega = ck$. This plot shows modes of only one polarization, for wich H is perpendicular to both the z and k directions. From [7]. 4-14
- 4.11 Band structure of fig. 4.7 with added light and substrate line (respectively yellow region and black dotted line). Modes above these lines are coupled to the surrounding material (resp. air or BCB) and as a result are lossy. Modelled with FDTD. 4-15
- 4.12 Eigenfrequencies (left panel) and field distributions (right panel) of localized cavity states for TE-polarized light in a 2D photonic crystal composed of a triangular lattice of air pores ($r/a=0.45$) in a dielectric matrix ($n=3.3$) against a variation of the index of a single hole. The field distributions display the magnetic field intensity. Depending on the strength n_{defect} of this deviation, different types of cavity modes such as doubly degenerate dipoles, (a), and quadrupoles, (b), as well as non-degenerate second-order monopoles, (c), and hexapoles, (d), develop. 4-17

-
- 4.13 Photonic nanocavities using a 2D photonic-crystal slab. a) Schematic of the base cavity structure having a triangular lattice of air holes with lattice constant a ($= 0.42 \mu\text{m}$). The thickness T of the slab and the radius R of the air holes are $0.6a$ ($0.25 \mu\text{m}$) and $0.29a$ ($0.12 \mu\text{m}$), respectively. b) Starting cavity structure with three missing air holes in a line. c) Designed cavity structure created by displacing the air rods at both edges to obtain an ultrahigh Q/V value. From [11] 4-18
- 4.14 a) The electric field profile (E_y) of the fundamental mode of the cavity of fig.4.13.b. b) The Fourier Transform (FT) spectra of a). The region inside the grey circle corresponds to the leaky region. c) and d) The electric field profile and 2D FT spectrum, respectively, for the slightly modified cavity shown in fig.4.13.c. The displacement of the air rods at the edges is set at $0.15a$ from the starting structure shown in fig.4.13.b. From [11]. 4-19
- 4.15 The 3D PhC bandstructure calculated using a guided mode expansion for an InP membrane with a BCB substrate and air superstrate (with air holes). The thick line (marked odd) corresponds to the odd TE-like defect mode and the thick line (marked even) the even TE-like defect mode. The TE-like band edge modes are shaded. The TM-like lattice modes are plotted as dotted lines. The period is $a=435 \text{ nm}$, hole radius $r=0.3 a$ and the height of the InP is 255 nm , the supercell is $5\sqrt{3}a$ wide. 4-21
- 4.16 Left - Dispersion relation of W1 waveguides for H-polarized light in a 2D photonic crystal composed of a hexagonal lattice of air pores (radius $r/a=0.34 a$, $a=435 \text{ nm}$) in a dielectric matrix ($n_{\text{host}}=3.3$) where the dielectric function of a row of pores has been modified (see inset). Shaded yellow regions correspond to the band gap of the surrounding PhC. Depending on the strength ϵ_{def} of this modification, we can tune the position of the different guided modes. For low values of the dielectric function (blue lines, $n_{\text{def}} = 2.2$), broad-band mono-mode waveguiding behaviour occurs, whereas for high values of the dielectric function (red lines, $n_{\text{def}} = n_{\text{host}}$), corresponding to non-etched pores the modes are shifted and the system begins to have a multi-mode behaviour. Right - Field profile for the symmetric and anti-symmetric mode in the case of $n=2.2$, corresponding respectively to point a) and b) on the dispersion curve. 4-22
- 4.17 Different type of optical trap and their respective Q factor and modal volume characteristics. From [26]. 4-23
- 5.1 Eigenmode expansion method. The structure is divided into sections. In each section the refractive index does not change along the propagation direction. 5-2

5.2	Example of a Yee cell in 2D. The points where the E and H field are calculated are space by half a period of this cell interleaving these two fields.	5-5
6.1	Close view of the basis of the experimental setup	6-1
6.2	Left - Schematic view of the $10 \times 10 \mu m^2$ gratings couplers etched in a SOI layer embedded in BCB. The fiber is tilted with an angle of approximatively 11 degrees for efficient coupling. Right - Transmission spectra of grating couplers.	6-2
6.3	Back imaging using a IR camera. Silicon waveguide and PhC structures are clearly visible, the white spot corresponding, this time, to the emission of the PhC.	6-4
6.4	General scheme of the experimental setup. Blue, red and green color line correspond respectively to short infrared, near infrared and visible light paths. Elements 1 and 2 correspond respectively to Mitutoyo objectives, dichroic mirror (transmitive at $1.5 \mu m$ and reflective at $0.8 \mu m$; elements 3 and 4 correspond to 700 to 900 nm beam splitters.	6-5
7.1	Hybrid III-V PhC/SOI wire structure and experimental configuration. The III-V semiconductors is a 265 nm InP based membrane with 4 QWs composing the gain medium. Our PhC defect waveguide hybrid structure is optically surface pumped, as indicated by the red arrow. The underlying Si wire waveguide captures the laser emission which is then diffracted by a grating coupler and collected by a cleaved SMF (blue arrow).	7-2
7.2	The 3D PhC bandstructure calculated using a guided mode expansion for an InP membrane with a BCB substrate and air superstrate (with air holes). The inset is a schematic top view of the linear defect inserted in the PhC, the blue line σ illustrate the symmetry plane considered. The thick line (marked odd) corresponds to the odd TE-like defect mode and the thick line (marked even) the even TE-like defect mode. The TE-like band edge modes are shaded. The TM-like lattice modes are plotted as dotted lines. The period is $a=435$ nm, hole radius $r=0.3a$ and the height of the InP is 255 nm, the supercell is $5\sqrt{3}a$ wide.	7-3
7.3	The TE-like (solid line) and TM-like (dashed line) modes of a 220×300 nm ² Si waveguide with a SiO ₂ substrate, and BCB superstrate. The light cones of the various cladding materials, air, SiO ₂ , and BCB are denoted by shading. The vertical dotted lines mark the range of lithographic tuning in the experiment. The horizontal line marks the peak gain wavelength of our QWs.	7-5

-
- 7.4 (a) Bandstructure for InP W1-Si wire (326 nm wide) hybrid system, for a period, $a=455$ nm, $r/a=0.3$, and a vertical separation of 400 nm (BCB layer). The ripple seen in the band structure is mainly due to coupling with lower Q modes. (b) The PL spectrum, coupled out via the Si wire, showing a single peak whose spectral position is consistent with the intersection with the even TE-like W1 mode. (c) Zooming in to the region of k -space close to the K point, we can observe at $k_x = 0.475 \times \pi/a$, $u=0.275$ an anti-crossing caused by the co-directional coupling between the odd TE-like W1 mode and the odd TE-like Si wire mode. 7-6
- 7.5 (a) Band structure for InP W1-Si wire (326 nm wide) coupled system, for period $a=405$ nm, $r/a=0.3$, and a vertical separation of 400 nm (BCB layer). (b) The PL spectrum, coupled out via the Si wire. As the emission is dominated by odd modes, here we only plot the even bands in the region $k_x=0.45-0.5 \times 2\pi/a$. The dashed black lines denote the emission bandwidth of our QWs. 7-7
- 7.6 SEM image of a PhC waveguide bonded on top of a silicon wire . 7-8
- 7.7 Photoluminescence spectra, measured via the silicon wire, of PhC waveguides with a varying period a , from 405 to 415 and 425 to 455 nm (from bottom to top - respectively blue and red curves) by steps of 10 nm, while keeping the ratio r/a constant. 7-9
- 7.8 The spectral positions of the various bands at the K point, $k_x = \pi/a$ as a function of PhC period. The top solid line represents the odd TE-like Si wire mode. The middle dot-dashed line denotes the odd TE-like W1 mode. The lower dashed line represents the even TE-like W1 mode. The crosses are surface detected PL. The PL extracted via the Si waveguide from the even mode is marked by squares and the circles correspond to the Si Bragg mode edge. . . 7-10
- 7.9 (a) Laser emission power captured by the Si wire as a function of the pump power in log-log scale. (b) Inset: laser spectrum at 1 mW pump power. (c) Laser peak wavelength as a function of pump power. (d) Laser FWHM as a function of pump power. . . . 7-12
- 7.10 (a) Band structure calculated using guided mode expansion for the W0.65 PhC membrane with a BCB substrate and air upper cladding (with air holes). Laterally odd modes are shown in blue, even in red. The thick blue line corresponds to the odd TE-like defect mode. The odd TE-like band edge modes are shaded in cyan. The odd and even TM-like lattice modes are plotted as fainter dotted lines. Low-vg modes are denoted A, B, and C. The light cones of the various cladding materials, air, SiO₂, and BCB are denoted by progressively darker shading for lower index. (b) Dispersion relation of TE-like modes of the hybrid structure calculated using 3D FDTD for wavevectors around π/a . Both coupled super-modes (solid lines) and uncoupled modes (dashed lines) are represented. . 7-13

7.11	Experimental setup of the system pumped via the silicon wire. TM polarised (in the Si wire) pump pulse at $1.18 \mu m$ is injected on the left side from the 12 tilted fiber. TE polarised (in the Si wire) at $1.55 \mu m$ is extracted via the 10 tilted fiber on the right.	7-14
7.12	(a) PL spectrum of the hybrid structure. The three peaks, A, B, and C correspond to the low-vg modes of fig.7.10.a and fig.7.10.b Laser emission intensity observed in mode A vs pump pulse energy.	7-15
7.13	(a) Peak emission wavelength vs pump energy; (b) FWHM vs pump energy.	7-16
8.1	SEM image of the sample	8-2
8.2	(c)-(f) Different vertical profiles of the magnetic field for different ratio a/λ in the upper part the Bloch mode of the mirror and in the lower part the fundamental mode of the wire surrounded by air ($n = 3.48$, width = 420 nm and height = 230 nm). From [11]	8-3
8.3	Evolution of the band structure against various holes radius and a fixed period of 315 nm in a 500 nm wide SOI wire. The yellow line represents the light line.	8-5
8.4	Band structure for every “pattern” of the cavity. The three first taper zones (black square- red triangles - green rhombus) and mirror (blue circles) respectively r equal to 69.5, 85.5, 99 and 97 nm and period a equal to 320, 337, 347 and 376.5 nm.	8-6
8.5	Top view of the E_y field for the second order (a) symmetric mode and anti-symmetric mode (b). The thick dotted line denotes the symmetry axis (σ_x) taken for the cavity mode.	8-8
8.6	Resonance wavelength plotted against cavity length. 3D FDTD simulation results are joined by dashed lines, and the dots show the corresponding experimental measurements. Arrow points to the second order symmetric mode.	8-8
8.7	Modelling of 2D wire cavities with (green dots) and without (blue squares) taper inserted. The mirror parameters are : period $a=0.376$ nm and holes radius $r=0.098$ nm.	8-10
8.8	Field profile of cavity modes for different wavelengths - a) $\lambda=1500$ nm, b) $\lambda=1550$ nm, c) $\lambda=1630$ nm.	8-11
8.9	Q factor extracted from the 3D FDTD simulations as a function of the resonance wavelength - blue circles correspond to the symmetric mode indicated by an arrow in fig.8.6 and red triangles to the anti-symmetric mode of a higher order.	8-12
8.10	Far field (top) and far field intensity (bottom) profiles for the symmetric (right) and anti-symmetric (left) modes. Note that the intensity scaling of the symmetric mode is 4 order of magnitude higher than the one used for the anti-symmetric mode.	8-13
8.11	Modal volume and confinement factor as functions of the resonance wavelength.	8-14

8.12	Measured threshold and corresponding fit of rate equations versus pump power. (a) Spectrum under lasing operation. (b) PL spectrum of the QWs.	8-15
8.13	Threshold of the studied cavities plotted as a function of the emission wavelength.	8-17
8.14	Experimental Q factors and modelled Q factors as functions of cavity length.	8-18
8.15	Scheme of the hybrid system: III-V semiconductor wire cavity bonded on top of a SOI wire. Gratings at the extremity of the 6 mm long silicon wire, allows extraction or injection of light via coupling to a single mode fiber.	8-19
8.16	Index of the 2 first modes of coupled InP wire of variable width (height=255nm) with a silicon wire (500×220nm) separated by a 465 nm thick BCB intermediate layer. Doted line correspond to the index of an uncoupled wire. Field profiles of points A-F are plotted on fig.8.17. Inset : Θ correspond respectively to the index difference between the symmetric and anti-symmetric and Δ the splitting between the original modes and the symmetric or anti-symmetric modes.	8-20
8.17	Modes profiles of the coupled system for different phase matching conditions, points A-F of fig.8.16. The field profile at the matching point (C and D) reveals two modes (symmetric and anti-symmetric, phase not shown here) where the field is located simultaneously in both waveguides.	8-21
8.18	Evolution of the cavity Q factor against the BCB intermediate layer thickness (ie. the thickness of BCB between the lower surface of the InP wire and the highest surface of the silicon wire), red dashed line correspond to the Q factor of the unloaded cavity .	8-22
8.19	SEM picture of an aligned wire cavities on top of a silicon wires .	8-23
8.20	Emitted light, extracted via the silicon wire, versus pump power for a coupled cavity operating at 1525 nm	8-23
8.21	SEM image showing pairs of cavities on single silicon wires. . . .	8-24
8.22	Lasing of four cavity pumped at the same time via the silicon wire at 1.1 micron.	8-25
8.23	Coupling scheme of a cavity and a waveguide with important parameters such as the coupling factor κ , the optical losses of the cavity (blue arrow) τ_{cavity} , the field amplitude in the cavity $a(t)$, and light incoming/outgoing from the right $S_{\pm 2}$ or left $S_{\pm 1}$	8-25
8.24	Plot of the theoretical transmission of the system depicted in fig.8.23 against τ_G expressed in fraction of τ_0	8-27
8.25	Schematic view of the pump probe experimental preparation. . . .	8-28
8.26	Typical transmission spectra measured for increasing pump power (from bottom to top)	8-29
8.27	Intensity of the transmission against pump power	8-30

8.28	Light-in/light out curve attesting continuous laser operation under 1.18 microns pumping (blue triangles) and FWHM (green dots) against pump power.	8-31
9.1	Emission intensity at λ (blue line) while injecting, at $\lambda + \delta\lambda$, the system, with various intensity, via the silicon wire (yellow line). It can be seen that the emission falls to zero for a given value of injected light and begin to recover its unperturbed emission state for a second value. The continuous variation of the injected light combined with the difference Δ (green lines) for which emission is turned off and after turned on indicate the existence of an hysteresis cycle.	9-4
9.2	Possible signature of loss recycling. While the increase of the Q factor can be foreseen for longer cavities, unexpected high Q appears for the smallest cavities modelled. Blue and Green dots correspond respectively to symmetric and anti-symmetric modes of the system.	9-6
9.3	Possible scheme for the doubly resonant cavities.	9-8

Resumé en francais

La photonique peut être définie, au sens large, comme l'étude des interactions entre la matière et la lumière dans un cadre où la nature duale, ondulatoire et corpusculaire, de cette dernière est prise en compte. Le développement de ce champ de recherche a permis de mieux comprendre l'origine de ces interactions entre la lumière et la matière et de démontrer la possibilité d'émettre, de détecter, de moduler ou encore de convertir la lumière. Ces études ont, entre autre, abouti à la réalisation d'un certain nombre de composants qui occupent aujourd'hui une place importante dans le monde des télécommunications. Le développement des lasers, la mise au point de fibres optiques, d'amplificateurs permettant de régénérer un signal ou encore de détecteurs pour la conversion d'un signal lumineux en signal électrique, sont autant d'exemples de composants qui ont permis d'enrichir le panel d'outils disponibles pour le traitement de l'information et augmenter ainsi considérablement le débit ou encore les distances accessibles. Cet apport au monde des télécommunications étant acté, l'optique est alors présentée comme une possible alternative à l'électronique [1], qui est confronté aujourd'hui à un certain nombre de limites, pour des fonctions très spécifiques telles que le traitement du signal à l'échelle d'une puce ou pour la communication inter-processeurs.

Ces avancées technologiques sont indissociables d'une connaissance relative des propriétés des semiconducteurs III-V. En effet, la particularité de ces matériaux est de posséder un gap électronique direct, ceci ayant pour conséquence de favoriser l'émission spontanée et stimulée, faisant des semiconducteurs III-V des matériaux idéaux pour la réalisation de lasers [2]. De plus, des développements techniques relativement récents [3] [4] ont permis la croissance contrôlée d'alliages de semiconducteurs III-V permettant la réalisation de puits quantiques, dont les niveaux d'énergie balayent le spectre des longueurs d'onde du visible au proche infra-rouge, et donc la réalisation de détecteurs et de sources sur cette large gamme de fréquences. Enfin, la possibilité de moduler l'indice de ces matériaux par l'action d'un pompage optique ou l'injection de courant permet d'envisager des structures "actives" permettant de réaliser des fonctionnalités tel que des "switchs" ou des "mémoires" optiques.

La photonique s'est enrichie, au début des années 80, grâce à un intense développement technologique porté par l'industrie électronique, d'un degré de liberté rendu accessible par la structuration de la matière à l'échelle de la centaine de nanomètres. Les structures ainsi réalisables [5] ont ouvert la voie à de nouvelles possibilités, en permettant de contrôler finement la propagation de la lumière ou encore de la stocker pour un temps τ_p ($\propto Q$) relativement long dans de très

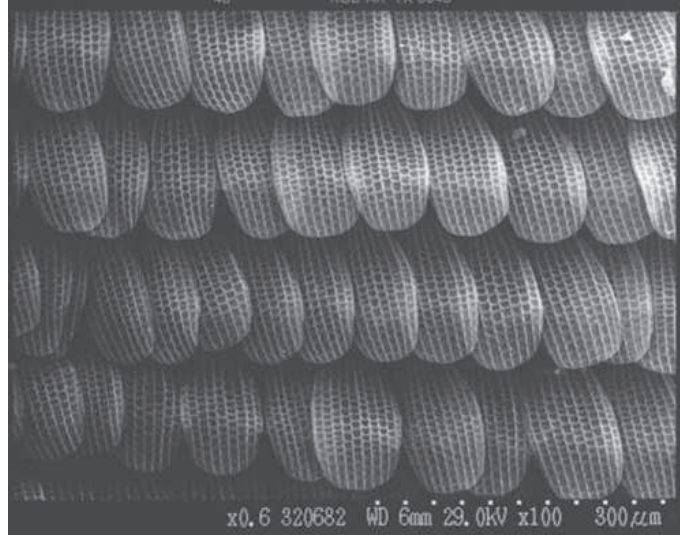


Figure 1: Image d'une aile de papillon réalisé à l'aide d'un microscope électronique à balayage. [Université d'Exeter]

petits volumes V , avec pour principale conséquence un plus grand contrôle et l'exaltation des interactions entre la lumière et la matière. Parmi ces structures, les "cristaux photoniques" [6] [7], consistant en un agencement périodique de différents matériaux tels le motif à l'origine de l'iridescence des ailes de papillons, visibles fig.1.1, présentent un attrait tout particulier. En effet, parmi les différentes structures connues dans le champ de la photonique (anneaux, sphères, etc.), ils permettent d'obtenir, par l'introduction de défauts localisés ou linéiques, d'une part le meilleur ratio Q/V [5] et d'autre part un contrôle très précis, grâce à la diversité des designs possibles, de la propagation d'un flux lumineux et de la vitesse de groupe v_g associée au mode guidé [8].

La combinaison de ces deux éléments, à savoir les semiconducteurs III-V et la nano-structuration de la matière, permet alors d'envisager le traitement efficace d'un signal lumineux par des composants de dimensions micro-métriques et ouvre ainsi la voie à l'optique intégrée moyennant la réalisation d'un certain nombre de préalables. La première condition étant de compléter ces blocs élémentaires "actifs" de guides permettant l'inter-connexion entre différents éléments, la seconde étant de proposer une solution complémentaire et compatible avec la fabrication des composants électroniques. Une partie de ces prérequis est réalisée en exploitant les propriétés optiques, l'existence d'un oxide naturel (SiO_2) bas indice et la qualité de fabrication de structures à base de silicium. Il est en effet possible de réaliser des composants, dits "passifs", tels que des de/multiplexeurs [9] ou des guides de très bonne qualité [10] dans ce matériaux. Ceci étant dit, il est important de noter ici, que d'une part le silicium et d'autre part les semiconducteurs III-V

sont respectivement des matériaux inappropriés pour la réalisation de fonctions actives, en raison du gap électronique indirect du silicium, ou passives, en autre en raison de l'absence d'un oxide naturel bas indice de bonne qualité. Apparaît alors clairement le potentiel que représente l'association de ces deux matériaux dans le but de réunir au moyen d'une seule et unique structure des fonctions optiques actives et passives. Un certain nombre d'options se présentent en vue de réaliser cette combinaison, tout en gardant un maximum de compatibilité avec les standards de fabrication des composants électroniques. La première approche consiste à faire croître les semi-conducteurs III-V directement sur le silicium [11]. Mais en raison d'un important desaccord de maille et de coefficients d'expansion thermique trop différents cette croissance est délicate et mène généralement à des dislocations dans la couche de semi-conducteurs III-V [12]. En conséquence les propriétés optiques et électronique sont fortement détériorées. Une autre approche, moins contraignante d'un point de vue technique, consiste à "coller" ces deux matériaux au moyen d'une couche intermédiaire, de SiO_2 ou de polymère par exemple, relaxant ainsi les contraintes matériaux évoquées précédemment. Cette méthode, validée par l'expérience, a d'ores et déjà permis la réalisation de lasers [13] ou flip-flop [14].

Les points évoqués lors des paragraphes précédents nous amènent donc à l'énoncé

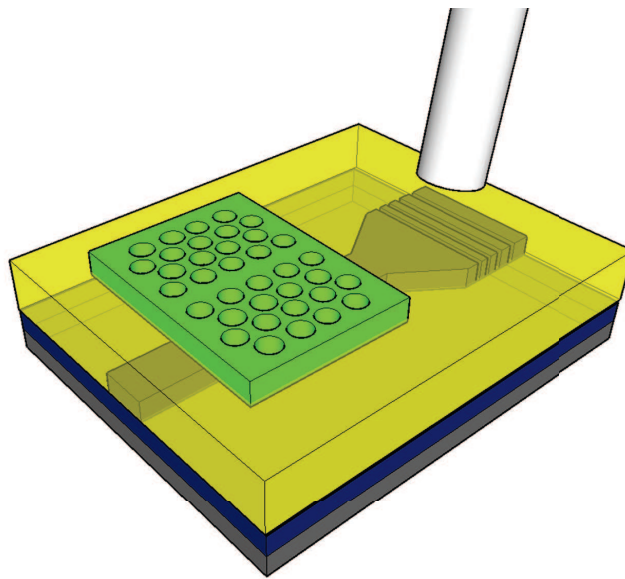


Figure 2: Vue schématique de la structure hybride étudiée. Le niveau inférieur (bleu/gris) consiste en un guide silicium pour le guide de la lumière. A l'extrémité du guide de silicium sont gravés des réseaux permettant le couplage à une fibre optique pour l'injection et l'extraction de lumière dans le système. Le niveau supérieur (vert) est un cristal photonique en semiconducteurs III-V à la source des effets non-linéaires étudiés.

de la problématique qui a fait l'objet de ce travail de thèse, à savoir : la conception, la réalisation et l'étude de structure hybrides, telles représentée fig.7.1, combinant un cristal photonique en semiconducteur III-V, au sein duquel sont incorporés des puits quantiques permettant la réalisation de fonctions actives telle l'émission, et d'un guide de silicium, et d'un guide d'onde en Silicium permettant de réaliser les fonctions dites passives, tel le guidage rendant potentiellement possible l'insertion de cette unité au coeur d'un système plus complexe connectant différents éléments optiques, voir électroniques. Les deux matériaux étant unis au moyen d'une technique de collage adhésif, par une couche intermédiaire de polymère, le Benzocyclobutene (BCB), déposée au préalable sur le substrat de silicium et recuite à 250 degrés [15]. Le résultat étant donc une structure à deux niveaux, d'une part de Silicium, d'autre part de semi-conducteurs III-V. Compléter la description de la structure et de la méthode employée lors de la fabrication amène à préciser que les guides sur le niveau silicium ont été gravés avant le collage. Il est à noter, qu'à chacune des extrémités de ce guide sont gravés des réseaux [16] permettant le couplage à une fibre optique, et ainsi l'injection et l'extraction de lumière. L'un des aspects les plus intéressants de la technique de collage utilisé apparaît puisqu'il est en effet possible, grâce aux propriétés de planéarisation du BCB, de travailler à partir d'un niveau silicium structuré antérieurement. La dernière étape menant à la réalisation de la structure hybride, consiste ensuite à graver, après collage, un cristal photonique dans le niveau supérieur. Les deux niveaux, le guide de silicium et le cristal photonique en semiconducteur III-V, séparés par une couche de quelques centaines de nanomètres de BCB, sont couplés par "couplage évanescent" [17]. Ce type de couplage permet un échange de 100 % d'énergie entre les deux niveaux tout en ayant un impact mineur sur les propriétés optiques de chacun des deux niveaux. Dans ces conditions, les deux niveaux peuvent être ainsi considérés comme deux structures optiques partiellement indépendantes, c'est-à-dire que la lumière est uniquement localisée dans l'une ou l'autre des deux structures, par opposition à une délocalisation partielle du mode simultanément dans les deux niveaux. Pour réaliser efficacement un tel type de couplage deux contraintes fortes s'imposent: mettre en jeu deux structures aux modes optiques satisfaisant le critère d'accord de phase, ie. ayant un indice effectif similaire, et aligner "parfaitement" ces deux niveaux. La première de ces contraintes est levée au moyen d'un judicieux travail de modélisation, la seconde nécessite la mise au point d'une nouvelle méthode appropriée pour l'alignement des deux niveaux avec une précision de l'ordre de la centaine de nanomètres.

Un important travail de développement a donc été nécessaire pour permettre la réalisation des structures hybrides, et notamment la mise au point d'une procédure d'alignement permettant le contrôle du couplage entre les deux niveaux. En parallèle, l'un des premiers résultats obtenus lors de ce travail technologique a été l'amélioration de la technique de collage. En effet, une amélioration sensible a été apportée à la technique de collage, mise au point dans le groupe Intec-Photonics à l'université de Gand, par le dépôt d'une couche de SiO_2 à l'interface entre le semiconducteur III-V et le BCB. Ainsi, le rendement de collages de pièces de quelques millimètres carrés, initialement de 50% a ainsi été élevé à quasiment 100

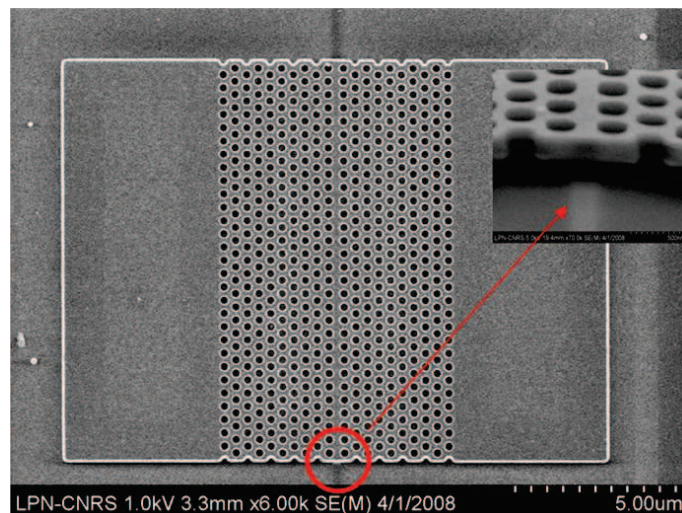


Figure 3: Image obtenue au microscope électronique d'un échantillon fini. Le guide en cristal photonique, de 10 microns de long, apparaît parfaitement aligné sur le guide silicium visible par transparence sous le BCB. La grossissement faisant clairement apparaître la structure à deux niveaux.

%. De plus, l'emploi d'une épaisseur variable de SiO_2 à permis un contrôle plus précis de la distance séparant les deux niveaux. L'alignement des deux niveaux, intervenant ensuite, est réalisé via la détection automatique, au moyen d'un faisceau d'électrons à 100 keV, de marques pré-gravées dans le niveau silicium, permettant de localiser avec précision la position des guides, la détection des marques précédant ainsi l'étape de lithographie électronique, et d'exposition de la résine définissant le motif périodique à graver dans le plan de la couche de semiconducteur III-V. La qualité de l'alignement obtenu par l'emploi de cette procédure, à l'état de l'art, est supérieure à 30 nm, bien au dessus des valeurs, extraites de modelisations ou calculs, requises pour le contrôle du couplage évanescent entre les deux niveaux [18]. L'image 6 obtenue avec un microscope électronique permet d'apprécier la qualité de l'alignement, de plus la structuration à deux niveaux est clairement visible. Enfin, la gravure des niveaux silicium et semiconducteurs III-V, respectivement réalisés dans le salle blanche de l'IMEC et du LPN, étant des technologies bien maîtrisées aucun n'apport n'a été nécessaire sur ce point. Le niveau en silicium étant gravé après insolation d'une résine sensible aux ultraviolet dans une ligne CMOS (complementary metal oxide semi-conductor) [19], et les cristaux photoniques gravés en plusieurs étapes, au moyen d'une insolation d'une résine électrosensible et de gravure physico-chimique à travers un masque de SiN [20].

Un cristal photonique 2D, ou motif périodique de trous, est donc gravé dans la couche de semiconducteur III-V, le confinement vertical étant assuré par reflec-

tion totale interne, où la différence d'indice optique entre le semiconducteur III-V et les deux interfaces BCB/air. Deux différents types de structures à cristal photonique ont été implementées au cours de ce travail. La première étant un guide à cristal photonique, qui permet d'accéder à des modes à faible vitesse de groupe v_g [21]. Le second étant une cavité ayant la caractéristique de permettre d'obtenir un ratio Q/V raisonnablement grand [22]. Le travail de modélisation s'est donc d'abord orienté vers la réalisation de structures aux propriétés de guidage et confinement au pic d'émission des puits quantiques (1530 nm) insérés dans la couche de semiconducteur III-V. Ce travail ayant été rendu délicat par la présence du substrat de BCB, d'indice de refraction relativement élevé, restreignant drastiquement la fenêtre de fréquences où le confinement vertical est effectif. En parallèle, il faut garder à l'esprit la finalité des structures modélisées, à savoir être couplées au guide de silicium sous-jacent, possédant donc des modes en accord de phase avec le mode du guide de silicium. Ce travail a ainsi permis de développer des guides d'onde aux modes lents et des cavités à fort ratio Q/V dont les modes confinés dans le niveau supérieur sont couplés de manière évanescente au guide de silicium gravé dans le niveau inférieur.

Expérimentalement, un dispositif satisfaisant aux critères d'alignement, à l'échelle de la centaine de nanomètres, des fibres avec les réseaux de silicium d'une part, pour l'injection ou l'extraction de la lumière, et de la pompe, à 800 nm et pulsée, focalisée sur le défaut dans le cristal photonique. C'est ainsi qu'il a été possible de démontrer l'émission laser, des deux types de structures étudiées, couplée au guide de silicium [21] [18] [23]. En complément, une exploration non exhaustive de nombreux paramètres, tels la taille des trous, la période du motif périodique du cristal photonique ou encore la taille des cavités, nous ont permis de démontrer un très bon accord entre les modélisations effectuées et les structures réalisées [22] [18]. Ainsi, les longueurs d'onde d'émission ou encore les seuils sont parfaitement corrélés avec les résultats attendus à partir du travail de modélisation. Ces études ont permis de mieux appréhender les mécanismes à l'origine du couplage dans nos structures hybrides, et finalement de mettre au point une expérience permettant de quantifier, le paramètre critique qu'est l'intensité du couplage entre les deux niveaux. En effet, la transmission d'un système composé d'une cavité couplée à un guide est intrinsèquement liée à l'intensité du couplage entre ces deux éléments. Ainsi, par l'étude de la transmission totale de notre système, sous différentes conditions de pompage, nous avons été capable d'évaluer qu'environ 80 % de la lumière émise dans le niveau supérieur est extraite via le guide de silicium. Cette valeur particulièrement élevée, en partie grâce au travail de modélisation concernant cet aspect des structures hybrides et en partie due à la qualité du processus de fabrication, permet d'obtenir des intensités dans le guide de silicium de l'ordre de quelques micro-watts. Deux éléments complètent cette étude des lasers "hybrides", en premier lieu nous avons démontré le bénéfice apporté par un tel schéma puisqu'il nous a été possible de faire du guide de silicium un double emploi en l'utilisant pour le guidage d'une pompe à 1.2 microns [21], à la limite de transparence du silicium et au dessus du niveau des barrières des puits quantiques. Ensuite, par pompage à cette même longueur d'onde l'émission laser en continu à

été observée [23]. Ce résultat est en partie dû au fait que l'échauffement induit par le pompage est plus faible qu'à 800 nm et en partie grâce à l'ajout de la couche intermédiaire de SiO_2 plus favorable à l'évacuation thermique vers le substrat de silicium que ne l'est le BCB très peu conducteur.

En résumé, ce travail a donc permis la mise au point et l'étude de lasers "hybrides", où l'émission d'un cristal photonique en semiconducteur III-V est couplée à un guide de silicium. L'accord entre les résultats expérimentaux et la modélisation met en valeur, d'une part la qualité du procédé de fabrication, et notamment la procédure d'alignement, à l'état de l'art, supérieur à 30 nm, et d'autre part une bonne compréhension du système ayant permis de réaliser des structures efficaces où 80 % de la lumière émise est extraite et potentiellement acheminée sur de relativement longues distances via le guide de silicium. Ainsi, il est possible d'imaginer la structure réalisée comme un potentiel composant de base pour l'optique intégrée, les dimensions, le seuil et l'intensité de la lumière couplée dans le guide de silicium mesurés, bornes inférieures de ce qu'il est possible d'obtenir avec un tel système, sont en effet pertinentes dans ce contexte. Enfin, pour aller plus loin dans cette direction, ie. le traitement tout optique d'un signal, la réalisation d'autres composants, tels que des mémoires optiques sera nécessaire. Le comportement bistable, que laisse présumer les toutes dernières expériences réalisées, des cavités hybrides mises au point, permet d'envisager la réalisation d'une telle fonctionnalité.

References

- [1] D. A. B. Miller. Proc. IEEE, 88:728, 2000.
- [2] J. D. Kingsley T. J. Soltys R. N. Hall, G. E. Fenner and R. O. Carlson. *Coherent Light Emission From GaAs Junctions*. Phys. Rev. Lett., 9:366368, 1962.
- [3] A.Y. Cho and J.R. Arthur. Prog. Solid State Chem., 10:157, 1975.
- [4] O.Thomas R.Madar A.Abrutis. J.P.Senateur, F.Weiss. Patent No 93/08838 PCT No FR94/00858 (Europe, U.S.A.), 1993.
- [5] K. J. Vahala. *Optical microcavities*. Nature, 422, 2003.
- [6] John S. *Strong localization of photons in certain disordered dielectric superlattices*. Phys. Rev. Lett., 58:2486–9, 1987.
- [7] Yablonovitch E. *Inhibited spontaneous emission in solid-state physics and electronics*. Phys. Rev. Lett., 58:2059–62, 1987.
- [8] Toshihiko Baba. *Slow light in photonic crystals*. Nature Photonics, 2:465–473, 2008.
- [9] F. Copping P. D. Trinh, S. Yegnanarayanan and B. Jalali. *Silicon on-insulator (SOI) phased-array wavelength multi-demultiplexer with extremely low-polarization sensitivity*,. Appl. Phys. Lett., 9:940942, 1997.
- [10] W. Bogaerts and al. *Nanophotonic waveguides in silicon-on-insulator fabricated with CMOS technology*. J. Lightwave Technol., 88:401–412, 2005.
- [11] Kar Wei Ng Wai Son Ko Linus C. Chuang Forrest G. Sedgwick Roger Chen, Thai-Truong D. Tran and Connie Chang-Hasnain. *Nanolasers grown on silicon*. Nature, 5:170–175, 2011.
- [12] C. A. Wang H. K. Choi and N. H. Karam. Proceedings of the Conference Laser and on Electra-Optics (CLEO), 334:170–175, 1991.
- [13] Ying-hao Kuo Richard Jones Oded Cohen Di Liang Omri Raday Matthew N. Sysak Mario J. Paniccia Alexander W. Fang, Hyundai Park and John E. Bowers. *Hybrid silicon evanescent devices*. Materials today, 10(7-8):28–35, 2007.
- [14] K. Huybrechts-T. Spuesens G. Roelkens E.-J. Geluk T. de Vries P. Regreny D. Van Thourhout R. Baets G. Morthier L. Liu, R. Kumar. *An ultra-small, low-power, all-optical flip-flop memory on a silicon chip*. Nature Photonics, 4:182–187, 2010.
- [15] G. Roelkens and al. *Adhesive Bonding of InP/InGaAsP Dies to Processed Silicon-on-Insulator Wafers using DVS-bis-Benzocyclobutene*. Journal of Electrochemical Society, 153(12):1015–1019, 2006.

- [16] M. Ayre W. Bogaerts D. Van Thourhout P. Bienstman D. Taillaert, F. Van Laere and R. Baets. *J. Appl. Phys.*, 45:6071, 2006.
- [17] W. Huang. *Coupled-mode theory for optical waveguides : an overview*. *J. Opt. Soc. Am.*, 11:963–983, 1994.
- [18] F. Raineri P. Monnier R. Braive L. Le Gratiet G. Beaudoin I. Sagnes G. Roelkens F. Van Laere D. Van Thourhout R. Raj T. J. Karle, Y. Halioua. *Heterogeneous integration and precise alignment of InP-based photonic crystal lasers to complementary metal-oxide semiconductor fabricated silicon-on-insulator wire waveguides*. *J. Appl. Phys.*, 107:063103, 2010.
- [19] Vincent Wiaux Johan Wouters Stephan Beckx Joris Van Campenhout Dirk Taillaert Bert Luyssaert Peter Bienstman Dries Van Thourhout Pieter Dumon, Wim Bogaerts and Roel Baets. *Low-Loss SOI Photonic Wires and Ring Resonators Fabricated With Deep UV Lithography*. *IEEE PHOTONICS TECHNOLOGY LETTERS*, 16, 2004.
- [20] G. Patriarche I. Sagnes K.-H. Lee, S. Guilet and A. Talneau. *Smooth sidewall in InP-based photonic crystal membrane etched by N₂-based inductive coupled plasma*. *J. Vac. Sci. Technol. B*, 26:1326–1333, 2008.
- [21] F. Raineri P. Monnier I. Sagnes R. Raj G. Roelkens D. Van Thourhout Y. Halioua, T. Karle. *Hybrid InP-based photonic crystal lasers on silicon on insulator wires*,. *Applied Physics Letters*,. 95(20):201119, 2009.
- [22] P. Monnier T. Karle I. Sagnes G. Roelkens D. Van Thourhout F. Raineri R. Raj Y. Halioua, A. Bazin. *III-V photonic crystal wire cavity laser on silicon wafer*,. *Journal of the Optical Society of America B*,. 27(10):2146, 2010.
- [23] P. Monnier T. J. Karle G. Roelkens I. Sagnes R. Raj Y. Halioua, A. Bazin and F. Raineri. *Hybrid III-V semiconductor/silicon nanolaser*,. *Optics express*, 19(10):9221–9231, 2011.

English summary

Photonics can be defined, in a broad sense, as the study of the interaction between light and matter in a framework where the dual nature, the wave and corpuscular character of light, is taken into account. The development of this field of research allowed a better understanding of the origin of these interactions and the demonstration of light emission, detection, modulation as well as frequency conversion. These studies have, among other things, allowed the conception of various types of components that today find an important place in the world of telecommunications. The development of lasers, optical fibers, amplifiers allowing signal regeneration or detectors for opto-electrical conversion of a signal are examples of the myriad of tools who allowed to improve significantly data rates or reachable distances. Having stated this contribution to the world of telecommunications, optics is presented today in literature as a possible alternative for electronics [1], facing nowadays a certain number of limits, for specific functions such as data processing at the scale of a chip or communication between processors.

III-V semiconductors have played an important role in this development. The particularity of these materials is the fact that they possess a direct electronic bandgap being favourable for spontaneous, or stimulated, light emission making the III-V semiconductors ideal for the fabrication of lasers [2]. Moreover, technical developments [3] [4] allowed a controlled growth of composites layers of III-V semiconductors allowing the fabrication of quantum wells, whose energy levels can be tuned over a large frequency bandwidth from the visible to the near-infrared, leading to the fabrication of detectors and sources over a broad wavelength range. Finally, the possibility of refractive index modulation of these materials by electrical current injection or optical pumping allowed to consider “active” functionalities such as switches or optical memories.

Photonics has been improved, during the early 80's, thanks to an intense technological development carried out by industry, exploiting nano-meter scale structuring of the material. These structures [5] opened the path to a myriad of new possibilities, by allowing to finely control light propagation or to confine it for reasonably long times $\tau_p (\propto Q)$ in very small volumes V of the order of $(\lambda/n)^3$, resulting in a better control of the non-linear effects and light-matter interaction enhancement. Among, these structures, “photonic crystals” (PhCs) [6] [7], consisting in a refractive index periodic pattern such as the ones from which butterfly iridescence takes its origin visible in fig.1.1, is of particular interest. Indeed, among the different structures studied, PhCs allow to reach, by inserting local or linear defects, on one hand the best ratio Q/V [5] and on the other hand a fine

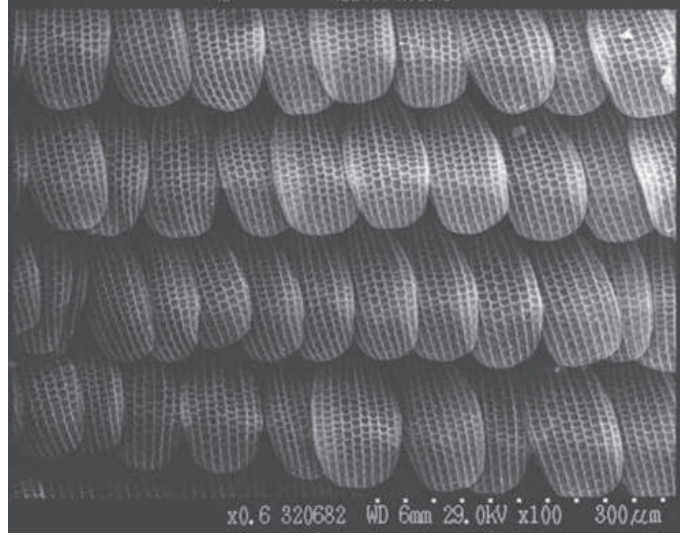


Figure 4: SEM image of a butterfly wing. [Exeter University]

control, thanks to the diversity of available designs, over the propagation of light and the group velocity v_g associated with the guided mode [8].

The combination of these two elements, that is to say III-V semiconductors and nano-structuring of matter, allows considering an efficient processing of light signals by the use of small foot print components and opens the path to integrated optical systems. In order to obtain this, several requirements need to be fulfilled. The first consists in completing these “actives” elementary units with waveguides allowing the inter-connection between different elements, the second being the proposition of a solution complementary and compatible with the fabrication of electronic components. A part of these requirements is fulfilled by exploiting the optical properties, the existence of a good low index natural oxide (SiO_2) and the quality of process of silicon based structures; indeed, it is possible to fabricate components, said “passives”, such as de/multiplexers [9] or wires with good performances [10]. This said, it is important to note here, that on one hand silicon and on the other hand III-V semiconductors are respectively inappropriate for achieving active functionalities, because of the indirect electronic bandgap of silicon, or passives, because, amongst other reasons, due to the absence of a good low index natural oxide for III-V semiconductors. Then, naturally comes the desire to combine these two materials in order to achieve in one and unique structure active and passive optical functions. A number of options opens up in view of combining III-V semiconductors and silicon, while keeping a maximum of compliance with the standard processing of electronic components. The first approach consists in the growth of the III-V semiconductors directly on silicon [11]. But, due to a strong lattice mismatch and too different thermal expansion coefficients between

these two materials, this growth is a delicate operation and leads in general to dislocations and defects in the active III-V semiconductor layer [12]. Thus the optical properties are drastically degraded. Another approach, less demanding from a technical point of view, consists in “bonding” with the use of an intermediate layer, consisting of polymers or SiO_2 , then relaxing the constraint just discussed. This method have been experimentally validated and lead to the fabrication of hybrid lasers [13] or flip-flops [14].

The points discussed in the precedent paragraphs leads us to the description of

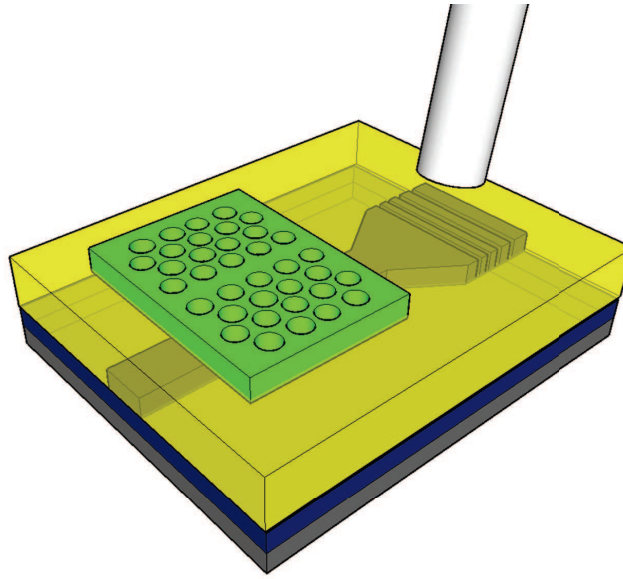


Figure 5: Schematic view of the hybrid structure studied. The lower level (blue/grey) consist in a SOI wire for the guiding of light. At the extremity of this wire grating couplers are etched for coupling to a single mode fiber allowing the extraction and injection of light in the system. The upper level (green) is a III-V semiconductor photonic crystal achieving in which all the non-linear effects and stimulated emission arise.

the present thesis subject, that is to say : the conception, fabrication and study of hybrid structures, as the one schematically depicted in fig.7.1, combining a III-V semiconductor photonic crystal, with quantum wells, emitting at 1550 nm, incorporated, in order to achieve active functionalities, such as emission, and a silicon waveguide, for passive functionalities, such as waveguiding, allowing to insert this unit in the heart of a more complex system connecting different optical elements. The two materials are being combined by the use of an adhesive bonding technique by the use of a polymer, benzocyclobutene (BCB), spin-coated preliminary on the silicon layer and cured at 250C [15]. The result of such a bonding, is a structure composed of two levels, on one hand silicon, one the other hand III-V semiconductors. To complete the description and the fabrication method, we note that the

silicon wires have been defined on the silicon level prior to bonding. One of the most interesting aspects of bonding by the use of BCB appears since it is indeed possible, thanks to the planarizing properties of BCB, to a priori implement various structures on the silicon level. The last step leading to the hybrid structure is the etching of a PhC, after bonding, on the upper level. These two levels, the silicon wire and the III-V semiconductors PhC, separated by a few hundred nanometers thick intermediate layer of BCB, are coupled by “evanescent coupling” [16]. This type of coupling allow an exchange of the energy of theoretically 100 % between the two levels without having a substantial impact on the optical properties of each structure. Under these conditions, the two levels can be considered as partially independent, ie. the optical modes in the hybrid structure belong only to one or the other level. In order to achieve efficient coupling two main constraints are imposed, the first is to achieve two structure with phase matched optical modes, ie. having similar effective index, the second being the alignment between the two levels. To overcome this last constraint, the first being solved by judicious modelling, it is necessary to develop an appropriate procedure of alignment of the order of sub-hundred nanometers.

An important part of the work was then dedicated to the fabrication of the hy-

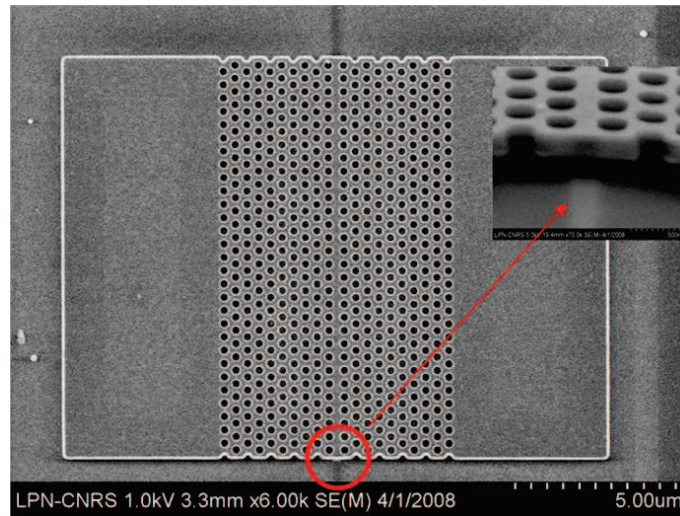


Figure 6: SEM image of a processed sample. The 10 micron long PhC waveguide appears perfectly aligned with the silicon wire underneath, visible through the transparency of the BCB layer. The inset clearly shows the two level structuring.

brid structures, and notably the development of an alignment procedure fulfilling the criteria in order to achieve an efficient and controlled coupling between the two levels. Prior to this, one of the first results obtained during this work was the improvement of the bonding technique. Indeed, a sensitive improvement of the bonding, developed in the Photonic Research Group in Gent, via the use of an

SiO₂ layer at the interface between BCB and III-V semiconductors was made in this work, thus the yield of bonding of pieces of few millimeters square, of initially 50 % has been brought to almost 100 %. Moreover, the use of a variable thickness layer of SiO₂ allowed a better control of the distance between the two levels. Next, the alignment between the two levels, is achieved by automatic detection, using the 100 keV e-beam, of marks pre-etched in the silicon layer, allowing thus to precisely locate the position of the Si wires, the detection being just prior to the exposure of the resist defining the III-V semiconductor pattern. The quality of the alignment obtained by the use of this technique, state of the art, procedure is superior to 30 nm, well above the criteria, extracted from modelling or analytical calculations, required for a control of the evanescent coupling between the two levels [17]. The SEM image of the sample on fig.6 allow to appreciate the quality of the alignment, moreover the structures in the two levels appear clearly.

A 2D PhC, or periodic pattern of holes, was thus etched in the III-V semiconductors layer, the vertical confinement being ensured by TIR or index contrast with the surrounding media. Two different type of PhC designs were implemented during this PhD. The first one was a photonic crystal waveguide, allowing to access to low v_g modes [18]. The second was a cavity with a reasonably high Q/V ratio [19]. The modelling work first focused on the search of designs with guiding or confinement properties at the maximum of emission of the QWs inserted in the III-V semiconductors layer. This work has been rendered difficult by the presence of the BCB substrate, of relatively high refractive index ($n=1.54$), drastically limiting the frequency windows where the vertical confinement remains effective. In parallel, we have to keep in mind the ultimate purpose of the designed structures, that is to say being coupled to the silicon wire underneath and thus having phase matched modes with the silicon wire. This allowed to extract a design of PhCs slow mode waveguides and high Q/V cavities in which guided modes in the upper level are evanescently coupled to the silicon wire etched in the lower level.

Experimentally, a setup satisfying the alignment criterias, at the scale of hundred of nanometers, between the single mode fibers and the grating couplers on one hand, for injection or extraction of light, and of the pump, pulsed at 800 nm, focused on the PhC defect was builded. It has been thus possible to demonstrate laser emission, of the two types of designs studied, coupled to the silicon wire [18] [17] [20]. Complementary, a non-exhaustive exploration of several parameters, such as the holes radius or period of the periodic pattern or length of cavities, allowed us to show a very good agreement between modelling and fabricated structures [19] [17]. Thus, the laser wavelength or the threshold are strongly correlated with the expected results from modelling. These studies allowed a better understanding of the coupling mechanisms and finally to develop a procedure to experimentally extract the critical parameter which is the strength of coupling. Indeed, the total transmission of a cavity coupled to a waveguide is intrinsically related to the coupling strength between these two elements. Thus, by studying the transmission of our system, under different pumping conditions, we have been able to estimate that around 80 % of the emitted light in the upper level is extracted via the silicon wire. This remarkably high value, partly thank to careful modelling of

the system concerning this aspect of the hybrid structures, allows coupling several micro watts of optical power in the silicon waveguide layer. Two elements complete this study of hybrid lasers, first we demonstrate the benefit we can take from our structures by a double use of the silicon wire, used for to carry an optical pump at 1.2 microns [18], close to the limit of transparency of silicon and absorbing in the QWs and barriers. Afterwards, pumping from the top at this wavelength have allowed us to observe continuous wavelength laser operation [20]. This result is partly due to the fact that the heating induced by pumping is lower at this value than at 800 nm, and partly due to the addition of an SiO₂ layer at the bonding interface, which is more favourable to thermal heat sinking to the silicon substrate than BCB.

In summary, this work thus resulted in the development and study of hybrid lasers, where emission of a III-V semiconductors PhC is coupled to a silicon wire. The agreement between experimental results and modelling emphasises, on one hand the quality of the fabrication technique, and notably the alignment procedure, superior to 30 nm, and on the other hand a good understanding of the system allowing us to build an efficient system where 80 % of the emitted light can be used further. Thus, it is possible to imagine the designed structure as a potential basic component for integrated optics given the small foot-print and low-power operation. Finally, to go further in this direction, ie. for the all optical processing of data, the conception of other components, such as optical memory is necessary. The possible bistable characteristic, as indicated by the very last experiments performed, allows considering achieving such a function.

References

- [1] D. A. B. Miller. Proc. IEEE, 88:728, 2000.
- [2] J. D. Kingsley T. J. Soltys R. N. Hall, G. E. Fenner and R. O. Carlson. *Coherent Light Emission From GaAs Junctions*. Phys. Rev. Lett., 9:366368, 1962.
- [3] A.Y. Cho and J.R. Arthur. Prog. Solid State Chem., 10:157, 1975.
- [4] O.Thomas R.Madar A.Abrutis. J.P.Senateur, F.Weiss. Patent No 93/08838 PCT No FR94/00858 (Europe, U.S.A.), 1993.
- [5] K. J. Vahala. *Optical microcavities*. Nature, 422, 2003.
- [6] John S. *Strong localization of photons in certain disordered dielectric superlattices*. Phys. Rev. Lett., 58:2486–9, 1987.
- [7] Yablonovitch E. *Inhibited spontaneous emission in solid-state physics and electronics*. Phys. Rev. Lett., 58:2059–62, 1987.
- [8] Toshihiko Baba. *Slow light in photonic crystals*. Nature Photonics, 2:465–473, 2008.
- [9] F. Coppinger P. D. Trinh, S. Yegnanarayanan and B. Jalali. *Silicon on-insulator (SOI) phased-array wavelength multi-demultiplexer with extremely low-polarization sensitivity*,. Appl. Phys. Lett., 9:940942, 1997.
- [10] W. Bogaerts and al. *Nanophotonic waveguides in silicon-on-insulator fabricated with CMOS technology*. J. Lightwave Technol., 88:401–412, 2005.
- [11] Kar Wei Ng Wai Son Ko Linus C. Chuang Forrest G. Sedgwick Roger Chen, Thai-Truong D. Tran and Connie Chang-Hasnain. *Nanolasers grown on silicon*. Nature, 5:170–175, 2011.
- [12] C. A. Wang H. K. Choi and N. H. Karam. Proceedings of the Conference Laser and on Electra-Optics (CLEO), 334:170–175, 1991.
- [13] Ying-hao Kuo Richard Jones Oded Cohen Di Liang Omri Raday Matthew N. Sysak Mario J. Paniccia Alexander W. Fang, Hyundai Park and John E. Bowers. *Hybrid silicon evanescent devices*. Materials today, 10(7-8):28–35, 2007.
- [14] K. Huybrechts-T. Spuesens G. Roelkens E.-J. Geluk T. de Vries P. Regreny D. Van Thourhout R. Baets G. Morthier L. Liu, R. Kumar. *An ultra-small, low-power, all-optical flip-flop memory on a silicon chip*. Nature Photonics, 4:182–187, 2010.
- [15] G. Roelkens and al. *Adhesive Bonding of InP/InGaAsP Dies to Processed Silicon-on-Insulator Wafers using DVS-bis-Benzocyclobutene*. Journal of Electrochemical Society, 153(12):1015–1019, 2006.

- [16] W. Huang. *Coupled-mode theory for optical waveguides : an overview*. J. Opt. Soc. Am., 11:963–983, 1994.
- [17] F. Raineri P. Monnier R. Braive-L. Le Gratiet G. Beaudoin I. Sagnes G. Roelkens F. Van Laere D. Van Thourhout R. Raj T. J. Karle, Y. Halioua. *Heterogeneous integration and precise alignment of InP-based photonic crystal lasers to complementary metal-oxide semiconductor fabricated silicon-on-insulator wire waveguides*. J. Appl. Phys., 107:063103, 2010.
- [18] F. Raineri P. Monnier I. Sagnes R. Raj G. Roelkens D. Van Thourhout Y. Halioua, T. Karle. *Hybrid InP-based photonic crystal lasers on silicon on insulator wires*,. Applied Physics Letters,, 95(20):201119, 2009.
- [19] P. Monnier T. Karle I. Sagnes G. Roelkens D. Van Thourhout F. Raineri R. Raj Y. Halioua, A. Bazin. *III-V photonic crystal wire cavity laser on silicon wafer*,. Journal of the Optical Society of America B,, 27(10):2146, 2010.
- [20] P. Monnier T. J. Karle G. Roelkens I. Sagnes R. Raj Y. Halioua, A. Bazin and F. Raineri. *Hybrid III-V semiconductor/silicon nanolaser*,. Optics express, 19(10):9221–9231, 2011.

Nederlandstalige samenvatting

Fotonica kan gedefinieerd worden als de studie van de interactie van licht en materie, waarbij het duale karakter van licht, zijnde licht als een golf en als een deeltje, in rekening wordt gebracht. De ontwikkeling van dit onderzoeksveld heeft een beter inzicht gecreëerd in de oorsprong van deze interactie. Deze ontwikkeling heeft geleid tot de concipering van een aantal belangrijke componenten die niet meer weg te denken zijn uit de wereld van de telecommunicatie. De ontwikkeling van lasers, optische vezels, versterkers,... lieten toe om data over een langere afstand en aan hogere snelheid te versturen. De toepassingen van fotonica zijn echter veel breder dan telecommunicatie. Gentegreerde optica wordt bijvoorbeeld vandaag de dag voorgesteld om bepaalde functies, die vandaag de dag vervuld worden door elektronische gentegreerde circuits, beter, sneller en met lager vermogenverbruik uit te voeren, zoals bijvoorbeeld de communicatie tussen processoren of zelfs het processen van data.

III-V halfgeleiders hebben een belangrijke rol vervuld in deze ontwikkelingen. Deze materialen hebben een directe bandgap, hetgeen spontane en gestimuleerde emissie efficiënte processen maakt, waardoor ze het materiaalplatform bij uitstek zijn om lasers in te realiseren. De ontwikkeling van epitaxiale groeiprocessen heeft toegelaten om halfgeleiderlegeringen te groeien op een substraat, hetgeen leidde tot de ontwikkeling van heterojunctiestructuren en bijvoorbeeld quantum well/quantum dot actieve lagen, hetgeen de prestaties van de lasers sterk verbeterde. De mogelijkheid om de brekingsindex van deze materialen te veranderen door elektrische injectie of door een optische pomp, liet toe om actieve optische functies zoals schakelaars en geheugenelementen te realiseren.

Nanometer-schaal structurering van halfgeleiders heeft gezorgd voor een verdere ontwikkeling van het onderzoeksveld. Deze structurering laat toe om de propagatie van licht te controleren en bijvoorbeeld het licht op te sluiten voor redelijk lange tijd in een klein volume, van de orde van $(\lambda/n)^3$, hetgeen resulteert in een sterkere licht-materie interactie en controle van niet-lineaire effecten. Fotonische kristallen, artificieel materialen bestaande uit een periodiek variërend brekingsindexprofiel, zijn hiervoor uitermate geschikt. Door het gewild toevoegen van defecten aan het rooster kan op die manier licht opgesloten worden in resonatoren met heel hoge kwaliteitsfactor/volumeverhouding. Bovendien kunnen golfgeleiders gevormd worden die een precieze controle over de propagatie van licht toelaten.

De combinatie van deze twee elementen (III-V halfgeleiders en nanostructurering) maakt het efficiënt verwerken van optische datasignalen met behulp van kleine en

sterk gintegreerde componenten mogelijk. Om dit te realiseren, moeten verschillende voorwaarden vervuld zijn. Eerst en vooral dient er een methode te zijn om de actieve componenten te interconnecteren met behulp van passieve golfgeleidercircuits. Bovendien moet de oplossing compatibel zijn met de integratie van elektronische gintegreerde circuits. Deze twee randvoorwaarden leiden tot het gebruik van silicium-op-isolator (SOI) als passief golfgeleidercircuit, waarop de actieve optische functies, gerealiseerd in III-V halfgeleiders, worden gintegreerd. Er zijn verschillende manieren waarop deze materialen kunnen gintegreerd worden. Een eerste methode is de hetero-epitaxiale groei van III-V halfgeleiders op een silicium substraat. Ten gevolge van de grootte mismatch in roosterconstante en thermische expansiecoëfficiënt van de twee materialen, maakt dat de gegroeide filmen veel dislocaties bevatten, hetgeen de optische eigenschappen van de laag minder goed maakt. Een andere aanpak bestaat in het transfereren van III-V halfgeleider lagenstructuren, gegroeid op hun originele rooster-aangepaste substraat, naar de silicium-op-isolator golfgeleiderwafer. Dit kan gebeuren met behulp van een intermediäre lijmlaag (een polymeer) of door middel van moleculaire bonding (gebaseerd op Van der Waals interactie tussen twee atomair vlakke oppervlakken). Deze methode is reeds experimenteel aangetoond en heeft geleid tot de demonstratie van hybride lasers, detectoren, enzoverder.

De hierboven gevoegde discussie leidt tot het huidige doctoraatsonderwerp: het ontwerp, fabricage en studie van hybride III-V/silicium laserstructuren, zoals de structuur weergegeven in figuur 1, die een actieve III-V fotonisch kristalstructuur combineert met passieve silicium golfgeleidercircuits. De heterogene integratietechniek die in dit werk wordt gebruikt is gebaseerd op een DVS-BCB adhesie bonding proces. Dit is een aantrekkelijke route aangezien het gebruik van een polymeer toe laat om op een niet-planair substraat te bonden (met name het SOI substraat waarin golfgeleiders getst zijn). Bovendien kan de afstand tussen de silicium golfgeleiders en het III-V willekeurig gekozen worden. Deze techniek werd gevoelig verbeterd binnen dit doctoraat, waardoor de yield van het proces sterk verhoogde. Aan de basis van de verbetering lag het deponeren van een SiO₂ laag op de III-V halfgeleider voor bonding, waardoor de adhesie van het DVS-BCB polymeer sterk verbeterde. Dit laat bovendien een betere warmtespreiding toe, gegeven de hogere thermische geleidbaarheid van SiO₂ ten opzichte van DVS-BCB.

Figuur 1: Schematische illustratie van de hybride structuur De koppeling tussen de III-V halfgeleiderlaag en de silicium golfgeleidercircuits is gebaseerd op evanescente koppeling. Een dergelijk type koppeling laat in principe toe om 1000p basis van deze technologische ontwikkelingen werden twee types fotonische kristalstructuren getst in de gebonde III-V halfgeleiderlaag. Het eerste design bestond uit een fotonisch kristal golfgeleider die traag propagerende Bloch modi ondersteunt, zoals weergegeven in figuur 2. Het tweede design is een hoge Q/V caviteit gebaseerd op het etsen van een eendimensionale rij gaatjes in een III-V gebonde fotonische draad.

Figuur 2: SEM foto van een gerealiseerd sample. De 10 micrometer lange fotonische kristalgolfgeleider lijkt perfect gealigneerd met de onderliggende sili-

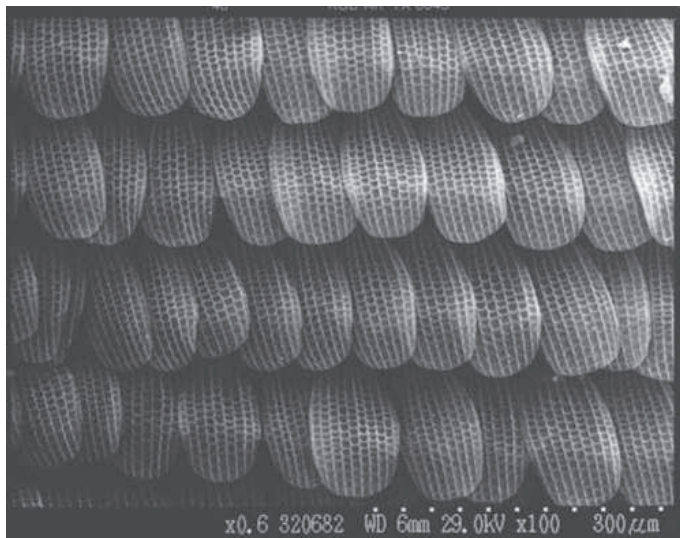


Figure 7: Image d'une aile de papillon réalisé à l'aide d'un microscope électronique à balayage. [Université d'Exeter]

ciumgolfeleider. Buiten het design en de fabricagetechnologie werd ook een experimentele setup gebouwd om de devices te karakteriseren. Deze setup bestaat uit een pomplaser, die de III-V halfgeleider quantum wells pompt (dit kan zowel door belichting van de III-V halfgeleiderstructuur langs boven of via de golfeleiderlaag) en een setup om de emissie van de de hybride structuur te monitoren (via het substraat, superstraat of golfeleiderlaag). Zowel gepulst pomplicht als continuous wave (CW) pomplicht werden gebruikt. In beide structuren (fotonisch kristal golfeleiders en caviteiten) werd laserwerking waargenomen en de waargenomen afhankelijkheid van de laseremissie golflengte matcht heel goed met de modellering. Verdere studie van de koppelingsefficientie van de III-V halfgeleiderlaser naar het silicium golfeleidercircuit, toonde aan dat we ongeveer 80Dit werk vormt de basis voor verder onderzoek naar ultra-compacte, laag vermogenverbruik hybride lichtbronnen op een siliciumcircuit. Recente resultaten, die bistabiliteit in de structuur aantonen, maakt het zelfs mogelijk te denken aan optische geheugenelementen gntegreerd on-chip, hetgeen een belangrijke component is voor de volledig optische processing van data.

References

- [1] D. A. B. Miller. Proc. IEEE, 88:728, 2000.
- [2] J. D. Kingsley T. J. Soltys R. N. Hall, G. E. Fenner and R. O. Carlson. *Coherent Light Emission From GaAs Junctions*. Phys. Rev. Lett., 9:366368, 1962.
- [3] A.Y. Cho and J.R. Arthur. Prog. Solid State Chem., 10:157, 1975.
- [4] O.Thomas R.Madar A.Abrutis. J.P.Senateur, F.Weiss. Patent No 93/08838 PCT No FR94/00858 (Europe, U.S.A.), 1993.
- [5] K. J. Vahala. *Optical microcavities*. Nature, 422, 2003.
- [6] John S. *Strong localization of photons in certain disordered dielectric superlattices*. Phys. Rev. Lett., 58:2486–9, 1987.
- [7] Yablonovitch E. *Inhibited spontaneous emission in solid-state physics and electronics*. Phys. Rev. Lett., 58:2059–62, 1987.
- [8] Toshihiko Baba. *Slow light in photonic crystals*. Nature Photonics, 2:465–473, 2008.
- [9] F. Copping P. D. Trinh, S. Yegnanarayanan and B. Jalali. *Silicon on-insulator (SOI) phased-array wavelength multi-demultiplexer with extremely low-polarization sensitivity*,. Appl. Phys. Lett., 9:940942, 1997.
- [10] W. Bogaerts and al. *Nanophotonic waveguides in silicon-on-insulator fabricated with CMOS technology*. J. Lightwave Technol., 88:401–412, 2005.
- [11] Kar Wei Ng Wai Son Ko Linus C. Chuang Forrest G. Sedgwick Roger Chen, Thai-Truong D. Tran and Connie Chang-Hasnain. *Nanolasers grown on silicon*. Nature, 5:170–175, 2011.
- [12] C. A. Wang H. K. Choi and N. H. Karam. Proceedings of the Conference Laser and on Electra-Optics (CLEO), 334:170–175, 1991.
- [13] Ying-hao Kuo Richard Jones Oded Cohen Di Liang Omri Raday Matthew N. Sysak Mario J. Paniccia Alexander W. Fang, Hyundai Park and John E. Bowers. *Hybrid silicon evanescent devices*. Materials today, 10(7-8):28–35, 2007.
- [14] K. Huybrechts-T. Spuesens G. Roelkens E.-J. Geluk T. de Vries P. Regreny D. Van Thourhout R. Baets G. Morthier L. Liu, R. Kumar. *An ultra-small, low-power, all-optical flip-flop memory on a silicon chip*. Nature Photonics, 4:182–187, 2010.
- [15] G. Roelkens and al. *Adhesive Bonding of InP/InGaAsP Dies to Processed Silicon-on-Insulator Wafers using DVS-bis-Benzocyclobutene*. Journal of Electrochemical Society, 153(12):1015–1019, 2006.

- [16] M. Ayre W. Bogaerts D. Van Thourhout P. Bienstman D. Taillaert, F. Van Laere and R. Baets. *J. Appl. Phys.*, 45:6071, 2006.
- [17] W. Huang. *Coupled-mode theory for optical waveguides : an overview*. *J. Opt. Soc. Am.*, 11:963–983, 1994.
- [18] F. Raineri P. Monnier R. Braive L. Le Gratiet G. Beaudoin I. Sagnes G. Roelkens F. Van Laere D. Van Thourhout R. Raj T. J. Karle, Y. Halioua. *Heterogeneous integration and precise alignment of InP-based photonic crystal lasers to complementary metal-oxide semiconductor fabricated silicon-on-insulator wire waveguides*. *J. Appl. Phys.*, 107:063103, 2010.
- [19] Vincent Wiaux Johan Wouters Stephan Beckx Joris Van Campenhout Dirk Taillaert Bert Luyssaert Peter Bienstman Dries Van Thourhout Pieter Dumon, Wim Bogaerts and Roel Baets. *Low-Loss SOI Photonic Wires and Ring Resonators Fabricated With Deep UV Lithography*. *IEEE PHOTONICS TECHNOLOGY LETTERS*, 16, 2004.
- [20] G. Patriarche I. Sagnes K.-H. Lee, S. Guilet and A. Talneau. *Smooth sidewall in InP-based photonic crystal membrane etched by N₂-based inductive coupled plasma*. *J. Vac. Sci. Technol. B*, 26:1326–1333, 2008.
- [21] F. Raineri P. Monnier I. Sagnes R. Raj G. Roelkens D. Van Thourhout Y. Halioua, T. Karle. *Hybrid InP-based photonic crystal lasers on silicon on insulator wires*,. *Applied Physics Letters*, 95(20):201119, 2009.
- [22] P. Monnier T. Karle I. Sagnes G. Roelkens D. Van Thourhout F. Raineri R. Raj Y. Halioua, A. Bazin. *III-V photonic crystal wire cavity laser on silicon wafer*,. *Journal of the Optical Society of America B*, 27(10):2146, 2010.
- [23] P. Monnier T. J. Karle G. Roelkens I. Sagnes R. Raj Y. Halioua, A. Bazin and F. Raineri. *Hybrid III-V semiconductor/silicon nanolaser*,. *Optics express*, 19(10):9221–9231, 2011.

1

Introduction

The present work takes place in the framework of the field of “nano-photonics”. By this we mean the study of the behaviour of light in elements with sizes of the order of its wavelength, or in other words, light-matter interaction in nano-scaled objects. This field of research has attracted a lot of attention in the last decades. Indeed, bringing “nano-objects” to the field of optics has been made possible thanks to increasing technological capabilities, ranging from material related developments, enabling light emission at any desired wavelength such as in quantum-dots or quantum wells, to nano-scale processing technology, enabling objects such as ultra-small photonic wires [1] or photonic crystals [2] [3]. Nano-photonics has lead to an opening in the landscape of accessible light-matter interaction effects, from the observation of the unique quantum properties in confined systems to enhanced parametric non-linear effects. Indeed, the ability to manipulate efficiently the electromagnetic field in nano-scaled structures, combined with the knowledge and control of material behaviour, has allowed the study of a myriad of effects such as strong coupling [4], single photon sources [5], new laser behaviour [6], various enhanced non-linear parametric effects [7] [8] [9], and so on.

In this field of research, the present thesis is one of the first realizations and study of a novel platform based on III-V semiconductor photonic crystals coupled to silicon photonic wires; combining - in an original manner - materials (III-V and silicon semiconductors) and structures (photonic crystals and photonic wires). Hybrid structures have received recently considerable attention and have shown to possess interesting optical properties through the combination of two relatively

different materials, since they take advantage of their respective assets and drawbacks. From a specific scheme of coupling or organisation, new possibilities in designing composite optical structures are opened. In this thesis, the active level properties rely on photonic crystals (PhC) etched in this layer, in order to benefit from the field enhancement realized by this type of structure. Basically, these hybrid structures may be considered as the sum of an active III-V semiconductor based level coupled to a passive silicon based one. And in doing this operation of addition, the aim is to prove that this type of hybrid structure can give rise to extra features, more complex than just the sum of its elements (III-V PhC and photonic silicon wire).

The thesis is presented in a chronological manner. Indeed, even if the present research subject benefits from previous studies such as the bonding method or prior knowledge on III-V photonic crystals properties, the novelty of the proposed structure and the lack of knowledge concerning the behaviour of such structures, take the starting point of this work to very fundamental aspects such as the practical realization of the hybrid structure and the modelling and understanding of the underlying physical mechanisms. The first chapter will give the reader a short view of the context of the present work, exposing similarities and differences to the few pre-existing studies. Then, in chapter 2, an overview of the hybrid structure will be given, providing the basics for a better understanding of the specificities and the expected behaviour of this hybrid scheme : III-V photonic crystal on silicon wire. Chapter 3 will be dedicated to the first major hurdle, that is the technological processing of the samples, strongly impacting the optical response of the entire structure. Indeed, in order to exploit the optical properties of the photonic crystal based level, reviewed in a concise chapter 4, and efficiently control its coupling to the underlying silicon wire, the alignment of the two levels will be crucial. An important part of the present work was devoted to modelling the active level using 3D FDTD (chapter 5), leading to two types of designs: PhC waveguides (chapter 7) and wire cavities (chapter 8). Finally, from the two different PhC designs, using a specifically built experimental setup (chapter 6), an exhaustive study of the proposed structure was performed and confronted with modelling, in order to arrive at a deep understanding of the coupling behaviour. Finally, both for PhC waveguides and cavities, laser emission coupled to the silicon wire are demonstrated. Moreover, the latest experiments demonstrate a highly controlled system, providing continuous wave laser operation of the active PhC level efficiently coupled to the silicon wire.

1.1 Context

An interesting guide line to the present work is given by the “photonic integration” field of research. The hybrid platform proposed can bring efficient solutions to the problems that electronics is confronted with such as limitations in speed, compactness and low power consumption. Moreover, photonic integration is thought to be complementary to electronics for specific operations needed such as short-distance communications inside information processing machines.

1.1.1 Photonic integration

Literature in the domain shows an important trend towards research for the development of optical devices for use in next-generation information and communication technology, due to their ability to bring efficient solutions to data transmission and processing. Telecommunication has known tremendous development, through optical fiber technology backed by related devices and circuits composed of light sources, optical amplifiers, wavelength multiplexers, photodetectors, etc, which has greatly revolutionized communication in general. Nowadays, the electronics industry, or CMOS industry, is facing severe difficulties, for specific applications [10]. For example, intra-chip interconnect, or inter-chip communication, is hitting the achievable performance limits for computer systems. These limits are roughly imposed by the fact that electrical interconnects do not scale in speed like transistors as their dimensions are shrunk, resulting in a decrease in reach for faster interconnects [11]. Following this assessment, the use of optical interconnects as an alternative to copper-based interconnects for on-chip communication was first proposed by Goodman in 1984 [12]. Several different options have emerged leading progressively to a better understanding of the needs and possible solutions offered by optics in this field. Increasing attention is thus being devoted to optical datacom mainly concentrated on intra- and inter-chip interconnection applications. Here the issues which need to be tackled are the routing of mind boggling amounts of information both on-chip and off-chip. This requires fast, reliable and low power consumption communication, for example between the individual cores that form a microprocessor. The very nature of optics offers the potential to obtain the required high data transmission and processing rates with low power consumption.

Further, over the past decades integrated optics has emerged as a major actor both in the industrial and academic scientific communities. “Integrated” takes on a particular meaning in that the propagation and processing of signals for datacom/telecom applications takes place on a single platform, that is thought to be included in a larger picture containing all the electronic functionalities, as shown in the scheme of fig. 1.1 where an optical processing level is electrically connected to a

transistor level via an intermediate electrical interconnect layer. In such a scheme the photonic circuits should consist of elements able to control the propagation of light with a view to realising passive functions such as guiding and filtering as well as elements dedicated to active functions such as emission, amplification, switching and a multitude of others capable of manipulating optically encoded information at will.

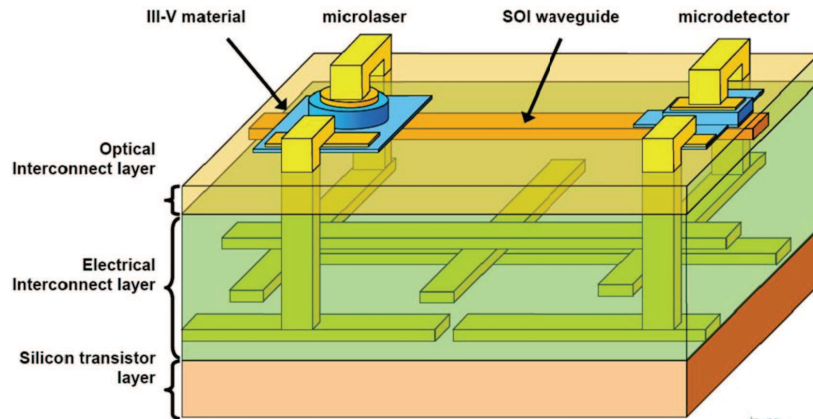


Figure 1.1: Possible scheme for optical integration. The top level consist in optical elements electrically connected to the bottom level composed of silicon electronic transistors. [Courtesy of Ghent University-Intec]

In this context, two principal technological choices have emerged : Silicon photonics and III-V semiconductors photonics.

1.1.2 Silicon photonics

Due to decades of investment from the microelectronics industry, silicon is a thoroughly studied material, and unsurpassed in quality of fabrication with very high yield. This area of research got a major impetus more than two decades ago, through the study by Soref and Lorenzo, in which the first silicon waveguide was demonstrated [13]. Soon after, work in silicon photonics concentrated on electro-optical control through the use of free carriers, e.g., by carrier injection, as a means of modulating light either by modifying the refractive index or the material absorption [14]. The results of this work led to the development of silicon-based optical modulators [15] [16] [17]. The work on free-carrier modulation in silicon was then followed by research in thermo-optic devices, which have a surprisingly high performance due to the favourable thermo-optic coefficient of silicon [18]. Rapid ad-

vances in both of these device types have continued into the present, including scaling down of the device “footprint”, reduction of power consumption and improved frequency response. Because of the favourable electronic, optical, and physical properties of silicon in conjunction with the mature complementary metal-oxide-semiconductor (CMOS) fabrication processing technology [19], large-scale integration of functional optical devices has become possible, including integration with relatively complex electronic components. The use of CMOS manufacturing technology also facilitates precise patterning of integrated optical circuits; this enables, for example, greatly reduced side-wall roughness and, hence, very low loss even in small high index contrast waveguides. The high index contrast of the silicon to air and silicon to silicon-dioxide enables the realization of extremely small waveguides for telecom wavelengths with sub-micron heights and widths and sharp bends [20]. This offers perspectives for high density optical interconnections. However, silicon suffers from one major handicap, due to its indirect electronic band gap silicon is not an ideal material for light emission and amplification. Even though silicon can be used for these functions (Raman lasers [21], SiO₂ Er-doped lasers on Si [22]). For these purposes III-V materials are far more efficient and suitable.

1.1.3 III-V photonics

Because of their direct band gap, III-V semiconductors have been widely studied, allowing efficient light emission or stimulated emission, which is extremely useful for making active devices [23]. Moreover, these materials offer the unique possibility to obtain a tailored electronic band structure [24] by playing on the combinations of elements and their respective compositions, to constitute alloys (for example AlGaAs, InGaAs, InGaAsP). This way it is possible to obtain direct electronic transitions covering a wide wavelength range from the visible to the mid-infrared. The use of quantum confinement allows to further engineer the band structure leading to performance improvement. The advent of growth techniques like MBE [25] and MOCVD [26] opened the path to the growth of semiconductors, atomic layer by atomic layer, leading to extremely precise control of the thickness of each layer and hence of the wavelength of operation. The development of new etching techniques further enhanced accuracy of fabrication. A new wave of products such as quantum well lasers, LED's, photodiodes, CCDs, electronic circuits and a myriad of other devices soon overtook opto-electronic industry. VCSELs, which were new devices in the 90's, are already considered “classical lasers” and are used for parallel optical interconnect. But, contrary to silicon, III-V semiconductors are not very well suited for guiding light in ultra small waveguides [27], where the propagation losses reported (10 dB/cm) is ap-

proximatively 4 times higher than for silicon wires, because of the absence of a good quality low refractive index ($n_{\text{AlO}_x}=1.6$) natural oxide and because of a less mature processing technology.

Years of work and research has resulted in a material, such as silicon, which appears tailor made for passive functions such as guiding, and another type of material, based on III-V semiconductors alloys, that has proved to be very useful for plenty of applications that have already found their place in our everyday world. Thus, merging those two materials in one structure, passive silicon photonics enhanced by III-V based optical functions, allows to combine the best of both worlds leading to a highly versatile silicon/III-V photonics platform which opens up the field of large-scale photonic integration. This domain is still in an early stage of research and a few groups have begun exploring these exciting hybrid structures [28] [29] [30].

1.1.4 III-V/Si hybrid structures

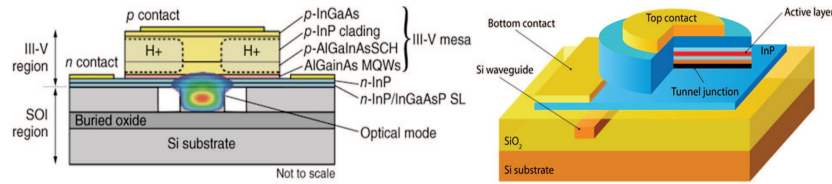


Figure 1.2: Possible configurations for hybrid InP/SOI structures. a) Hybrid silicon evanescent device, from [28] - b) III-V photonic device coupled evanescently to an SOI wire, from [31]

Once the concept of hybrid structures is proposed we immediately confront, the difficulty of the growth of III-V on silicon due to the lattice mismatch between these materials [32]. However, this path is being pursued through methods involving complicated technologies [33]. In parallel, two possibilities, based on bonding technologies, have opened up for hybrid structures.

In the first approach, the devices are patterned completely in the SOI waveguide layer and an unstructured III-V epi-layer is directly bonded on top and very close (tens of nanometers) to the SOI structure. A typical example of this type of device is depicted in fig 1.2.a, and consist in a silicon wire with an active III-V layer bonded on top of that SOI structure. In this approach, the light is almost entirely confined within the SOI waveguide; it is the evanescent tail of the optical mode which feels the gain provided by the InP active layer. This approach has been used by Bowers and co-workers [34] to demonstrate lasers, amplifiers and detectors and

is now incorporated in INTEL's programs concerning photonics research. This approach is now also being adopted by the Photonic Research Group [35]. However, one of the drawbacks of this type of hybrid structures, is the high operation power that is required because of the relatively weak interaction between the field and the gain medium.

The second approach consists in bonding III-V active devices onto silicon wires by the use of a low refractive index bonding material (BCB or SiO_2 [29]). In this configuration, each level of the system possesses its own optical modes and the two are "weakly" coupled by evanescent wave coupling. This makes a strong difference with the previous work. We thus expect higher efficiency of the non-linear effects in such an hybrid structure since 100% of the field can be located in the upper active structure. This choice is beginning to give interesting results; and has lead to the fabrication of micro-disk lasers [36] (see fig 1.2.b) with bistable operation between the clockwise and counter-clockwise propagating modes [30], leading to optical switching. Our choice is to use photonic crystals due to the possibility of increased confinement in this active level.

1.1.5 Photonic crystals

Indeed, in recent years 2D PhCs have raised a lot of interest. PhCs [37] are structures consisting of a periodic arrangement of materials with different refractive indices where the lattice constant is of the order of the wavelength of light, as for example, a lattice of air holes drilled in a semiconductor (see fig. 1.3). In such

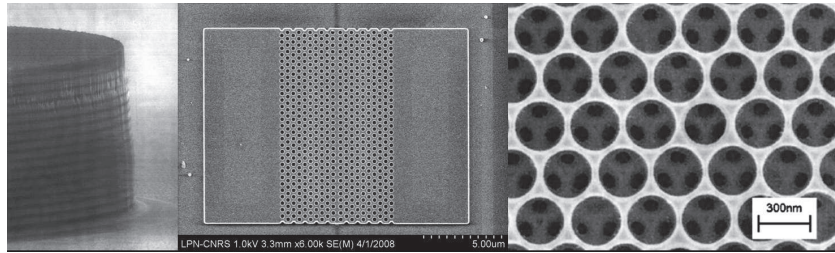


Figure 1.3: Example of photonic crystal structures. From left to right : 1D Bragg mirror of alterned $\text{AlOx}/\text{AlGaAs}$ layers (LPN), InP photonic crystal with a line of holes removed to form a waveguide (LPN), 3D TiO_2 inverse opal [38]

a periodic structure, the behaviour of light can be described through the use of a band structure, in a quasi-perfect analogy with electrons in the periodic potential of a crystal [2] [3]; this aspect is related to the common wave nature of photons and electrons. This way, a periodic structure can be designed to affect the properties of photons in a way similar to that in which semiconductor crystals affect the

properties of electrons. Of particular interest is the possibility to obtain structures for which the propagation of light is forbidden in all directions, due to the presence of the so-called “photonic band gap” (PBG) in the dispersion relation of the patterned medium. For instance, a PBG defines a range of frequencies for which light is barred from propagating. Barred that is, unless there is a defect in the otherwise perfect crystal. A defect can lead to new photon states, in which the light is confined in volumes V , close to the diffraction limit $(\lambda/2n)^3$, for a respectably long time τ (or high Q with $Q = \omega\tau/2$), thus enhancing the light intensity which scale with Q/V . For example, in a 2D PhC made of a lattice of holes (of radius 130 nm) drilled in a semiconductor layer (in a triangular lattice of period 435 nm), a waveguide can be formed in a missing row of holes (fig 1.3.b) or a cavity can be formed when one or several holes are missing in the lattice (fig. 1.3.c)). These states confined by the PBG find applications in many areas of physics and engineering, including coherent electron-photon interactions [39], ultra-compact filters [40], low threshold lasers [41], nonlinear optics [42] and quantum information processing [43].

Therefore, photonic crystals are considered by many as one of the ultimate ways to reduce the size of optical components and will most certainly play an important role in the integration on a photonic chip.

To benefit from these promising properties, we proposed a hybrid structure made of a PhC etched in an active InP upper layer; as depicted in fig. 1.4 schematically representing the typical hybrid structure studied in this work. The active level is a III-V semiconductor photonic crystal bonded, using an intermediate BCB layer, on top of a passive level consisting in a silicon wire. Those two structures will be evanescently coupled.

The ultra small dimensions and properties of the photonic digital units, based on photonic crystals, are expected to result in record short response times [44] and low activation energies [45]. Building photonic circuits with these digital units together with the low propagation losses in the SOI waveguides are expected to result in very competitive speed and power consumption characteristics. This leads to the possibility of integrating a large number of photonic digital units together, but also to integrate them with compact passive optical routers and opens new perspectives for the design of integrated optical circuits.

1.2 Objectives

The starting point of this exciting project, was the promising results obtained by the two groups involved in the present joint PhD, that is to say knowledge of LPN (CNRS) on active and non-linear photonic crystals and processing [46] [47] and the work on the bonding technology and SOI passive waveguide circuits by the

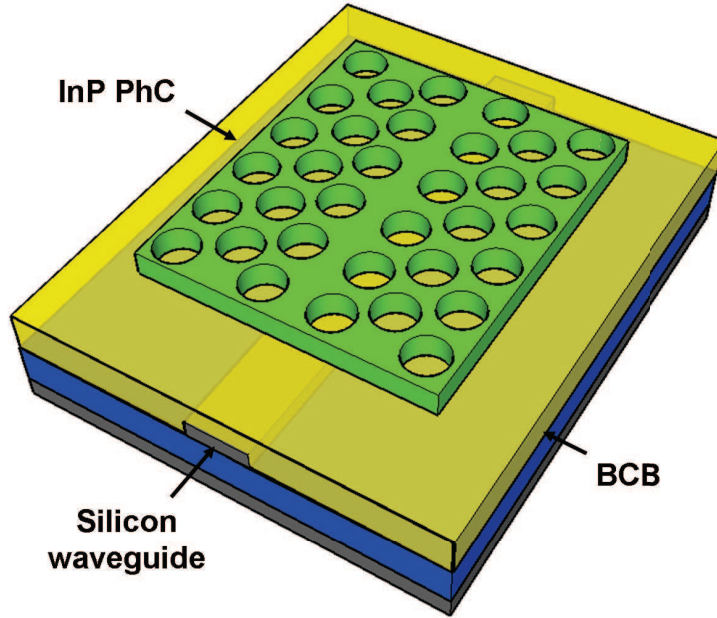


Figure 1.4: Schematic representation of the hybrid structures studied in the present work. The upper level consist in a III-V semiconductor layer photonic crystal structure (green). The lower level consist in a silicon wire on insulator (grey correspond to silicon, deep blue to silicon oxide). Bonding is achieved via the use of an intermediate BCB layer (yellow layer). Those two structures are evanescently coupled. For typical sizes please refer to fig. 2.1

Photonics Research Group at Ghent University and IMEC. [19] [48]. We initially focused on the conception of the various elements making up the hybrid structure through the modelling of various III-V semiconductor photonic crystal devices and the matching waveguide structures in the SOI layer. Then, considering that this work introduces new needs in processing technology and optical experiments, an important fraction of this work was devoted to fabrication, characterisation and understanding of the hybrid structures behaviour. To summarize, we can divide these efforts in four major categories :

- *Processing.* A customized processing scheme, in order to realize these types of structures. Furthermore, particular attention had to be given to bonding and to the critical alignment of the photonic crystal to the silicon waveguide layer in order to have a controlled coupling between the two levels.
- *Modelling.* This work could not leverage from any previous work, since

many differences exist between the structures proposed here and the existing designs which demand a lot of attention in order to design and make PhCs compatible with the requirements imposed in this work, such as phase matching with a silicon wire or the necessary presence of a BCB under-cladding of relatively high index. Furthermore, the designs proposed should be reliable and have as high performance in terms of speed and power consumption.

- *Experimental demonstration.* The study of this new type of structure will demand to built an original and dedicated experimental setup. The experimental studies will result in the first demonstration of the non-linear, or laser, operation of these hybrid structures coupled to the silicon wire underneath.

- *General understanding.* Those clear objectives cannot be achieved without a work dedicated to a better understanding of the behaviour of light in such an hybrid structure. For example, the coupling scheme has to be carefully studied in order to, gradually, increase our knowledge on such a system leading to better design for the active and passive levels.

Overcoming these difficulties, as an objective, should lead to the successful realization of an active hybrid III-V photonic crystal/SOI wire structure. And as a first step laser operation, in suitable active level PhC design, efficiently coupled to the underlying silicon waveguide should be demonstrated.

1.3 Conclusion

The proposal made at the beginning of this thesis, that is to say the realisation and study of hybrid III-V photonic crystal coupled to a silicon wire, is a relatively recent topic in the field of nano-photonics. It involved an exploration of various aspects going from modelling to processing development to the demonstration of laser operation coupled to the silicon waveguide. The idea is to explore the possibilities of such a scheme combining two different materials, getting the best of each, enhanced by the use of photonic crystals.

Concluding this chapter and opening the path to the realization and studies of 2D PhC hybrid structures, it is maybe relevant, or at least interesting, to note that apart from offering a solution for integrated optics, this work can also be considered as the “physical” study of a configuration rather more complex than just the sum of two well known elements, such as silicon waveguides and III-V PhCs, opening a wide range of applications since each level, the silicon and III-V, “act and react” on each other opening possibilities of efficient exploration of a wide variety of non-linear effects (as bistability, slow light, optomechanics, quantum optics...) and even more elaborate systems, such as cascaded cavities [49] [50] (see section

9.2.2-9.2.3), can be envisaged to be implemented quite easily in this system.

References

- [1] V. Wiaux J. Wouters S. Beckx J. Van Campenhout D. Taillaert B. Luyssaert P. Bienstman D. Van Thourhout R. Baets P. Dumon, W. Bogaerts. *Low-loss SOI Photonic Wires and Ring Resonators Fabricated with Deep UV Lithography*. IEEE Photonics Technology Letters, 16(5):1328–1330, 2004.
- [2] Yablonovitch E. *Inhibited spontaneous emission in solid-state physics and electronics*. Phys. Rev. Lett., 58:2059–62, 1987.
- [3] John S. *Strong localization of photons in certain disordered dielectric superlattices*. Phys. Rev. Lett., 58:2486–9, 1987.
- [4] D. Martrou A. Lematre J. Hours J. M. Grard J. Bloch E. Peter, P. Senellart. *Exciton photon strong-coupling regime for a single quantum dot in a microcavity*. Phys. Rev. Lett., 95:067401, 2005.
- [5] C. Becher W. V. Schoenfeld P. M. Petroff Lidong Zhang E. Hu A. Imamoglu P. Michler, A. Kiraz. *A quantum dot single-photon turnstile device*. Sciences, 290-5500:2282–2285, 2000.
- [6] Kevin Hennessy Stefan Strauf Antonio Badolato Pierre M. Petroff Dirk Bouwmeester Yong-Seok Choi, Matt T. Rakher and Evelyn L. Hu. *Laser Photon Statistics in High-Beta Quantum-Dot Photonic-Crystal Nanocavities*. Quantum Electronics and Laser Science Conference (QELS), 2006.
- [7] F. Raineri G. D’Aguanno J. Trull Y. Halioua R. Raj I. Sagnes R. Vilaseca M. Scalora V. Roppo, C. Cojocar. *Field localization and enhancement of phase-locked second- and third-order harmonic generation in absorbing semiconductor cavities*. Phys. Rev. A, 80-043834, 2009.
- [8] A. Schliesser R. Holzwarth P. Del’Haye, O. Arcizet and T.J. Kippenberg. *Microresonator based optical frequency comb*. Nature, 4, 2007.
- [9] S. Combri I. Sagnes C. W. Wong A. De Rossi P. Colman, C. Husko. *Temporal solitons and pulse compression in photonic crystal waveguides*. Nature Photonics, 4:862868, 2010.
- [10] Bahram Jalali and Sasan Fathpour. *Silicon Photonics*. Journal of Lightwave Technology, 24:4600–4615, 2006.
- [11] D. A. B. Miller. Proc. IEEE, 88:728, 2000.
- [12] J. W. Goodman. Proc. IEEE, 72:850, 1984.

- [13] R. A. Soref and J. P. Lorenzo. *Single-crystal silicon: a new material for 1.3 and 1.6 μm integrated-optical components*. Electron. Lett., 21:953–954, 1985.
- [14] R. A. Soref and B. R. Bennett. *Electro-optical effects in Silicon*. IEEE J. Quantum Electron., 23:123–129, 1987.
- [15] A. Liu and al. *A highspeed silicon optical modulator based on a metal-oxide-semiconductor capacitor*. Nature, 427:615–618, 2004.
- [16] Q. Xu and al. *Micrometre-scale silicon electro-optic modulator*. Nature, 435:325–327, 2004.
- [17] V. R. Almeida and al. *All-optical control of light on a silicon chip*. Nature, 431:1081–1084, 2004.
- [18] Y. A. Vlasov and al. *Active control of slow light on a chip with photonic crystal waveguides*. Nature, 438:65–69, 2005.
- [19] W. Bogaerts and al. *Nanophotonic waveguides in silicon-on-insulator fabricated with CMOS technology*. J. Lightwave Technol., 88:401–412, 2005.
- [20] Yurii A. Vlasov and Sharee J. McNab. *Losses in single-mode silicon-on-insulator strip waveguides and bends*. Optics Express, 12-8:1622–1631, 2004.
- [21] Richard Jones Oded Cohen Dani Hak Remus Nicolaescu Alexander Fang Mario Paniccia Haisheng Rong, Ansheng Liu. *An all-silicon Raman laser*. Nature, 433:292–294, 2005.
- [22] A. Polman K. J. Vahala T. J. Kippenberg, J. Kalkman. *Demonstration of an erbium-doped microdisk laser on a silicon chip*. Phys. Rev. A, 74, 2006.
- [23] V. Pudikov Hanmin Zhao Gye Mo Yang; M.H. MacDougal, P.D. Dapkus. *Ultralow threshold current vertical-cavity surface-emitting lasers with AlAs oxide-GaAs distributed Bragg reflectors*. Photonics Technology Letters, IEEE, 7-3, 1995.
- [24] R. C. Miller and al. *Uniaxial Strain Effects in Gallium Arsenide Laser Diodes*. 7th Intl. Conf. Phys. Semicond., Academic Press, 1964.
- [25] A.Y. Cho and J.R. Arthur. Prog. Solid State Chem., 10:157, 1975.
- [26] O.Thomas R.Madar A.Abrutis. J.P.Senateur, F.Weiss. Patent No 93/08838 PCT No FR94/00858 (Europe, U.S.A.), 1993.

- [27] R. Zhang E. J. Geluk F. Karouta J.J.G.M. van der Tol P.J. van Veldhoven R. Ntzel D. Van Thourhout R. Baets F. Bordas, G. Roelkens and M.K. Smit. *Compact Passive Devices in InP Membrane on Silicon*. 35th European Conference on Optical Communications - ECOC, Austria, page p.4.2.4, 2009.
- [28] Ying-hao Kuo Richard Jones Oded Cohen Di Liang Omri Raday Matthew N. Sysak Mario J. Paniccia Alexander W. Fang, Hyundai Park and John E. Bowers. *Hybrid silicon evanescent devices*. Materials today, 10(7-8):28–35, 2007.
- [29] P. Regreny A. Kazmierczak C. Seassal X. Letartre G. Hollinger D. Van Thourhout R. Baets J.M. Fedeli L. Di Cioccio P. Rojo Romeo, J. Van Campenhout. *Heterogeneous integration of electrically driven microdisk based laser sources for optical interconnects and photonic ICs*. Optics Express, 14:3864–3871, 2003.
- [30] K. Huybrechts T. Spuesens G. Roelkens E.-J. Geluk T. de Vries P. Regreny D. Van Thourhout R. Baets G. Morthier L. Liu, R. Kumar. *An ultra-small, low-power, all-optical flip-flop memory on a silicon chip*. Nature Photonics, 4:182–187, 2010.
- [31] P. Regreny C. Seassal D. V. Thourhout S. Verstuyft L. Di Cioccio J.-M. Fedeli C. Lagahe J. V. Campenhout, P. R. Romeo and R. Baets. *Electrically pumped InP-based microdisk lasers integrated with a nanophotonic silicon-on-insulator waveguide circuit*. Phys. Rev. A, 15, 2007.
- [32] C. A. Wang H. K. Choi and N. H. Karam. Proceedings of the Conference Laser and on Electra-Optics (CLEO), 334:170–175, 1991.
- [33] Kar Wei Ng Wai Son Ko Linus C. Chuang Forrest G. Sedgwick Roger Chen, Thai-Truong D. Tran and Connie Chang-Hasnain. *Nanolasers grown on silicon*. Nature, 5:170–175, 2011.
- [34] A. W. Fang and al. *Hybrid evanescent silicon devices*. Material today, 10:28, 2007.
- [35] D. Van Thourhout R. Baets R. Ntzel F. Raineri I. Sagnes G. Beaudoin G. Roelkens, L. Liu and R. Raj. *Light emission and enhanced nonlinearity in nanophotonic waveguide circuits by III-V/silicon-on-insulator heterogeneous integration*. Journal of applied physics, 104, 2008.
- [36] J.V. Campenhout and al. *Electrically pumped InP-based microdisk lasers integrated with a nanophotonic silicon-on-insulator waveguide circuit*. Opt. Express, 15:6744, 2007.

- [37] J. D. Joannopoulos and al. *Photonic Crystals*. Princeton University Press, 1995.
- [38] Ivan S. Nikolaev Arie Irman Karin Overgaag Daniel Vanmaekelbergh Willem L. Vos Peter Lodahl, A. Floris van Driel. *Controlling the dynamics of spontaneous emission from quantum dots by photonic crystals*. Nature, 430, 2004.
- [39] K. G. Gibbs and al. *Nonlinear optics of normal mode coupling semiconductor microcavities*. Rev. Mod. Phys., 71:1591, 1999.
- [40] S. Noda and al. *Trapping and emission of photons by single defect in photonic bandgap structure*. Nature, 407:608, 2000.
- [41] O. Painter and al. *2D photonic band-gap defect mode laser*. Science, 300:1537, 1999.
- [42] M. Notomi and al. *Nonlinear and adiabatic control of high- Q photonic crystal nanocavities*. Opt. Express, 15:17458, 2007.
- [43] J. Vukovic and al. *Design of photonic crystal microcavities for cavity QED*. Phys. Rev. E, 65:016608, 2001.
- [44] Dirk Englund Hatice Altug and Jelena Vuckovic. *Ultrafast photonic crystal nanocavity laser*. Nature Physics, 2:484–488, 2006).
- [45] Mitsugi S Shinya A Tanabe T, Notomi M and Kuramochi E. *All-optical switches on a silicon chip realized using photonic crystal nanocavities*. Appl. Phys. Lett., 87-151112, 2005).
- [46] F. Raineri and al. *Optical amplification in 2D photonic crystals*. Appl. Phys. Lett., 86, 2005.
- [47] A.M. Yacomotti and al. *All-optical bistable band-edge Bloch modes in a two-dimensional photonic crystal*. Appl. Phys. Lett., 88, 2006.
- [48] G. Roelkens and al. *Adhesive Bonding of InP/InGaAsP Dies to Processed Silicon-on-Insulator Wafers using DVS-bis-Benzocyclobutene*. Journal of Electrochemical Society, 153(12):1015–1019, 2006.
- [49] John D. Joannopoulos Peter Bienstman Roel Baets Simon-Pierre Gorza Bjrn Maes, Marin Soljacic and Marc Haelterman. *Switching through symmetry breaking in coupled nonlinear micro-cavities*. Optics Express, Vol. 14, Issue 22, pp. 10678-10683 (2006), 14:10678–10683, 2006.
- [50] Kirk A. Fuller A. T. Rosenberger David D. Smith, Hongrok Chang and Robert W. Boyd. *Coupled-resonator-induced transparency*. Physical Review A, 69, 2004.

2

III-V photonic structures on SOI wires: general considerations and discussion

The concepts and general behaviour of hybrid structures with silicon and III-V semiconductors are still at an early stage of exploration and their potential still has to be demonstrated. After briefly discussing the two levels of the hybrid structures we will go on to discuss the evanescent coupling which actually links the two and “hybridises” them.

2.1 General scheme of the structure

The III-V PhC structures and silicon waveguides on silica are bonded together using an adhesive technique relying on a polymer called Benzo-cyclo-butene (BCB) (see fig.2.1). The two levels are denoted as an “active level” and “passive level” respectively. Indeed, the idea behind the combination of these materials, as explained in introduction, is to use the large non-linearities and light emission properties of III-V for active functions and the silicon for passive functions such as guiding.

2.2 Passive layer : SOI waveguide layer

The “passive” denomination for the silicon layer comes from the fact that this level is used for propagation and guiding of light, and thus injection or extraction

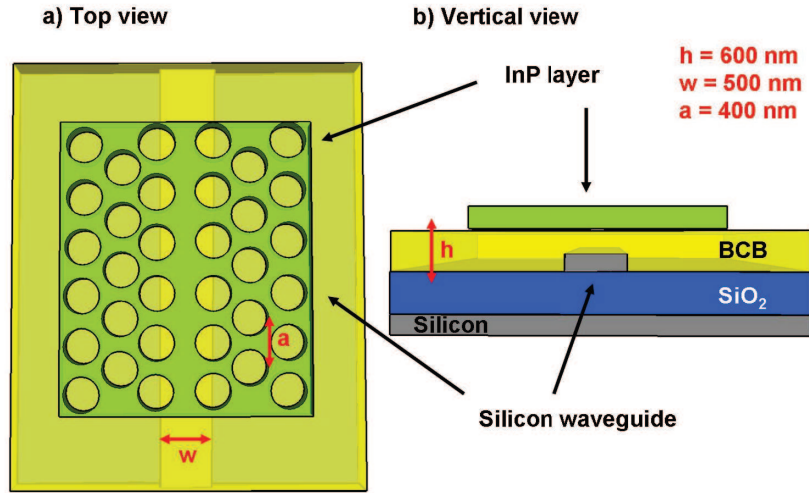


Figure 2.1: Top view (a) and vertical view (b) of the hybrid structure. Typical scales are reported on the figure : $h=600$ nm, $a=300$, $w=500$ nm

to, or from, the III-V “active” level. It consists of low loss silicon waveguides that can also be used to connect several active units. SOI takes advantage of silicon’s natural oxide as a highly effective waveguide cladding material, for the fabrication of ultra-small waveguides. These wire waveguides, with dimensions of $220\text{nm} \times 500\text{nm}$, provide tight confinement of the optical field [1] and single mode operation around telecommunication wavelengths. They can be implemented with small radii of curvature ($<5\mu\text{m}$) [2] making it possible to build compact optical circuitry. A wide variety of passive components have already been demonstrated [3] [4] [5] using this type of patterned SOI.

Since the idea is to study the opportunities of the hybrid structure for optical interconnects, we tried to keep the process as much as possible CMOS compatible, regarding the fact that the temperature used during the processing are well below the limits imposed by CMOS requirements (400 degrees). The silicon on insulator layer is completely processed in a CMOS line in the framework of Epixfab using Deep Ultra-Violet (DUV) lithography. DUV lithography is better suited for mass fabrication, with a lower resolution, but offering large throughput and a large field size.

2.3 Active level : III-V Photonic Crystal layer

The upper level, corresponding to the “active” region in the system, is a III-V layer incorporating quantum wells (QW). This level is the source of all the effects under study since quantum wells act as emitting or absorbing regions, leading to emission or strong index modulation due to external injection or pumping [6] [7].

These properties are mainly related to the energy band structure of electrons in those semiconductors. Indeed, in this type of material the electrons can have energies only within certain bands, named the “conduction band” - corresponding to higher energy, and the “valence band” - for lower energy, separated by a band gap. Without any energy channelled to the system all the carriers are located in the valence band while the conduction band remains empty. Under excitation, through absorption of photons of higher energy than the band gap, it is possible to populate those higher energy states leaving the system with a certain density of electrons in the conduction band and holes in the valence band. This results in a refractive index, imaginary and real part, change. Moreover, when the band gap is direct, as in the III-V semiconductors used in this work, that is to say the wave-vector of the electron in the highest energy state of the valence band is equal to the one in the lowest energy state of the conduction band, radiative recombination, between holes in the valence band and electrons in the conduction band, is a very efficient process. Under strong excitation, this system can go in population inversion, thus stimulated emission can become the main process of recombination, leading to laser operation.

Epitaxial growth of composite III-V semiconductors layers allows the realization of QWs resulting in a material where radiative recombinations are promoted at desired wavelengths, corresponding to the quantized levels of the well states, around 1.55 microns in this work (see fig 2.2).

2.4 Evanescent coupling

As mentioned above, the “active” and “passive” layers are bonded together, through an adhesive bonding technique using an intermediate BCB layer, to make a hybrid structure. The proximity of the two structures leads to light transfer between the two levels through evanescent coupling. Evanescent coupling can be seen as an optical analogue to quantum tunnelling, and in the same manner the coupling strength is proportional to the field overlap between the two structures. Moreover, the proximity of these two structures induces a reciprocal perturbation of the refractive index that can disturb their respective optical properties. For example, as will be seen in chapter 7, the presence of a PhC waveguide bonded with 400 nm separation on top of a silicon wire can lead to the opening of a bandgap in the latter.

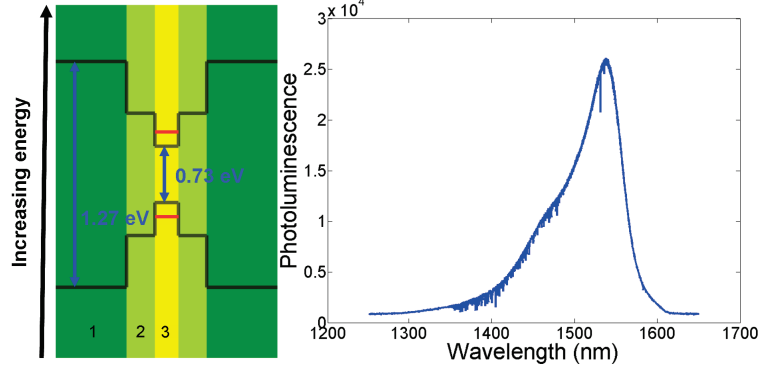


Figure 2.2: Left - Energy levels in the InP/InGaAsP/InGaAs quantum wells (black line): 1- InP around 60 nm thick (gap around 900 nm), 2- InGaAsP around 16 nm thick (gap around 1200 nm), 3- InGaAs around 13.5 nm (gap around 1698 nm); The red line represent a possible quantified state in the well. Right - Photoluminescence spectra of the composite layer

Thus, particular attention has to be given to the distance between those two layers, in order to obtain a good coupling while keeping in mind that the perturbations induced on the optical properties of each structure should be as small as possible. Under this last condition of small perturbation the two levels can be considered as mostly “independent”. In that sense the “coupled mode theory” [8], describing this scheme of coupling, starts on the basis of the unperturbed optical modes of each structure and a coupling term is added in a second step.

Coupled mode theory for two parallel waveguides

Considering two coupled waveguides (as depicted in fig. 2.3) gives enough insights to have a clear understanding on the “evanescent coupling” mechanism and the impact of various parameters.

Following the theory explained in [9], the starting point, using a perturbative approach, is the solution of the propagation equations for each waveguide involved :

$$\frac{da_1}{dz} = -j\beta_1 a_1 \quad (2.1)$$

$$\frac{da_2}{dz} = -j\beta_2 a_2 \quad (2.2)$$

where a_1 and a_2 correspond respectively to the mode amplitudes in each waveguide, with an implicit time dependence $e^{j\omega t}$ while β_1 and β_2 are the propagation constants of the modes in the respective waveguides. When the waveguides are brought close to each other, the modes interact through the overlap of the respec-

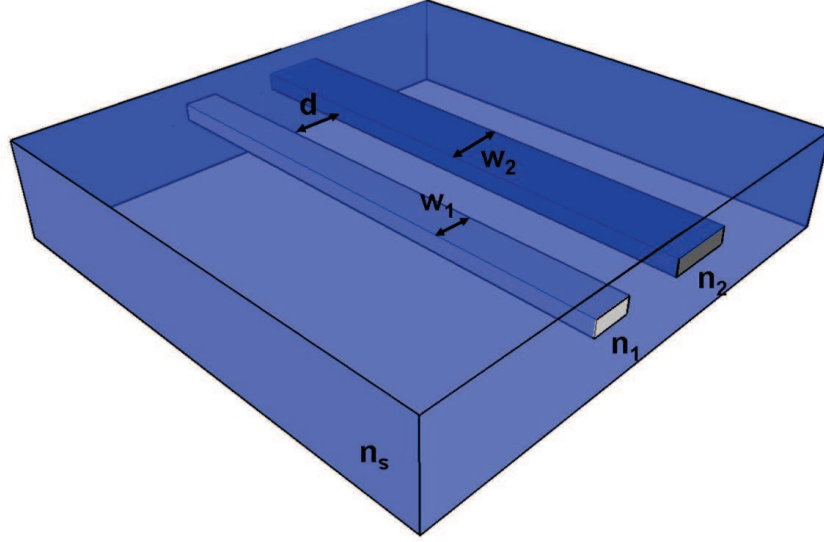


Figure 2.3: Scheme of two parallel waveguides of index and width respectively n_1 , w_1 and n_2 , w_2 separated by a distance d and embedded in a material of index n_s

tive evanescent fields and thus coupling terms are introduced in the equations. This way, the equations of propagation will become :

$$\frac{da_1}{dz} = -j(\beta_1 - K_{11})a_1 - jK_{12}a_2 \quad (2.3)$$

$$\frac{da_2}{dz} = -j(\beta_2 - K_{22})a_2 - jK_{21}a_1 \quad (2.4)$$

where K_{12}, K_{21} and K_{11}, K_{22} are respectively the mutual and the self-coupling coefficients. Note, that, more than adding a coupling coefficient to the original equations, the propagation constant for each mode is perturbed and is changed respectively in $\beta_1 - K_{11}$ and $\beta_2 - K_{22}$.

Assuming that the two waveguides modes are power orthogonal, the total power carried through the waveguides is just the sum of each :

$$P(z) = |a_1|^2 + |a_2|^2 \quad (2.5)$$

If the system can be considered as lossless we have :

$$\frac{dP(z)}{dz} = 0 \quad (2.6)$$

Because eq.2.5 is independent of the initial conditions, one can show that coupling coefficients K_{11}, K_{22} have to be real and that :

$$K_{12} = K_{21}^* = \kappa \quad (2.7)$$

Note that the coupling factor κ is proportional to the overlap of the mode of each waveguide. These coefficients are functions of the different index and sizes in the structure [10] :

$$K_{ij} = \frac{\omega}{4} \int a_i^* (n_s^2 - n_j^2) a_j da \quad (2.8)$$

For uniform waveguides both propagation constants and coupling coefficients are independents of z . Then eq.2.3 and can be solved analytically. For simplicity one can take out a common phase factor using the change of variable :

$$a_i(z) = \hat{a}_i \cdot \exp\left(-j \frac{\beta_1 + K_{11} + \beta_2 + K_{22}}{2} z\right) \quad (2.9)$$

then the equations of propagation can be rewritten as :

$$\frac{d\hat{a}_1}{dz} = -j\delta\hat{a}_1 - j\kappa\hat{a}_2 \quad (2.10)$$

$$\frac{d\hat{a}_2}{dz} = +j\delta\hat{a}_2 - j\kappa\hat{a}_1 \quad (2.11)$$

with

$$\delta = \frac{\beta_1 + K_{11} - \beta_2 - K_{22}}{2} \quad (2.12)$$

the detuning or phase mismatch factor (ie. the difference in the propagation constants between the modes in each waveguides).

Equations 2.10 and 2.11 can be recast in a matrix form

$$\frac{d}{dz} \mathbf{A} = -j\bar{\mathbf{H}}\mathbf{A} \quad (2.13)$$

with

$$\mathbf{A} = \begin{pmatrix} \hat{a}_1 \\ \hat{a}_2 \end{pmatrix} \quad (2.14)$$

$$\bar{\mathbf{H}} = \begin{pmatrix} +\delta & \kappa \\ \kappa & -\delta \end{pmatrix} \quad (2.15)$$

Since $\bar{\mathbf{H}}$ is Hermitian for a lossless system, it can be diagonalized by a unitary matrix such that :

$$\mathbf{O}^t \bar{\mathbf{H}} \mathbf{O} = \mathbf{B} \quad (2.16)$$

where \mathbf{B} is a diagonal matrix

$$\mathbf{B} = \begin{pmatrix} \beta_s & 0 \\ 0 & \beta_a \end{pmatrix} \quad (2.17)$$

and

$$\mathbf{O} = \begin{pmatrix} \cos(\eta/2) & -\sin(\eta/2) \\ \sin(\eta/2) & \cos(\eta/2) \end{pmatrix} \quad (2.18)$$

where the parameter η is defined by

$$\tan(\eta) = \frac{\kappa}{\delta} \quad (2.19)$$

The diagonal elements β_s and β_a are the propagation constants of the eigen-modes of the parallel waveguides, ie. the composite modes. To see this, one can make the transformation

$$\mathbf{A} = \mathbf{O}\mathbf{W} \quad (2.20)$$

under which the coupled-mode equation 2.13 reduces to

$$\frac{d}{dz}\mathbf{W} = -j\mathbf{B}\mathbf{W} \quad (2.21)$$

Hence \mathbf{W} may be interpreted as the amplitude matrix for the eigen-modes of the parallel waveguides with propagation constant β_s and β_a , representing the symmetric-like and antisymmetric-like composite modes, respectively. The mode amplitude may be expressed in terms of the transfer matrix as

$$\mathbf{A}(z) = \mathbf{T}(z)\mathbf{A}(0) \quad (2.22)$$

where

$$\mathbf{T} = \mathbf{O} \begin{pmatrix} e^{-j\beta_s z} & 0 \\ 0 & e^{-j\beta_a z} \end{pmatrix} \mathbf{O}^{-1} \quad (2.23)$$

or more explicitly, the matrix elements can be given by

$$t_{11} = t_{22} = \cos(Sz) - j\cos(\eta)\sin(Sz) \quad (2.24)$$

$$t_{12} = t_{21} = -j\sin(\eta)\sin(Sz) \quad (2.25)$$

where

$$S = \sqrt{\delta^2 + \kappa^2} \quad (2.26)$$

The propagation constants of the composite modes are

$$\beta_s = \beta_0 + S \quad (2.27)$$

$$\beta_a = \beta_0 - S \quad (2.28)$$

where

$$\beta_0 = \frac{\beta_1 + K_{11} + \beta_2 + K_{22}}{2} \quad (2.29)$$

The resulting propagation constants of the composite modes are therefore de-phased by $\pm S$ from a common propagation constant β_0 .

Suppose that, at the input, only one waveguide is excited, ie. $a_1(0) = 1$ and $a_2(0) = 0$. The guided power in waveguides 1 and 2 can then be given by

$$P_1(z) = \cos^2(Sz) + \cos^2(\eta)\sin^2(Sz) \quad (2.30)$$

$$P_2(z) = \sin^2(\eta)\sin^2(Sz) \quad (2.31)$$

Maximum power transfer from guide 1 to guide 2 occurs then at $z = L_c$, where

$$L_c = \pi / (2S) \quad (2.32)$$

and is equal to

$$P_{2max} = \sin^2(\eta) \quad (2.33)$$

It should be noted that, for complete power transfer, the two waveguide modes have to be phase matched, ie. $\delta = 0$. According to the coupled-mode theory the modes are orthogonal. Hence the power extinction ratio is defined as :

$$E.R. = \frac{P_{1min}}{P_{2max}} = \frac{1}{\tan(\eta)} \quad (2.34)$$

One of the physical interpretation of this energy transfer is that the beating re-

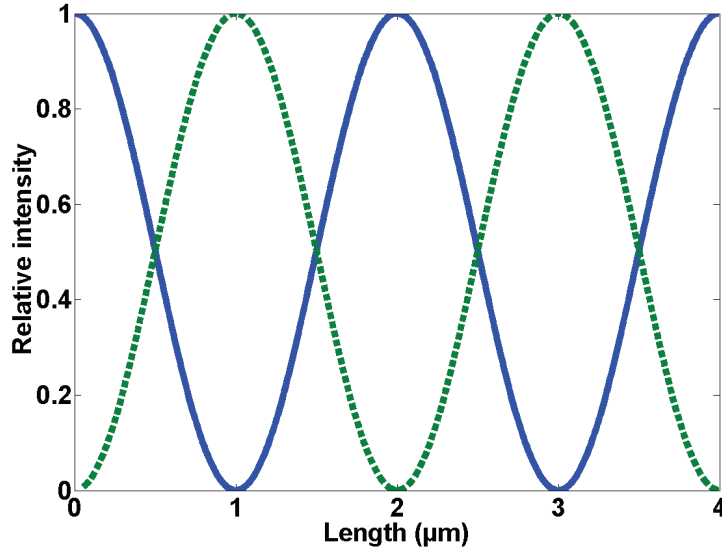


Figure 2.4: Energy transfer between two similar waveguides against wavelength for initial parameter $a_1=1$ and $a_2=0$, the line correspond to waveguide 1 and the dashed line to waveguide 2, for two different detuning - blue correspond to zero detuning and then a maximum transfer of 100 percent, - green correspond to a detuning of 3 percent with a maximum energy transfer around 96 percent

sulting from interferences between the composite symmetric mode (bound state, higher n_{eff}) and antisymmetric mode (anti-bond state, lower n_{eff}) with different propagation vector (β_s, β_a) leads to an intensity profile where destructive interference occurs locally in one waveguide while at the same time the interference is constructive in the other one, and vice-versa. The intensity pattern depends on

the dephasing term S between the composite modes, and consequently fixes the length for maximum transfer. Figure 2.4 depict this energy transfer for the cases of perfectly matched and slightly detuned waveguides.

We conclude from this theoretical analysis that the phase matching parameter is critical. In order to reach the maximum of exchange energy it is strictly necessary to fulfil the phase matching condition. This can be understood by looking at the index of the modes of the uncoupled and coupled waveguides system as plotted in fig. 2.5. On this picture it can be seen that coupling induces a clear splitting in the dispersion relation located around the phase matching point.

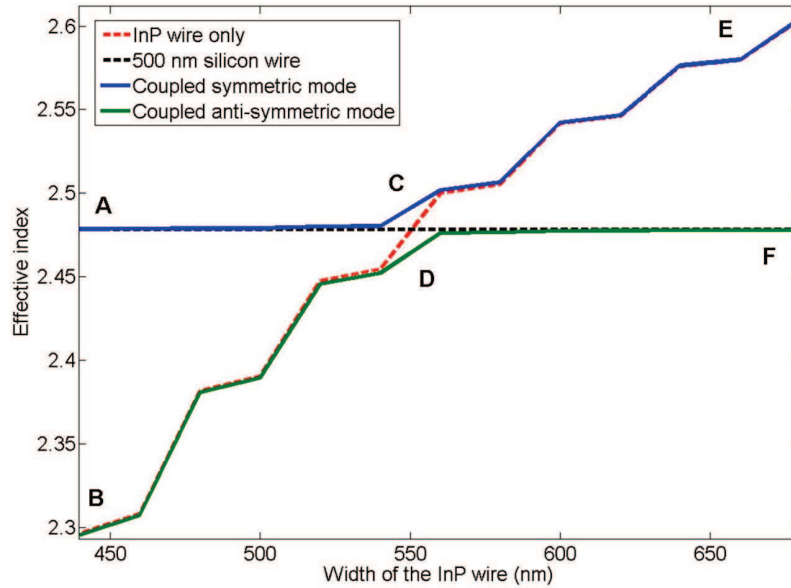


Figure 2.5: Index of the 2 first modes of the coupled InP wire of variable width (height=255nm) with a silicon wire (500×220nm) separated by a 465 nm thick BCB intermediate layer. Dashed line corresponds to the index of an uncoupled wire. Field profiles of points A-F are plotted on fig. 8.17.

2.5 Conclusion

The description of the hybrid structure given here uses a picture where the passive SOI waveguide layer was considered independently of the active III-V photonic layer. In this picture all the non-linear effect, as well as emission, concern light located in the upper level while the silicon waveguide is the channel for transporting light in and out of the system connecting it, for example, to silicon circuitry.

This picture is legitimate in the limit where the coupled mode theory is valid, that is to say when the unperturbed modes of each structure gives the basis to solve the coupled system problem. This characteristic will be of great help for the modelling study, indeed since the two levels are optically almost independent, modelling of each level can be done separately while keeping in mind the need for phase matching. The analysis of the coupled mode theory shows that for an optimal coupling of the two levels phase matching is an important parameter. Moreover, since the overlap between the respective mode of each structure will impact the coupling parameter, it is of importance to control the thickness of the intermediate layer. As will be seen in the coming chapter, this last point renders alignment of the two levels critical, therefore the development of an accurate technique of alignment during the processing will be required.

References

- [1] W. Bogaerts and al. *Nanophotonic waveguides in silicon-on-insulator fabricated with CMOS technology*. J. Lightwave Technol., 88:401–412, 2005.
- [2] Vincent Wiaux Johan Wouters Stephan Beckx Joris Van Campenhout Dirk Taillaert Bert Luyssaert Peter Bienstman Dries Van Thourhout Pieter Dumon, Wim Bogaerts and Roel Baets. *Low-Loss SOI Photonic Wires and Ring Resonators Fabricated With Deep UV Lithography*. IEEE Photonics Technology Letters, 16, 2004.
- [3] E. K. Liu Y. Gao C. Z. Zhao, G. Z. Li and X. D. Liu. *Silicon on insulator MachZehnder waveguide interferometers operating at 1.3 μ m*. Appl. Phys. Lett., 67:24482449, 1995.
- [4] F. Copping P. D. Trinh, S. Yegnanarayanan and B. Jalali. *Silicon on-insulator (SOI) phased-array wavelength multi-demultiplexer with extremely low-polarization sensitivity*. Appl. Phys. Lett., 9:940942, 1997.
- [5] S. Yegnanarayanan P. D. Trinh and B. Jalali. *Integrated optical directional couplers in silicon-on-insulator*. Electron. Lett., 31:20972098, 1995.
- [6] P. N. Butcher and D. Cotter. *The elements of nonlinear optics*. Cambridge University Press, 1990.
- [7] Robert W. Boyd. *Nonlinear Optics, Second Edition*. Academic Press; 2 edition, 2002.
- [8] W. Streifer A. Hardy. *Coupled mode theory of parallel waveguides*. Journal of Lightwave Technology, 3:1135–1146, 1982.
- [9] W. Huang. *Coupled-mode theory for optical waveguides : an overview*. J. Opt. Soc. Am., 11:963–983, 1994.
- [10] Shun-Lien Chuang. *A coupled mode formulation by reciprocity and variational principle*. Journal of Lightwave Technology, 1:5–15, 1987.

3

Hybrid III-V photonic crystal on silicon wire technology

Our first goal is the realization of the hybrid structures keeping in mind two main requirements. Firstly, while the bonding technique used in the present work has been the object of a lot of work during the last years, leading to promising results [1], it was still necessary to work on this technological step in order to obtain highly reliable bonding, by improving the control of the thickness of the intermediate layer and increase the yield. Secondly, considering the smallness of the objects envisaged, we had to develop an alignment technique which would result in almost perfectly aligned structures in order to control the coupling between the two layers. Since the silicon layer was the result of a standard process in the CMOS line of Leti/IMEC no particular work was devoted to the passive layer technology. As mentioned before, the basic processing know how of photonic crystals was already available in LPN. In this work, adaptations to this process were needed however to apply the PhC processing to our specific hybrid structure. When developing processing steps one should try to keep the process as simple as possible, in order to improve the process window, to increase the repeatability and yield.

3.1 Silicon layer processing

Silicon is a well-studied material and a lot of investments in processing have been made during the last decade making this material unsurpassed in terms of photonic

device quality. In the present work the silicon layer was fabricated in the CMOS line of IMEC and LETI. The processing is based on deep UV (193nm) lithography, resulting in high performance waveguide structures (loss around 2.4 dB/cm) with sub-micron cross-sectional dimensions [2]. The silicon waveguide layer is etched using a Cl_2/HBr Reactive Ion Etch (RIE). The 220nm thick Si layer is entirely etched through, leaving a 220nm thick strip waveguide on a $2\mu m$ buried oxide (BOX) on top of a silicon substrate (this silicon oxide thickness does not introduce any leakage in the substrate). In the same step, $10\mu m \times 10\mu m$ marks for subsequent alignment (as will be discussed in section 3 of the present chapter) are defined in the Si. The Si wires are fanned out to a width of $10\mu m$ for out coupling, via shallow etched grating couplers [3]. The silicon waveguide dimensions have been confirmed by SEM measurements, the wire width being varied deliberately across the 8" wafer, following the exposure dose.

The technology used in this work leads to a very good control on the process-

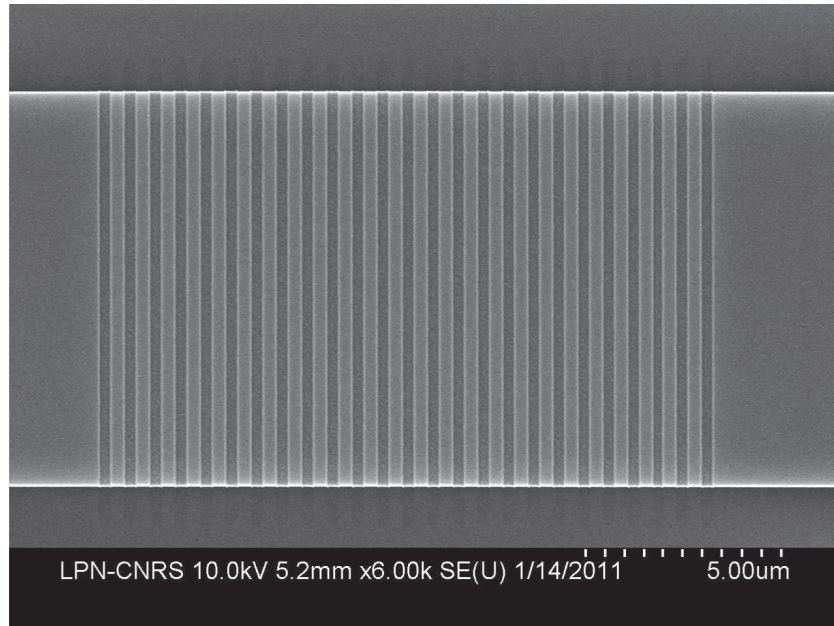


Figure 3.1: SEM image of grating couplers etched in the LETI fab. The periodicity of the gratings is of the order of 610 nm and the etch depth around 50 nm. The coupling efficiency with a single mode fiber is around 30% over a bandwidth of approximatively 40 nm.

ing and etching of the silicon layer. as can be seen on fig. 3.1 after the two steps etching of grating couplers in the LETI fab. DUV, as said already, offers large throughput and a large field size but has as main drawback limited resolution compared to electronic-beam lithography (e-beam). Defining PhC, designed for 1.55

μm is a real challenge. Anyway, it is still possible to make very small and rather complicated structures such as grating couplers.

3.2 Bonding technologies

Since silicon does not seem very suitable for active opto-electronic functions, as was discussed in the first chapter, we chose to locally integrate an active material, III-V semiconductors, on top of the silicon. Several ways of doing this integration process were studied during the last years and is still a hot topic of research. For example, some efforts have been devoted to the hetero-epitaxial growth of an active material, like InGaAs [4], on silicon. Unfortunately, this is not straight forward because of the strong lattice mismatch between Silicon and III-V semiconductors (4% between GaAs and Si, and 7.8 % between InP and Si) giving rise to dislocations in the grown material. The dislocation density is in the range of $10^6/\text{cm}^2$ [5] leading to undesirable effects such as decreasing the carrier lifetime or degrading the emission properties of the semiconductor.

Another way to integrate an active III-V semiconductor layer on silicon is to use a bonding technique. Here bonding refers to a technology that brings wafers into contact to realize a strong bond between them either by interfacial bonds or by using a "glue", e.g. polymers or metals. The two mainstream bonding technologies available, which are molecular bonding and adhesive bonding, are outlined below.

3.2.1 Molecular bonding technique

Molecular bonding is a technique which consists in creating links between two surfaces of different materials by molecular rearrangement. The technique is to apply pressure on the two layers brought face to face and the sample is heated (at temperatures as high as 600 degrees) in a controlled atmosphere. This technique has shown to be suitable to make lasers (VCSEL), as for example InGaAs/GaAs on silicon lasers [6]. But the resulting composite structure suffers from dislocations at the interface, arising from the mismatch of the thermal expansion coefficient between the two materials, severely reducing the quality of the laser.

More recently, this method has been improved by the use of an intermediate silicon oxide layer. This approach relies on the deposition of SiO_2 both on the Si and III-V surface. After proper cleaning and chemical activation of the deposited SiO_2 layers [7], the two surfaces are brought together in a controlled environment and annealed at temperatures below 300 degrees which results in a rearrangement of the atoms at the interface, creating covalent bonds. Hence, high quality bonding can be obtained, since the use of lower temperature, allowed by the relatively low energy necessary to create $\text{SiO}_2 - \text{SiO}_2$ bonds, relaxes the thermal expansion co-

efficient mismatch constraint in a high temperature environment. This technique has lead to structures such as the lasers made by Bowers group [8] or in a collaboration between LETI and the Photonics Research Group [9]. One drawback of this method is that from a technological point of view this technique is very demanding since it requires substantial surface preparation and wafer quality.

3.2.2 Adhesive bonding technique

Adhesive bonding relies on the Van der Waals binding of the two materials involved on each side with an intermediate layer, for example a layer of polymer between silicon and III-V. This technique has the advantage of being usually less restrictive in terms of cleaning and surface preparation. Many polymers can be used as intermediate adhesive bonding layers, such as epoxies or negative photoresists [10]. Given the drawbacks of $SiO_2 - SiO_2$ bonding and the advantage of adhesive bonding, we decided to elaborate on the adhesive bonding technique for the structures developed in this work, and more particularly adhesive bonding using benzocyclobutene (BCB). Indeed, as will be shown in this chapter, the use of this polymer allows to work on already pre-patterned surfaces thanks to its planarization capabilities. Moreover, BCB possesses a high resistance to all sorts of chemicals used in standard III-V processing, which is of importance for the present work where photonic crystal will have to be etched in the bonded III-V semiconductors layer. Finally the ease, compared to molecular bonding, to carry out this process will become clearer later on this section.

Basically, the processing steps are the following (illustrated in Fig. 3.2):

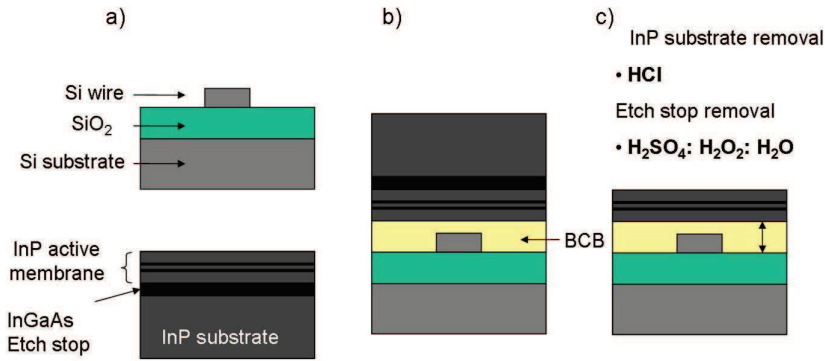


Figure 3.2: Main processing steps for bonding, a) Starting materials consist of the III-V semiconductor layer and a prepatterned silicon substrate, b) after spin coating of BCB on the silicon layer the InP is gently placed on the sample, c) entire structure obtained after a curing step and the substrate removal.

- Spin-coating of BCB on the cleaned silicon substrate.

- Positioning of the III-V layer on top of the BCB layer.
- Curing of the BCB.

The starting point of the bonding process is the spin-coating of BCB on the silicon substrate. The cleaning of the silicon layer is done, after removal of a protecting resist layer, by the use of a standard process named RCA-1 consisting in DI water + NH_4OH + H_2O_2 , with respective fractions 5:1:1, heated up to 70 degrees. The III-V layer is cleaned using acetone + isopropyl-alcohol (IPA). The spin-coating parameters, 5000 rpm/s during 30 seconds, are kept constant and the thickness is controlled by dilution of the commercial 1 μm thick BCB in a solvent : mesitylene. Indeed, as can be seen on the data reported in fig. 3.3 the addition of mesitylene allows to control the thickness of the bonding layer from 1 μm to 200 nm.

The use of a pre-patterned silicon layer is made possible by the strong planariza-

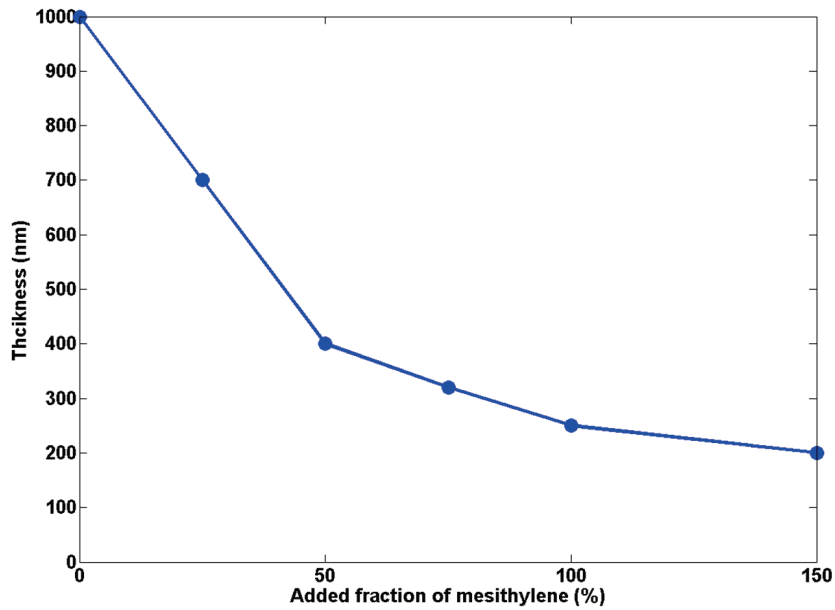


Figure 3.3: Thickness of BCB against the fraction of added mesitylene. Data from [11]

tion power of BCB. For example, on fig. 3.4 is reported the profile (made using a Dektak profiler) of 300 nm thick BCB on a silicon-on-insulator layer with silicon waveguides of 220 nm height and 1 μm width surrounded by etched trenches of 5 or 10 microns. It can be seen from these measurements that the profile of the BCB surface strongly depends of the underlying pattern. We observe a relative modulation of 60 nm (blue full line) around the silicon wires and a strong modulation between the zones corresponding to different trench widths around the wire. This

modulation correspond to a planarization close to 80 % (relatively to the height modulation of the Si waveguides) around the waveguides which is already a relatively high value. But, in fact, we will mostly work with a total thickness of the order of 800 nm, as desired from modelling to be the typical thickness of BCB to use for evanescent coupling (see section 8.4). For layers this thick we expect to obtain a quasi-perfectly flat surface of BCB. Moreover, after spin-coating, the BCB is softly cured at 80 degrees during 10 minutes to remove solvents and residual trapped air bubbles and this thermal treatment also causes a reflow of the DVS-BCB, which improves its planarisation.

In addition, during this work, we were able to obtain a better adhesion and pla-

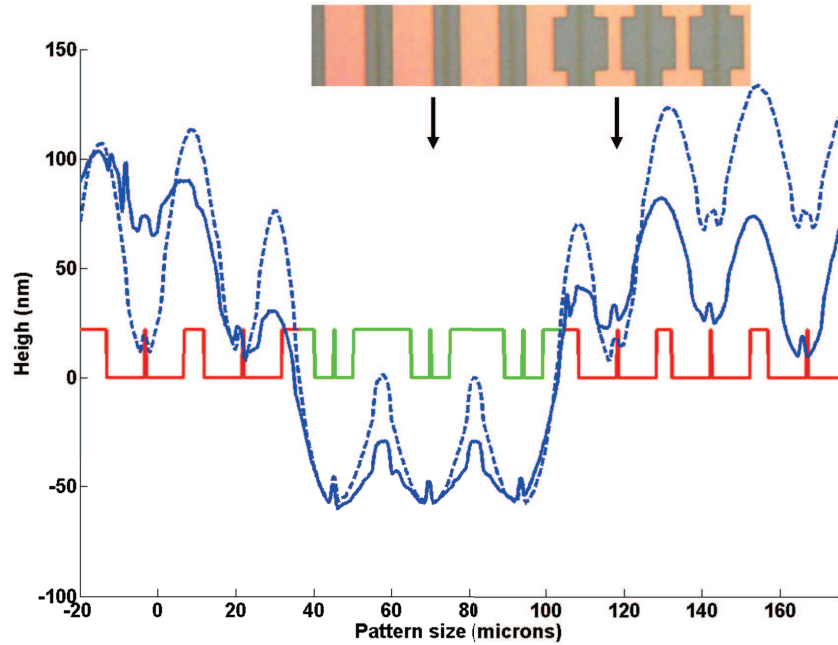


Figure 3.4: Relative planarization of a 300 nm thick layer of BCB with (blue dotted line) and without oxygen plasma exposure (blue line) on the $220\text{ nm} \times 1\text{ }\mu\text{m}$ height surrounded but trenches of 5 or 10 μm SOI cross-section (red and green line). Two different patterns are etched in the SOI layer : Zone A (red line) - 300 nm width silicon wire inserted in 5 microns trenches separated by 15 microns of silicon, Zone B (green line) - 300 nm width silicon wire inserted in 10 microns trenches separated by 10 microns of silicon. Inset correspond to a photography of the sample.

narization of BCB by first exposing the SOI layer to an RIE oxygen plasma. This is most probably due to the activation of the native oxide at the surface. Indeed, compared to the previous results showing trenches of 60 nm height (blue full line in fig. 3.4) we obtain after this process 30 nm height of BCB around the wave-

uides (blue dotted line in fig. 3.4). This consideration is of importance since in the following step a III-V layer (pieces of around $3 \times 3 \text{ mm}^2$) is placed on top of this BCB layer. Thus a good planarization prevent the trapping of air between the BCB and the III-V semiconductors layer, consequently avoiding any problems that can arise during the curing step. Then the III-V semiconductor layer is brought into contact. Adhesion occurs at 150 degrees, as DVS-BCB has about the lowest viscosity at this temperature. The final step is curing of the whole structure during 3 hours around 250 degrees, by increasing the temperature steeply. After bonding, the InP substrate is removed by wet etching in a HCl solution.

Another major improvement made concerns the yield. Indeed, in the context of

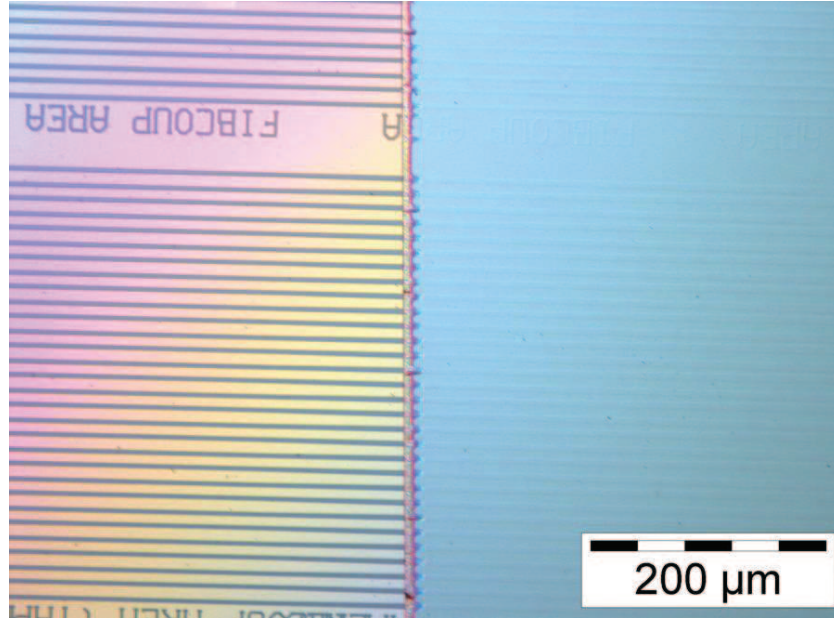


Figure 3.5: Photograph of a bonded InP layer (blue zone on the right) above a SOI chip patterned with waveguides (left part of the picture)

collaborations with other groups, we observed that it was difficult to bond InGaAs layer to the SOI. This was attributed to the fact that, after the substrate preparation, the InGaAs layer is hydrophobic, while the InP layer is hydrophilic. This implies that the surface properties of the bonded layer is crucial in realizing high yield bonding. In order to solve this problem we deposit a thin SiO_2 layer on top of InGaAs/InP layers resulting in a dramatic improvement of the InGaAs bonding and an increase in the bonding yield with InP layers from 50% to almost 100%. An example of the quality of the bonded InP layer bonded on the patterned SOI is shown on fig. 3.5.

Furthermore, this SiO_2 layer has two other advantages. First, it provides a way to control the thickness of our intermediate layer. Indeed, we can adjust the distance between the two layers by changing the thickness of this added SiO_2 layer. Secondly, since SiO_2 possesses a higher thermal conductivity the heat is better spread in this intermediate layer and is more efficiently sunk in the silicon substrate. The bonding technology presented was already available and developed at Gent university. It was transferred to CNRS-LPN, to allow for a faster turn around in processing the hybrid photonic crystal structures and resulted in several improvements. Moreover, this work has gone further than the context of the present thesis since it has been useful for several other groups. First as a feedback to the Photonics Research Group. Then the work on bonding of InGaAs has allowed measurements of intra-band transitions in InGaAs/GaAs quantum dots performed at IEF [12] or for bonding GaAs on Bragg mirrors in the study of phase-locked second harmonic generation [13] in collaboration with the university polytechnic of Catalonia in Barcelone.

3.3 Alignment technology

As already presented in chapter 2, a good alignment of the two levels is critical. Reminding that the typical sizes of the silicon waveguides or III-V semiconductor photonic crystal slab is hundred of nanometers, it is clear that the alignment requirements are of the order of tens of nanometers. It was therefore necessary to develop a new alignment technique to comply with this need. In order to achieve this

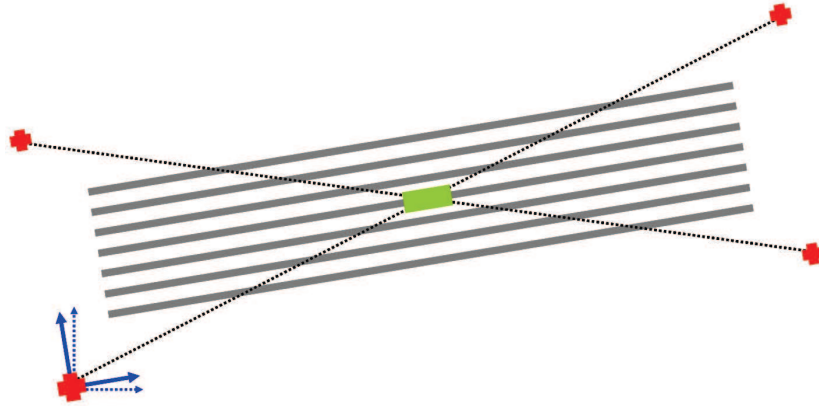


Figure 3.6: Alignment technique : red cross represents the marks defining the basis (blue lines) used for silicon waveguide definition in the CMOS line against the basis of the e-beam writer (blue dotted lines). Green square represent the PhC location.

important alignment step we add four markers, being squares of 10×10 microns²

in the design of the silicon level, relatively far from the silicon wires. Those markers, form a basis for the silicon layer (see fig. 3.6), and thus contain all the informations about the wire positions and scaling used during the silicon processing. Several tests were performed in order to realize automatic detection of the marks via the use of the e-beam, such as gold deposition on markers, but the best result was obtained after wet etching, using hydrofluoric acid (HF), of the 2 microns of SiO_2 underlying the silicon markers, resulting in a well of $10 \mu\text{m}^2 \times 2 \mu\text{m}$ depth surrounded by a large surface of silicon on top. The marker detection is, in fact, based on the sensitive contrast in reflectivity between the upper silicon surface and the silicon located $2 \mu\text{m}$ below in the etched mark. The abruptness of the edges of the marks is of paramount importance to ensure a correct measurement of the position of their centre. Because of the high electron writing energy (100 keV) employed, the backscattered signal is characteristically weak and of poor contrast. Furthermore, we have to remember that the markers detection step is done after bonding, the marks are then less visible as they are covered by a BCB layer which is prone to charging. It is then necessary to etch the BCB above the marks. Precautions had to be taken while uncovering the marks. Indeed, it has been observed that HF destroys links between the BCB and the silicon layer, it was then necessary to locally etch the BCB as far as possible from the silicon wires. Since BCB is just etched around the marks it will also acts as a cap layer for the rest of the silicon substrate which turns out to be useful since post-processing of the photonic crystal via RIE or ICP can severely damage a non-protected silicon layer. Once these marks are semi-automatically detected, it is possible to deduce a matrix transfer (translation and homothety/dilatation transformations) between the e-beam basis and the silicon chip which allows to automatically locate the position of the silicon wire in a very accurate way and to compensate for an angular misalignment.

With this procedure we have been able to obtain very good results on this critical step of alignment, as can be seen fig. 3.7. In this figure a perfect alignment between the silicon wire and the PhC waveguide level is visible. Moreover this does not induce any complications in the further processing steps, that is to say the photonic crystal etching.

3.4 III-V Photonic crystal etching

The active layer used in this work consists of MOCVD grown InP, containing 4 quantum wells (QWs) emitting at a peak photoluminescence wavelength of $1.53 \mu\text{m}$ (see fig. 2.2). The QWs consist of four alternated layers of InGaAs (13.5 nm) and InGaAsP (16 nm) embedded between two layers of 60 nm thick InP. The total III-V slab thickness is then 265nm and was measured, using a Dektak surface profiler, by wet-etching the InP and QW layers.

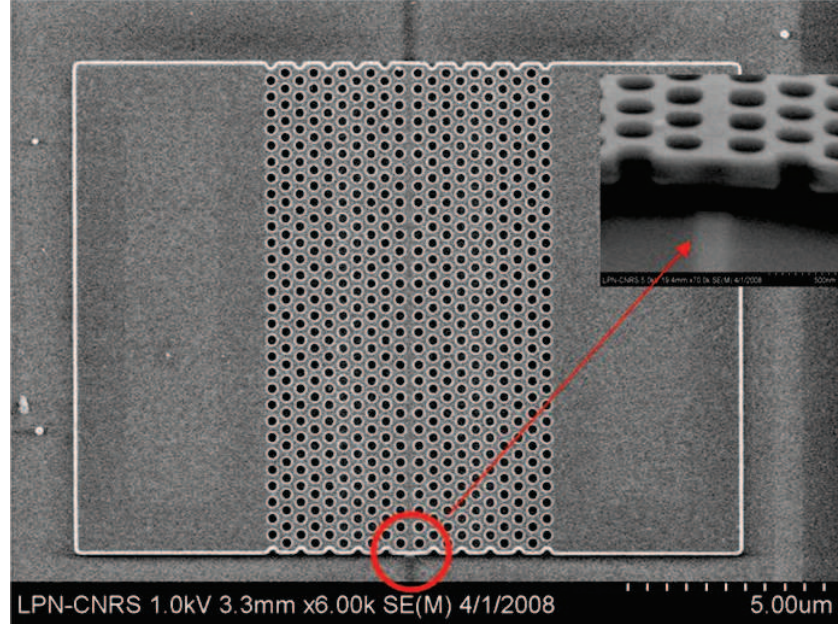


Figure 3.7: SEM picture of an InP PhC waveguide, of 50 microns long, etched on top of silicon wire, clear alignment between the two levels is visible

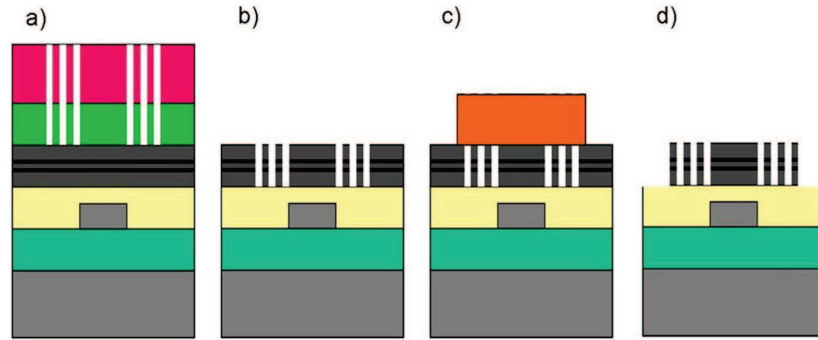


Figure 3.8: PhC etching process (vertical view), a) PC pattern transferred through the PMMA positive resist (in pink) in the hard mask (in green), b) etched PC in the InP (grey zone) after removing of the masks, c) MAN, negative electron resist, cap layer (orange) after a second alignment step and development of the latter resist, d) PhC after removing of the surrounding InP

After bonding of this active layer on top of our patterned silicon substrate, the InP substrate and the InGaAsP etch-stop layers are removed, we then proceed to the etching of the desired PhC structure. Etching of photonic crystals in InP-based

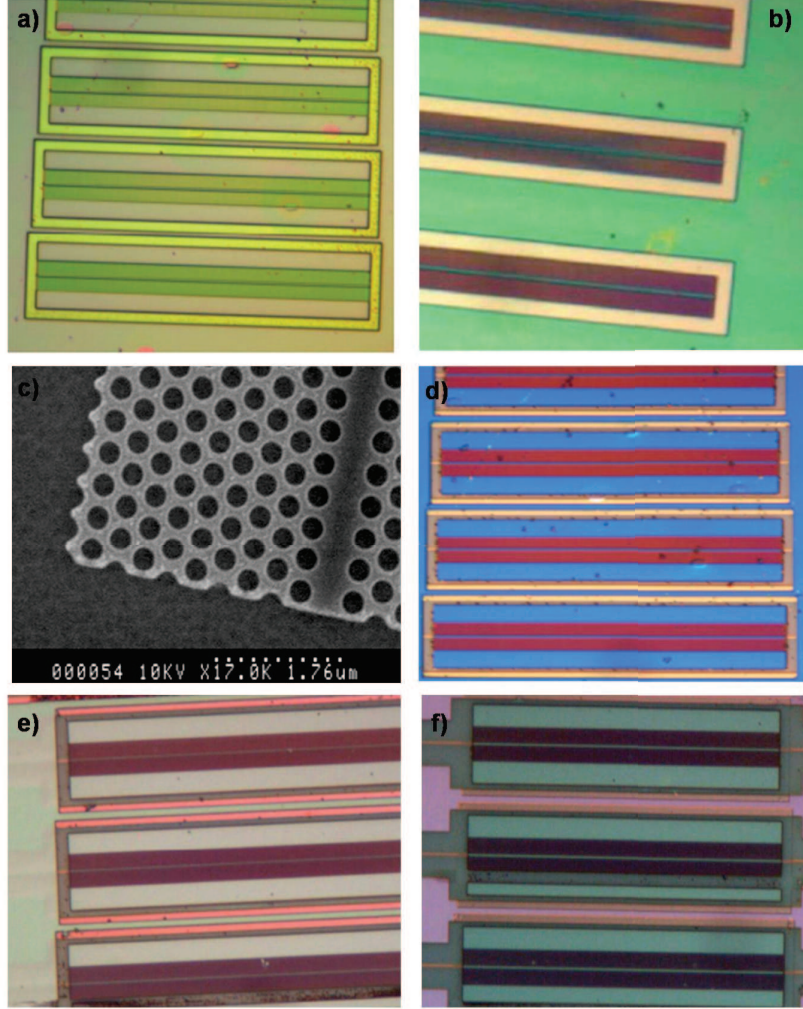


Figure 3.9: Picture of the sample at different process step : a) picture of the PMMA after e-beam insolation, b) etched Si_3N_4 hard mask picture, c) SEM of the etched hard mask, d) picture etched InP below the hard mask, e) picture of the etched InP, f) final result after the surround InP removal, note the visible silicon layer below and waveguides in pink which attest for the accuracy of the alignment method.

epitaxy was already developed at the start of this thesis [14]. It consists of several steps briefly depicted in fig. 3.8. After deposition of a 300 nm silicon nitride (Si_3N_4) mask, a positive electron-beam resist (PMMA) of 400 nm is spin coated on the sample and soft baked. This hard mask also serves to protect, for a while, the exposed BCB layer. E-beam lithography is then performed, after achieving the

previously addressed steps of high-accuracy alignment. After development of the resist using a solvent (see fig. 3.9.a), MIF diluted in DI water, the photonic crystal pattern is transferred in the hard mask by a Reactive Ion Etch using a SF_6/CHF_3 chemistry (gas ratio 10/14 sccm) (see Fig. 3.9.b and .c). To avoid reflow during the subsequent step, the PMMA is also removed in a RIE dry etch organic (O_2 plasma) cleaning process. The holes for the photonic crystal are then etched into the InP layer by ICP-RIE through the pattern previously defined in the silicon nitride mask (see Fig. 3.9.d) with $Cl_2/BCl_3/N_2$ chemistry. Finally, the Si_3N_4 mask is removed by repeating the previous RIE process (see Fig. 3.9.e). Using the alignment marks and a negative resist (maN 2410), a low resolution area is exposed, using e-beam lithography. This mesa protects the underlying photonic crystal from a three step wet etching cycle using HCl, $H_2SO_4:H_2O_2:H_2O$ (3:1:1) and followed by HCl, which removes the superfluous InP and the InGaAs/InGaAsP Quantum Wells (see Fig. 3.9.f).

3.5 Characterization and discussion

3.5.1 Characterization

After the sequence of processing described in the previous sections, we obtain samples as on the SEM image of fig. 3.7, consisting of a PhC structure etched in a III-V layer, with an intermediate BCB bonding layer, on top of a silicon waveguide. Then, it is important to discuss some points concerning the quality of the samples thus made and the alignment accuracy. In order to characterize those aspects, we first studied the samples using an atomic force microscope (AFM) followed by a numerical treatment of a SEM image of the sample in order to extract quantitative values concerning the alignment. An AFM image taken after bonding

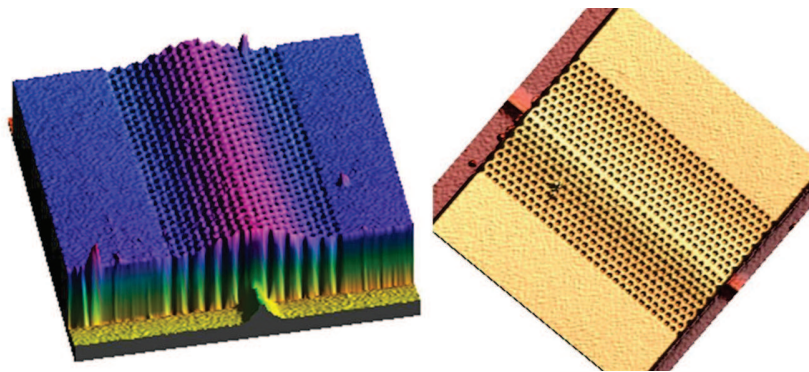


Figure 3.10: AFM profile (left) and top view (right) of first generation hybrid PhC waveguides

and PhC patterning is shown in fig. 3.10. This allows us to observe the transfer of the topography of the SOI surface through the subsequent layers measured across the InP photonic crystal. In the first generation of samples we observe, due to incomplete planarisation of the BCB [15], a $2\ \mu\text{m}$ wide gaussian-shaped elevation, of 60 nm at the max, of the surface caused by the underlying silicon waveguide. This result illustrates the importance of the BCB planarisation process, which is critical, since an insufficiently planar III-V semiconductors layer would results in strongly modified, electronic and optical, properties of the III-V semiconductors PhC structure. In the subsequent batches of samples the use of an intermediate silicon oxide layer is expected to reduced this elevation. This said, what is really striking in the AFM pictures is the agreement between the position of the lattice of holes and the gaussian profile, corresponding to the silicon wire underneath, which points to a high alignment accuracy.

The resolution (5 nm) of the AFM images is, however, not sufficient to give a satisfactory estimate of the alignment error between the two patterned layers. Fortunately, the BCB was slightly thinned in the InP etching step and actually allowed us to obtain reasonably contrasted SEM images of the ends of the photonic crystals and the silicon waveguide layer, beneath the residual BCB, as can be seen in fig. 3.7. By fitting the waveguide position and the holes centres over a selection of guides, we can gain a statistical measure of our alignment capabilities. In order to determine the position of the waveguide at the end of the PhC an adaptive super-gaussian function (variable width, height and centre) is fitted to each transverse section of the wire (this also provides the largest error, as displayed in the 3rd and 5th columns of table 3.12). A linear fit through these centre positions is extrapolated to the end of the PhC. After thresholding, the edges of all the shapes (around 30 holes) in the PhC region are detected, using a custom-written code. Each promising candidate is fitted with a circle using Taubin's method [16] as shown in fig. 3.11. The circle centre coordinates are then least-squares fitted to the designed structure ($\pm 1\text{nm}$ error). The predicted end position of the PhC is then subtracted from the waveguide position. The results are displayed in table 3.12. From an average over the two ends of nine different 100 microns long waveguides we determine our statistical alignment accuracy. Averaging over the alignment errors for left and right hand side ends of the PhC waveguides give $26 \pm 19\text{nm}$, from this values we can also approximate the error angle to be around $4 \cdot 10^{-4}$. This accuracy is well below the criteria for evanescent coupling as will be discussed in the coming subsection. Note also that from this numerical treatment we measured that the ratio of the radii, r , of the fitted holes to the lattice constant, a , is $r/a = 0.3 \pm 1.4$ percent, which allows to expect a good agreement between modelling and experiments.

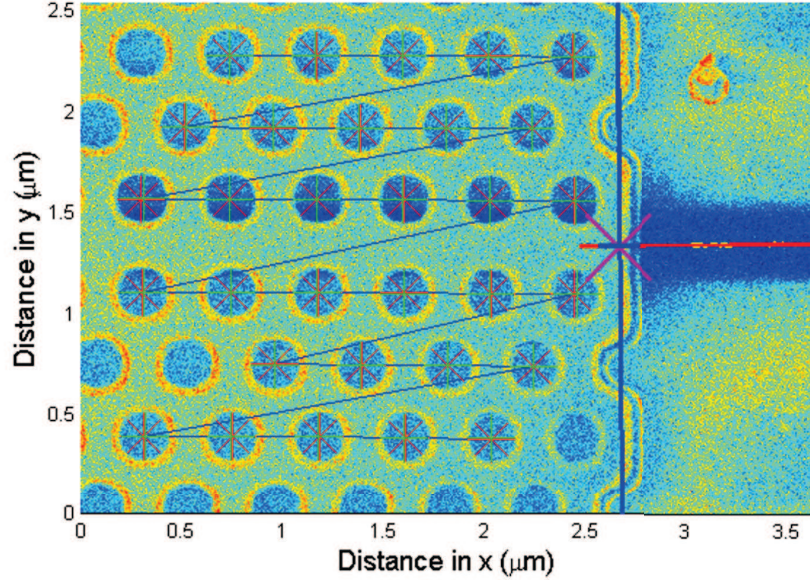


Figure 3.11: Fitted data showing the located hole centers (+ crosses) and the fitted lattice (* asterisks joined by continuous zig-zagging line). The cross (\times at 2.669, 1.324) shows the predicted end of the PhC waveguide. The waveguide center is shown as a noisy line and the linear fit (overlaid) predicts the intersection between the center of the waveguide and the PhC facet at the position marked by the darker cross (+ at 2.669, 1.338).

3.5.2 Discussion on the importance of alignment accuracy

With the aim of discussing the alignment requirements of the hybrid structures and confronting them with the actual processed samples, we first, briefly investigate, using numerical calculations, the coupling between two index matched waveguides modes and its dependence upon vertical and lateral misalignment. Using a Finite Difference fully-vectorial mode solver, we find the parameters which phase match the fundamental mode (at 1.55 microns with TE polarization) of a $220\text{nm} \times 300\text{nm}$ SOI waveguide (SiO_2 substrate and BCB superstrate with respective index 1.54 and 1.45) with that of a $255\text{nm} \times 360\text{nm}$ InP/InGaAs QW waveguide (BCB substrate and air superstrate). As expected, the coupling distance increases exponentially with vertical separation. Indeed, the length of coupling is given by $L_c = \pi/2\kappa$, for phase matched waveguides, and κ is proportional to the overlap of the exponentially decaying fields (roughly proportionnal to $\kappa \propto e^{-h}$ where h is the distance between the two waveguides). Secondly, it can be seen (in Fig. 3.13) that tight lateral positioning control is required on a scale of about 100nm (which is only possible using e-beam or DUV stepper alignment) since the length of coupling dependency is of the scale of hundreds of nanometers.

	Left hand side		Right hand side	
	Alignment offset (nm)	WG error (nm)	Alignment offset (nm)	WG error (nm)
Guide 1	-21	7	-34	5
Guide 2	16	8	15	3
Guide 3	-7	5	12	3
Guide 4	-32	3	14	4
Guide 5	18	4	21	3
Guide 6	-57	4	-80	4
Guide 7	16	6	44	3
Guide 8	3	4	33	3
Guide 9	-18	4	28	3

Figure 3.12: The fitted alignment offset tolerances for nine $90\text{ }\mu\text{m}$ PhC long waveguides, along with the error in determining the waveguide position, WG error.

Next, we complete this evaluation of the requirements for a good control of the

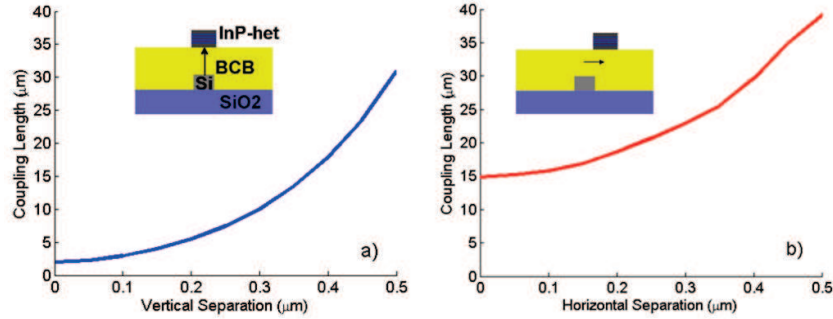


Figure 3.13: The variation in coupling length of an InP-based ($255 \times 360\text{ nm}^2$) wire phase matched to a ($220 \times 360\text{ nm}^2$) Si wire as a function of the (a) vertical and (b) lateral offset between the guides at a constant vertical offset of 400 nm for $\lambda = 1.55\text{ }\mu\text{m}$.

coupling using the results given by the analytical calculations of section 2.4. From these results we can show that a change of around 3 percent between the respective k – vector would give a decrease of 6 percent in the maximum intensity transferred. This correspond to an index mismatch of around 0.1 or, under the approximation that the detuning is proportional to the scalar product between the propagation vectors, to an error of 15 degrees in the angle between the two waveguides. This is illustrated in figure 3.14 showing the power distribution between

two waveguides for different detuning values.

Thus, from those analytical and numerical studies on phase matching we can

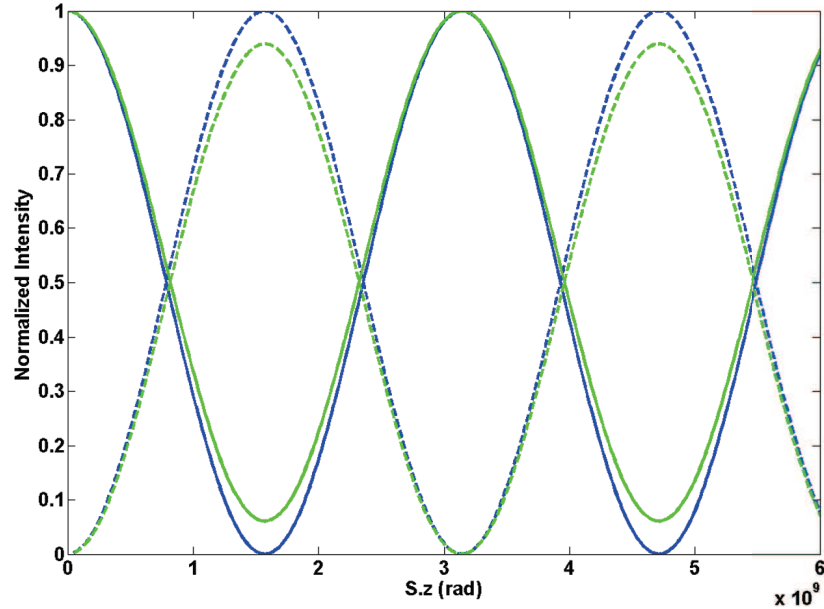


Figure 3.14: Energy transfer between two similar waveguides against wavelength for initial parameter $a_1=1$ and $a_2=0$, the line correspond to waveguide 1 and the dashed line to waveguide 2, for two different detuning - blue correspond to zero detuning and then a maximum transfer of 100 percent, - green correspond to a detuning of 3 percent with a maximum energy transfer around 96 percent

affirm that our processing give us a quasi perfect control of the coupling strength between the two levels of the hybrid structures. Indeed, the lateral or angular alignment accuracy obtained are clearly far above the requirements. The control on the vertical off-set is still, at this point, a little bit uncertain but will be shown to be relatively good, for example the experimental study of the coupling (section 8.4) will extract a coupling parameter of the order of the expected one.

3.6 Conclusion

In this chapter, the various technological processing steps were outlined that renders the realization of hybrid photonic crystal structures possible. A high yield bonding process was developed by the use of an intermediate SiO_2 layer. Moreover, this added layer gives us a better control on the intermediate layer thickness and allow for a better heat sinking. More critical was the alignment procedure. The technique developed during this thesis, based on e-beam automatic detection

of etched marks in the silicon layer, has lead to a state of the art alignment, with a precision of the order of 30 nm. Numerical and analytical studies of the impact of the alignment on the coupling parameters shows that the errors made in the processing procedure are far below the requirements, thus allowing a very accurate control on the hybrid structures. This last statement will appear clearly when modelling and experimental results are confronted, showing a very good agreement.

References

- [1] J. Van Campenhout J. Brouckaert D. Van Thourhout R. Baets L. Liu, G. Roelkens. *III-V/silicon-on-insulator nanophotonic cavities for optical network-on-chip*. Journal of Nanoscience and Nanotechnology, 10:1461–1472, 2010.
- [2] Vincent Wiaux Johan Wouters Stephan Beckx Joris Van Campenhout Dirk Taillaert Bert Luyssaert Peter Bienstman Dries Van Thourhout Pieter Dumon, Wim Bogaerts and Roel Baets. *Low-Loss SOI Photonic Wires and Ring Resonators Fabricated With Deep UV Lithography*. IEEE PHOTONICS TECHNOLOGY LETTERS, 16, 2004.
- [3] M. Ayre W. Bogaerts D. Van Thourhout P. Bienstman D. Taillaert, F. Van Laere and R. Baets. J. Appl. Phys., 45:6071, 2006.
- [4] Kar Wei Ng Wai Son Ko Linus C. Chuang Forrest G. Sedgwick Roger Chen, Thai-Truong D. Tran and Connie Chang-Hasnain. *Nanolasers grown on silicon*. Nature, 5:170–175, 2011.
- [5] C. A. Wang H. K. Choi and N. H. Karam. Proceedings of the Conference Laser and on Electra-Optics (CLEO), 334:170–175, 1991.
- [6] R. Bhat Y. H. Lo, C. Chua D. M. Hwang, and C.-H. Lin. *Semiconductor lasers on Si substrates using the technology of bonding by atomic rearrangement*. Appl. Phys. Lett., 62:1038–1040, 1993.
- [7] Di Liang Richard Jones Alexander Fang Brian Koch Gunther Roelkens, Liu Liu and John Bowers. *III-V/silicon photonics for on-chip and inter-chip optical interconnects*. Laser Photonics Rev., 4:170–175, 1991.
- [8] Ying-hao Kuo Richard Jones Oded Cohen Di Liang Omri Raday Matthew N. Sysak Mario J. Paniccia Alexander W. Fang, Hyundai Park and John E. Bowers. *Hybrid silicon evanescent devices*. Materialstoday, 10(7-8):28–35, 2007.
- [9] P. Regreny C. Seassal D. Van Thourhout S. Verstuyft L. Di Cioccio J.-M. Fedeli C. Lagahe J. Van Campenhout, P. Rojo-Romeo and R. Baets. *Electrically pumped InP-based microdisk lasers integrated with a nanophotonic silicon-oninsulator waveguide circuit*. Optics Express, 15:6744–6749, 2007.
- [10] J. Q. Lu F. Niklaus, G. Stemme and R. J. Gutmann. *Adhesive wafer bonding*. J. Appl. Phys., 99, 2006.

- [11] Di Liang Richard Jones Alexander Fang Brian Koch Gunther Roelkens, Liu Liu and John Bowers. *III-V/silicon photonics for on-chip and inter-chip optical interconnects*. Laser Photonics Rev., 4:751–779, 2010.
- [12] S. Sauvage and al. *Homogeneous broadening of the S to P transition in InGaAs/GaAs quantum dots measured by infrared absorption imaging with nanoscale resolution*. Phys. Rev. B, 83:035302, 2011.
- [13] F. Raineri G. D’Aguanno J. Trull Y. Halioua R. Raj I. Sagnes R. Vilaseca M. Scalora V. Roppo, C. Cojocar. *Field localization and enhancement of phase-locked second- and third-order harmonic generation in absorbing semiconductor cavities*. Phys. Rev. A, 80, 2009.
- [14] G. Patriarche I. Sagnes K.-H. Lee, S. Guilet and A. Talneau. *Smooth sidewall in InP-based photonic crystal membrane etched by N₂-based inductive coupled plasma*. J. Vac. Sci. Technol. B, 2008:1326–1333, 26.
- [15] P. Regreny C. Seassal D. V. Thourhout S. Verstuyft L. Di Cioccio J.-M. Fedeli C. Lagahe J. V. Campenhout, P. R. Romeo and R. Baets. *Electrically pumped InP-based microdisk lasers integrated with a nanophotonic silicon-on-insulator waveguide circuit*. Phys. Rev. A, 15, 2007.
- [16] G. Taubin. *Estimation Of Planar Curves, Surfaces And Nonplanar Space Curves Defined By Implicit Equations, With Applications To Edge And Range Image Segmentation*. IEEE Trans. PAMI, 13:1115–1138, 1991.

4

Photonic crystals

The concept of “photonic crystals” and “photonic bandgap” were introduced in 1987 by Yablonovitch [1] and John [2]. The designation “photonic crystals” (PhC) refers to structures with a periodic index pattern, in 2D as well as in 3D. PhCs may be viewed as an extension of a Bragg mirror to higher dimensions. Some examples represented on fig. 4.1 show the diversity of possible periodic material arrangements. The typical index patterns are of the order of the wavelength which result, under certain conditions, in the opening of a “photonic bandgap”, ie. a frequency window where light propagation is forbidden. The presence of this gap, and the associated optical properties, give rise to very interesting characteristics mainly based on either the strong reflectivity in the bandgap wavelength range or the strongly modified dispersion close to the edge of the gap. Therefore, PhC structures have drawn towards them a lot of attention in the past years and are now appreciated as powerful tools to access, and probe, interesting phenomena in various fields ranging from quantum physics to non-linear optics. For these reasons, we chose a photonic crystal based design for the active level since it is a tempting way to efficiently enhance light matter interactions, allowing to access to very low group velocity modes or high Q cavities with small modal volume. The subject of this chapter is to give the keys for the understanding of PhCs characteristics, starting from their physical origin and concluding with practical designs used to exploit them. Thus, the first section is a general mathematical development leading to a discussion concerning the origin of the band-gap and some related properties. The second section is a consideration of practical interest, that is to say PhC structures in slabs or 2.5D PhC. Then, the two subsequent sections concern two commonly

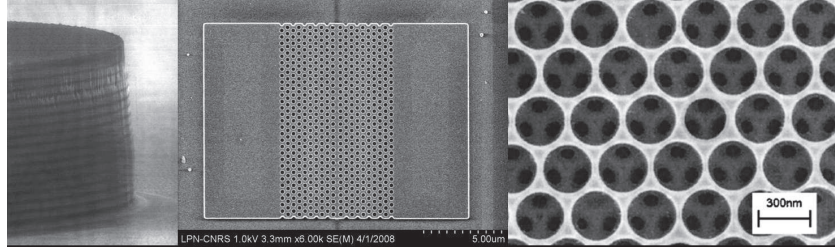


Figure 4.1: Example of photonic crystal structure, from left to right : 1D Bragg mirror of alternated AlOx/AlGaAs layers (LPN), InP photonic crystal with a line of holes removed to form a waveguide (LPN), 3D TiO₂ inverse opal [3]

used designs, PhC cavities and PhC waveguides. This chapter will conclude with a brief summary and a brief opening related to the opportunities brought to the optical community by the use of photonic crystals. Finally, the discussions in this chapter are aimed at giving enough insight to allow the understanding of the work discussed in the chapters related to PhCs design modelling and studies of hybrid PhCs waveguides and wire cavities.

4.1 Underlying physics and properties

4.1.1 Maxwell's equations for a photonic crystal

Starting from the general expression for macroscopic the Maxwell's equations (in cgs units), we have :

$$\begin{aligned} \nabla \cdot \mathbf{B} &= 0 & \nabla \times \mathbf{E} + \frac{1}{c} \frac{\partial \mathbf{B}}{\partial t} &= 0 \\ \nabla \cdot \mathbf{D} &= 4\pi\rho & \nabla \times \mathbf{H} - \frac{1}{c} \frac{\partial \mathbf{D}}{\partial t} &= \frac{4\pi\mathbf{j}}{c} \end{aligned}$$

The electric field \mathbf{E} is related to the electric displacement field \mathbf{D} via the tensor dielectric function $\bar{\epsilon}(\mathbf{r}, t)$ through the relation :

$$\mathbf{D}(\mathbf{r}, t) = \int \bar{\epsilon}(\mathbf{r}, t - t') \cdot \mathbf{E}(\mathbf{r}, t') dt' \quad (4.1)$$

A similar relation connects the magnetic field \mathbf{H} to the magnetic induction \mathbf{B} via the magnetic permeability $\bar{\mu}(\mathbf{r}, t)$. Few simplifications can be made in our case. First, we assume that the materials composing the photonic crystal are isotropic, then the dielectric and magnetic tensors reduce to scalars, $\bar{\epsilon}(\mathbf{r}, t) \Rightarrow$

$\epsilon(\mathbf{r}, t); \bar{\mu}(\mathbf{r}, t) \Rightarrow \mu(\mathbf{r}, t)$. We also assume that the dielectric function is non dispersive $\epsilon(\mathbf{r}, t - t') = \epsilon(\mathbf{r})\delta(t - t')$, real and non negative. And finally, that the materials are non magnetic, ie. $\mathbf{B} = \mu_0\mathbf{H}$ and free of charges and currents, $\rho = 0$ and $\mathbf{j} = 0$. With these hypotheses, Maxwell's equations are simplified to :

$$\nabla \cdot \mathbf{H} = 0; \quad \nabla \times \mathbf{E} + \frac{1}{c} \frac{\partial \mathbf{H}}{\partial t} = 0 \quad (4.2)$$

$$\nabla \cdot \epsilon(\mathbf{r})\mathbf{E} = 0; \quad \nabla \times \mathbf{H} - \frac{1}{c} \frac{\partial}{\partial t} \epsilon(\mathbf{r})\mathbf{E} = 0 \quad (4.3)$$

Thanks to the linearity of Maxwell's equations, it is convenient to look for solutions for harmonic fields :

$$\mathbf{E}(\mathbf{r}, t) = \mathbf{E}(\mathbf{r})e^{-i\omega t} \quad \mathbf{H}(\mathbf{r}, t) = \mathbf{H}(\mathbf{r})e^{-i\omega t} \quad (4.4)$$

A general solution can then be obtained consisting in a superposition of harmonic modes. Plugging the formulae 4.4 into eqs. 4.2 and 4.3, it is possible to recast Maxwell's equations in a closed form for either the magnetic or the electric fields :

$$\nabla \cdot \mathbf{H}(\mathbf{r}) = 0; \quad \nabla \times \left(\frac{1}{\epsilon(\mathbf{r})} \nabla \times \mathbf{H}(\mathbf{r}) \right) = \frac{\omega^2}{c^2} \mathbf{H}(\mathbf{r}) \quad (4.5)$$

$$\nabla \cdot \epsilon(\mathbf{r})\mathbf{E}(\mathbf{r}) = 0; \quad \nabla \times \nabla \times \mathbf{E}(\mathbf{r}) = \frac{\omega^2}{c^2} \epsilon(\mathbf{r})\mathbf{E}(\mathbf{r}) \quad (4.6)$$

Up to now, the derivation of these master equations is valid for any system for which the initial assumptions are fulfilled.

To solve the electromagnetic problem for a photonic crystal, it is necessary to impose that the dielectric function is periodic. Then the photonic crystal is defined, in real space, by a lattice of vectors \mathbf{a}_i and the following relation on dielectric permittivity :

$$\forall \mathbf{R} \in V, \epsilon(\mathbf{r} + \mathbf{R}) = \epsilon(\mathbf{r}) \quad (4.7)$$

where V defines a vector space with basis a_i .

The periodicity of the dielectric function, or its invariance under translation, leads naturally to express the solution of the equation 4.6 in terms of the so-called Bloch waves, or spatial harmonics, of the form :

$$\mathbf{H}_k(r) = e^{i\mathbf{k}\mathbf{r}} \mathbf{u}_k(\mathbf{r}) \quad (4.8)$$

with $\mathbf{u}_k(\mathbf{r})$ a periodic function.

4.1.2 Bloch-Floquet theorem

Indeed, the Bloch-Floquet theorem [4] states that the general solution of a master equation invariant under $\hat{\mathbf{T}}_{\mathbf{R}}$ (the unitary operator associated with a discrete translation $\mathbf{R} \in V$) is a periodic function multiplied by a phase factor $e^{i\mathbf{k}\cdot\mathbf{r}}$. The period

of $\mathbf{u}_k(\mathbf{r})$ is determined by $\hat{\mathbf{T}}_{a_i}$.

The general form of the periodic function $\mathbf{u}_k(\mathbf{r})$ can be recovered with the following steps. First, because of the translational invariance of the system $\mathbf{H}(\mathbf{r})$ is an eigenfunction of $\hat{\mathbf{T}}_{\mathbf{R}}$, ie.

$$\hat{\mathbf{T}}_{\mathbf{R}}\mathbf{H}(\mathbf{r}) = \alpha\mathbf{H}(\mathbf{r}) \quad (4.9)$$

whose natural solutions are plane waves and the eigenvalues are complex numbers with unitary modulus :

$$\mathbf{f}_k(\mathbf{r}) = \hat{\mathbf{f}}e^{i\mathbf{k}\cdot\mathbf{r}}; \quad \hat{\mathbf{T}}_{\mathbf{R}}\mathbf{f}_k(\mathbf{r}) = e^{-i\mathbf{k}\cdot\mathbf{R}}\mathbf{f}_k(\mathbf{r}); \quad \alpha = e^{-i\mathbf{k}\cdot\mathbf{R}} \quad (4.10)$$

Note that all the eigenfunctions $\mathbf{f}_{k'}(\mathbf{r})$ and $\mathbf{f}_k(\mathbf{r})$, with $\mathbf{k}' = \mathbf{k} + \mathbf{G}$ for any \mathbf{G} such that $\mathbf{G}\cdot\mathbf{R} = 2\pi n$, are degenerate. In fact, this last condition defines the reciprocal space Γ , defined by a set of vectors g_i , associated to the real space V .

Therefore, the general solution of the master equation is

$$\mathbf{H}_k(\mathbf{r}) = \sum_{\mathbf{G} \in \Gamma} c(\mathbf{k} + \mathbf{G})\mathbf{f}_{\mathbf{k}+\mathbf{G}}(\mathbf{r}) \quad (4.11)$$

Moreover, the divergence condition $\nabla \cdot \mathbf{H}_k(\mathbf{r}) = 0$ is automatically fulfilled if $(\mathbf{k} + \mathbf{G}) \cdot \mathbf{f}_{\mathbf{k}+\mathbf{G}} = 0$, ie. $\mathbf{f}_{\mathbf{k}+\mathbf{G}}$ is also transverse. We can then make use of the Bloch-Floquet theorem and express the solution $\mathbf{H}_k(\mathbf{r})$ as

$$\mathbf{u}_k(\mathbf{r}) = e^{-i\mathbf{k}\cdot\mathbf{r}} \sum_{\mathbf{G} \in \Gamma} c(\mathbf{k} + \mathbf{G})\mathbf{f}_{\mathbf{k}+\mathbf{G}}(\mathbf{r}) \Rightarrow \mathbf{H}_k(\mathbf{r}) = e^{i\mathbf{k}\cdot\mathbf{r}}\mathbf{u}_k(\mathbf{r}) \quad (4.12)$$

where $\mathbf{u}_k(\mathbf{r})$ has the same periodicity as the index, as stated in the Floquet-Bloch theorem. Again, it can be seen from eq. 4.11 that $\mathbf{H}_{k'}(\mathbf{r}) = \mathbf{H}_k(\mathbf{r})$ if $\mathbf{k}' - \mathbf{k} \in \Gamma$ because of the sum over \mathbf{G} . This means that two different \mathbf{k} do not necessarily correspond to different solutions $\mathbf{H}_k(\mathbf{r})$, ie. in a photonic crystal \mathbf{k} is conserved within a vector \mathbf{G} . This degeneracy fixes a strong relationship between different \mathbf{k} vectors that are equal to each other modulo \mathbf{G} . This relation can be re-expressed through the use of the concept of the Brillouin zone which states that all the solutions of a periodic problem can be characterised in a reduced reciprocal space called the first Brillouin zone (B.Z.) :

$$B.Z. \equiv [\mathbf{k} \in \Gamma^3 : |\mathbf{k}| = \min_{\mathbf{z} \in |\mathbf{k}|} (|\mathbf{z}|)] \quad (4.13)$$

Note that the choice of this cell is in general not unique.

The eigenfunctions of the master equation can be classified by means of the Bloch vector \mathbf{k} . Besides the eigenfunctions, the Bloch vector can also label the corresponding eigenvalues Λ . As \mathbf{k} varies inside the Brillouin zone, the eigenvalues obey to the dispersion relation $\Lambda = \Lambda(\mathbf{k})$. There is no one-to-one correspondence between the Bloch vector and the solutions of the master equation. In fact it is possible that two solutions $\mathbf{H}_k(\mathbf{r})$ have the same Bloch vector, but different expansion

coefficients $c(\mathbf{k} + \mathbf{G})$ in eq. 4.11. There are infinite choices for $c(\mathbf{k} + \mathbf{G})$ yielding independent linear combinations of the basis functions $\mathbf{f}_{\mathbf{k}+\mathbf{G}}(\mathbf{r})$. Therefore, it is consistent to add a label n to $\mathbf{H}_{\mathbf{k}}(\mathbf{r})$ to represent a certain linear combination of the basis functions. At the same time, the label is also attached to the corresponding eigenvalue Λ

$$\mathbf{H}_{\mathbf{k},n}(\mathbf{r}) = \sum_{\mathbf{G} \in \Gamma} c_n(\mathbf{k} + \mathbf{G}) \mathbf{f}_{\mathbf{k}+\mathbf{G}}(\mathbf{r}) \quad \Lambda = \Lambda_n(\mathbf{k}) \quad (4.14)$$

In addition to the Bloch vector and the index n , there is another important degree of freedom that characterizes the solutions of the master equation : the polarization σ (the polarization is defined as having the electric, TE, or magnetic field, TM, in the plane of periodicity); since this parameter is not of particular interest for the present discussion it will be discussed later in the section 4.2.1 concerning 2D photonic crystal where this parameter is relevant. Note that all the statements and derivations above are also valid for the electric field leading to the same results.

Thus the set \mathbf{k} and n are used to qualify the eigenfunctions and the eigenvalues of the master equation. The step to the concept of photonic bands is then short. The eigenfrequencies $\omega/c = \sqrt{\Lambda}$ take on the labels $\mathbf{k}, n \Rightarrow \omega = \omega_n(\mathbf{k})$. Calling n the band index, the n -th photonic band is defined as the portion of the spectrum with dispersion $\omega_n(\mathbf{k})$ as \mathbf{k} varies inside the first Brillouin zone. The photonic band structure is just the ensemble of photonic bands, with n running from 1 to ∞ .

Before proceeding it's worthwhile to make some remarks :

- $\omega_n(\mathbf{k}) = \omega_n(-\mathbf{k})$ because of invariance of the master equation under time inversion.
- Spatial symmetries have not been considered yet (rotations, inversion, reflections). Taking them into account can drastically reduce the calculation of the band structure to the so-called irreducible Brillouin zone.
- Furthermore, to avoid solving the master equation for every point of the irreducible Brillouin zone, it is often enough to do it along the symmetry lines, because they correspond to a higher degree of symmetry with respect to the internal points and, for this reason, they are more representative.

4.1.3 Band structure and photonic band gap

What remains to be done is the study of the solutions $w_n(\mathbf{k})$ of the master equation, also named the “band structure”, and explore the physical path leading to the opening of a band gap. A mathematical expression for a photonic band gap is that in a frequency window $[\omega_1, \omega_2]$ there is a null density of states (D.O.S.) $\rho(\omega)$, which can be defined as

$$\rho(\omega) = \sum_n \sum_{\mathbf{k} \in B.Z.} \delta(\omega - \omega_n(\mathbf{k})) \quad (4.15)$$

The D.O.S. is another important quantity characterizing the photonic crystal. Indeed, contrary to the smoothly varying D.O.S. for a homogeneous medium, the D.O.S. of a photonic crystal presents jumps with peaks and dips around a mean value given by the effective medium theory [5]. The calculation of the D.O.S. is an important check for the existence of a photonic band gap, because it accounts for all the Bloch vectors in the B.Z., whereas the band structure is often limited to the symmetry lines of the B.Z. However, the following discussion deals only with the band structure.

In order to simplify, without loss of any physical meaning, in the discussion con-

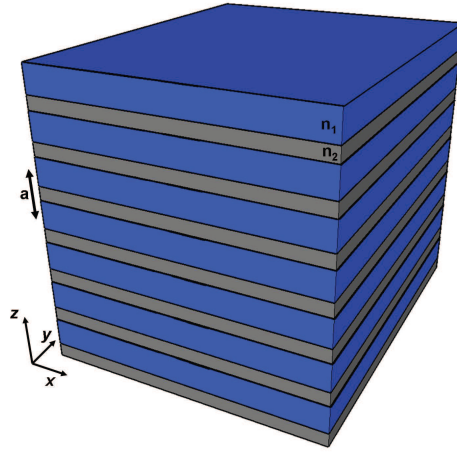


Figure 4.2: The multilayer film, a one-dimensional photonic crystal. The term “one-dimensional” is used because the dielectric function $\epsilon(z)$ varies along one direction (z) only. The system consists of alternating layers of materials (blue and green) with different dielectric constants, with a spatial period a in the z direction. We imagine that each layer is uniform and extends to infinity along the x and y directions.

cerning the concept of photonic band structure and the formation of a band gap, it is convenient to consider a simple one dimensional periodic system : the multilayer (see fig. 4.2). The lattice constant is a and the periodicity is along the z axis and the system is homogeneous in the other directions x, y . The right panel of fig. 4.3 compares the band structure given by an homogeneous medium (a), with the band structure obtained for multilayers with different index contrast (b) and (c), for propagation along the z axis, i.e. $\mathbf{k} = (0; 0; \mathbf{k})$. As explained previously it is sufficient to only draw the dispersion relation on the symmetry axis in the first Brillouin zone corresponding to \mathbf{k} in $[-\pi/a, \pi/a]$. The band structure (a) is obtained by simply folding the dispersion relation $\omega/c = \frac{k}{\sqrt{\epsilon_d}}$ when it reaches the edge of the Brillouin zone. Note that for the cases (b) and (c) a band gap opens at the B.Z. edge. The mathematical reason is that the free-photon

bands $n, n + 1$, which are degenerate for $\mathbf{k} = \pi/a$, are split by the potential due to the periodic dielectric function. As will be seen in the next section, the bandwidth of the gap is a function of several parameters such as the index contrast (fig. 4.3) or the relative thickness of each material layer. Physically, a wave prop-

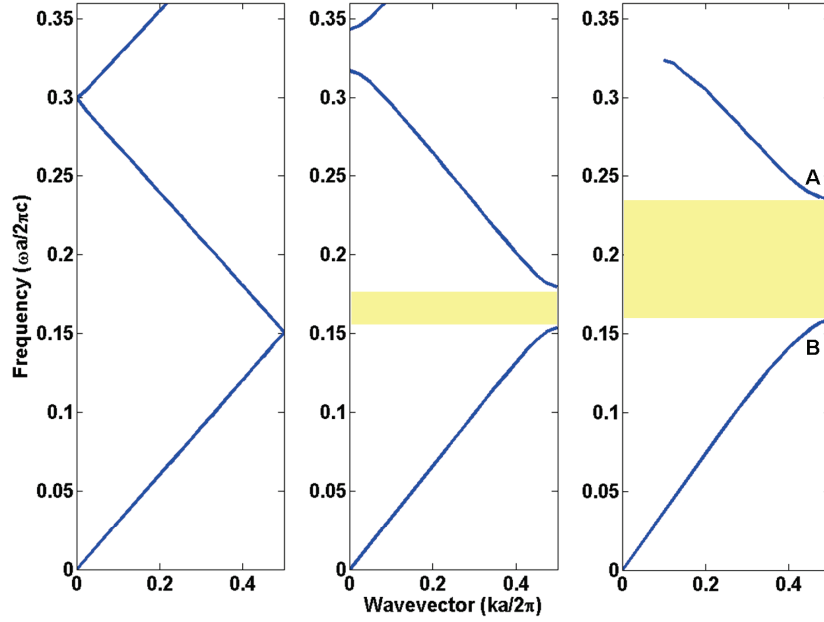


Figure 4.3: The photonic band structures for on-axis propagation, as computed for three different multilayer films. In all three cases, each layer has a width $0.5a$. Left : every layer has the same dielectric constant $n = 3$. Center : layers alternate between n of 3.3 and 2.5. Right : layers alternate between n of 3.3 and 1. The yellow shaded zone correspond to the bandgap. Modelled with FDTD.

agating in a photonic crystal with $\mathbf{k} = \pi/a$ is coupled to a backward wave, with $\mathbf{k} = -\pi/a$ and vice versa. Then the resulting Bloch mode is the sum of co and contra-propagating waves. In other words, those harmonics are “bound” together by the grating, forming a coherent group of discrete waves that share a common group velocity. This results in a Bloch mode that cannot propagate in the photonic crystal, or in other words the solution of the master equation at this point for the corresponding parameters ω, k leads to an imaginary effective wavevector k_{eff} . Thus, light incident on a PhC, for wavelengths inside the gap, will be strongly reflected and decay exponentially as it propagates through the PhC. Particular attention is needed for the two modes belonging to the lower and upper band edges respectively, ie. $\omega_1(\pi/a)$ and $\omega_2(\pi/a)$. They are extended modes since they are Bloch waves, but, at the same time, they cannot propagate as they are coupled to contra-propagating waves. Actually, these modes are not propagating modes but

rather stationary waves, with their group velocity $\mathbf{v}_g = \frac{\partial \omega(k)}{\partial k} \mathbf{z}$ equal to zero. Furthermore, the linear dispersion in the homogeneous case is deflected close to the band edge. This is again due to coupling between co and contra-propagating waves but with a non-symmetric balance between those co- and contra-propagating harmonics, which lead to slow propagating Bloch modes. This picture of coupled co- and contra-propagating waves is summarized in fig. 4.4. Analytical calculations carried out in a 1D periodic system [6], using the two first Bloch harmonics, clearly shows that the interplay between contra-propagative harmonics leads to either the opening of a bandgap or slow mode propagation. Indeed, from these calculations, it can be seen that the group velocity follows the balance between the contra-propagating modes, while in the bandgap the balance is exactly equal to 0.5. Besides, the bandwidth of the forbidden gap is proportional to two parameters : the strength M of the reflectivity and a dephasing term ω_B/ω , where $\omega_B \propto 1/a$, a being the period of the multilayer.

Last important characteristic that needs to be taken into account when dealing

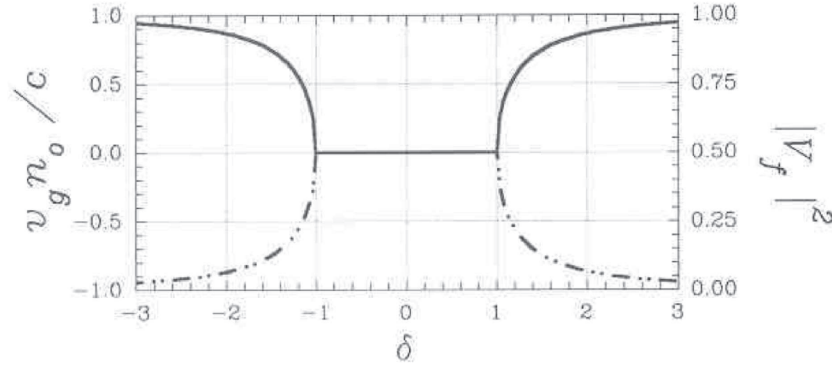


Figure 4.4: Low group velocity and balance between forward and backward propagating modes intensity (respectively left and right vertical axis) against a “detuning parameter” $\delta \propto (1 - \frac{\omega_B}{\omega})/M$, where ω_B is inversely proportional to the periodicity of the structure and M is the reflectivity strength at the interfaces. Moreover, δ allows the discrimination between the evanescent modes, when $\delta^2 < 1$, and the propagating modes, when $\delta^2 > 1$.

with periodic structures, is the field profile of the different modes. Indeed, there exist strong differences in terms of field localization between the various modes in a PhC. For the simplest case of the multilayer, we plotted in fig. 4.5 the intensity profile of the modes corresponding to the band edge modes, located at the points **A** and **B** in fig. 4.3. One can see that the intensity of the field for the lowest frequency mode **B**, is located mostly in the material of high refractive index, while the highest frequency mode **A** is mostly concentrated in the material with lower refractive index. We will sometimes refer along this thesis to “valence band” for the lower band and “conduction band” for the higher band of a bandgap by anal-

ogy with semiconductor physics. Thus, the field profile is of importance when dealing with active materials. Indeed, one should preferentially work with modes where the intensity of the field has a good overlap with the active material. Note that higher order modes possess more complicated field patterns while maintaining in a general sense this property of field localization, specific to "valence band modes" and "conduction band modes" in one or the other material depending on the index. All the properties and their origin in a 1D periodic structure can be

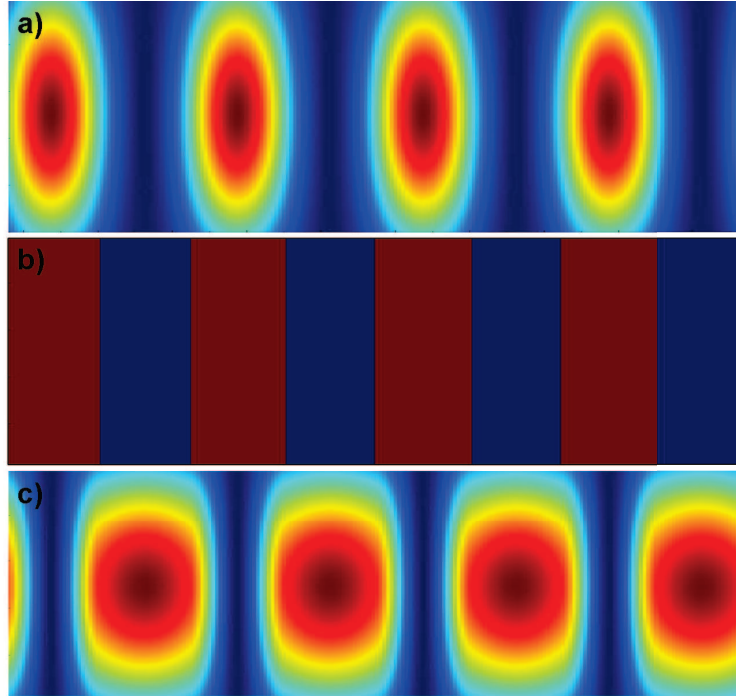


Figure 4.5: Intensity corresponding to the band edge modes in fig. 4.3 right. (a) correspond to the mode at the lowest band edge (point B) and (c) to the mode at the upper band edge (point A). (b) is the index profile of the structure, blue zone correspond to index equal to 1, and brown to index equal to 3.3. The distinction, via intensity localisation, between valence and conduction band modes appears clearly. Modelled with FDTD.

generally extended to the 2D and 3D periodic case. Starting from this assessment about photonic crystal characteristics, it is therefore necessary to find the best way to access the properties which are the most tempting: namely low group velocity modes and high reflectivity of the band gap. The best way to achieve this in a controlled manner is to carefully add defects in the photonic crystal structure. For example, removing a line to tailor the dispersion of propagating modes or locally removing holes to create a high Q cavity. But before that, it is necessary to get closer to practical cases by introducing "2.5D" PhC, ie. photonic crystals where

the periodicity is located in a 2D plane while the confinement in the third direction is ensured by index contrast between a slab and a surrounding material.

4.2 2D and 2.5D photonic crystals

4.2.1 2D photonic crystals

The discussion above on photonic crystals, to be relevant in the context of this work, has to be extended to 2D patterning in a slab. This requires the introduction of specific considerations. First, a 2D photonic crystal is a structure where the periodic index pattern is in the plane of an infinite material in the third direction. Note that the mathematical description given in sections 1.2 and 1.3 encompasses the 2D case. Moreover, all the physical considerations made in the 1D case are still valid and transferable to higher dimensions PhC. The underlying concepts are basically the same even if the 2D case adds more complexity. Indeed, having a full band gap in 2D is more complicated since propagation has now to be forbidden for all the \mathbf{k} vectors, in the plane of periodicity, at a fixed wavelength. It means that the conditions that lead to evanescent modes have to be fulfilled along all the symmetry lines of the Brillouin zone. One of the most commonly used 2D

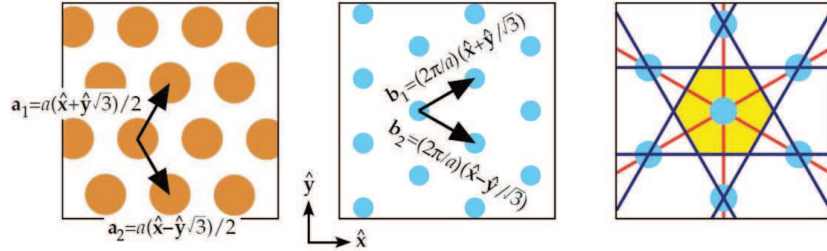


Figure 4.6: The triangular lattice in real space (left pannel), the corresponding reciprocal space (middle panel) with possible basis axis and the related Brillouin zone (right panel).

From [7]

PhC design is based on a triangular lattice of low index holes patterned in a higher index material. This is due to the fact that this periodic lattice allows to obtain relatively large Transverse-Electromagnetic (TE, ie. with the electric field in the plane of periodicity) or even full bandgap (ie. for both polarization) with an index contrast around 3. We also use this PhC design in our work. We use this structure as a support for the discussions concerning 2D PhC characteristics. An example of a triangular lattice and corresponding reciprocal lattice and Brillouin zone is depicted in fig. 4.6. This Brillouin zone can be reduced, by use of symmetries,

without loss of information to a smaller zone of interest namely irreducible Brillouin zone (see inset of fig.4.7). A band structure usually represents the modes on the high symmetry axes of this reduced zone Γ - K ; Γ - M ; K - M . A typical 2D band structure of a triangular lattice of air holes embedded in a material of index 2.8 is plotted on fig. 4.7. Both TE and TM modes are shown in this figure. Having

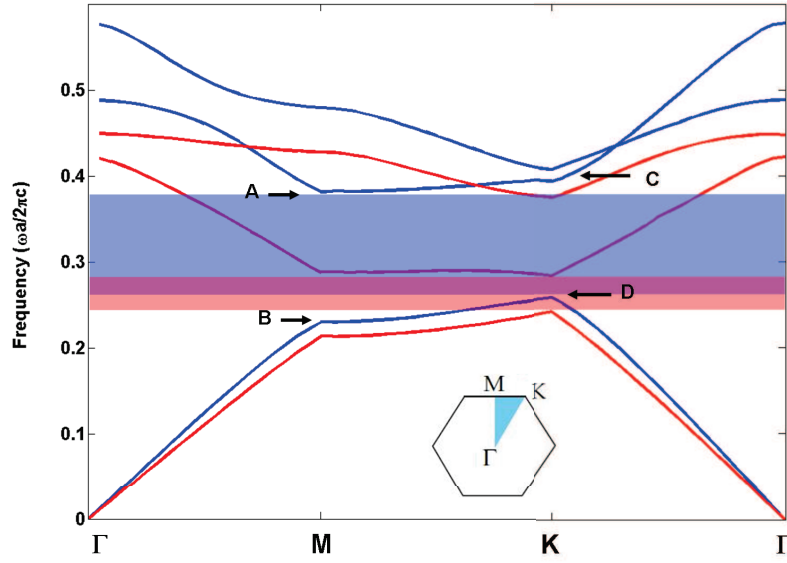


Figure 4.7: The photonic band structure for the modes of a triangular array of air columns drilled in a dielectric substrate ($n=2.8$). The blue lines represent TE bands and the red lines represent TM bands. The shaded regions, blue and red, represent the bandgaps of respectively TE and TM modes. The superposition of the shaded regions corresponds to a full bandgap. The inset represents the symmetry axis followed in drawing the band diagram encapsulating the irreducible Brillouin zone. Modelled with FDTD.

no allowed modes between the maximum of certain bands and the minimum of the higher bands above implies that a forbidden gap is present in the structure for a certain interval of wavelengths, as it is the case in fig. 4.7. Note that minima and maxima are not necessarily lying on the same symmetry axis. Consistent with the mathematical description previously developed, the modes on the axis Γ - K and Γ - M are Bloch modes on the basis of the reciprocal space. The modes between these axes, as on K - M in the fig. 4.6, are composite modes based on those Bloch harmonics. This gives an insight on the field profile in the band structure: the field along the Γ - K and Γ - M axis are perpendicular to their respective symmetry axis (see fig. 4.8 in regard to fig. 4.7), while fields in the zone K - M possess a more complicated pattern resulting from its composite origin. As in the 1D case, "valence band" intensity (resp. "conduction band") is mainly localized in the high

index (resp. low index) material.

As it appears on the plotted band structure (fig. 4.7), the dispersion diagrams

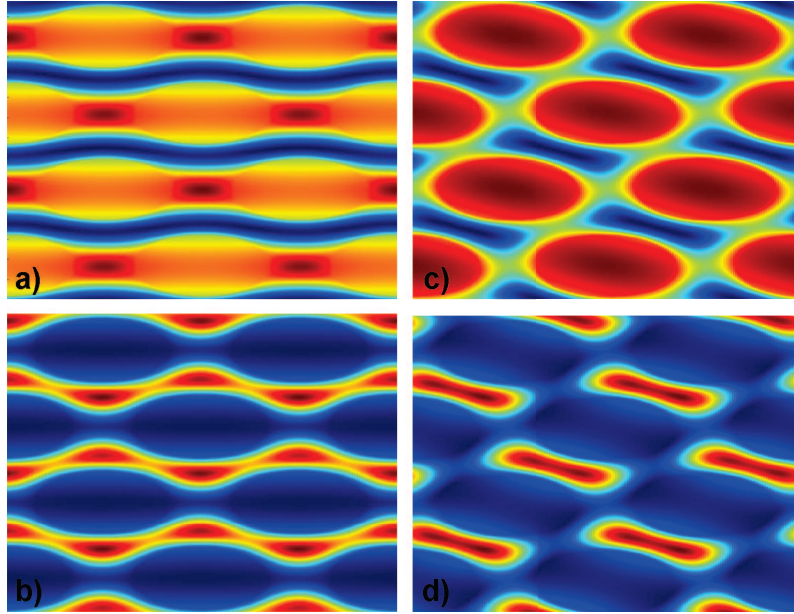


Figure 4.8: Profile of the modes corresponding to point A-D of band structure plotted on fig. 4.7. Modelled with FDTD.

for TE and TM modes are very different. Therefore, it is not obvious that the conditions for the opening of a gap will be fulfilled in the same structure for TE and TM modes at the same time. If this not the case, ie. there is a gap for only one polarization, one then has to take into account the coupling between those two polarizations. Indeed, even if ideally TE and TM modes are orthogonal, since they are independent solutions of Maxwell's equations (ie. the polarization corresponds to a degree of freedom of the system), in practice, because of disorder for example, coupling between those modes can arise reducing the performance of a "one-polarization" gap. It can then be important to design a structure that possesses a complete gap, ie. an overlap of the TE and TM gap, or at least takes into account this possible coupling between the two polarization. In order to explore this possibility it is useful to draw a "gap map", as is done in fig. 4.9 representing the TE and TM bandgap edge versus various parameters such as the period a or the radius r of the holes. It is also interesting to notice from this figure that, for a given index contrast between the two materials involved, gaps opening is strongly dependent on the ratio r/a .

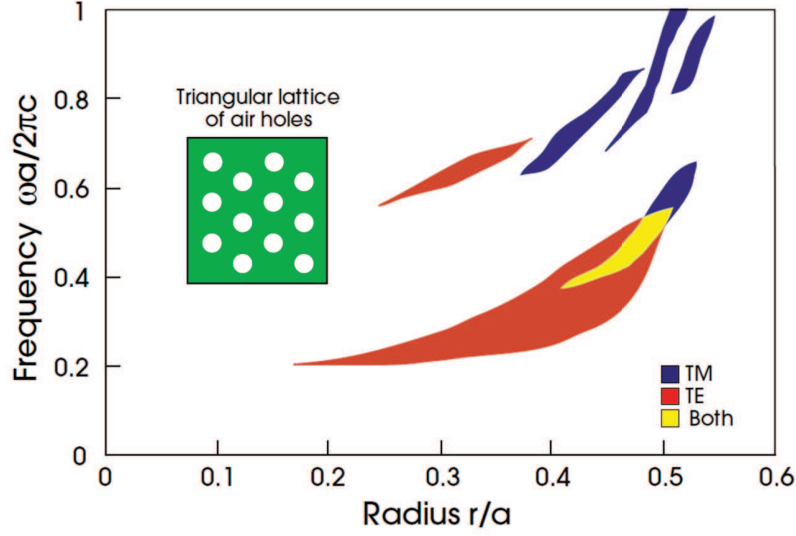


Figure 4.9: Gap map for a triangular lattice of air holes in a dielectric ($\epsilon=11.4$). From [7]

4.2.2 2.5D Photonic crystals

There is yet another consideration that has to be added to link this theoretical discussion on photonic crystals to effective structures. In practice, 2D photonic crystal are etched in finite structures in the third direction surrounded by other materials, as for example air and/or BCB as in our case. In a PhC slab, or 2.5D photonic crystal, the vertical index contrast confinement impacts strongly the PhC properties. Indeed, the solutions of Maxwell's equations have to give real \mathbf{k} in the slab and imaginary \mathbf{k} perpendicular to the direction of propagation in the surrounding material to provide guided modes. As an example the guided modes for a slab of index 3.4 are plotted in fig. 4.10. From this figure two observations can be made. First the finite vertical size of the slab perturbs the linear dispersion of the material changing thereby the effective index for a given wavelength. In the present case the mode of the slab around 1550 nm has an approximative effective index of 2.8. Thus, in a band structure dealing with \mathbf{k}_{\parallel} vectors along the symmetry axis, \mathbf{k}_{\perp} is no longer a free variable. Consequently, the modes allowed in the 2.5D PhC will be a function of the variables \mathbf{k}_{\parallel} and \mathbf{k}_{\perp} . Secondly, the zone of the guided modes in the slab is delimited by a line of slope c/n (n being the index of the surrounding material), above this region of the dispersion diagram modes are coupled to the surrounding material and no perfectly guided modes exist. Incorporating this constraint in a PhC band structure adds then a limit on the range of wavelengths for which light is perfectly confined (see fig. 4.11) and where properties of PhC may be exploited efficiently. Note that the represented band structure is in fact

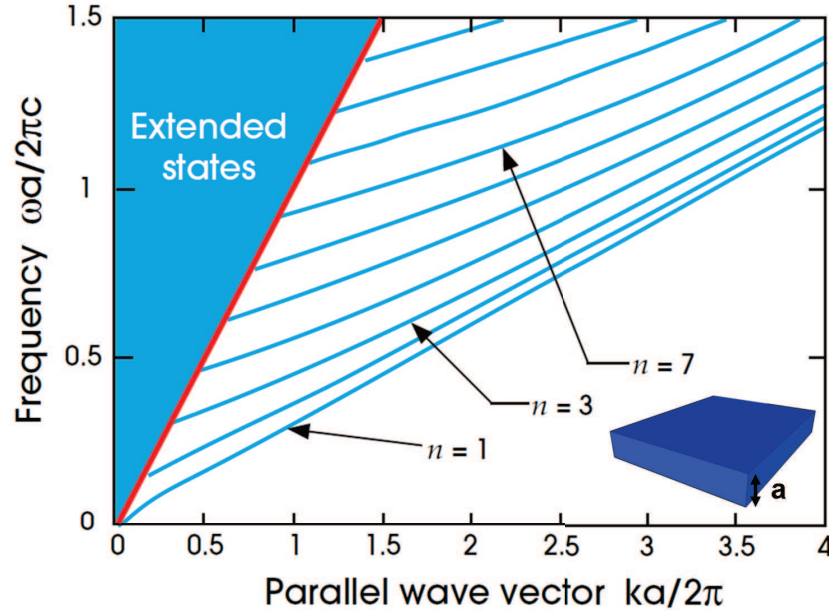


Figure 4.10: Harmonic mode frequencies for a plane of material of dielectric constant $\epsilon=11.4$ and thickness a surrounded by air. The shaded blue region is a continuum of states that extend into both the high index material and air around it. The red line is the light line $\omega = ck$. This plot shows modes of only one polarization, for which H is perpendicular to both the z and k directions. From [7].

calculated via 2D modelling taking the index of the material to be 2.8, which is valid in first approximation. In summary, a 2.5D configuration offers interesting confinement properties, combining an in-plane band gap and the index contrast for a vertical confinement.

Before concluding on PhC slabs, the relative importance of the two polarizations in our structures needs to be emphasized. QW emitters can preferentially emit in one polarization, and in our case the electric field in the plane of the QWs, depending on several parameters such as the materials composition and the growth conditions [8]. Added to this, in a slab the TM mode is higher in energy and less confined so in the following work on design, more attention is given to the TE gap than to the TM one.

As was touched upon in the conclusion of the previous section, accessing the properties of PhCs is sometimes done through the use of defects. These defects can be divided in two general families : “point defects”, consisting in changing locally the “nature” (size, shape, periodicity...) of the holes, or “linear defects”, where a line of holes is modified in the PhC. The first type of defect leads to a cavity, while the second type results in a waveguide. In this work both types of designs have

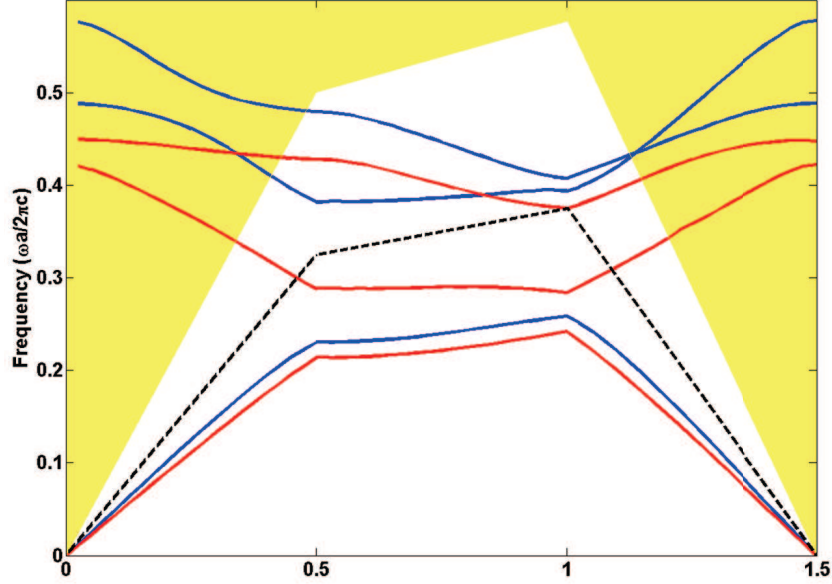


Figure 4.11: Band structure of fig. 4.7 with added light and substrate line (respectively yellow region and black dotted line). Modes above these lines are coupled to the surrounding material (resp. air or BCB) and as a result are lossy. Modelled with FDTD.

been used to attain specific properties, accessing different aspects of the hybrid structure. It is therefore of importance to give general insights on the available parameters and properties expected for each design, as will be done in the following two sections. Note that the examples presented are based on lower index holes embedded in a higher index medium.

4.3 Photonic crystal cavities

4.3.1 Generalities

Photonic crystals acting as a strong reflector are used to make cavities by modifying the PhC structure so as to create a location where a mode of a wavelength belonging to the bandgap exists. In a general way, creating a localized deviation from perfect periodicity destroys the translational symmetry of the ideal infinite photonic crystal. As a result, the Floquet-Bloch theorem does not apply anymore and for photonic crystals that exhibit bandgaps, a novel class of localized eigenmodes with eigenfrequencies inside the frequency forbidden band may appear. In a simplified picture, most of the properties of those local defects states can be understood in terms of “effective index”. Indeed, the two band edges of the photonic

bandgap have very different effective indices. Since the mode of the valence band is mostly located in the higher index material it has a higher effective index than the conduction band mode where the field is located mostly in the lower index material. It is then possible by changing locally the periodicity to create a mode that has an effective index between those two extrema. For instance, in a PhC slab with air holes, slightly changing the size of one or several holes from the size in the periodic structure to zero will give rise locally to a mode within the bandgap. This effect is depicted in fig. 4.12 where, with similar consequences, instead of size of the hole, the local dielectric function of the defect is changed. Consistently with the picture used here, it can be seen that for an index of the defect close to one, which is the index of the holes, the first order mode is located at the conduction band edge, where this mode is asymptotically approaching the valence band when ϵ goes to 12 (ie. the dielectric constant of the surrounding material). On this figure higher order modes behaviour is also plotted. Drawing a parallel with the standard Fabry-Perot resonator and linking the effective index to the effective length of the defect (since $k = \frac{2\pi n_{eff}}{\lambda}$), one can understand the emergence of higher order modes. Obviously, for a fixed index of the defect, increasing the size of the cavity by removing and/or acting on several holes instead of one will give the same behaviour. As will be explained later (in chapter 8) the dependence of ω on ϵ , is a typical effect of the photonic crystal band gap. Indeed, the penetration length, or the imaginary part of the cavity mode in the PhC, is dependent on the wavelength of the resonance (where a Fabry-Perot mirror is considered to result in a constant penetration depth versus wavelength) leading to a different “effective length”.

4.3.2 Q-factor and losses

It is important to note that using a PhC band gap as reflector is fundamentally different from other types of reflectors based on total-internal-reflexion (TIR) or metallic mirrors. Indeed, first a PhC bandgap leads to high reflectivity independently of the incident k vector, which is in strong contrast with TIR which is limited to certain angles (this is strictly true for 3D PhC, in the case of 2.5D PhC this assessment remains valid for \mathbf{k} -vector with limited \mathbf{k}_\perp value). Secondly, since the reflectivity of a PhC is the result of collective effects of wave diffraction, high reflectivity can be attained compared to a metallic mirror where reflection is intrinsically associated with absorption. Pointing out those differences leads us to considerations concerning the Q factor, and loss mechanisms, of PhC-based cavities. Then, as just said, because of the limitation imposed by vertical TIR confinement, 2.5D PhC slabs present some drawbacks, as compared to a perfect 3D PhC trap, for light storing, decreasing the limit of the reachable Q factor of PhC cavities. One source for loss in the 2.5D case under study is the out-of-plane loss.

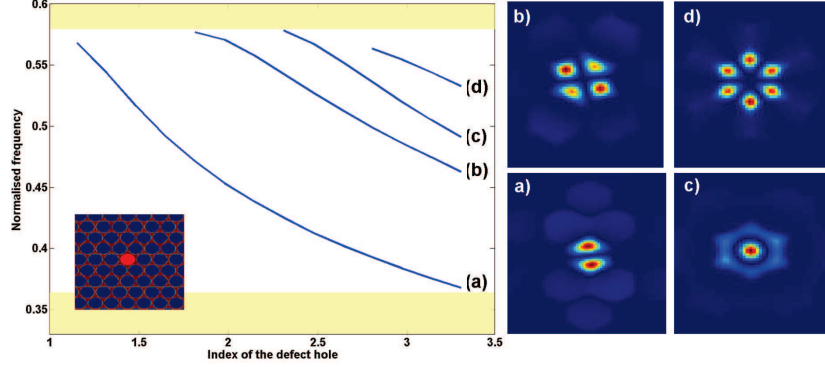


Figure 4.12: Eigenfrequencies (left panel) and field distributions (right panel) of localized cavity states for TE-polarized light in a 2D photonic crystal composed of a triangular lattice of air pores ($r/a=0.45$) in a dielectric matrix ($n=3.3$) against a variation of the index of a single hole. The field distributions display the magnetic field intensity. Depending on the strength n_{defect} of this deviation, different types of cavity modes such as doubly degenerate dipoles, (a), and quadrupoles, (b), as well as non-degenerate second-order monopoles, (c), and hexapoles, (d), develop.

This type of loss is proportional to the modal mismatch η [9] between the cavity mode and the mode in the surrounding PhC. Indeed, the mode in the cavity possesses a particular index and profile as compared to the evanescent mode at the same wavelength in the mirror. When the mode of the cavity penetrates the mirror, reflection arises from the fact that an evanescent mode of the photonic bandgap is excited, but at the same time, depending on the impedance mismatch, between the incident mode and the evanescent mode a fraction of the field is diffracted at the interface between the cavity and the PhC in a triple scattering process [10]. First the incident wave is scattered into the PhC evanescent mode with efficiency η , then this mode is coupled back into the counter-propagating PhC mode without losses, and finally this counter-propagating mode is scattered back into the incident mode with efficiency η (reciprocity theorem). Thus, the out-of-plane losses are proportional to $1-\eta^2$. Moreover, because of the finite size of the mirror, the evanescent Bloch mode is associated with a spreading in \mathbf{k} -space and hence a fraction of light is located inside the light cone.

One way to reduce this type of loss is to create a tapering zone. The mechanisms and consequences of this tapering zone will be discussed and explained more in detail in the chapter concerning the modelling of the wire cavity (chapter 8). However, it is of importance to discuss this point here, using a different picture, since this technique is the most common approach used to achieve high Q cavities in PhC. Tapering means creating an intermediate zone, between the cavity and the

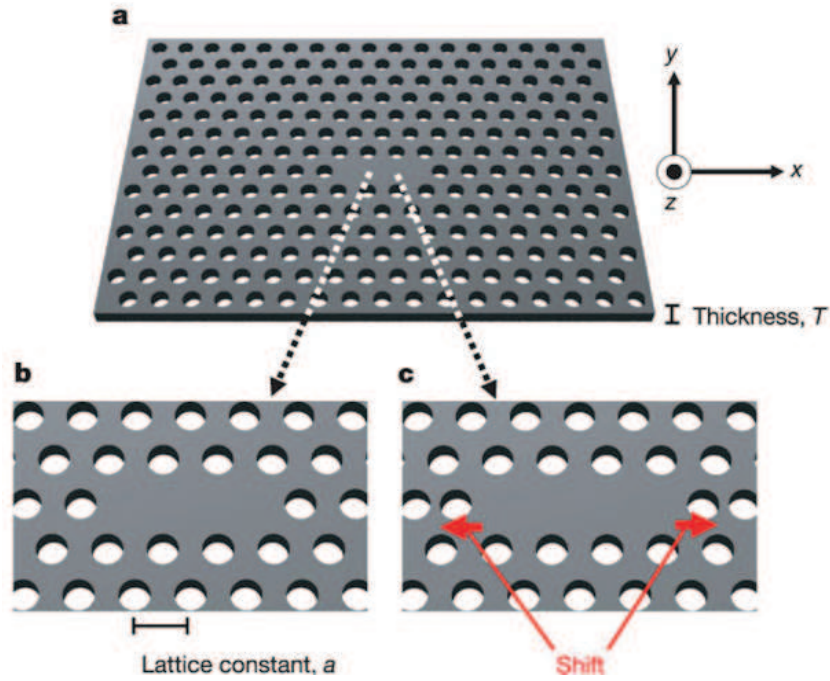


Figure 4.13: Photonic nanocavities using a 2D photonic-crystal slab. *a)* Schematic of the base cavity structure having a triangular lattice of air holes with lattice constant a ($= 0.42 \mu\text{m}$). The thickness T of the slab and the radius R of the air holes are $0.6a$ ($0.25 \mu\text{m}$) and $0.29a$ ($0.12 \mu\text{m}$), respectively. *b)* Starting cavity structure with three missing air holes in a line. *c)* Designed cavity structure created by displacing the air rods at both edges to obtain an ultrahigh Q/V value. From [11]

surrounding periodic structure, where the radius and/or the period of one or several holes is modified from the original PhC. This has as a consequence that the interface between the mirror and the cavity is “smoothened”. For example in the design proposed by Noda and al. [11], very high Q is obtained by slightly moving, from its original position, one hole on each side of a PhC cavity, see fig. 4.13.

The effect of this small displacement can be viewed as inducing a modification of the longitudinal profile of the mode inside the cavity. Without going into the behaviour of waves in a photonic crystal, the impact of this slight change can be understood, as discussed in [11], using a simple model of a Fabry-Perot made of a slab that ensures vertical confinement by TIR and two mirrors on each side for longitudinal confinement. It can be seen, that the Fourier transform of a Fabry-Perot cavity mode with abrupt reflectivity at the interface, shows some components of the field located inside the leaky region, ie. the line corresponding to the limits of vertical TIR. If now the field in the cavity has a Gaussian profile, which is the

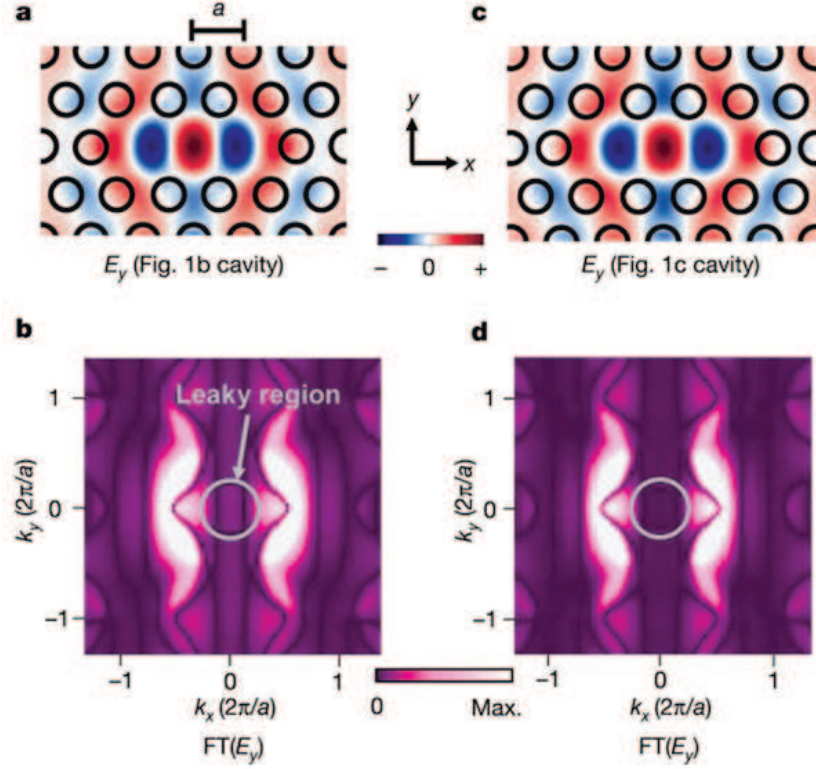


Figure 4.14: a) The electric field profile (E_y) of the fundamental mode of the cavity of fig.4.13.b. b) The Fourier Transform (FT) spectra of a). The region inside the grey circle corresponds to the leaky region. c) and d) The electric field profile and 2D FT spectrum, respectively, for the slightly modified cavity shown in fig.4.13.c. The displacement of the air rods at the edges is set at 0.15a from the starting structure shown in fig.4.13.b.

From [11].

consequence of changing the reflectivity profile of the mirrors (as for example by moving the two side holes of a PhC cavity), the Fourier transform of the field has quasi-zero components in the leaky zone and thus less out-of-plane loss. This study therefore shows that by playing with the structure in the zone surrounding the defect cavity, changing the size of a few holes or translating some of them slightly, it is possible to radically change the Q factor. Note that this tapering zone also has an impact on the volume of the mode in the cavity. This idea is illustrated on fig. 4.14 where the Fourier transform of the field in a cavity (fig.4.14.a) and its “tuned” version (fig.4.14.c) are plotted respectively on fig.4.14.b and fig.4.14.d. The strong decrease of components in the leaky region (circle inside which, for a given wavelength, the \mathbf{k}_\perp value is beyond the TIR limit of the slab) is visible

corresponding to reduced out-of-plane losses.

4.4 Photonic crystal waveguides

As discussed above, complementary to photonic crystal cavities, another type of defect is often used : photonic crystal waveguides. This defect corresponds to a structural change along one axis of the photonic crystal. For example, as can be seen in the left panel of fig. 4.15, one line of holes can be removed along one periodicity axis of a triangular lattice. This has the effect of creating a zone of specific index where light can travel in a composite structure of material surrounded by a PhC. This defect line, embedded in a zone where propagation is forbidden, leads to a particular type of waveguiding. Typically we can distinguish 2 “types” of propagation in a PhC waveguide as can be seen on the dispersion relation of a PhC waveguide plotted on fig. 4.15. The flat bands in A and C are related to purely PhC diffraction properties, whereas between the points A and B guiding is more related to the index contrast between the defect (of high index material) and the surrounding structure (high index material and air holes). The same effect leading to flat band edges in PhC slabs are the source of the dispersion at the band edges \mathbf{k} -vectors. The guided mode here really feels the reflectivity induced by the periodic structure, giving rise to slow Bloch modes, reaching zero group velocity. The zone around B is a combination of these two types of guiding.

Usually, photonic crystal waveguides are designed so as to access the flat bands at the edge of the Brillouin zone where it is possible slow down the propagation of light to values as low as $c/90$ [12], which is very interesting for all optical-buffering applications. Certain types of non-linear effects also depend on this parameter. The second interest of these low group velocity modes ($\partial\omega/\partial k = 0$) is that in this slowed regime we expect various light-matter interaction to be enhanced in slow light media.

Moreover, at this point, through the choice of the size of the defect, and consequently the effective index of the guided modes, an accurate tailoring of the dispersion is possible. It is possible to play on various parameters, such as the width of the line defect, to control the wavelength range where low group velocity modes occurs. As an example, the band structure of a 2D PhC waveguide, consisting in a line of holes with a different index than those of the surrounding PhC, is shown in fig. 4.16(blue line). It can be seen that acting on the defect allows to tune the slow mode over the bandgap range. However, more complex designs than the one used here for illustration would show the flexibility of PhC waveguides in tailoring the dispersion curves of the guided modes and use, for example, very particular feature such as “mini-stop bands” [13] [14].

So, photonic crystal waveguides are very good candidates when the dispersion relation has to be finely controlled to have very low v_g , in order to compensate

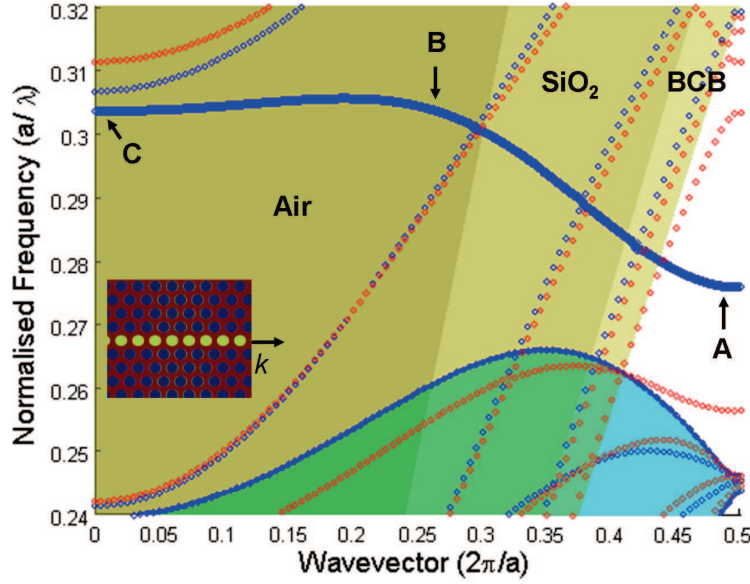


Figure 4.15: The 3D PhC bandstructure calculated using a guided mode expansion for an InP membrane with a BCB substrate and air superstrate (with air holes). The thick line (marked odd) corresponds to the odd TE-like defect mode and the thick line (marked even) the even TE-like defect mode. The TE-like band edge modes are shaded. The TM-like lattice modes are plotted as dotted lines. The period is $a=435$ nm, hole radius $r=0.3a$ and the height of the InP is 255 nm, the supercell is $5\sqrt{3}a$ wide.

for linear dispersion [15] for instance or to compensate non-linear effects to allow temporal solitons [16]. But PhC waveguides are not ideally suited for passive functions. Indeed, first, it has been shown that disorder induced losses are proportional to $1/v_g^2$, thus PhCs waveguide are not suitable for guiding light. Secondly, one of the major drawbacks of PhC is that it is very difficult to inject light into this kind of structures since the impedance mismatch with respect to any other type of waveguide is very high. Efficient coupling of light in that kind of system requires an intensive optical engineering. This is the reason why we restrict the role of PhC to active functionalities in this work.

4.5 Conclusion

Since the time photonic crystal designs were proposed and their fabrication was mastered through accurate processing techniques, a flourishing new field of research has opened up. Understanding of the underlying physics and design rules of

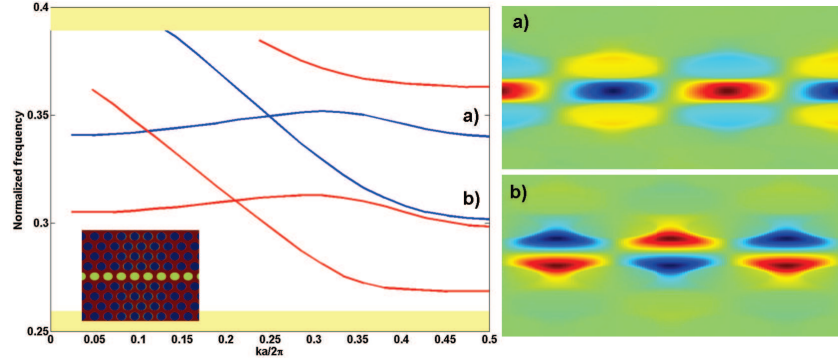


Figure 4.16: Left - Dispersion relation of W1 waveguides for H-polarized light in a 2D photonic crystal composed of a hexagonal lattice of air pores (radius $r/a = 0.34$, $a = 435$ nm) in a dielectric matrix ($n_{\text{host}} = 3.3$) where the dielectric function of a row of pores has been modified (see inset). Shaded yellow regions correspond to the band gap of the surrounding PhC. Depending on the strength ϵ_{def} of this modification, we can tune the position of the different guided modes. For low values of the dielectric function (blue lines, $n_{\text{def}} = 2.2$), broad-band mono-mode waveguiding behaviour occurs, whereas for high values of the dielectric function (red lines, $n_{\text{def}} = n_{\text{host}}$), corresponding to non-etched pores the modes are shifted and the system begins to have a multi-mode behaviour. Right - Field profile for the symmetric and anti-symmetric mode in the case of $n = 2.2$, corresponding respectively to point a) and b) on the dispersion curve.

more and more complex structures, such as Coupled-Resonators-Optical-Waveguides [17] have blossomed during the last two decades leading to a jungle of experimental results on light-matter interaction. Indeed, photonic crystal cavities allow high Q factor [18] [19], as high as millions, in a very small modal volume [20] allowing, on one hand QED studies [21], thanks to the width the resonance that can be of the order of the homogeneous broadening of an emitter, and on the other hand the observation of new types of laser behaviors [22]. Regarding the latter, recalling that the β values (ie. the ratio of spontaneous emission coupled to the cavity mode) of standard lasers, such as edge emitters, were around 10^{-5} , now it is possible with PhC to reach values close to 1 [23]. Even if, in all fairness, it is true that certain structures [24] [25] allow to reach higher Q values than PhC, these cavities remain unsurpassed in the ratio Q/V , which is the most relevant factor in many non-linear effects. A quick glance at the most common systems used and their Q and modal volume values reported in fig. 4.17 convinces us immediately. Moreover, the flexibility of the PhC design opens many opportunities for specific ways to manipulate light within the material system.

In the same manner, photonic crystal waveguides have been shown to drastically slow down the propagation of light [27] [28]. Even though other processes such as electromagnetically induced transparency [29] gives better results, PhC is a system

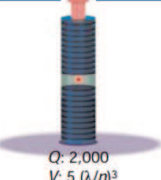
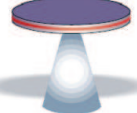
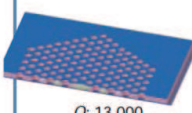
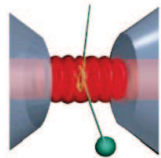
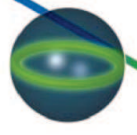
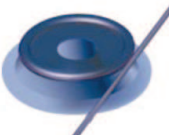
	Fabry-Perot	Whispering gallery	Photonic crystal
High Q	 $Q: 2,000$ $V: 5 (\lambda/n)^3$	 $Q: 12,000$ $V: 6 (\lambda/n)^3$	 $Q: 13,000$ $V: 1.2 (\lambda/n)^3$
Ultrahigh Q	 $F: 4.8 \times 10^5$ $V: 1,690 \mu\text{m}^3$	 $Q: 8 \times 10^9$ $V: 3,000 \mu\text{m}^3$	 $Q: 10^8$

Figure 4.17: Different type of optical trap and their respective Q factor and modal volume characteristics. From [26].

which is less delicate to prepare and to implement thereby making them good candidates for photonic integration. Furthermore, the strong tailoring of the dispersion relation of PhC structures allows “molding” of the flow of light. For example, a well chosen design can give phase matching for parametric non-linear effects such as second harmonic generation [30] [31].

In our case, the choice for PhC is driven by the aim to increase the light-matter interaction, either benefiting from high Q/V or low v_g to reach components with very low power consumption. In the context of photonic integration the consequent increased speed and lowering of activation energies of several non-linear effects, or the small foot print attainable, are very crucial arguments in favor of PhCs.

References

- [1] Yablonovitch E. *Inhibited spontaneous emission in solid-state physics and electronics*. Phys. Rev. Lett., 58:2059–62, 1987.
- [2] John S. *Strong localization of photons in certain disordered dielectric superlattices*. Phys. Rev. Lett., 58:2486–9, 1987.
- [3] Ivan S. Nikolaev Arie Irman Karin Overgaag Daniel Vanmaekelbergh Willem L. Vos Peter Lodahl, A. Floris van Driel. *Controlling the dynamics of spontaneous emission from quantum dots by photonic crystals*. Nature, 430, 2004.
- [4] F. Bloch. Z. Physik., 52:555–560, 1928.
- [5] C. M. Soukoulis A. Kirchner, K. Busch. *Transport properties of random arrays of dielectric cylinders*. Phys. Rev. B, 57,1:277–288, 1998.
- [6] P. ST. J. Russell. *Bloch wave analysis of dispersion and pulse propagation in pure distributed feedback structures*. Journal of Modern Optics, 38-8:1599–1619, 1991.
- [7] J. Winn R. Meade J. Joannopoulos, S. Johnson. *Photonic crystals. Molding the Flow of Light*. Princeton University Press, 2008.
- [8] G. Bastard. *Wave Mechanics Applied to Semiconductor Heterostructures*. Les edition de physique, 1988.
- [9] D. Marcuse. *Theory of dielectric optical waveguides*. Academic, New York., 1991.
- [10] M. Palamaru and Ph. Lalanne. *Photonic crystal waveguides : Out-of-plane losses and adiabatic modal conversion*. Appl. Phys. Lett., 78-11:1466–1468, 2001.
- [11] Bong-Shik Song Yoshihiro Akahane, Takashi Asano and Susumu Noda. *High Q photonic nanocavity in a two-dimensional photonic crystal*. Nature, 425:944–947, 2003.
- [12] Shinya A. Takahashi J. Takahashi C. Notomi M., Yamada K and Yokohama I. *Extremely large group-velocity dispersion of line-defect waveguides in photonic crystal slab*. Phys. Rev. Lett., 87, 2001.
- [13] Mario Agio and Costas M. Soukoulis. *Ministop bands in single-defect photonic crystal waveguides*. Phys. Rev. E, 64:055603, 2001.

- [14] H. Benisty C. Weisbuch C. J. M. Smith R. M. De La Rue T. F. Krauss U. Oesterle S. Olivier, M. Rattier and R. Houdr. *Mini-stopbands of a one-dimensional system: The channel waveguide in a two-dimensional photonic crystal*. Phys. Rev. B, 63:113311, 2001.
- [15] A. Yu. Petrov and M. Eich. *Zero dispersion at small group velocities in photonic crystal waveguides*. Applied Physics Letters, 85-21, 2004.
- [16] S. Combri I. Sagnes C. W. Wong A. De Rossi P. Colman, C. Husko. *Temporal solitons and pulse compression in photonic crystal waveguides*. Nature Photonics, 4:862868, 2010.
- [17] Lee R. K. Yariv A., Xu Y. and Scherer A. *Coupled-resonator optical waveguide: a proposal and analysis*. Opt. Lett., 24:711–3, 1999.
- [18] Franck I. W. Khan M; Deotare P. B., McCutcheon M. W. and Loncar M. *High quality factor photonic crystal nanobeam cavities*. Appl. Phys. Lett., 94, 2009.
- [19] Asano T. Song B. S., Noda S. and Akahane Y. *Ultra-high Q photonic double hetero-structure nanocavity*. Nature Mater., 4:207–10, 2005.
- [20] A. Scherer A. Yariv J. D. O’Brien P. D. Dapkus O. Painter, R. K. Lee and I. Kim. *Two-dimensional photonic band-gap defect mode laser*. Science, 284:1819–21, 1999.
- [21] J. Hendrickson G. Khitrova H. M. Gibbs G. Rupper C. Ell O. B. Shchekin D. G. Deppe T. Yoshie, A. Scherer. *Vacuum Rabi splitting with a single quantum dot in a photonic crystal nanocavity*. Nature, 432:200–203, 2004.
- [22] H. J. Photon Rice, P. R. Carmichael. *Photon statistics of a cavity-QED laser - a comment on the laser-phase transition analogy*. Phys. Rev. A, 50:43184329, 1994.
- [23] L. Le Gratiet A. Talneau G. Beaudoin I. Robert-Philip I. Sagnes R. Hostein, R. Braive and A. Beveratos. *Demonstration of coherent emission from high- β photonic crystal nanolasers at room temperature*. Optics Letters, 35(8):1154–1156, 2010.
- [24] H. J. Kimble J. R. Buck. *Optimal sizes of dielectric microspheres for cavity QED with strong coupling*. Phys. Rev. A, 67:555–560, 2003.
- [25] Kippenberg T. J. Spillane S. M. Vahala K. J. Armani, D. K. *Ultra-high-Q toroid microcavity on a chip*. Nature, 421:925–928, 2003.
- [26] K. J. Vahala. *Optical microcavities*. Nature, 422, 2003.

- [27] A. Shinya J. Takahashi C. Takahashi M. Notomi, K. Yamada and I. Yokohama. *Extremely Large Group-Velocity Dispersion of Line-Defect Waveguides in Photonic Crystal Slabs*. Phys. Rev. Letters, 87-25, 2001.
- [28] Engelen R J P Bogaerts W Korterik J P van Hulst N F Krauss T F Gersen H, Karle T J and Kuipers L. *Real-Space Observation of Ultraslow Light in Photonic Crystal Waveguides*. Phys. Rev. Lett., 94:073903, 2005.
- [29] P. Monnier J. A. Levenson V. Rouget E. Baldit, K. Bencheikh. *Ultraslow light propagation in an inhomogeneously broadened rare-earth ion-doped crystal*. Phys. Rev. Lett., 95:143601, 2005.
- [30] A. R. Cowan and Jeff F. Young. *Mode matching for second-harmonic generation in photonic crystal waveguides*. Phys. Rev. B, 65:085106, 2002.
- [31] T. J. Karle F. Raineri J. Trull R. Raj K. Staliunas C. Nistor, C. Cojocaru. *Lossless backward second-harmonic generation of extremely narrow subdiffractive beams in two-dimensional photonic crystals*. Phys. Rev. A, 82:033805, 2010.

5

Numerical methods

Anticipating the behaviour of light in a structure as complex as a photonic crystal is not straight forward, and can become more complicated when a defect is introduced. Dealing with this kind of problems is often driven by goals such as obtaining the band structure of a PhC or the Q factor of a cavity. This leads us to the use of different numerical methods depending on the question addressed. It is therefore critical to choose the right modelling tool. In the first part of this chapter we will discuss some of the most used numerical methods. This first section will consist of a concise and non-exhaustive overview. In a second part of this chapter, we shall highlight the relevance, drawbacks and assets, of the tool chosen for the modelling during this work, ie. a “Finite-Difference in Time-Domain” (FDTD) based software [1], giving some basics on this algorithm and discussing the routine used. Finally, since our work is very specific, in term of the materials involved (InP plus quantum wells with an underlying BCB layer) or spatial 3D organisation (PhC with an underlying silicon wire), and the evanescent coupling of the active and passive layer, special care has to be taken in choosing an appropriate modelling tool.

5.1 Frequency domain methods

There are two families of computational methods : frequency and time domain solvers. Time domain methods such as FDTD consist in solving iteratively Maxwell’s equations, independent of the problem, where the frequency domain solvers allows

to obtain the eigenmodes of certain structures.

5.1.1 Scattering-matrix technique

The first step, using this type of algorithm, is to divide the structure into sections where the refractive index does not change along the direction of propagation (see fig. 5.1). Then, N eigenmodes of every section are calculated, including guided and radiation modes. Hence, the total field can be written in a good approximation as a linear combination of those eigenmodes. Moreover, the propagation of the field in each section can be calculated. Brought together all these stacks form the

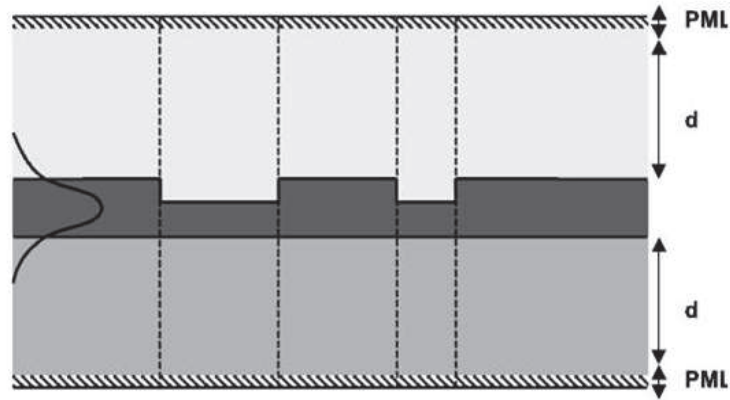


Figure 5.1: Eigenmode expansion method. The structure is divided into sections. In each section the refractive index does not change along the propagation direction.

total structure. By using a mode-matching technique at the interfaces between the different sections [2] [3], the scattering matrix of the entire stack is calculated. The resulting scattering matrix gives then the reflection and transmission coefficients of the total structure. The fields and the radiated power can also be calculated at any position in the stack, for a given excitation at a particular frequency. Obviously, the vertical window cannot be infinite. It is therefore necessary to truncate vertically the modelling area with an artificial material known as a Perfectly Matched Layer (PML) [4], an artificial strongly absorbing material avoiding parasitic reflections at those boundaries. This method of solving can also be extended to PhC because of the frequency-domain nature of this method. It is indeed possible to extract the Bloch-harmonics amongst the modes of a section, via the periodicity of the solutions [5], at defined frequencies and then extend the calculation to a PhC structure on this basis. Note, that this method allows also the modelling of PhC with embedded defects.

5.1.2 Plane wave expansion

The plane wave expansion method is based on the truncation of the sum in the following equation (see eq. 4.11), deduced from the application of the Bloch-Floquet theorem (section 4.1.2), reducing the master equation to a matrix-eigenvalue problem :

$$\mathbf{H}_{\mathbf{k}}(\mathbf{r}) = \sum_{\mathbf{G} \in \Gamma} \sum_{\sigma} c_{\sigma}(\mathbf{k} + \mathbf{G}) \mathbf{f}_{\sigma} e^{i(\mathbf{k} + \mathbf{G}) \cdot \mathbf{r}} \quad (5.1)$$

The coefficients $c_n(\mathbf{k} + \mathbf{G})$ and the eigenfrequencies $\omega_n(\mathbf{k})$ are obtained by a numerical diagonalization of the related “Hamiltonian”, by truncating the sum over Γ to a cut-off value. This way eq. 5.1 becomes a finite expansion. Note that this equation is nothing more than the Fourier expansion of \mathbf{H} with a cut-off in the coefficients $c(\mathbf{k} + \mathbf{G})$. Therefore, the starting point of this method is to recast the master eq. 4.5 in the Fourier space :

$$\sum_{\mathbf{G}' \in \Gamma, \sigma'} H_{\mathbf{G}, \mathbf{G}'}^{\sigma, \sigma'} c_{\sigma'}(\mathbf{k} + \mathbf{G}) = \frac{\omega^2}{c^2} c(\mathbf{k} + \mathbf{G}) \quad (5.2)$$

where the Hamiltonian matrix is

$$H_{\mathbf{G}, \mathbf{G}'}^{\sigma, \sigma'} = |\mathbf{k} + \mathbf{G}| |\mathbf{k} + \mathbf{G}'| \eta_{\mathbf{G}, \mathbf{G}'} \begin{pmatrix} \mathbf{f}_{\sigma 2} \cdot \mathbf{f}_{\sigma' 2} & -\mathbf{f}_{\sigma 2} \cdot \mathbf{f}_{\sigma' 1} \\ \mathbf{f}_{\sigma 1} \cdot \mathbf{f}_{\sigma' 2} & \mathbf{f}_{\sigma 1} \cdot \mathbf{f}_{\sigma' 1} \end{pmatrix} \quad (5.3)$$

and the matrix η is the inverse of the dielectric function Fourier transform.

The final step is the diagonalization of the matrix H which gives the eigenfrequencies $\omega_n(\mathbf{k})$ and the coefficients $c_n(\mathbf{k} + \mathbf{G})$. In order to calculate the whole band structure, the operation has to be repeated for a certain ensemble of \mathbf{k} vectors of the B.Z., usually the edges of the irreducible B.Z.. The chosen cut-off will determine the reliability of the method. This method is often used for constructing band diagrams in 2D or 3D.

Moreover, coupling this algorithm with the super-cell method [6] allows computation of defects or 2.5D photonic crystals [7] [8] by adding an additional periodicity in the index profile. The super-cell method consists in creating a “super-cell” containing the defect and a certain number of periods of the surrounding “bulk” PhC, giving a whole structure composed of a periodic array of defects. Interaction between these cells, or defects, is small if the number of PhC periods in the super-cell is sufficiently large.

5.1.3 Application to hybrid systems

The two algorithms discussed above are often used when dealing with PhC modelling and have proven to be powerful tools in designing such kinds of systems, but some aspects of these programs have to be revisited for the specific aim of

modelling our hybrid structures.

For example, since these algorithms are in the frequency-domain having a resolution $\Delta\omega$ in the results, to obtain the band structure or the Q factor of a cavity, they require that we calculate a loop over frequencies. This can become a problem in terms of time. This is true all the more when attacking a new problem where it is sometimes difficult to anticipate the final result. Moreover, the problem we are dealing with is a truly 3D one, which is not straight forward to model with the frequency-domain algorithm. Bared on these findings, we decided not to use frequency-domain methods for the study of the hybrid structure. The other family of algorithm for optical modelling, which are less sensitive, a priori, to the problems mentioned above and are more flexible are the “Finite-Difference in Time Domain” (FDTD) based solvers as will be discussed in the next section.

5.2 Finite-Difference Time-Domain

5.2.1 Introduction

FDTD is an algorithm proposed by Yee K. S. (1966) [9] for solving the time-dependent Maxwell curl equations, which transforms the differential operators into finite differences in space and time. This method has proven during the last years to be a very powerful tool for studying and designing building blocks for micro- and nano-phonic structures [10].

The equation below represents the classical technique used in numerical analysis for calculating the first derivative of a function :

$$f'(x) = \frac{f(x+h) - f(x-h)}{2h} + O[h^2] \quad (5.4)$$

The Yee algorithm is based on the same principle, extended to curl equations such as Maxwell’s equations. For simplicity, the method will be briefly presented for the 2D case.

First, the real space is defined on a discrete uniform rectangular mesh x-y, likewise time is discretized by division in uniform intervals Δt . A point in the mesh can then be defined by a pair of integers i, j

$$(i, j) = (i\Delta x, j\Delta y) \quad (5.5)$$

where Δx and Δy are, respectively, the lattice space increments in the x and y coordinate directions. Further, we denote any function f of space and time evaluated at a discrete point in the grid and a discrete point in time as

$$f(i\Delta x, j\Delta y, n\Delta t) = f|_{i,j}^n \quad (5.6)$$

Consider application of eq. 5.4 for the evaluation of the first spatial space derivative of f in the x direction, at the fixed time t_n

$$\frac{\partial f}{\partial x}(i\Delta x, j\Delta y, n\Delta t) = \frac{f|_{i+1/2,j}^n - f|_{i-1/2,j}^n}{\Delta x} + O[(\Delta x)^2] \quad (5.7)$$

where the $\pm 1/2$ increment in the i subscript of f represents a space finite-difference over $\pm 1/2\Delta x$. Of course, the above expansion is identical for the variables y and t . Note that in this equation, the data used for central differentiation are taken to the left and the right of the observation point i, j by only $\Delta x/2$, rather than a full Δx . Yee chose this notation because he wanted to interleave the \mathbf{E} and \mathbf{H} components in the space lattice at intervals of $\Delta x/2$, as shown in figure 5.2.

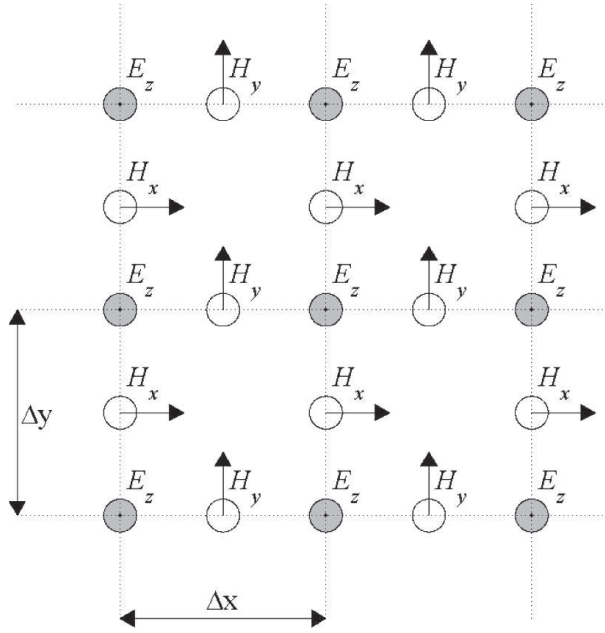


Figure 5.2: Example of a Yee cell in 2D. The points where the E and H field are calculated are space by half a period of this cell interleaving these two fields.

Recasting Ampere's and Faraday's law it is possible to express the corresponding \mathbf{E} and \mathbf{H} field at a time t using values of those fields at a precedent time, thus :

$$E_y|_{i+1/2,j}^{n+1/2} = E_y|_{i+1/2,j}^{n-1/2} - \frac{c\Delta t}{\epsilon_{i+1/2,j}\Delta x} (H_z|_{i+1,j}^n - H_z|_{i,j}^n) \quad (5.8)$$

$$H_z|_{i,j}^{n+1} = H_z|_{i,j}^n + \frac{c\Delta t}{\Delta x}(E_y|_{i+1/2,j}^{n+1/2} - E_y|_{i-1/2,j}^{n+1/2}) - \frac{c\Delta t}{\Delta y}(E_x|_{i,j+1/2}^{n+1/2} - E_x|_{i,j-1/2}^{n+1/2}) \quad (5.9)$$

After evaluation of the field equation for H and E at the respective time steps 0 and 1/2, a loop over the precedent equations allows to update the field to the desired time step. For each time step a loop has to be performed to evaluate the equations over the (i,j) grid, to update the field on the grid. 3D calculation is based on the same principle; it involves introducing an additional degree of propagation in the third direction.

The FDTD method does appear to be a very efficient and simple technique for solving Maxwell's equation in many types of structures. In practice, however, there are some precautions that have to be taken for efficient modelling of actual structures. These precautions will as much as possible be illustrated by the work performed for the modelling the hybrid structures.

5.2.2 Definition of the grid

The basis of FDTD, in all its aspects, is the grid. Obviously, the accuracy of the modelling can be improved by using smaller and smaller space increments, but, in general, having the smallest wavelength twenty times larger than the grid's pitch is enough for converged results. Therefore, to avoid any kind of "numerical dispersion", in the sense that for a fixed grid results converge under a certain frequency cut-off, it is required to work in a limited wavelength bandwidth to ensure the validity of the results. Note also that, indirectly, the grid fixes the limits of the steps in time one can take, since length and time are related. The algorithm is known to be stable if :

$$\Delta t \leq \frac{1}{c\sqrt{\frac{1}{(\Delta x)^2} + \frac{1}{(\Delta y)^2}}} \quad (5.10)$$

As for the eigenmode solvers, the simulation window has to be closed. There are several possible ways of doing this. The two cases used in the course of this work were closing using PML or Bloch condition boundaries. When using PML, to minimize the impact of this strongly absorbing material, for example on the evanescent field of a guided mode, the edges have to be far enough away from the structure, in a zone where the field is almost zero. Moreover, the absorbing strength of PML is a function of the angle of incidence of light. It is necessary to leave this boundary as far as possible from diffracting elements to avoid any parasitic reflections. Using Bloch conditions it is, of course, necessary to put the boundary at the edge of the periodic lattice considered.

5.2.3 Inclusion of the material

The structure under study is defined on the grid leading to discretization of the refractive index distribution in the simulation field. It is therefore important to try to match as much as possible the structure with the grid. Relevant steps when changing the size of the structure are multiples of Δx , Δy and Δz . Indeed, under these minimum changes, a clear digitisation will be visible in the results. Moreover, we modelled our rather complicated III-V layer via an approximation of the index. Indeed, the spatial resolution needed to model the III-V semiconductor composite structure would have resulted in an important increase of the calculation time. We thus extrapolated an effective index via the formula

$$n_{composite} = \frac{\sum_i h_i \cdot n_i}{\sum_i h_i} \quad (5.11)$$

where n_i and h_i are the index and thickness of the different embedded materials. In the course of this thesis the resulting values for the index resulting from this calculation have been good enough to provide clear agreement between modelling and experiments.

5.2.4 Initiation of the calculation

At the beginning of the modelling a source term is added in the equation at a specific point of the grid. This source term is a finite function in time, keeping in mind that FDTD is a time-domain based algorithm, thus the temporal “shape” is restricted by the fact that this function has to be continuous and its derivative too. This source term in time will fix the wavelength spectrum of the excitation, via Fourier transformation, (and it is therefore impossible to work with perfectly monochromatic waves). Usually, in dealing with a new design the relevant source to be used is a dipole with a bandwidth as large as possible to ensure a broad exploration of the system response. Last point about the source is its positioning. Indeed wrong positioning can lead to surprising results. For example, if the source is located at a node of a mode it will be impossible to excite this mode. So, in practice, several sources are placed at random locations. Another consideration concerns the use of well positioned sources in order to obtain under certain conditions destructive interferences for modes at certain \mathbf{k} -vectors. A typical example of this need concerns the modelling of the band structure of a triangular periodic lattice. Indeed, in that case the simulation zone, on the grid basis, encompass more than one periodic pattern, implying that modes belong to the second Brillouin zone appear in the results. In order to remove them from the results, one option is to use two sources, located in each cell, dephased by $-\pi/a$ resulting in destructive

interference for modes having a \mathbf{k} -vector equal to $\mathbf{k} \pm \pi/a$.

5.2.5 Simulation time

As in any work, using FDTD does not exempt us from time saving, even more with 3D calculations that can be very demanding in terms of memory needed or size of the data collected. Indeed, since the calculation of the field at a time t requires to keep in memory the field calculations at a previous time, a lot of data is stored during the modelling. This requires very performant computational systems. In order to simulate 3D structures as efficiently as possible, some methods can be used. The first is to exploit the symmetries of the studied system, then with respect to the symmetry or anti-symmetry plane, only half of the simulation zone has to be calculated. Then, the calculation window is reduced. Another interesting property is the use of parallel FDTD, consisting in dividing the area of modelling in several parts, each region calculated simultaneously on different processors. The connection between each zone being mutual data transfer of the field values at the edges of each simulated region. This technique often results in a remarkable gain of time, but note that this gain of time is not always significant, as for 2D modelling, since in that case the limiting time becomes the inter-processors communication time.

5.2.6 Processing of the data

The result of the calculation is a 4D matrix (x,y,z,t) , the field components at each point in space at any time. Performing a Fourier transform of this data will give the result in frequency domain; this is one of the most interesting features of FDTD-based computational methods, in that the complete spectral response is calculated in just one simulation. To complete the extraction of the information contained in the data we used “Harminv” software [11] which decomposes any temporal signal in Fourier space on the following basis $\sum_k C_k \sin(\omega_k t + \phi_k) e^{\alpha_k t}$, giving the decay in time α_k for any frequency and thereby allowing identification of resonant modes and their respective Q factors. The convergence of “Harminv” is very sensitive to the data collected. Therefore it is important not to use a too large k -basis and to choose carefully the time length (T_{tot}) used for the simulation. Indeed, Fourier transform fixes relationship between T_{tot} and the frequency resolution that can be obtained. Note that the grid resolution impacts the time of calculation for a given spectral resolution. Indeed, the grid resolution fixes the step time Δt , as discussed in the section 5.2.2, and the spectral resolution is a function of the ratio $\Delta t/T_{tot}$. Finally, it is important to remove from the data the perturbation signal originating from the source term. In order to do this a smooth filtering of the temporal data collected is performed to clean the source induced perturbations at

the beginning of the simulation. It is worth noting that its not always necessary to compute for a long time. In certain cases, methods can be used to reduce the necessary amount of data collection by deducing a “time transfer matrix” ($A(t + \tau) = M(\tau)A(t)$).

5.3 Conclusion

In conclusion, FDTD seems to be the most interesting tool for the work done here because of its flexibility and the accurate results that this method provides. FDTD is even sometimes presented as a “numerical experiment”. There are not many limitations, except in dealing with non-linear materials where the algorithm has to be extended for specific cases [12] [13]. A wide variety of structures can be designed, taking a minimum of precautions, as discussed in the previous sections. In this thesis modelling has gone from waveguides to cavities, from band structures to Q factors, and successfully matching the experimentally obtained results to the numerical simulations, as will be shown in the next chapters.

References

- [1] www.lumerical.com.
- [2] C. Chen K. A. zaki, S. Chen. *Modeling discontinuities in dielectric-loaded waveguides*. IEEE Trans. Microwave Theor. Tech., 36-12:1804–1810, 1988.
- [3] Lifeng Li. *Use of Fourier series in the analysis of discontinuous periodic structures*. JOSA A, 13-9, 1996.
- [4] J. Berenger. *A perfectly matched layer for the absorption of electromagnetic waves*. Journal of Computational Physics, 114:185–200, 1994.
- [5] F. Bloch. Z. Physik., 52:555–560, 1928.
- [6] Benisty H. *Modal analysis of optical guides with two-dimensional photonic band-gap boundaries*. Journal of Applied Physics, 79:74837492, 1996.
- [7] Villeneuve P. R. Joannopoulos J. D. Johnson S. G., Fan S. and Kolodziejski L. A. *Guided modes in photonic crystal slabs*. Physical Review B, 60-8:5751–5758, 1999.
- [8] Lucio Claudio Andreani and Dario Gerace. *Photonic-crystal slabs with a triangular lattice of triangular holes investigated using a guided-mode expansion method*. Phys. Rev. B, 73-235114, 2006.
- [9] Kane Yee. *Numerical solution of initial boundary value problems involving Maxwell's equations in isotropic media*. IEEE Transactions on Antennas and Propagation, 14:302–307, 1966.
- [10] Allen Taflove and Susan C. Hagness. *Computational Electrodynamics: The Finite-Difference Time-Domain Method*. Artech House, 2005.
- [11] ab-initio.mit.edu/harminv/.
- [12] Xin Wang. *Low threshold laser cavities of two-dimensional photonic crystal line defect mode*. International Journal for Light and Electron Optics, 2010.
- [13] X. Letartre J. A. Levenson F. Raineri, Y. Dumeige. *Nonlinear decoupled FDTD code: phase-matching in 2D defective crystal*. Electron. Lett., 38:1704, 2002.

6

Experimental setup : general scheme

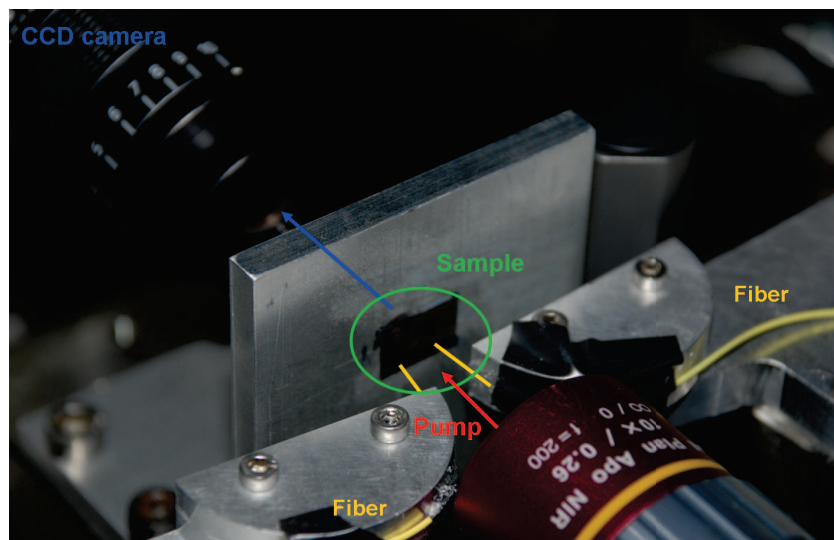


Figure 6.1: Close view of the basis of the experimental setup

Before going to the experimental results obtained, we will elaborate on the experimental setup used during this work. A picture of the sample, its imaging using a microscope and its addressing using fiber is given in fig. 6.1. Since no fundamental differences exist between the several designs studied in this work, we

can give a general scheme of the setup implemented in order to study the hybrid structures. This setup can be divided in several independent parts corresponding to different needs such as optical pumping, imaging and detection.

6.1 Coupling to the passive layer

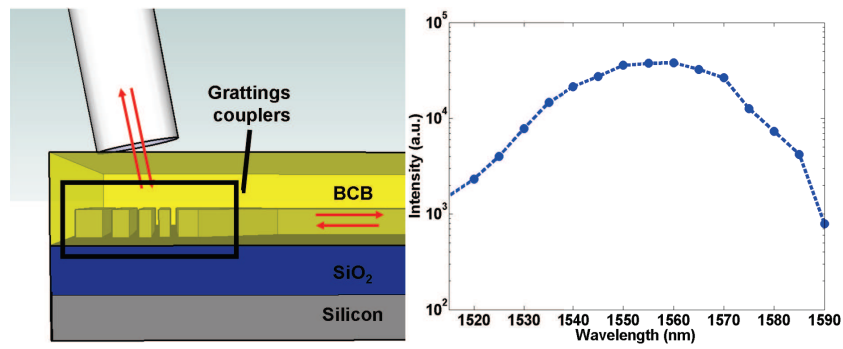


Figure 6.2: Left - Schematic view of the $10 \times 10 \mu\text{m}^2$ gratings couplers etched in a SOI layer embedded in BCB. The fiber is tilted with an angle of approximately 11 degrees for efficient coupling. Right - Transmission spectra of grating couplers.

First and foremost, light has to be coupled in and out of the silicon wire. In order to achieve this coupling easily and efficiently, as compared to cleaving and butt-coupling for example, grating couplers [1] have been etched at the extremities of the silicon waveguides to allow extraction of infra-red light in the waveguide and coupling to a single mode fiber as depicted on fig 6.2-left. These gratings cover an area of approximately 10×10 microns. Their properties are strongly dependent on the angles of the coupling fibers. This means, first, that we have to use a 3 translational axes micrometer controller mounts (with 0.5 microns resolution) to accurately place the fibers on the gratings. Subsequently, concerning the angle, the fibers are glued, using a standard UV glue, on a metal mount with a V-groove to ensure a first control on the horizontality of the fibers, relatively to the sample which is oriented vertically as can be seen in fig. 6.1. Additionally, we had to add to the 3 axis translational micrometer mounts a rotational one (2.10^{-3} degrees resolution) to give an accurate angular control allowing to reach the optimal 10 degrees fiber tilt angle. Two complete controller stages of this kind are used for each extremity of the silicon wires, which are 6 mm long. The measured efficient bandwidth is rather large and around 50 nm, as can be seen on the experimental transmission spectra plotted on fig. 6.2-right. The efficiency of coupling obtained with our system is around 25% at 1550 nm. The use of grating couplers to couple

the silicon wire to an optical fiber is interesting from a practical point of view. Indeed, even if some drawbacks exist, for example it is important to pay attention to the polarization in the fiber since the grating couplers are strongly polarization dependent (this point was solved by using polarization controllers or polarization maintaining fibers) we gain much more by the use of fibers since it is really easy to connect them to detectors or light sources or to switch the connections from one side to the other which turns out to be very useful for alignment or just to gain in flexibility and time.

6.2 III-V level addressing

Next step concerns the III-V level of the sample. We deal with active material which optical properties are strongly dependent of the carrier density in the upper levels of the electronic band structure of the III-V composite material. As we optically pump, using a photon energy above the electronic gap of the barriers (In-GaAsP), the refractive index, imaginary and real part, of the III-V semiconductor layer is changed. These carriers are created locally where the sample is pumped and the intensity of the tuning is proportional to the pump power per surface unit. It is then of highest importance to be able to locate and focus the incoming pump light on a surface of the order of the photonic crystal defect. We used objectives to attain this goal, in our case Mitutoyo $\times 10$ or $\times 50$ long working distance objectives. In fact a trade off have to be found between numerical aperture, and therefore focusing, and the working distance of those objectives. Indeed, as said before (see fig. 6.1) we are limited technically by the fact that we are working with 6 mm long silicon waveguides and therefore we needed to find space for the objective between the mounts for fibers. The position of the objectives is fixed and the sample was mounted on a 3 axis micro-controlled allowing us to appreciably control the zone of pumping. Moreover, these objectives have also been used to collect the infrared light emitted from the sample surface. The separation of these two different wavelengths, the incoming pump and the emitted light by the sample, is ensured by the use of a dichroic mirror, which is transparent (around 1.5 microns) or reflective (at 800 nm) depending on the wavelength of the light incident on it. These two paths are schematically represented on fig. 6.4. We are thus able to detect either the light emitted from the top of the sample, resulting from cavity losses, or coupled in the silicon wire, via the coupled single mode fibers. Note that the objectives were not perfectly achromatic, consequently focusing of the pump or the collection of light were not optimal for the same distance to the sample. Depending on the cases we preferably adjust the distance for optimisation of the collection of the emitted light or for focusing the pump light. As we will discuss later, the poor thermal properties of our hybrid structure did not allow us

to work under continuous pumping. Consequently, most of the studies made here have been made under pulsed pumping using either 1.2 microns or 800 nm diodes electrically driven, using a current source generator, to fix the shape of the train of pulses, or using Ti:Sa/OPO femtosecond sources which are modulated at 80 MHz.

6.3 Imaging

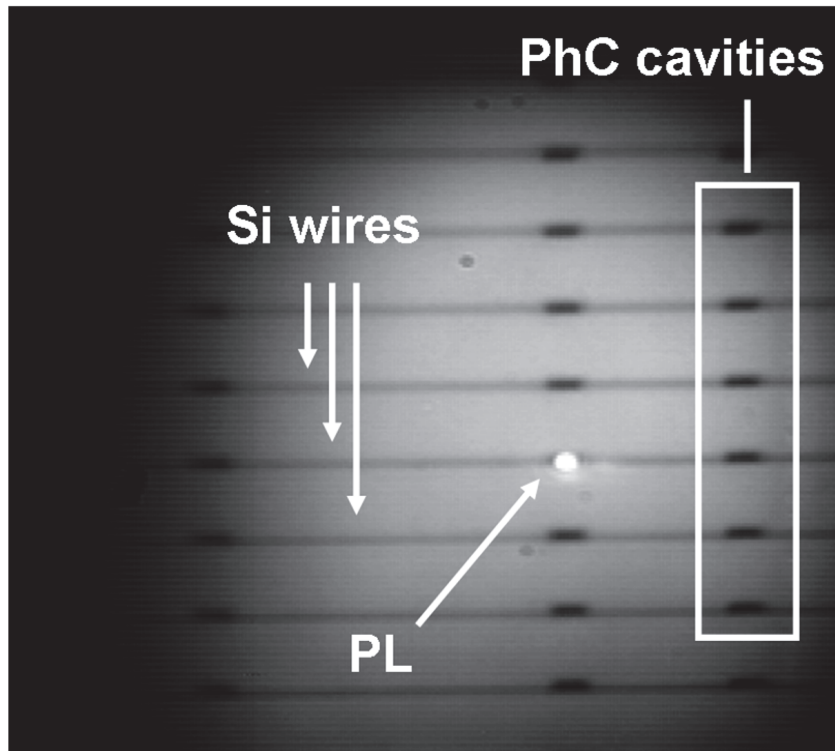


Figure 6.3: Back imaging using a IR camera. Silicon waveguide and PhC structures are clearly visible, the white spot corresponding, this time, to the emission of the PhC.

Since efficient pumping and signal extraction were inevitably our main pre-occupations, imaging was the last step in building the experimental setup. Fortunately, inserting an imaging modality was easy in the built scheme. We first benefit from the transparency of silicon in the infrared and its absorption at pumps wavelength, thus by backside imaging the sample, acting then as a filter, we were able to obtain an infrared image and see the emission from the sample, as can be seen on fig. 6.3. In addition, an extra beam splitter was introduced on the path of the

pump beam to bring in visible light to image the top surface of the sample which allows to accurately locate the focused pump beam.

6.4 Conclusion

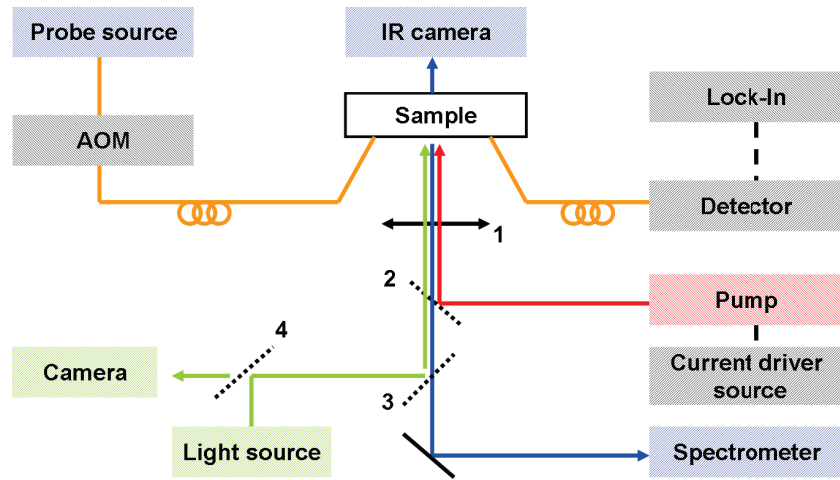


Figure 6.4: General scheme of the experimental setup. Blue, red and green color line correspond respectively to short infrared, near infrared and visible light paths. Elements 1 and 2 correspond respectively to Mitutoyo objectives, dichroic mirror (transmitive at $1.5\ \mu\text{m}$ and reflective at $0.8\ \mu\text{m}$; elements 3 and 4 correspond to 700 to 900 nm beam splitters.

As a summary, a scheme of the general setup used is depicted on fig. 6.4. This resulting experimental setup was the starting point of every experimental work done during this thesis. This chapter outlined the general scheme of the setup for every experiment done, additional informations, as when an heterodyne detection is performed, will be given if necessary before presenting the experimental results.

References

- [1] Pieter Dumon Wim Bogaerts Dries Van Thourhout Bert Luyssaert Vincent Wiaux Stephan Beckx Johan Wouters Dirk Taillaert, Roel Baets. *Silicon-on-Insulator Platform for Integrated Wavelength-Selective Components*. Proc. IEEE/LEOS Workshop Fibres and Opt. Passive, page 115120, 2005.

7

Photonic crystal waveguide laser integrated on SOI

The first design we implemented for our active structure was a photonic crystal waveguide as shown in fig.7.1. We made this first choice because of the difficulties we confronted in designing a good cavity design having a relatively high index substrate such as BCB ($n=1.54$) and having a Q high enough to obtain laser emission. Instead we opted for the use of the low group velocity of PhC waveguide modes, in order to capitalise on the associated gain enhancement due to increased light-matter interaction [1] [2]. This was also the first test of the alignment which would permit to demonstrate experimentally the coupling between the two layers. As will be presented in this chapter, we demonstrate lasing emission which was coupled to the wire waveguide in accordance with the results expected from modelling, as will be shown through the study of the emission of the PhC waveguide modes against various PhCs parameters.

7.1 W1 photonic crystal waveguides

Photonic crystal (PhC) based structures have been the object of numerous experimental and modelling studies during the last years [3] [4] [5] [6]. As a consequence, from these studies, a good understanding of the behaviour of light in such a structure and clear design rules have been obtained, such as the influence of the defect size on their properties. We, of course, but only partially, benefited from the

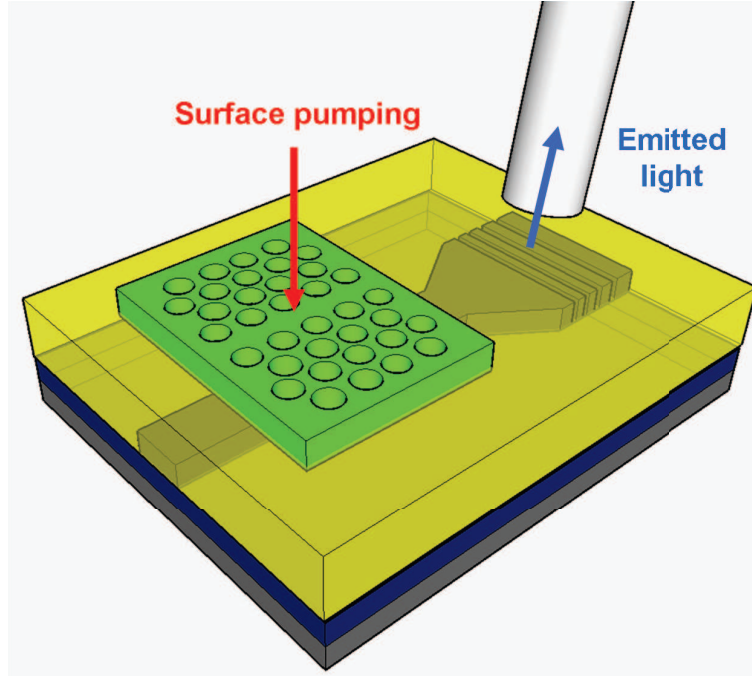


Figure 7.1: Hybrid III-V PhC/SOI wire structure and experimental configuration. The III-V semiconductor is a 265 nm InP based membrane with 4 QWs composing the gain medium. Our PhC defect waveguide hybrid structure is optically surface pumped, as indicated by the red arrow. The underlying Si wire waveguide captures the laser emission which is then diffracted by a grating coupler and collected by a cleaved SMF (blue arrow).

recent developments in this field. Indeed, our structures are substantially different, in terms of spatial organization, materials used and their objectives. As a consequence a careful modelling of the structure is required. Indeed, the point here is to design a guided slow mode in a III-V photonic crystal coupled to a silicon wire underneath, consequently some specific difficulties have to be overcome, as obtaining a confined mode with a relatively “high” index substrate and coupling to a fundamentally different waveguide such as the Si wire waveguide. This last point is a fundamental aspect of photonic crystals. Indeed coupling light to the slow mode is difficult and requires particular attention [7]. For those reasons modelling of all aspects of this complex issue an important part of the work.

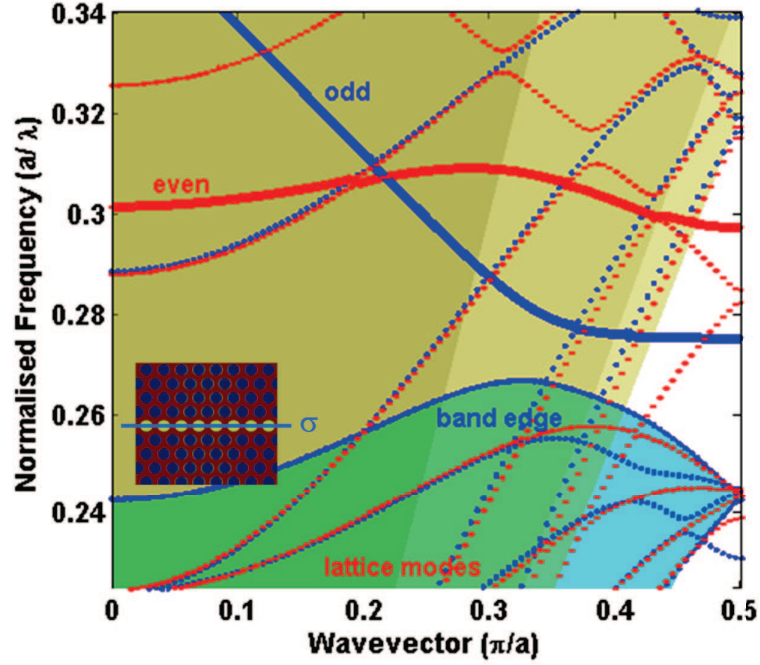


Figure 7.2: The 3D PhC bandstructure calculated using a guided mode expansion for an InP membrane with a BCB substrate and air superstrate (with air holes). The inset is a schematic top view of the linear defect inserted in the PhC, the blue line σ illustrates the symmetry plane considered. The thick line (marked odd) corresponds to the odd TE-like defect mode and the thick line (marked even) the even TE-like defect mode. The TE-like band edge modes are shaded. The TM-like lattice modes are plotted as dotted lines. The period is $a=435$ nm, hole radius $r=0.3a$ and the height of the InP is 255 nm, the supercell is $5\sqrt{3}a$ wide.

7.1.1 Modelling : III-V semiconductors PhC waveguide

As discussed in the modelling chapter the specificities of the coupling scheme used in this work allows to consider the III-V level design independently from the passive silicon wire. Then as explained in section 2.4, evanescent coupling can be seen as a perturbative mechanism of coupling in the sense that the starting point of calculations are the independent modes of each structure (see chapter 2 and 3). We therefore begin this work by modelling the upper active level. The PhC waveguide used here corresponds to one line of holes removed in a triangular lattice thus allowing a guided mode in the structure with a dominant $\mathbf{k} - \text{vector}$ along the axis of the defect. While designing a PhC waveguide two main parameters can be explored, the first one is the PhC lattice surrounding the defect, as done in this section concerning the “W1” waveguide. The second parameter is

the defect itself, as will be shown in the second section concerning the so-called “W0.65” waveguides. In the case of the “W1” waveguide, playing on the lattice constant and on the ratio r/a , where r is the radius of the holes and a the period, it was possible to move the wavelength of the gap and the position of the slow guided mode in the gap. Consequently, after a scan of different parameters, we extract the following parameters : a period $a=435$ nm and a hole radius $r=0.3a$, for our fixed 255 nm high InP membrane, corresponding to the thickness of our active layers. This configuration leads to the dispersion relation, calculated with “Guided mode expansion” [8], plotted along the $\Gamma - K$ direction in fig.7.2. As can be seen, these parameters give us the desired results, that is to say a TE odd slow mode (around $k = \pi/a$, with $u = a/\lambda = 0.275$) at $1.58 \mu\text{m}$ and a second flat band corresponding to a TE even mode around $1.5 \mu\text{m}$ ($u = a/\lambda = 0.29$) located, both, below the BCB light line. These modes are classified ($\sigma_{xz} = +1$) even and odd ($\sigma_{xz} = -1$) corresponding to a mirror reflection with respect to the vertical plane ($x - z$), illustrated by the blue line σ in the inset fig.7.2. The typical profile of such modes is close to the ones plotted in section 4.4. We then vary the period of the PhC lattice to move the position of the modes and thereby explore a large bandwidth of our gain region as shown in section 7.1.3.2. Note on fig.7.2, how the bandwidth where modes are still confined (modes below shaded regions) is severely limited by the BCB light line. On this figure, TM modes leading to flat bands are also represented. It is important to notice here that the vertical asymmetry of our system, by breaking the orthogonality of the TE and TM modes, can lead to coupling between the quasi-TE and quasi-TM modes of the PhC waveguide or silicon wire. Since QWs emit predominantly in the TE polarization, we do not expect any important perturbations in the emission spectra, or lasing operation, induced by the presence of these TM modes in the PhC band diagram.

7.1.2 Modelling : hybrid structure

Having designed a suitable structure for the active level, we can now go back to the coupling considerations. In order to achieve coupling of the PhC waveguide mode with the silicon wire mode the first requirement to fulfil is the phase matching condition. Because of the low effective index of PhC waveguides modes with respect to the effective index of guided modes in silicon wires [9], we decided to work with slightly different silicon waveguides than the standard 500×220 nm ones. Indeed, looking at the dispersion relation of the PhC waveguide, one can see that the flat mode possesses approximately a $\mathbf{k} - \text{vector}$ in the x direction of $7 \mu\text{m}^{-1}$. In order to obtain the same $\mathbf{k} - \text{vector}$ in the silicon wire we had to decrease the width to 300 nm, increasing thus the slope of the dispersion. The dispersion relation in fig.7.3 shows that such a waveguide possesses a guided TE mode around 1580 nm with a propagation constant around $7 \mu\text{m}^{-1}$. This will lead, theoretically, to the

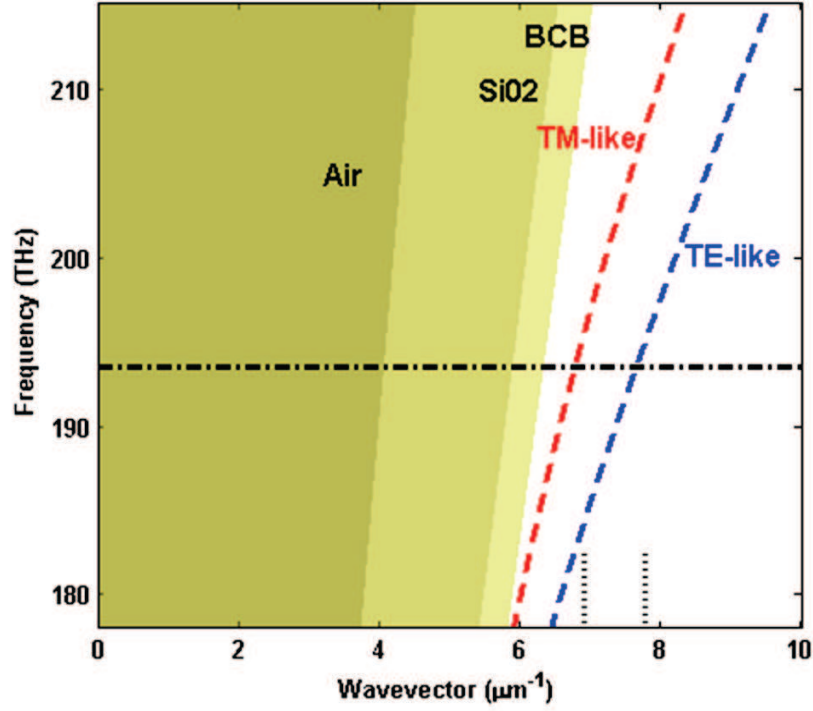


Figure 7.3: The TE-like (solid line) and TM-like (dashed line) modes of a $220 \times 300 \text{ nm}^2$ Si waveguide with a SiO_2 substrate, and BCB superstrate. The light cones of the various cladding materials, air, SiO_2 , and BCB are denoted by shading. The vertical dotted lines mark the range of lithographic tuning in the experiment. The horizontal line marks the peak gain wavelength of our QWs.

intersection of the two respective waveguide dispersion relations, fulfilling thus the phase matching condition, which will then ensure a good coupling between the two levels.

In order to check the validity of this last statement we modelled, using 3D FDTD, the two-level system and extracted the band diagram of the entire hybrid structure, with a 400 nm thick layer of BCB inserted between the III-V semiconductors and the silicon layers. Results are plotted, for a PhC lattice, etched in a 255 nm thick InP layer, with period $a=455 \text{ nm}$ and with a ratio $r/a=0.3$ and a $220 \times 326 \text{ nm}^2$ silicon wire, in fig.7.4.a. The superposition of the silicon and PhC band diagrams obtained previously, depicted respectively in fig.7.2 and fig.7.3, is clearly visible. Looking closely, it can be seen that, due to the interaction of each structure, the initial band diagrams are disturbed. An interesting feature appears at the point where the respective dispersion relations cross, more specifically between silicon

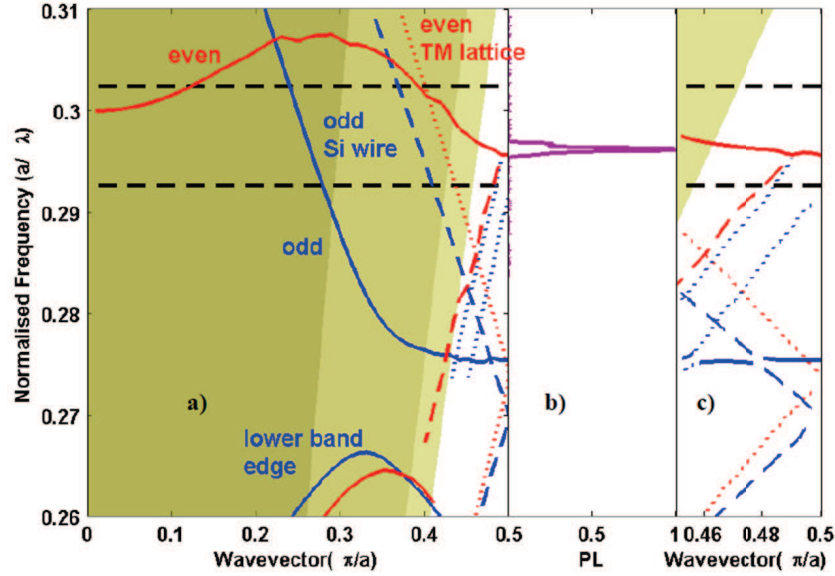


Figure 7.4: (a) Bandstructure for InP W1-Si wire (326 nm wide) hybrid system, for a period, $a=455$ nm, $r/a=0.3$, and a vertical separation of 400 nm (BCB layer). The ripple seen in the band structure is mainly due to coupling with lower Q modes. (b) The PL spectrum, coupled out via the Si wire, showing a single peak whose spectral position is consistent with the intersection with the even TE-like W1 mode. (c) Zooming in to the region of k -space close to the K point, we can observe at $k_x = 0.475 \times \pi/a$, $u = 0.275$ an anti-crossing caused by the co-directional coupling between the odd TE-like W1 mode and the odd TE-like Si wire mode.

wire and PhC modes of same symmetry below the BCB line. At this point, a splitting arises. This is represented in fig7.4.c by zooming on the frequency region $0.45 - 0.5 \times \pi/a$. To complete this modelling study, we investigate the effect of coupling with a slightly dephased PhC waveguide. In fig.7.5.a, the PhC structure has now a period $a=405$ nm while keeping the ratio $r/a=0.3$, and surprisingly the impact of the III-V semiconductors PhC seems to be strong enough to open a gap in the silicon wire dispersion (around $u = a/\lambda = 0.255$), away from the anti-crossing region. This effect is the consequence of a distributed feedback induced on the silicon wire by the periodic structure etched in the III-V layer 400 nm above the Si wire. These splitting effects are clear signatures of coupling between the two levels and this concludes the modelling work related to this structure and gives a validation of the method used based on the design where the two levels are treated independently.

In addition, note that considering two different periods while keeping the filling factor, induces a red shift of both the even and odd mode wavelength which can

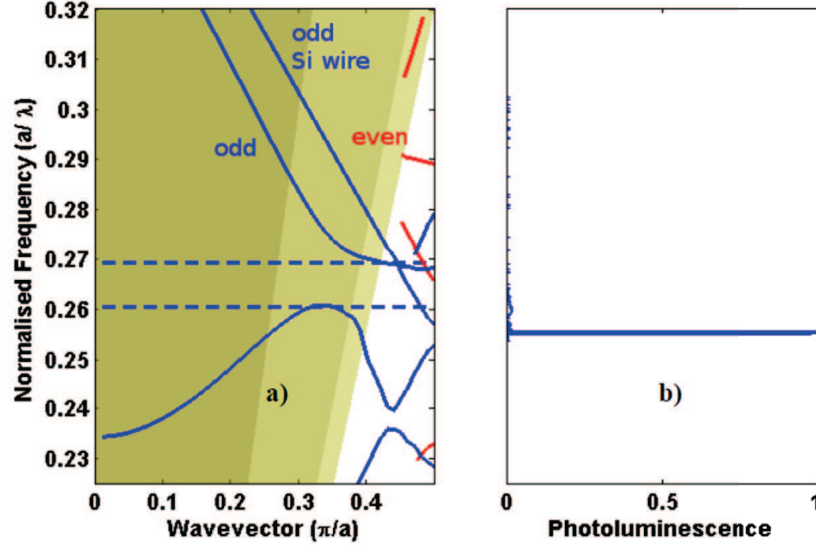


Figure 7.5: (a) Band structure for InP WI-Si wire (326 nm wide) coupled system, for period $a=405$ nm, $r/a=0.3$, and a vertical separation of 400 nm (BCB layer). (b) The PL spectrum, coupled out via the Si wire. As the emission is dominated by odd modes, here we only plot the even bands in the region $k_x=0.45-0.5 \times 2\pi/a$. The dashed black lines denote the emission bandwidth of our QWs.

be considered a very interesting tool for further designs and experiments since we will be able to scan our gain bandwidth by tuning the PhC lattice period.

7.1.3 Experimental studies

7.1.3.1 Experimental setup

Samples were fabricated using the technological process presented in chapter 3, aligning a PhC structure on top of a silicon wire (see fig.7.6) using a 400 nm thick bonding BCB layer (ie. approximately 200 nm between the top of the silicon wire and the lowest part of the InP layer). The active layer is a 255 nm InP-based membrane containing 4 QWs (alternative layers of InP - 60nm, InGaAsP - 16 nm, InGaAs - 13.5 nm) emitting around 1540 nm. The targeted parameters for the fabricated PhC waveguides were extracted from our modelling. We additionally tune the period from 405 nm to 455 nm while keeping the filling factor constant ($r/a = 0.3$).

The samples are explored at room temperature using the standard setup (see chapter 6) for surface pumping. The source for pumping used in these experiments is a Ti:Sa laser operating at a repetition rate of 80 MHz providing 100 fs pump pulses

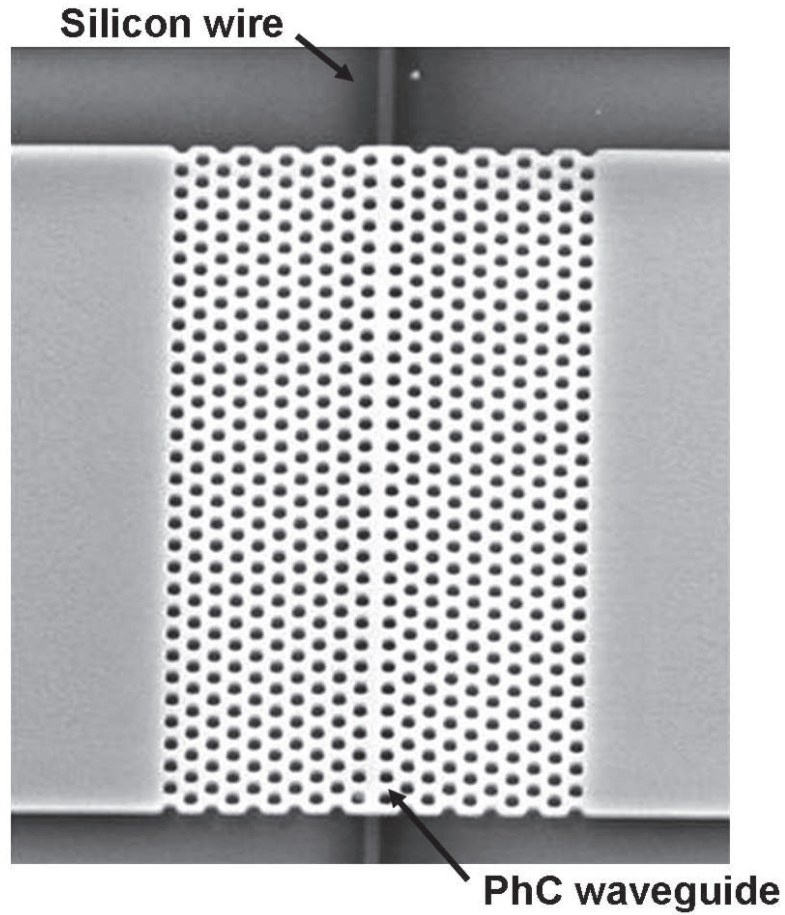


Figure 7.6: SEM image of a PhC waveguide bonded on top of a silicon wire

at 810 nm. The emitted light is collected either from the top or extracted from the silicon wire, via grating couplers, and directed to a spectrometer equipped with to an array of cooled InGaAs detectors. The spectra obtained will be analysed in the following sections.

7.1.3.2 Low group velocity modes of the PhC waveguides

First, we observe the photo-luminescence (PL) spectra. The emitted light is coupled to the silicon wires and diffracted by the grating couplers into the single mode fiber as shown schematically in fig.7.1. This allows us to identify the wavelengths where the emission is enhanced by the low v_g modes of the PhC structure. Typical

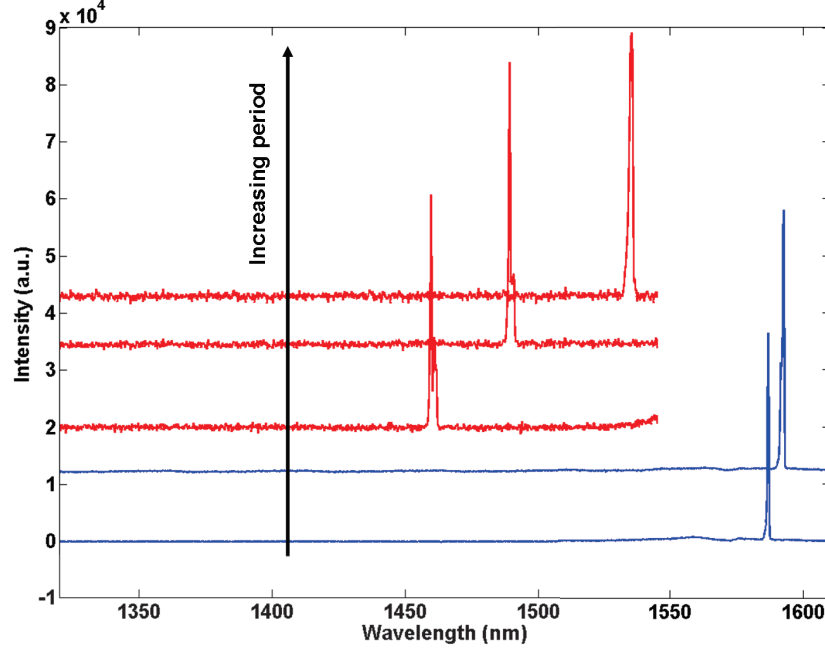


Figure 7.7: Photoluminescence spectra, measured via the silicon wire, of PhC waveguides with a varying period a , from 405 to 415 and 425 to 455 nm (from bottom to top - respectively blue and red curves) by steps of 10 nm, while keeping the ratio r/a constant.

spectra are plotted on fig.7.7 where it is seen that the wavelengths of the modes change as a function of the period of the various processed structures. As can be seen on the measured spectra, we observe a two shift behaviour of the emission peaks as the period of the PhC is tuned in steps of 10 nm, from 405 to 455 nm. Indeed, the modes plotted in red on fig.7.7 are red shifted in steps of 25 nm or slightly more, while the change on the longer wavelength modes (blue lines) the blue shift is smaller and about 5 nm. By comparing these measurements with modelling, it is clear that these emission peaks correspond to two different types of modes of the PhC hybrid structure. Indeed, we plot in fig.7.8 the measured peaks as well as the calculated wavelength of the low group velocity modes of the hybrid structure against period a . The superposition of data coming from modelling and experimental measurements shows a close agreement allowing an unambiguous interpretation of the emission spectra. First, the modes for the two smallest lattice constants (blue spectra on fig.7.7) originate from the slow flat band in the even TE silicon wire dispersion due to the DFB effect induced by the patterned III-V layer above, as can be seen in fig.7.5.b (blue line around a normalized frequency equal to 0.255). On the other hand, for shorter wavelengths, the slope of the wavelength

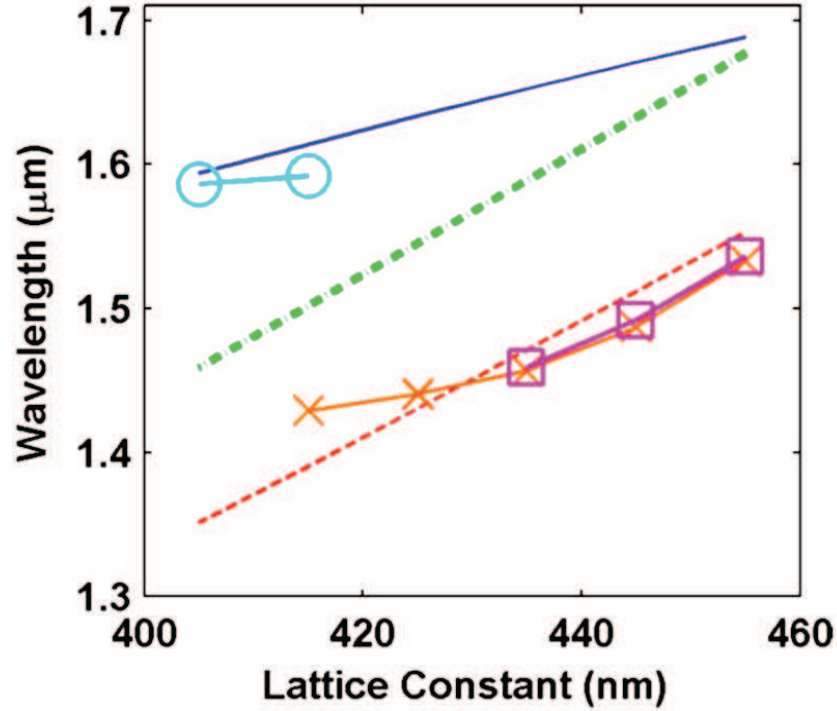


Figure 7.8: The spectral positions of the various bands at the K point, $k_x = \pi/a$ as a function of PhC period. The top solid line represents the odd TE-like Si wire mode. The middle dot-dashed line denotes the odd TE-like W1 mode. The lower dashed line represents the even TE-like W1 mode. The crosses are surface detected PL. The PL extracted via the Si waveguide from the even mode is marked by squares and the circles correspond to the Si Bragg mode edge.

mode against period is much stronger and fits undeniably with the modal behavior against the period (as can be seen by comparing the position of the mode for two different periods on fig.7.5 and fig.7.4) of the TE even slow PhC waveguide mode and match with the band diagram (for $a=455\text{nm}$) plotted in fig.7.4.b.

This whole identification of the low group velocity modes of the PhC waveguides was done, as mentioned before, by using PL spectra coupled to the silicon wire. Adding the spectra measured from the surface emission we can discuss the coupling characteristics of the PhC waveguide modes of the hybrid structure.

7.1.3.3 PhC waveguides modes and coupling to the Si wire

On fig.7.8 are reported the resonance wavelengths of the emission spectra measured either from the surface emission of the sample or coupled and extracted from

the silicon wire for various samples. The comparison between these two methods of observing the emission reveals that some modes are visible only in the silicon wire while others are visible in the surface emission or they are observable through both channels.

Concerning the modes corresponding to the splitting at the band edge of the dispersion relation of the silicon wire (blue circles in fig.7.8), coupling is almost self explanatory since the mode naturally belongs to the silicon wire, it is also the reason why this mode is invisible in the spectra measured from the top of the sample. On the other hand, modes attributed to the TE even modes of the PhC waveguide (cross in fig.7.8) are visible both from the surface and in the silicon wire. First, this mode is always visible from surface emission since it belongs to PhC waveguide and small disorders in this structure give rise to some out-of-plane losses. Secondly, it can be seen on fig.7.4.a that the dispersion curve of the even TE PhC waveguide mode crosses the TM mode of the silicon wire (red lines around a normalized frequency equal to 0.295). Theoretically coupling between these TE and TM modes cannot arise because of their respective symmetry. However, we attribute coupling between those modes to their shared lateral symmetry and the lack of vertical symmetry. Note that for certain periods a these PhC modes are uncoupled but still visible in the vertical emission. Indeed, having a look on fig.7.5, it appears that for the smallest periods a the coupling between the two levels arise in a region, above the BCB light line, when the PhC waveguides modes are no longer guided.

Last observation that can be made from these measurements is the surprising absence of the odd PhC waveguide TE slow mode, for which the hybrid structure was initially designed. Anyway, we can argue that the coupling, optimized at this point, strongly disturbs the PhC mode in this zone thus reducing the properties of non-linear effect enhancement by the odd TE slow mode. Then, mode competition with the even mode or the silicon wire slow mode that are less disturb, which are less coupled, turns out to be more favourable to these latter modes which gives laser operation.

7.1.3.4 Lasing operation

Both the modes discussed above show characteristics of lasing behaviour as attested by the S-shape of the curve [10]. In fig.7.9.a the emitted power is plotted against the pump power, for a $91\ \mu\text{m}$ long (200 periods a) PhC structure of period 455 nm. The transition from the spontaneous to the stimulated emission regime arises when the incident external pump power is greater than 0.4 mW (5 pJ at 80 MHz). This power does not take into account the limited absorption in the membrane or the effective area of pumping. Moreover, the behaviour of the resonance (fig.7.9 inset (c) and (d)) is another confirmation of lasing operation: as the pump

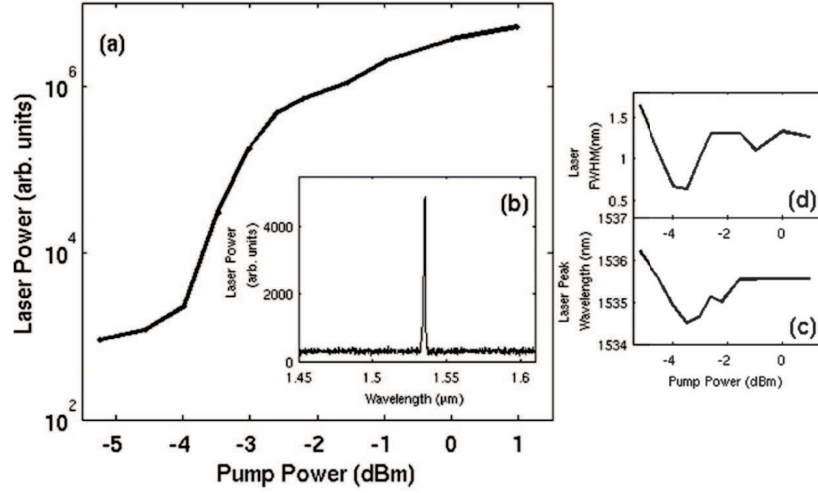


Figure 7.9: (a) Laser emission power captured by the Si wire as a function of the pump power in log-log scale. (b) Inset: laser spectrum at 1 mW pump power. (c) Laser peak wavelength as a function of pump power. (d) Laser FWHM as a function of pump power.

power is increased both the laser peak wavelength and the emission full width at half maximum (FWHM) initially decrease and then they increase attaining a constant value for higher pump power. This is an evidence of the carrier population clamping above laser threshold. The maximum output pulse energy coupled to the single mode fiber is 1.2 fJ (equivalent to 100 nW average power). Similar results are also obtained with shorter PhC waveguides (30 periods long).

This is the first demonstration of laser operation coupled to the silicon wire in our hybrid structure. This study allowed us to confirm the quality of our technological processing, and the method used for modelling. The agreement between numerical work and experiments validates the method used for modelling. The understanding gained from these early studies led to an improvement in the PhC waveguide design as will be shown in the coming section.

7.2 W0.65 photonic crystal waveguides

7.2.1 Modelling

In a second batch of devices, improvement of the PhC waveguide structures is achieved by acting on the width of the W1 photonic crystal waveguide used previously to make a so-called W0.65 waveguide. Indeed, by playing now on the defect itself, here on the width, it is possible to push the even mode outside the bandgap, avoiding, as a result, competition between different modes. We maintain the tri-

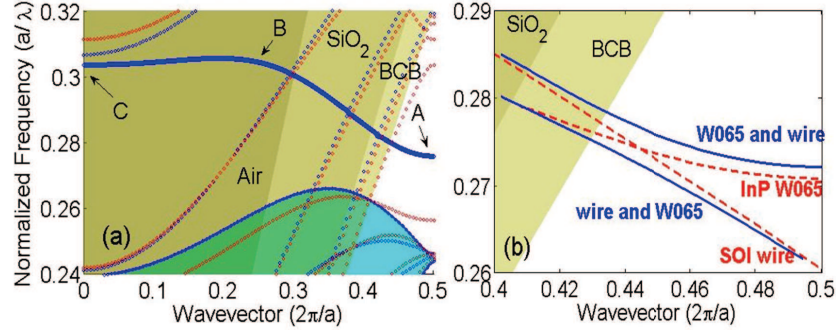


Figure 7.10: (a) Band structure calculated using guided mode expansion for the W0.65 PhC membrane with a BCB substrate and air upper cladding (with air holes). Laterally odd modes are shown in blue, even in red. The thick blue line corresponds to the odd TE-like defect mode. The odd TE-like band edge modes are shaded in cyan. The odd and even TM-like lattice modes are plotted as fainter dotted lines. Low-vg modes are denoted A, B, and C. The light cones of the various cladding materials, air, SiO₂, and BCB are denoted by progressively darker shading for lower index. (b) Dispersion relation of TE-like modes of the hybrid structure calculated using 3D FDTD for wavevectors around π/a . Both coupled super-modes (solid lines) and uncoupled modes (dashed lines) are represented.

angular lattice (period $a=455$ nm, $r/a=0.3$) and reduce the width w of the defect to $0.65\sqrt{3}a$. Using the same procedure as for the W1 waveguide we modelled the band diagram of the entire structure. The dispersion relation of this PhC waveguide is plotted in fig.7.10.a and shows the existence of a slow odd TE like mode. Moreover, as can be seen the structure is now clearly single mode. Note that three regions appears to be favorable for light emission enhancement. Indeed, points A, B and C, indicated in fig.7.10.a, correspond to flat zone in the dispersion of the waveguide mode. The coupling between the W0.65 and a 326 nm silicon waveguide below, embedded in a 400 nm thick BCB layer, appears clearly as attested by the splitting of the dispersion curves of the coupled system, visible on fig.7.10.b.

7.2.2 Experimental studies

7.2.2.1 Experimental setup

The samples were fabricated as in the previous work on W1 with a slightly different width of the defect.

The pump laser source used now is an optical parametric oscillator providing 100 fs long pulses at a repetition rate of 80 MHz. The wavelength of operation of the pump is set at $1.18 \mu\text{m}$ where silicon is transparent and where the InGaAsP QW barriers material are still absorbing. The choice of this wavelength allows to experiment on a new scheme of pumping since the silicon wire is now used for

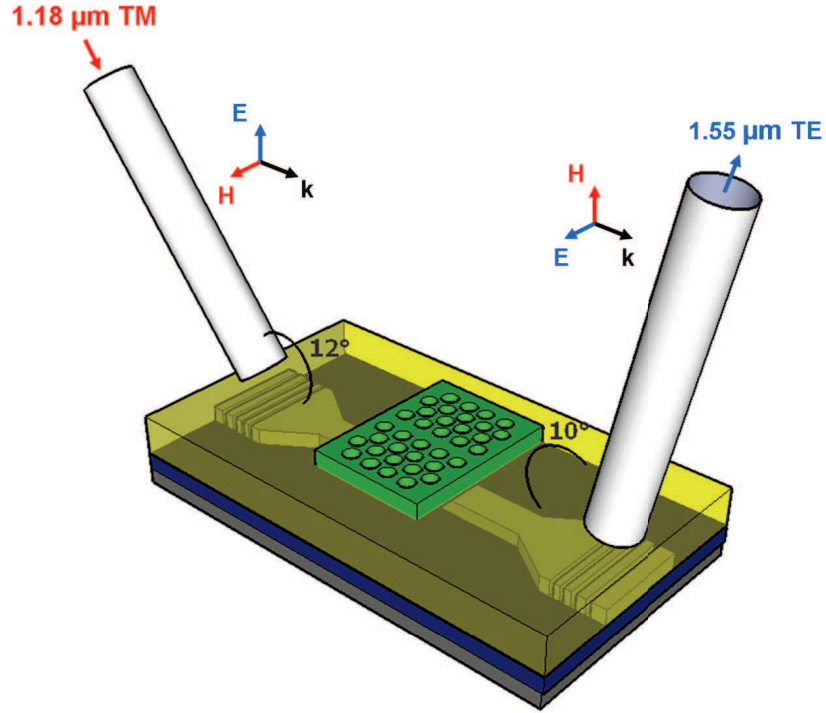


Figure 7.11: Experimental setup of the system pumped via the silicon wire. TM polarised (in the Si wire) pump pulse at $1.18 \mu\text{m}$ is injected on the left side from the 12° tilted fiber. TE polarised (in the Si wire) at $1.55 \mu\text{m}$ is extracted via the 10° tilted fiber on the right.

pump injection. Note that, even if the gratings couplers are originally optimized for operating at $1.55 \mu\text{m}$, it is possible to use TM-polarisation and set the angle between the fiber and the sample at 12 degrees to couple the pump at $1.18 \mu\text{m}$ into the TM mode of the SOI waveguides. When perfect alignment of the III-V PhC waveguide above the Si wire is assumed, which is not far from reality (30 nm), we calculate, using 3D FDTD, that 33% of the pump light is absorbed within $100 \mu\text{m}$. The emitted light is now measured only via the silicon wire keeping the fiber tilted at an angle of 10 degrees on the other grating optimal for $1.55 \mu\text{m}$ detection. A scheme of the experimental setup used in this specific case is depicted on fig.7.11.

7.2.2.2 Lasing operation

The PL is plotted in fig.7.12.a as a function of the normalized wavelength in order to bring out the clear correspondence between the three peaks, denoted *A*, *B* and *C* in fig.7.12 and fig.7.10, and the flat zones of the dispersion relation of the W0.65 PhC waveguide. As the pump power is increased, clear behaviour of laser

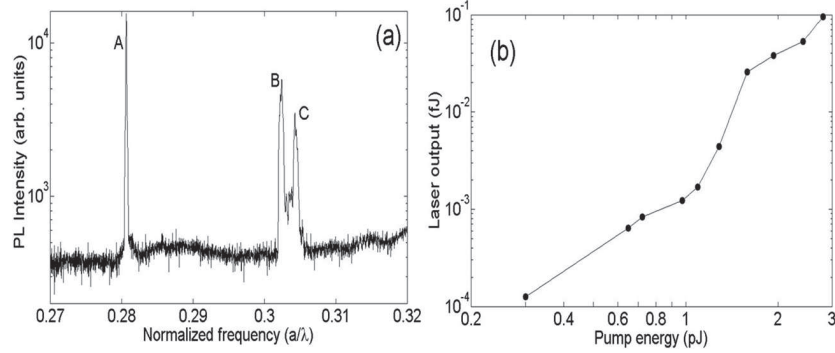


Figure 7.12: (a) PL spectrum of the hybrid structure. The three peaks, A, B, and C correspond to the low-vg modes of fig.7.10.a and fig.7.10.b Laser emission intensity observed in mode A vs pump pulse energy.

emission arises for the mode denoted A. This is comprehensible since this mode is located below the BCB line and is theoretically lossless while the two other modes above the BCB line are leaky. The typical "S-shape" of the emitted power against the pump power curve is plotted in fig.7.12. In this case the threshold is 1 pJ. Even though it is difficult to compare two different structures with different pumping methods, we can note that the threshold is this time 5 times lower than for the W1 case. Thus even if only a third of the pump power is absorbed, this decrease in threshold is partly due to a more efficient pumping scheme since the pump field is exactly directed towards the PhC waveguide. Moreover, in this case the entire length PhC waveguide is pumped, as a consequence the absorption is now reduced along the entire defect. Considering that having such a low group velocity mode in a PhC waveguide requires theoretically the interaction of an infinite sum of Bloch harmonics (see section 4.1.2), or diffraction on an infinity of holes, the consequence of bleaching all the defect is thus get closer, than in the state where only a fraction of the defect is pumped, to this ideal case. The study on the resonance wavelength and width against pump power, plotted respectively in fig.7.13.a and fig.7.13.b, attest to laser emission as argued before. The resonance blue shifts until laser emission occurs at which point that the carrier level gets clamped and the emission wavelength at a value of 1585.5 nm. At the same time the FWHM versus pump energy clearly shows a decrease of the linewidth from the spontaneous emission regime to laser emission where it attains a value of 0.7 nm. For higher pumping energies (2 pJ onwards) the emission linewidth broadens due to chirping arising from comparable carrier and photon lifetimes [11]. In this experiment, the maximum measured laser output pulse energy is approximately 1.7 pJ corresponding to an average power of 20 nW. Improvements of our design have been made, giving better results in terms of power coupling to the silicon wire. More-

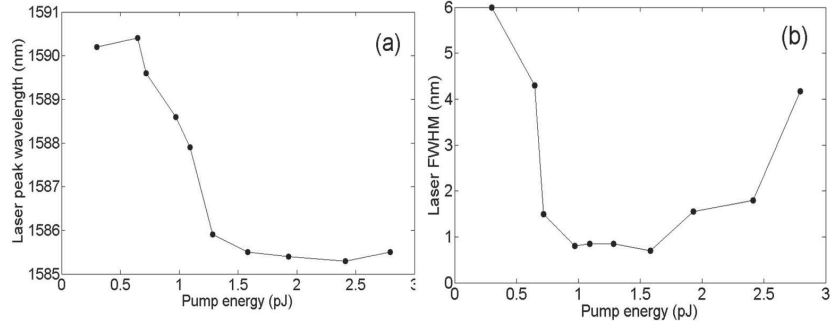


Figure 7.13: (a) Peak emission wavelength vs pump energy; (b) FWHM vs pump energy.

over, we also demonstrated that we can obtain improved performance such as the lowering of the threshold, using the silicon wire for pump injection. Furthermore, this scheme of pumping can be thought as an alternative to electrical pumping by using an external optical pump source coupled to the system to drive the device.

7.3 Conclusion

In conclusion, we demonstrated lasing operation coupled to the silicon wire for several designs. Moreover, these experimental results gave us a clear understanding of the two-level structure, gave a validation of the modelling method and of the processing technology, as the experimental results match very well the calculations. Therefore, placing this work in its context, these studies on photonic crystal waveguides were our first results and more than just giving us insights on our system behaviour it was an important proof of principle that these hybrid structures are good candidates for more advanced realisations. In terms of threshold and power coupled to the silicon wire, the system studied here fulfils, or is close to, requirements for further integration. It complied with one of the important milestones in the European project HISTORIC [12]. Furthermore, by pumping our sample through the silicon wire, we added a possible scheme for further integration taking advantage of the hybrid structure properties. This can be an interesting option to bypass to the difficulty to pump such type of PhC based structures electrically.

At this point of the work, there are still open questions and some device improvements are still to be done. Indeed, the strength of the coupling between the two levels was not experimentally extracted and lasing is a step to, but not yet, the ultimate goal, that is to say the control of an incoming light flux via an external action on the active III-V PhC layer. In order to answer to those questions and to achieve such a functionality we opted to switch to another design based on cavities as will be presented in the next chapter.

References

- [1] K. Sakoda. *Optical Properties of Photonic Crystals*. Springer-Verlag, Berlin, 2001.
- [2] N. Yokouchi T. Ide K. Kiyota, T. Kise and T. Baba. *Photonic-crystal slabs with a triangular lattice of triangular holes investigated using a guided-mode expansion method*. Appl. Phys. Lett., 88:201904, 2006.
- [3] A. Shinya J. Takahashi C. Takahashi M. Notomi, K. Yamada and I. Yokohama. *Extremely Large Group-Velocity Dispersion of Line-Defect Waveguides in Photonic Crystal Slabs*. Physical Review Letters, 87(25):253902, 2001.
- [4] C. Grillet P. Rojo-Romeo X. Letartre, C. Seassal, D. Cassagne P. Viktorovitch, M. Le Vassor dYerville, and C. Jouanin. *Group velocity and propagation losses measurement in a single-line photonic-crystal waveguide on InP membranes*. Applied Physics Letters, 79(15):2312–2314, 2001.
- [5] A. Yu. Petrov and M. Eich. *Zero dispersion at small group velocities in photonic crystal waveguides*. Applied Physics Letters, 85(21):4866–4868, 2004.
- [6] H. Benisty. *Modal analysis of optical guides with two-dimensional photonic band-gap boundaries*. J. Appl. Phys. 79 (10), 79(10):7483–7492, 1996.
- [7] T. P. White J. P. Hugonin, P. Lalanne and T. F. Krauss. *Coupling into slow-mode photonic crystal waveguides*. Optics Letters, 32-18, 2007.
- [8] C. Andreani and D. Gerace. *Photonic-crystal slabs with a triangular lattice of triangular holes investigated using a guided-mode expansion method*. Phys. Rev. B, 73:235114, 2006.
- [9] Kartik; Borselli Matthew; Painter-Oskar Barclay, Paul E; Srinivasan. *Efficient input and output fiber coupling to a photonic crystal waveguide*. Optics Letters, 29:697–699, 2004.
- [10] E. Kapon. *Semiconductor Lasers*. Academic, 1999.
- [11] C. Cojocaru P. Monnier J.A. Levenson A. M. Yacomotti, F. Raineri and R. Raj. *Nonadiabatic Dynamics of the Electromagnetic Field and Charge Carriers in High-Q Photonic Crystal Resonators*. Phys. Rev. Lett., 96:093901, 2006.
- [12] <http://www.ict-historic.eu>.

8

Wire cavity laser integrated on SOI

As a second design for the active level, we designed a PhC cavity which we will be referred to as “wire cavity”. This design, used already by several groups in the field of integrated optics, has proven to exhibit interesting properties, in terms of Q factor and small modal volume, on a relatively high index substrate. Indeed, this design has already been successfully implemented in silicon-on-insulator with good performance [1] [2]. To the best of our knowledge, this work was the first use of this design in an active device context. Simultaneously few other groups also came up with similar structures for different purposes [3] [4] [5]. By using an active material we gained access to more informations than in the passive case and we showed that this type of design is very promising in order to achieve complex functionalities with our hybrid structures.

8.1 Wire cavity : history and principle

The “wire cavity” design was proposed by Foresi in 1997 [6] and has since been improved by several groups [7]. This structure can be viewed as an extension of the standard Fabry-Perot resonator embedded in a wire waveguide. Indeed, looking at the scheme of the cavity, as drawn in fig.8.1, the mechanisms ensuring the electromagnetic field confinement appear to be very basic. Laterally, the confinement results from TIR due to index contrast between the “wire” and the surrounding materials, BCB below and air around. Longitudinally, two sets of several holes drilled in the waveguide, spaced by a distance L , acts as mirrors on each side to form a

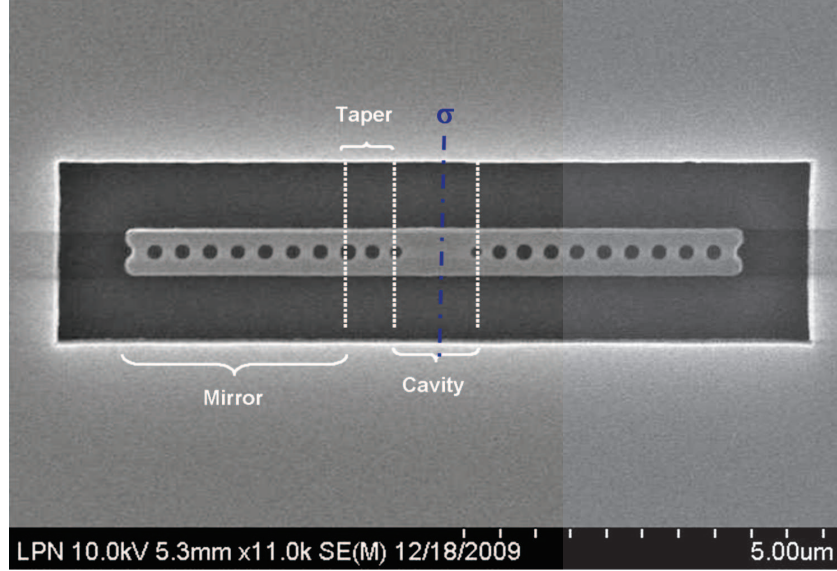


Figure 8.1: SEM image of the sample

cavity (fig.8.5) confining the field in the central unpatterned zone. The number of holes in the mirror has to be sufficient to ensure that, through the extension of the evanescent field in this direction, no light is lost at the end of the structure.

This type of cavity was shown to possess in its first design a Q factor around 600 [6] which is obviously not enough for our goal. Improvements made in the design of these cavities allow to reach theoretical values as high as 10^5 or 10^6 in silicon-on-insulator. This increase in Q factor is due to the addition of several tapering holes, of various diameter and period, between the undrilled zone of the wire and the mirrors (8.1). Indeed, the main loss in such a system arises from the fact that the mode of the cavity and the corresponding evanescent mode of the mirror have very different field profiles as depicted in fig.8.2.a. In other words, there is an “impedance” mismatch, defined in the following formula (η) [8], between these two modes. Therefore, it is impossible to transfer 100 percent of the wire mode to the evanescent mode of the mirror and vice-versa, the difference leading to out-of-plane loss.

$$\eta = \frac{\text{Re}\left\{\left[\int \int dxdy (\mathbf{E}_\omega \times \mathbf{H}_m^*) \mathbf{e}_z\right] \int \int dxdy (\mathbf{E}_m \times \mathbf{H}_\omega^*) \mathbf{e}_z\right\}}{\int \int dxdy (\mathbf{E}_\omega \times \mathbf{H}_\omega^*) \mathbf{e}_z} \left[\int \int dxdy (\mathbf{E}_m \times \mathbf{H}_m^*) \mathbf{e}_z \right] \quad (8.1)$$

In order to solve this problem a taper zone, consisting in few holes with varying radius and period, is inserted between the mirror and the cavity [9]. The

tapered holes are designed to minimize the modal mismatch between the propagating guided mode and the evanescent mirror mode, by adiabatically converting the incident mode, and thereby decreasing the losses at the cavity-mirror interface. Furthermore, modelling the structure showed that the reachable Q factor converges to a certain value with increasing number of holes in the mirror, as also discussed in [10]. In the cavity designed in this work we will limit the mirror to 7 holes as it gives Q factors above 10^4 at 1550 nm.

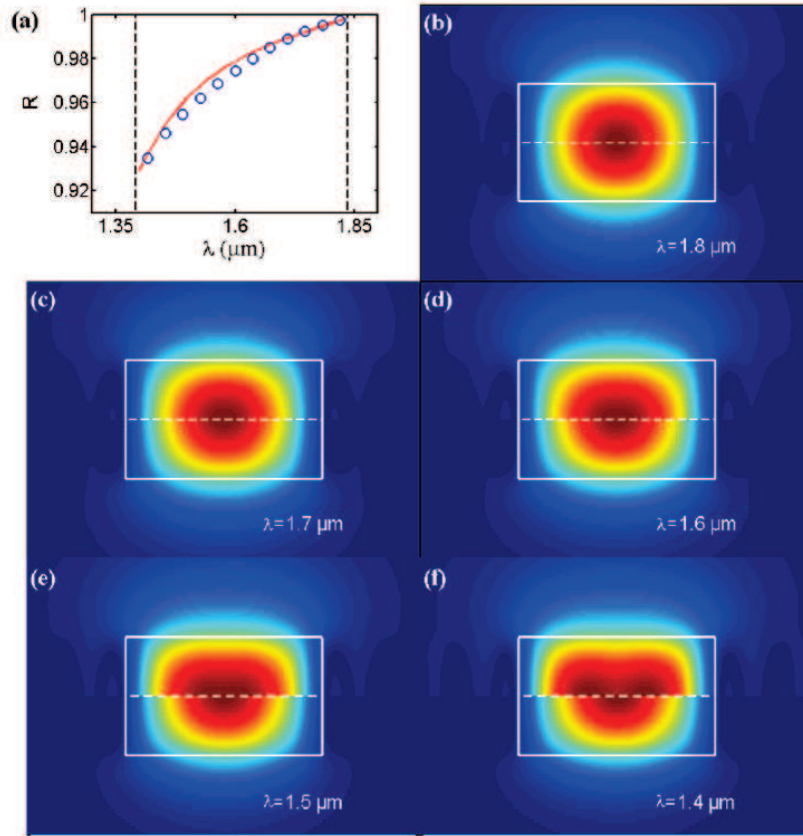


Figure 8.2: (c)-(f) Different vertical profiles of the magnetic field for different ratio a/λ in the upper part the Bloch mode of the mirror and in the lower part the fundamental mode of the wire surrounded by air ($n = 3.48$, width = 420 nm and height = 230 nm). From [11]

8.2 Adaptation of an existing design

We used as a starting point a design which has proven to provide high Q factor and small modal volume in SOI systems [10]. Then, we used the scaling properties of Maxwell's equations to find the correct parameters for our structure. Scaling of Maxwell's equations, for the \mathbf{H} field (eq.4.5), are driven by the following rules :

1- A change of variable of the spatial distribution of the dielectric constant, $\epsilon'(\mathbf{r}) = \epsilon(\mathbf{r}/s)$, where s is a scaling parameter, via the spatial changes $\mathbf{r}' = \mathbf{r}s$ and $\nabla' = \nabla/s$

$$\nabla' \times \left(\frac{1}{\epsilon'(\mathbf{r}')} \nabla' \times H(\mathbf{r}'/s) \right) = \frac{\omega^2}{(cs)^2} \mathbf{H}(\mathbf{r}'/s) \quad (8.2)$$

leads to a resulting change of the mode profile $\mathbf{H}'(\mathbf{r}') = \mathbf{H}(\mathbf{r}/s)$ and eigen-values $\omega' = \omega/s$.

2- In the same way changing the value of the index following the scaling $\epsilon'(\mathbf{r}) = \epsilon(\mathbf{r})/s^2$:

$$\nabla \times \left(\frac{1}{\epsilon'(\mathbf{r})} \nabla \times H(\mathbf{r}) \right) = \frac{(s\omega)^2}{c^2} \mathbf{H}(\mathbf{r}) \quad (8.3)$$

leave the harmonic modes unchanged but all the eigenfrequencies are multiplied by a factor s , $\omega' = s\omega$.

Practically, using the two precedent rules, we modelled using 3D FDTD an existing high Q design on SOI, resonant at $\omega=1550$ nm and incorporated our refractive index values, ie. that of the InP/QW membrane and the underlying BCB. As a consequence, the resonant wavelength ω' of the system, is changed as expected by the scaling concerning the index values change (eq.8.3). Consequently, in a second step, we apply the first rule of spatial scaling of the index profile (eq.8.2), using the ratio ω'/ω , similar to the ratio of the effective index, to extract a scaling parameter.

Note that the scaling was not perfect. Indeed, the change of index does not follow the same scaling rule for all materials involved but the difference remains small enough not to impact strongly on the results on the effective index change ($n_{Si}/n_{InP} = 3.48/3.3 = 1.05$, $n_{SiO_2}/n_{BCB} = 1.45/1.54 = 0.94$ and n_{air} scaling equals 1 at 1550 nm). The same is true for the spatial scaling since few parameters, such as the thickness of the InP/QW layer or the width of the wire were imposed. The InP width was fixed by phase matching criteria (see chapter 2.3) with a 500 nm width silicon wire embedded in BCB (see section 8.4). Thus, the scaling procedure followed for these first modelling steps is an approximation. But, it has been shown [11] than the predominant parameter is the band gap position of the mirror, the tapering being relatively robust. Therefore, in addition, to balance the approximations made above and to ensure a cavity with high Q, a careful play on the holes size and period in the mirror was performed in order to that obtain the largest bandgap centred at the desired value and therefore the strongest

confinement, keeping the ratio between the taper holes and the mirror parameters constant. Acting on two parameters, the period a and the radius of the holes r , we place the maximum of the mirror reflectivity at the desired wavelength. The evolution of the band structure against one of these parameters can be foreseen on fig.8.3 where various band structures of a 500 nm wide SOI wire are plotted. For a given period, as the holes radius r is increase the gap bandwidth becomes wider and wider. At the same time, the valence and conduction band are moved to higher frequencies because their respective effective index is lowered, simply because the fraction of the lower index material becomes more and more important (fig.8.3). A similar behaviour is seen for a period change (not shown here) for a given size of holes, increasing the period goes with a closing and a shifting of the gap to lower frequency, asymptotically this change converge to a structure were the relative impact on the dispersion curve becomes smaller and smaller.

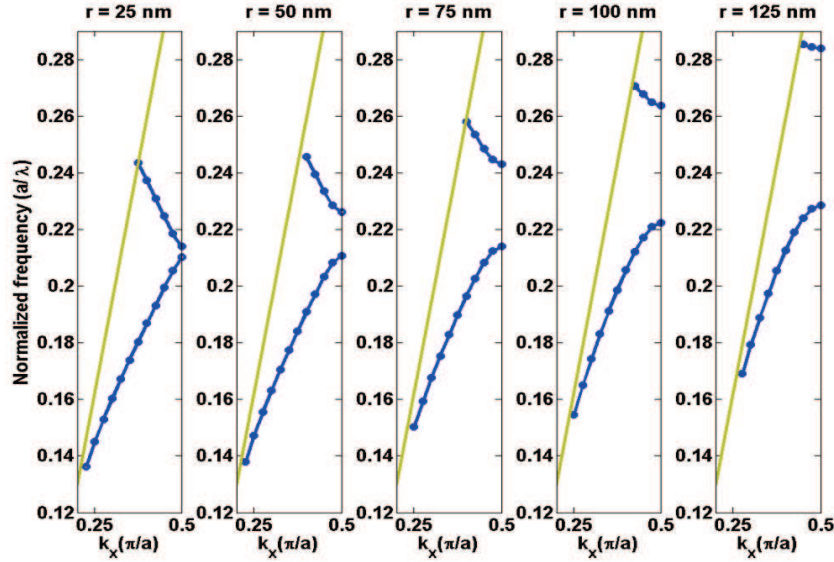


Figure 8.3: Evolution of the band structure against various holes radius and a fixed period of 315 nm in a 500 nm wide SOI wire. The yellow line represents the light line.

Thus, by playing on these two parameters, we aligned the center of the mirror's high reflectivity response with the wavelength ($\lambda = 1.55\mu m$) where maximum gain is expected from our active layer. As a summary of the whole modelling first steps, on fig.8.4 are plotted the different band structures for each periodic pattern involved and the InP wire dispersion. The main features that can be extracted from these modelling results is, first, the fact that the first hole of the taper (black squares) gives a valence band edge mode close to 1.55 microns, thereby the critical impedance mismatch between the wire mode profile and the Bloch-mode profile

of the first taper hole is drastically decreased. Secondly, the bandgap of the mirror (blue circle) appears to be almost centred around 1.5 microns, this configuration gives the highest reflectivity, located closer to the valence band, at 1.55 microns.

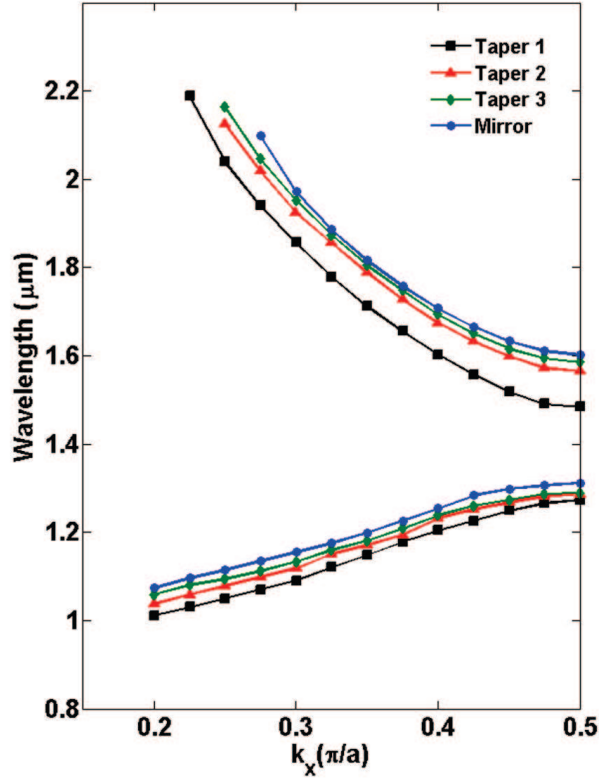


Figure 8.4: Band structure for every “pattern” of the cavity. The three first taper zones (black square- red triangles - green rhombus) and mirror (blue circles) respectively r equal to 69.5, 85.5, 99 and 97 nm and period a equal to 320, 337, 347 and 376.5 nm.

The scaling rules of Maxwell equations allowed to obtain rapidly a first set of parameters for our structures. These parameters were then refined by calculating the band structure of the mirror. As will be shown in the next section, we managed to obtain relatively high Q cavities, of the order of the previous works in silicon and close to those reported in papers on similar systems.

8.3 InP based wire cavity on silicon substrate

In order to get an insight into the physical properties of this type of structures and to check if they are suitable for further work, such as integration on silicon waveguide circuits, we decided to first study these cavities on an un-patterned silicon substrate. In this section, modelling and experimental results will be confronted. The cavities under investigation in this first characterization experiments are made in a 550 nm wide 255 nm thick InP strip waveguide incorporating four InGaAs/InGaAsP quantum wells (QWs) bonded on a silicon substrate via a 1 μm thick intermediate BCB layer. Since, vertically, the amplitude of the field decays rapidly and can be considered as null after 500 nm in the bonding layer we do not expect any disturbance from the presence of the silicon substrate below (see also fig.8.18). The distance between the two sets of holes drilled on each side of the cavity, 8 mirror and 3 taper holes, is varied in order to explore the behaviour of our system under variation of the length L (distance between the center of the left and right first holes). One way to scan the wavelength in our structure is, in the same way it is done in a standard Fabry-Perot resonator, to vary the length of the cavity. The resonant wavelength is fixed by $m\lambda_{\text{resonance}} = 2n_{\text{eff}}L_{\text{eff}}$ where m is an integer, where n_{eff} and L_{eff} are the effective index and length. These parameters take into account the modal dispersion and the effective round trip. In such a cavity, the resonance wavelength is fixed by several parameters : the length of the cavity (ie. the distance between the two first holes), the effective index of the mode confined in the wire and the phase change induced by the mirror reflection. Taking into account several factors such as wavelength, Q factors, mode matching and reflectivity, from the simulations we arrived at the following optimal parameters : for the periodic section of the mirror zone, a period of 376 nm and a hole radius of 97 nm; for the tapered-hole section of the mirror we space the holes by 347, 337, and 320 nm and decrease their radii to 99, 85.5, and 69 nm, respectively. Note that we chose here to use 8 holes for the mirror as no increase of the Q factor was observed for more holes.

8.3.1 Numerical studies

We first calculate, as a function of the cavity length L , using 3D FDTD, four essential parameters : the resonant wavelengths, the Q factor, the modal volume, and the confinement factor. Fig.8.5 shows the typical field profile for symmetric and anti-symmetric modes in the cavity.

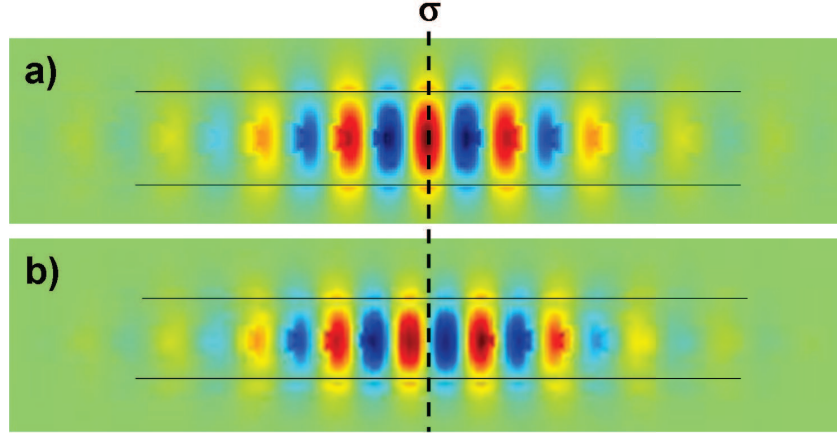


Figure 8.5: Top view of the E_y field for the second order (a) symmetric mode and anti-symmetric mode (b). The thick dotted line denotes the symmetry axis (σ_x) taken for the cavity mode.

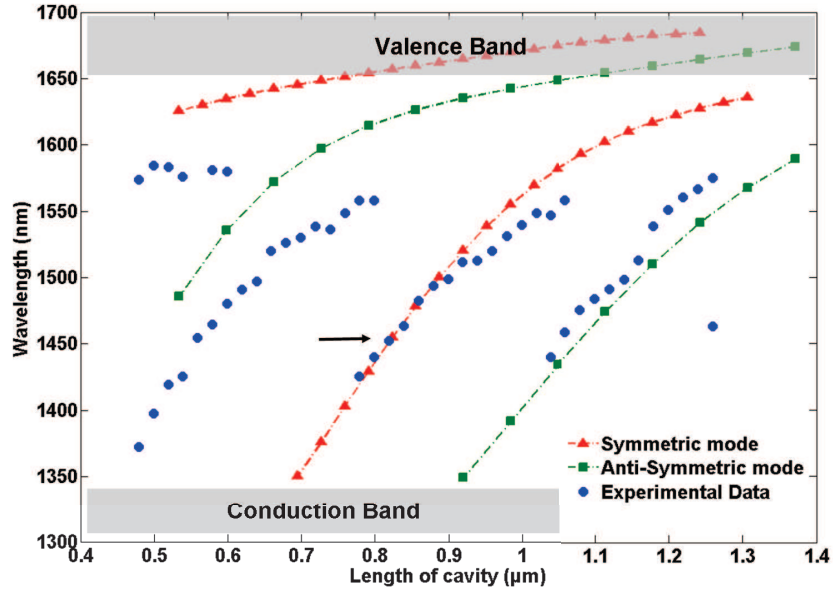


Figure 8.6: Resonance wavelength plotted against cavity length. 3D FDTD simulation results are joined by dashed lines, and the dots show the corresponding experimental measurements. Arrow points to the second order symmetric mode.

8.3.1.1 Wavelength behaviour

The resonant wavelengths are plotted in fig.8.6 against the cavity length. Two orders of the Fabry-Perot (FP) for the symmetric (triangles) and antisymmetric

(squares) longitudinal modes are represented (see the symmetry axis shown in fig.8.5). Few simple observations can be made from this curve. First, as expected, resonant modes are only present in the high reflectivity bandgap of the mirror, ie. between the valence and conduction band deduced from modelling of the mirror band structure (plotted on fig.8.4). Modes that are still visible in the valence band correspond to very low Q factor as will be seen later (see fig.8.9). Secondly, as the length of the cavity L is increased, the standard FP resonator behaviour is observed below 1600 nm and the resonant wavelength of the cavity red shifts steeply and linearly. Above 1600 nm, this “dispersion” curve ($d\lambda/dL$) shows a decreased slope close to the valence band. Noting that the length of the undrilled zone is too short to really introduce a strong wavelength dependence, we attribute this effect to be mostly due to the wavelength dependent variation into the system taper/mirror, in other words the frequency dispersion induced by the propagation in the InP wire is not sensitive for small cavities in regards to the dispersion induced in the taper and mirror. Indeed, the imaginary part, associated with the penetration depth, of the evanescent modes decreases going from the center of the gap to the band edge, where the dispersion curve becomes flat, either for the evanescent modes or the guided modes. As a consequence the effective length L_{eff} increases, as the penetration depth in the mirror increases, and the dispersion induced becomes more and more important as we are close to the band edge, this effect can be foreseen on fig.8.7, especially for lower frequency. On this figure are reported the resonant wavelengths against the length of a wire cavity with (green dots) or without (blue squares) the tapering zone. Note that 2D simulations show that the taper to strongly increase this inflexion as can be seen on fig.8.7. Also, it is striking that the taper induce a strong “dispersion” at the edge, this can be attributed to the fact that at these wavelength the highly dispersive bandedge modes are excited.

A view of the field (corresponding to the symmetric modes) at different wavelengths summarises and depicts the explanations given above. First, the intensity profile corresponding to the cavity with the highest Q (fig.8.9) is represented in fig.8.8.b. By comparison, for shorter wavelengths, the field fig.8.8.a) extension in the mirror remains small but the intensity in the cavity is relatively low. In this frequency range the field is much less confined and conduction band evanescent modes are excited. As a consequence, the intense part of the field is located in air, characterised by increased losses. Getting closer to the valence band edge of the mirrors, where the gradient becomes gradually shallower (small $d\lambda/dL$) and varying the length has little effect on the wavelength, the field is weakly confined in the defect and leaks through the mirrors (see fig.8.8.c) and the relatively high intensity in the taper can be attributed to the excitation of band edge modes of the tapering holes, and the related increase of the local field intensity.

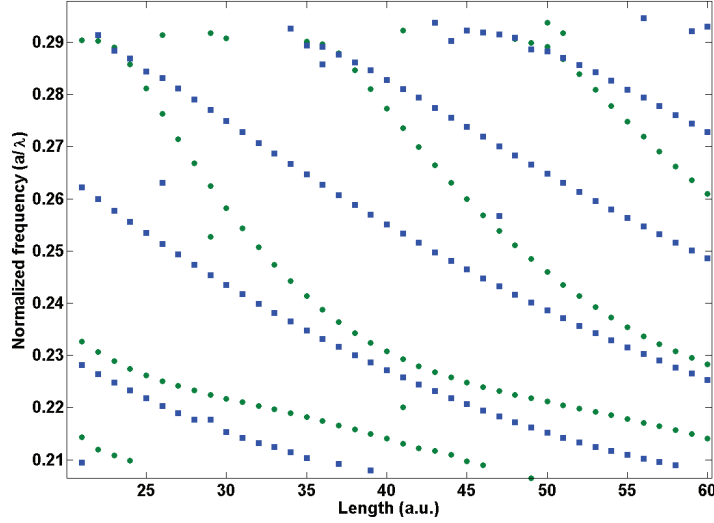


Figure 8.7: Modelling of 2D wire cavities with (green dots) and without (blue squares) taper inserted. The mirror parameters are : period $a=0.376$ nm and holes radius $r=0.098$ nm.

8.3.1.2 Q factor against wavelength

Regarding the Q factor, we plot in fig.8.9 the simulated Q values versus the cavity length corresponding to the symmetric mode (circles), indicated by the arrow in fig.8.6. It is seen, for the second order symmetric mode, that Q attains, in our system, a maximum of 1.3×10^4 for a cavity length of $1 \mu m$, giving a resonance at 1556 nm. We expect that the maximum Q factor is reached when the tapered mirror reflectivity is maximum. As indicated in [7] this is found at wavelengths where the best modal matching between the cavity and the mirror modes is obtained thanks to the tapered zone, thereby fixing the cavity lengths that give the best Q factor. Starting from shorter wavelengths, the Q -curve shows a smooth rise, following the increasing imaginary part of the system “mirror + taper” (the imaginary part discussed here is related to the penetration depth in the mirror or the reflectivity strength of the band gap), whereas it falls off rather abruptly for longer wavelengths, because of the decreasing reflectivity of the system “mirror+taper”. The fact that the wavelength associated with the highest Q cavity mode is closer to the valence band edge of the mirrors, as can be seen in fig.8.6, is understood by the fact that there is a trade off between the two mechanisms described above (confinement and reflectivity in the gap). Indeed, PhCs slab are known to give better cavities close to the valence band where the mode is confined in the material,

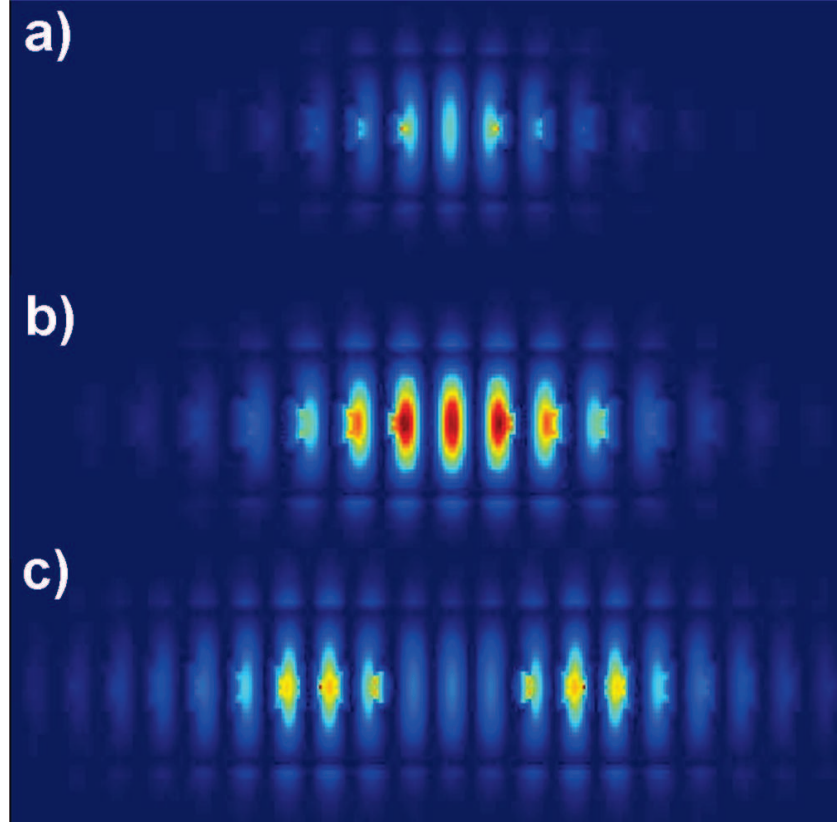


Figure 8.8: Field profile of cavity modes for different wavelengths - a) $\lambda = 1500 \text{ nm}$, b) $\lambda = 1550 \text{ nm}$, c) $\lambda = 1630 \text{ nm}$.

in analogy with an acceptor defect located close to the valence band in semiconductors [12]. This reason also explains the asymmetry of the curve. To go a little bit further on the study of the Q factor several comments can be added. First, one can see that anti-symmetric modes give higher Q factors than the symmetric ones (red triangles in fig.8.9). This is explained by the fact that this anti-symmetric configuration gives rise to interferences between the vertical radiation of different poles of the mode, decreasing thereby the radiated field intensity [13]. As can be seen on fig.8.10 the anti-symmetry leads to a configuration where poles radiation in the vertical direction interferes destructively. Secondly, modelling showed that while the length of the cavity is increased the maximum Q factor increase almost linearly, this can be understood by the fact that most of the losses are located at the mirror interface. Thereby increasing the length of a low-loss zone, which is the undrilled wire part, leads to an increase in the photon life time in the cavity.

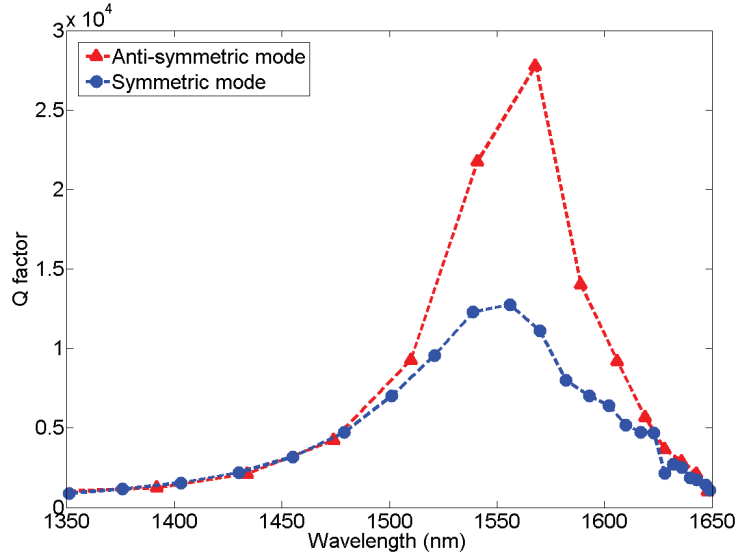


Figure 8.9: Q factor extracted from the 3D FDTD simulations as a function of the resonance wavelength - blue circles correspond to the symmetric mode indicated by an arrow in fig.8.6 and red triangles to the anti-symmetric mode of a higher order.

These last observations open up questions concerning the ratio Q/V , essential parameters impacting non-linear effects, threshold and intensity. For example, the Q of the anti-symmetric mode is 2 times higher than the symmetric one, but at the same time the length of the cavities are also related by a factor two in favour of the symmetric case, thus giving an equal ratio. Adding to this, longer cavities gives rise to multi-modal behaviour, so we decided to focus on the symmetric mode.

8.3.1.3 Modal volume and confinement factor

So, we calculate the modal volume, defined in eq.8.4, of the cavities using 3D FDTD [14].

$$V = \frac{\int \epsilon(\mathbf{r}) |\mathbf{E}(\mathbf{r})|^2 d^3\mathbf{r}}{\text{Max}[\epsilon(\mathbf{r}) |\mathbf{E}(\mathbf{r})|^2]} \quad (8.4)$$

The result are plotted as a function of the resonant wavelength in fig.8.11 (dots). We obtained modal volumes ranging from 0.38 to $0.92(\lambda/n)^3$ for cavity lengths of $0.7 \mu\text{m}$ ($\lambda=1351 \text{ nm}$) to $1.3 \mu\text{m}$ ($\lambda=1636 \text{ nm}$). The volume increases rapidly with the length and the wavelength, up to an L value of $1.05 \mu\text{m}$ and is then almost constant for longer cavities. As from the “dispersion” plotted in fig.8.6 two regimes are visible. The first slope is attributed to the fact that moving from the conduction band to the valence band (respectively lower and higher wavelengths)

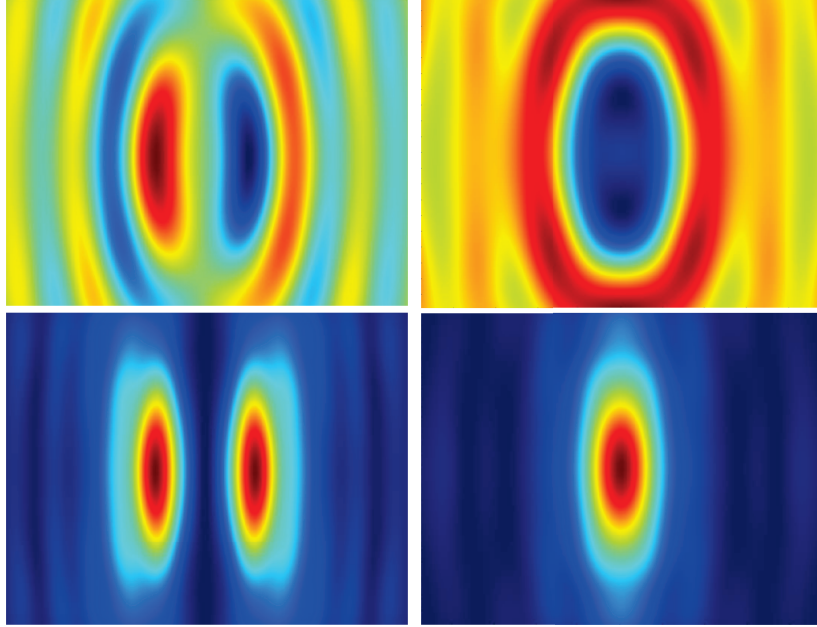


Figure 8.10: Far field (top) and far field intensity (bottom) profiles for the symmetric (right) and anti-symmetric (left) modes. Note that the intensity scaling of the symmetric mode is 4 order of magnitude higher than the one used for the anti-symmetric mode.

the field becomes more and more localised in the high index material but the impact of this effect decreases as the mode gets closer to the valence band. Finally, we calculate the confinement factor, Γ which is defined as the ratio of the electric field energy density confined in the semiconductor active material (here the four InGaAs QWs) to the total electric field energy density stored in the mode. This parameter is important when laser emission is considered, since only the field overlapping the active material is amplified. As seen in fig.8.11 (squares), Γ varies from 0.243 to 0.252, meaning that only a variation of 3 percent is obtained for the whole set of cavities. A trade off between these two parameters and the Q factor will determine the optimal operation point for laser action.

8.3.2 Experimental study

We then explore the fabricated samples, with a length ranging from 465 to 1465 nm in steps of 25 nm in order to obtain resonances over the full range of the QW gain. These measurements were done at room temperature by measuring the photoluminescence spectra under optical pumping. The samples are surface pumped using a $50\times$ IR long working distance objective which focuses the pump

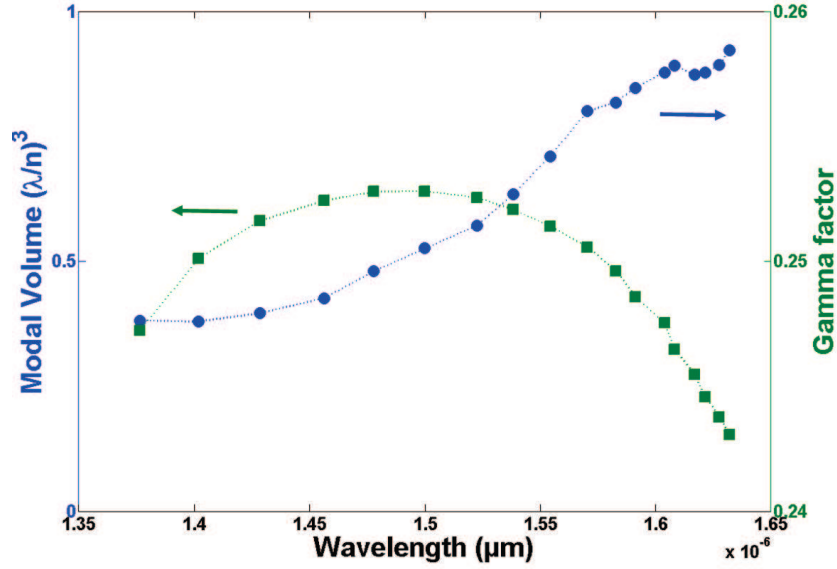


Figure 8.11: Modal volume and confinement factor as functions of the resonance wavelength.

light down to a spot size around $1.5 \mu m$. The laser source for the pump is a diode laser at 808 nm modulated to produce 10 ns pulses at 333 kHz repetition rate. These characteristics are chosen so as to reduce device heating.

For each cavity, the wavelength of the peaks observed in the PL spectra are plotted in fig.8.6 with dots, as a function of the cavity length. Resonances are observed over the entire QW gain bandwidth, i.e., from 1373 to 1575 nm. The experimental measurements agree very well with the simulated predictions. We see that for cavities with lengths between 0.78 and $1.05 \mu m$ the experimental results closely follow the $d\lambda/dL$ trend from simulations. For longer cavities, the resonant wavelengths also follow the simulated cavity mode dispersion closely. For very short cavities, however, there is a shift which is expected to be induced by slight changes in the radii of the holes or undrilled zone due to electron beam lithography proximity effects, which are stronger when the two mirrors are closer.

Furthermore, laser operation is obtained over a wide range of wavelengths with a threshold ranging from 1 mW to 7.8 mW external peak power, ie. total input power incident upon the sample. Note that we estimate the factor to apply in order to obtain the effective threshold to be around 0.01, indeed just considering the ratio of the estimated pump spot size against the cavity surface gives is a factor 24, in addition the absorption of our active layer at 800 nm is estimated to be around 30%. As an example of laser operation, we plot in fig.8.12 the variation of the

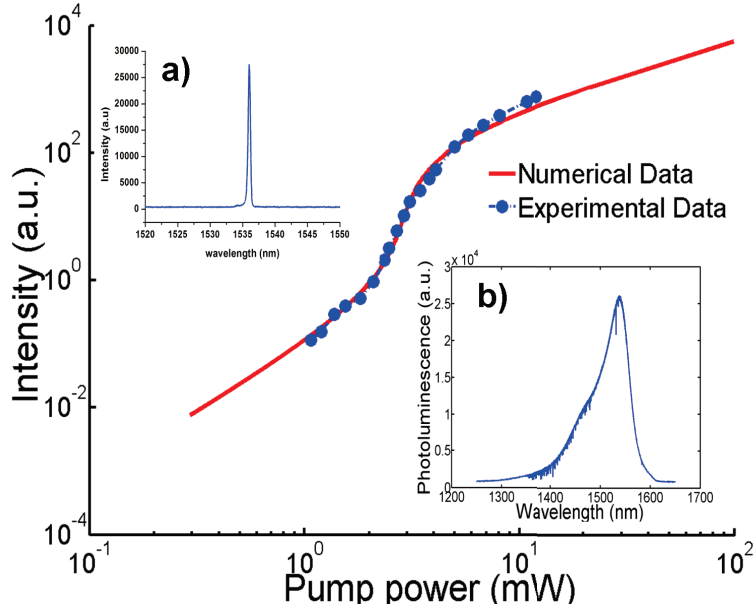


Figure 8.12: Measured threshold and corresponding fit of rate equations versus pump power. (a) Spectrum under lasing operation. (b) PL spectrum of the QWs.

emitted power (circles) as a function of the pump peak power on a log-log scale for one cavity (cavity length=920 nm, 1535 nm lasing wavelength). We observe the typical S-shape, illustrating the transition from spontaneous emission to stimulated emission [15], at 3.4 mW of peak pump power. These measurements are performed for each of the cavities, corresponding to the second order longitudinally symmetric modes (left arrow in fig.8.6), in order to deduce their respective thresholds. Then, a quantitative study of the many S-curves obtained is performed by solving the standard rate equations for QW lasers :

$$\frac{dS}{dt} = -\frac{S}{\tau_p} + \Gamma v_g g(N)S + \Gamma \beta B N^2 \quad (8.5)$$

$$\frac{dN}{dt} = -\frac{N}{\tau_{nr}} - B N^2 - v_g g(N)S + R \quad (8.6)$$

where S represent the photon density, N the carrier density in the quantum wells (per unit volume), τ_p is the photon lifetime, Γ is the optical confinement factor which takes into account the overlap of the mode field with the active region, v_g is the group velocity, $g(N) = \sigma(N - N_{tr})$ is the gain in the linear gain model with N_{tr} the carrier density at transparency and $\sigma = dg/dN$ the differential gain, β is the spontaneous emission factor, B is the radiative recombination coefficient

in the resonator, τ_{nr} is the non-radiative carrier recombination lifetime and R is the pumping rate. In order to ensure a better convergence of the numerical solution we preferred the following normalized equations [16]:

$$\frac{ds}{dt} = \frac{1}{\tau_p} [-s + (n - n_{tr}s + \gamma_{sp}n^2)] \quad (8.7)$$

$$\frac{dn}{dt} = \frac{1}{\tau_{nr}} \left[-n - \frac{n^2}{\bar{\tau}_{rad}} - (n - n_{tr})s + \frac{R(t)}{R_{th}}(1 + n_{tr}) \right] \quad (8.8)$$

where $n = \Gamma v_g \sigma \tau_p N$, $n_{tr} = \Gamma v_g \tau_p N_{tr}$, $s = v_g \sigma \tau_{nr} S$, $\bar{\tau}_{rad} = \tau_{rad}/\tau_{nr}$, $\gamma_{sp} = \beta \tau_{nr}/\tau_{rad}$. We use the known values [17] [18] for the differential gain ($3 \times 10^{-16} \text{ cm}^{-2}$), confinement factor (0.25), carrier density at transparency ($2 \times 10^{18} \text{ cm}^{-3}$), carrier lifetime (200 ps), and the group velocity ($10^{10} \text{ cm s}^{-1}$). Then the S-curves are fitted by varying the photon lifetime τ_p and the fraction of the spontaneous emission rate captured by the laser mode, β , which are different for each cavity. From the fits we extract the thresholds (see fig.8.13) using the condition that at the threshold for laser emission the photon density is equal to 1 [19]. Thus, it is seen that the laser threshold diminishes slowly as the cavity emission shifts from 1437 nm (cavity length=0.8 μm) up to 1515 nm (cavity length of 0.94 μm), hitting a minimum threshold peak power of 1 mW. Then, as the cavity mode goes beyond 1539 nm (cavity length $\geq 1 \mu\text{m}$), the threshold increase sharply.

In order to establish a relationship between the Q factor and the optimal operation of these lasers, the photon lifetimes obtained from the rate equation fit are compared to the Q factors obtained by modelling ($Q = \tau_p \omega/2$). These Q values are plotted in fig.8.14, showing that whereas the calculated Q factors reach a maximum value of 1.3×10^4 , the experimental values peak at 8×10^3 . The two data sets correspond very well, with the slightly lower values obtained in the experiment, which can be attributed to roughness scattering loss due to side-wall roughness in the holes and the walls of the wire structure.

So, in conclusion, we have demonstrated lasing operation with a fairly low threshold of InP-based wire cavity structures on a silicon substrate over a wavelength range from 1437 to 1565 nm. The influence of the cavity length upon the resonant wavelength, the impact of the Q factor, the modal volume and the confinement factor was meticulously analysed both numerically and experimentally. Our results show that an optimal value for the cavity length can be found to obtain the lowest laser threshold. Moreover, the close correspondence between the experimental measurements and the numerical calculations illustrates the quality, the accuracy of the technological processing and the robustness of the wire cavity design. These results are a clear proof that III-V wire cavities are excellent candidates for ultracompact (μm^2 scale footprint) building blocks in active nanophotonics on silicon, as it is possible to obtain high Q factors in such a substrate based hybrid

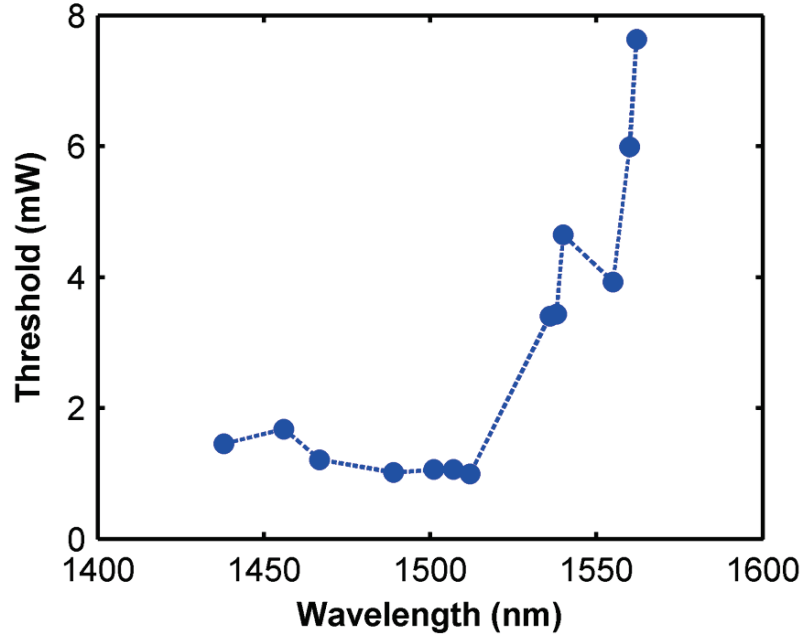


Figure 8.13: Threshold of the studied cavities plotted as a function of the emission wavelength.

system possessing both mechanical and thermal stability.

8.4 Wire cavity coupled to a silicon wire

With the experience gained from studies on wire cavities on top of an unpatterned silicon substrate we can go further and implement the wire cavities on top of a silicon waveguide circuit as depicted on fig.8.15. Analogous to chapter 7, modelling was carried out in order to obtain efficient coupling between the wire cavity and the underlying silicon waveguide.

8.4.1 Modelling of the hybrid system

The two main parameters to deduce from modelling were the optimal thickness of the intermediate BCB layer and the width of the InP wire which gives phase matching with the underlying silicon wire.

First, the width of the InP wire was chosen to ensure phase matching with the

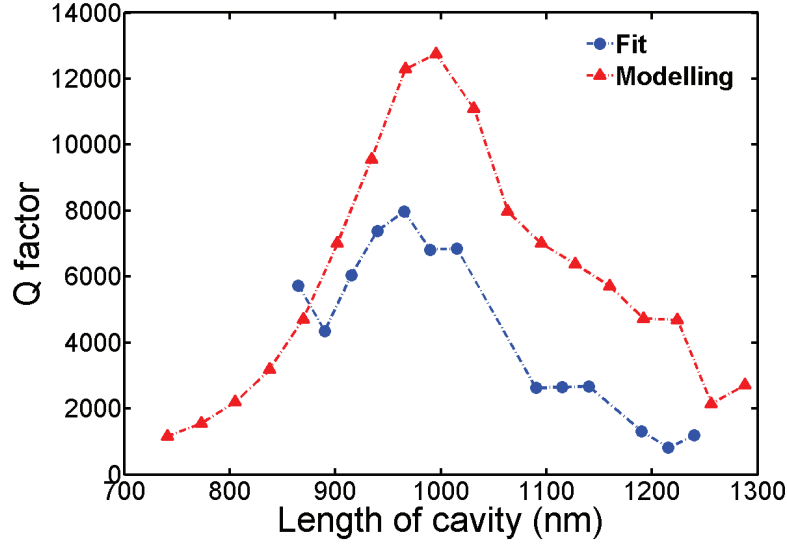


Figure 8.14: Experimental Q factors and modelled Q factors as functions of cavity length.

500 nm wide silicon wire below. In order to arrive at an optimal width we extracted the effective index of the guided mode at 1550 nm for several widths of the InP wire on BCB, using an analytical mode solver integrated in “Lumerical”. The results are shown on fig.8.16 (red dotted line). As can be seen, the effective index varies from 2.3 to 2.6 as the width varies from 440 nm to 680 nm. In addition we indicate the effective index of a 500×220 nm silicon wire mode embedded in BCB at 1550 nm in the figure. Since the silicon wire width is fixed, the corresponding index of the silicon guided mode is represented as an horizontal line (black dotted). From these results, we expect phase matching to occurs, at 1550 nm, for an InP wire width of 550 nm, with a BCB thickness around 460 nm. To check for the validity of this assessment we perform complementary modelling on the coupled system, ie. an InP wire separated from the 500 nm wide SOI wire by a 465 nm high layer of BCB. The index of two first order modes are plotted on fig.8.16. A clear anti-crossing between the dispersion curves of the respective modes is observed at the expected width of 550 nm. This mode splitting is an evidence of coupling.

8.4.1.1 Mode profiles

Indeed, completing the discussion opened in section 2.4, the two first order modes of the coupled system correspond to the symmetric and anti-symmetric solutions. Thus, at the crossing point, modes of the coupled system are located in both wave-

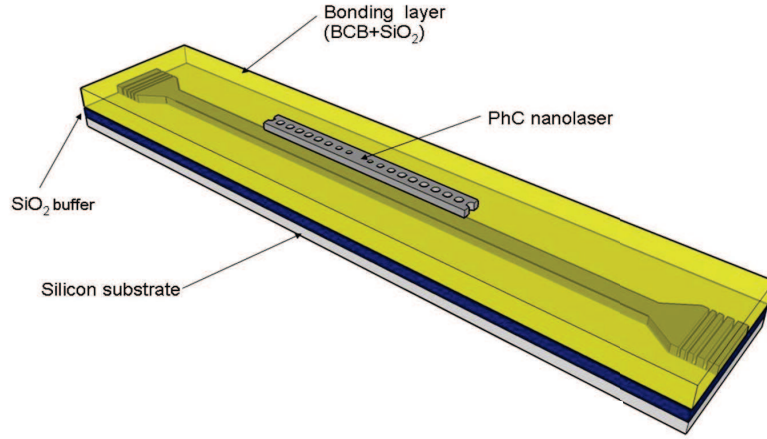


Figure 8.15: Scheme of the hybrid system: III-V semiconductor wire cavity bonded on top of a SOI wire. Gratings at the extremity of the 6 mm long silicon wire, allows extraction or injection of light via coupling to a single mode fiber.

uities, as can be seen on the mode profiles (see fig.8.17.c and d) corresponding to points **C** and **D** in fig.8.16. Moreover, the distinction between the symmetric and anti-symmetric mode can be made by looking at the phase in each waveguide. Note that, each dispersion curve converges, far from phase matching, to the respective unperturbed waveguide modes, which is confirmed by the profile pictures a),b),e) and f) of fig.8.17 which correspond respectively to points **A,B** and **E,F** on fig.8.16. These results show that phase matching, in the present system, remains effective under an index interval of 0.05 around the optimum value, corresponding to a wavelength interval of 60 nm.

8.4.1.2 Coupling strength and length of coupling

Furthermore, we can extract more information from the modelling (ref. section 2.4), valid in the case where the self-coupling coefficients are neglected. Indeed, comparing the effective indices of the uncoupled waveguides (Θ in the inset of fig.8.16), it is possible to deduce an approximated value of the dephasing δ via the formula :

$$\delta = \frac{\beta_1 - \beta_2}{2} = \frac{2\pi\Theta}{\lambda} \quad (8.9)$$

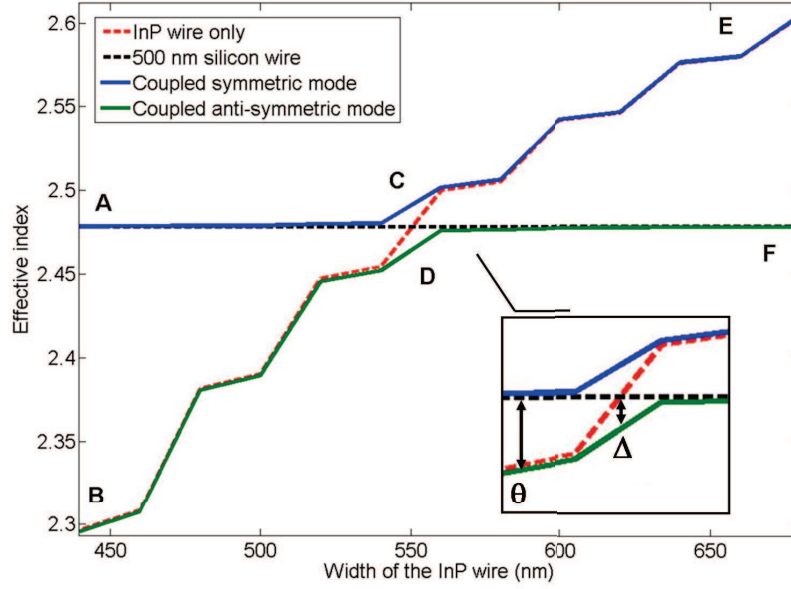


Figure 8.16: Index of the 2 first modes of coupled InP wire of variable width (height=255nm) with a silicon wire (500×220nm) separated by a 465 nm thick BCB intermediate layer. Dotted line correspond to the index of an uncoupled wire. Field profiles of points A-F are plotted on fig.8.17. Inset : Θ correspond respectively to the index difference between the symmetric and anti-symmetric and Δ the splitting between the original modes and the symmetric or anti-symmetric modes.

β_1 and β_2 being the respective propagation vectors of each waveguides involved. Moreover, it is also possible to extract the coupling strength κ , and hence the length of coupling, since :

$$\beta_{s,a} = \beta_0 \pm S \quad (8.10)$$

with

$$S = \sqrt{\delta^2 + \kappa^2} \quad (8.11)$$

Thus, for zero detuning, $\beta_{s,a} - \beta_0 = \pm\kappa$, where $\beta_0 = \beta_1 = \beta_2$ at phase matching. The different effective indices, and hence the propagation constants, involved in these latter formula are directly readable as the parameter Δ (equal to 0.025) in fig.8.16, thus $\kappa = \frac{2\pi\Delta}{\lambda}$. After calculations, at phase matching, the length of coupling is, for the system used for fig.8.16, $L_{coupling} = \frac{\lambda}{4\Delta} = 15\mu m$, more than one order above the length of the cavities under study, which means that it will be relatively valid to consider, in view of the coupling, the cavity as a point. Moreover, we expect the coupling Q factor is of the order of 10^3 . Indeed, since we have $L_{coupling}$, we expect the decay time associated to be $\tau_{coupling} = L_{coupling}/v_\phi$, with v_ϕ the

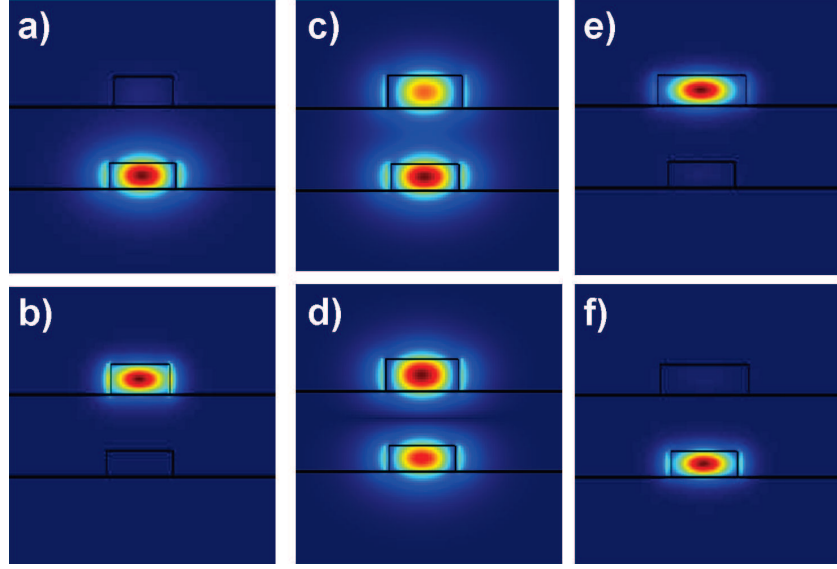


Figure 8.17: Modes profiles of the coupled system for different phase matching conditions, points A-F of fig.8.16. The field profile at the matching point (C and D) reveals two modes (symmetric and anti-symmetric, phase not shown here) where the field is located simultaneously in both waveguides.

phase velocity equals approximately 10^8 , thus $Q = \omega\tau_{coupling}/2 = 91$.

8.4.1.3 Silicon wires influence on the Q factor

Furthermore, a more direct study of the influence on the cavity Q factor induced by an underlying silicon wire has been done by modelling, with 3D FDTD, an InP cavity coupled to a silicon wire underneath with variable intermediate BCB thickness. On fig.8.18 are plotted the cavity Q factor, for a given cavity resonant at 1570 nm (note that this value does not gives a perfect phase matching with the silicon wire), against the thickness of BCB. It shows that, for the silicon wire, to have an impact on the Q factor, the intermediate layer thickness of BCB has to be approximately 450 nm, or lower. This result is coherent with the fact that the field of the TE mode of each wire, silicon and InP, in the material of lowest index is expected to be null after 500 nm. Then, since we are interested, as will be discussed later, in the highest ratio of Q_{cavity} on $Q_{coupling}$, the choice of the thickness will be a trade off in order to obtain a high efficiency of coupling while keeping a total Q high enough to allow laser operation of the coupled cavity system.

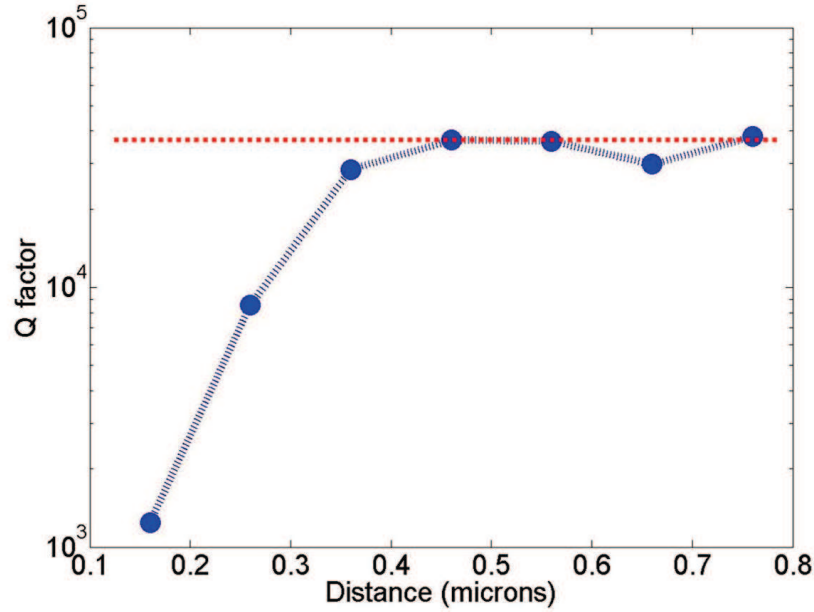


Figure 8.18: Evolution of the cavity Q factor against the BCB intermediate layer thickness (ie. the thickness of BCB between the lower surface of the InP wire and the highest surface of the silicon wire), red dashed line correspond to the Q factor of the unloaded cavity

8.4.2 Laser emission coupled to the wire

The samples, under study, were made with the standard procedure and with the same active layer (InP plus 4 QWs embedded) and aligned on top of the silicon wire with a total BCB thickness of 600 nm (ie. 400 nm between, respectively, the top and bottom of the silicon and InP wire). A SEM picture of the sample is given in fig.8.19.

As in the previous study, samples with several cavity lengths were fabricated in order to cover the bandwidth of our gain medium. We pump the sample from the top using an $\times 10$ objective with a diode pump at 800 nm using pulses of 40 ns at a frequency of 300 kHz. The detection is performed on light extracted from the silicon wire using a spectrometer coupled to a cooled InGaAs CCD camera. The first result is the observation of laser operation coupled to the silicon wire for several cavities covering the range of our gain material bandwidth with external thresholds (ie. without taking into account losses due to the pump path, pump spot size or just partial absorption of the active layer) around 1 milliwatt. The typical light-in/light-out S-curve is plotted on fig.8.20 with in inset the spectrum of emission. Besides using an optical pump from the top, also experiments were carried out using the silicon wire for pump injection (as done in section 7.2). The power

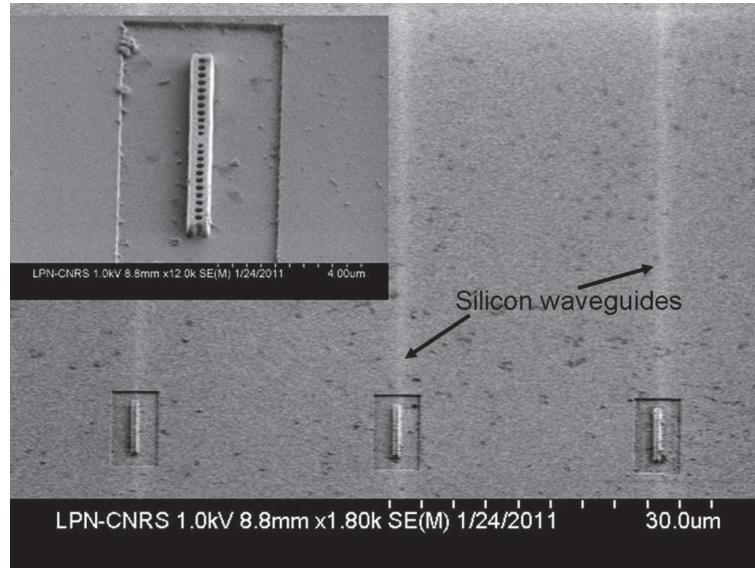


Figure 8.19: SEM picture of an aligned wire cavities on top of a silicon wires

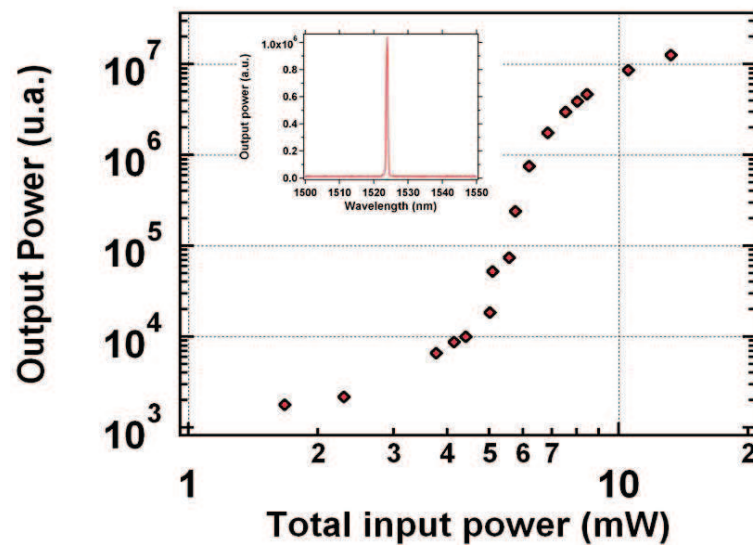


Figure 8.20: Emitted light, extracted via the silicon wire, versus pump power for a coupled cavity operating at 1525 nm

coupled to the silicon wire is a few micro-watts.

8.4.2.1 Multi wavelength operation

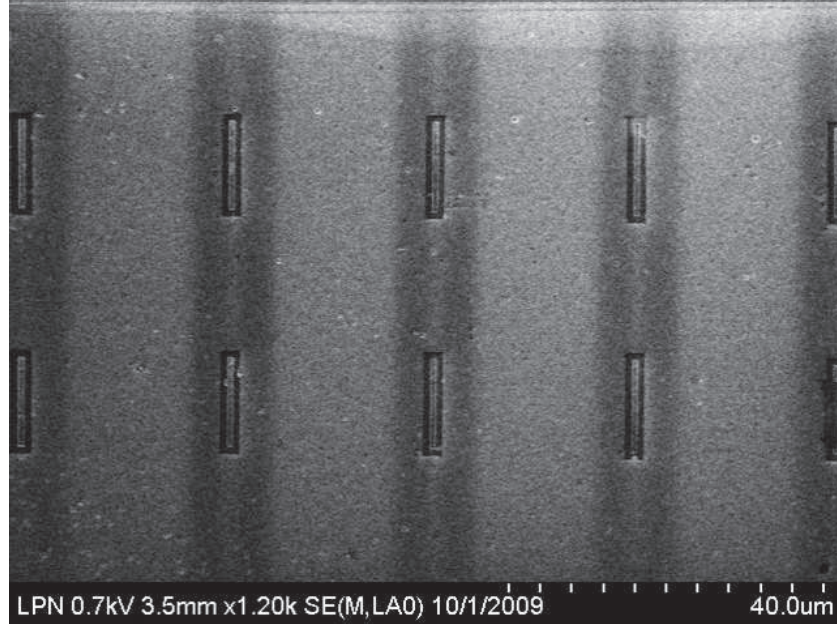


Figure 8.21: SEM image showing pairs of cavities on single silicon wires.

Moreover, as we implemented several cavities on one silicon wire, as illustrated by the SEM image of fig.8.21, it is possible to pump all of them by injecting a 1.18 micron pump. The spectrum obtained is plotted on fig.8.22. Multiple peaks are visible in the spectrum, each corresponding to a different cavity. Because several cavities were not optimized plus the fact that this curve have to be convoluted with the transmission spectra of the grating couplers, it is not possible to draw conclusions from the relative peaks power. However, this experiment was a proof of principle of the possible use of PhC hybrid/silicon circuitry to obtain a multi-wavelength laser system.

We thus demonstrate laser operation of wire cavities coupled to the silicon wire. Moreover, using wire cavities opened a lot of new possibilities. Indeed, as will be discussed in the conclusion many schemes that can be implemented to obtain new functionalities with such kind of system have already been proposed, but more interestingly, with this system we were able to experimentally extract an important, and still unknown, parameter which is the “coupling strength” between the active and passive level of the hybrid structure.

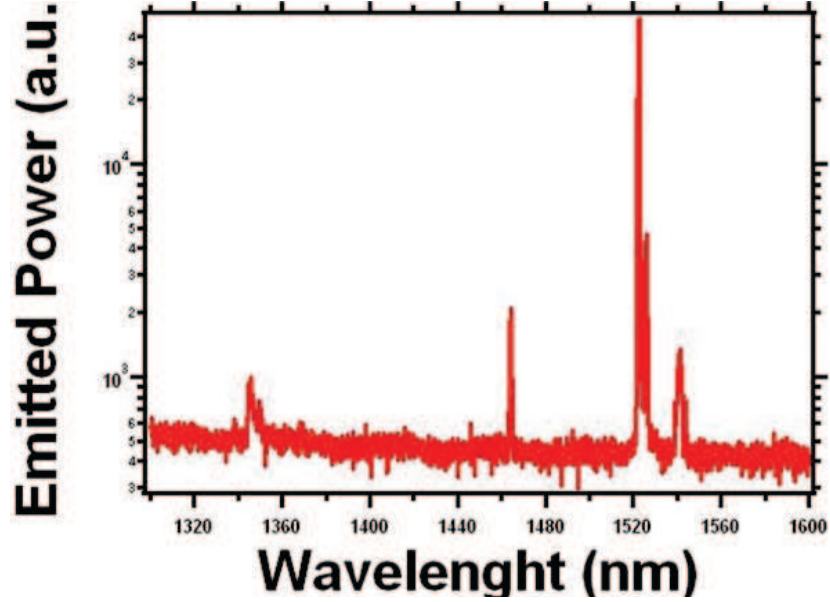


Figure 8.22: Lasing of four cavity pumped at the same time via the silicon wire at 1.1 micron.

8.4.3 Study of the coupling

8.4.3.1 Theoretical model : a cavity coupled to a wire

Before going to the experiments it is important to present the model describing our system (depicted in fig.8.23) composed of a cavity coupled to a waveguide.

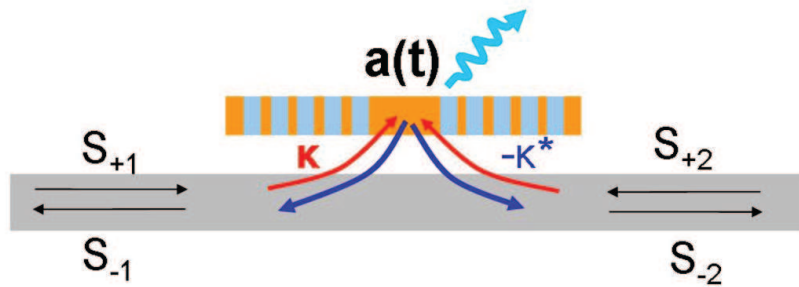


Figure 8.23: Coupling scheme of a cavity and a waveguide with important parameters such as the coupling factor κ , the optical losses of the cavity (blue arrow) τ_{cavity} , the field amplitude in the cavity $a(t)$, and light incoming/outgoing from the right $S_{\pm 2}$ or left $S_{\pm 1}$

The major point is that the transmission spectrum of such a system contains all informations concerning the coupling strength κ and the Q_0 factor of the unloaded cavity. Indeed, the overall transmission, results from interferences between the light going through the waveguide and the light coupled in and out of the cavity. The resulting outgoing field is determined by all the parameters involved in the system, coupling and losses or gain, in the cavity. The relationship between incoming light and outgoing light intensity, respectively S_{+1} and S_{-2} , (the squared amplitude of these field amplitudes is equal to the power in the waveguide) [20] may be written as :

$$S_{-2} = S_{+1} - \kappa^* . a \quad (8.12)$$

and $a(t)$ the field in the cavity, resonant at ω_0 , is given by :

$$\frac{\partial a}{\partial t} = (i\omega_0 - \frac{1}{\tau_{coupling}} - \frac{1}{\tau_{cavity}}) . a + \kappa . S_{+1} \quad (8.13)$$

where $\tau_{coupling}$ is the time constant associated with κ , $\kappa = \sqrt{\frac{1}{\tau_{coupling}}}$, and τ_{cavity} the time constant corresponding to the photon lifetime in the unloaded cavity. The resulting transmitted, in intensity, is then given by

$$T = \left| \frac{S_{-2}}{S_{+1}} \right|^2 = \left| 1 - \frac{\frac{1}{\tau_{coupling}}}{j(\omega - \omega_0) + \frac{1}{\tau_{cavity}} + \frac{1}{\tau_{coupling}}} \right|^2 \quad (8.14)$$

In our system, due to the presence of an active medium, $1/\tau_{cavity}$ is in fact the sum of two terms: $1/\tau_0$ and $1/\tau_G$. The first term denotes the time constant associated with optical losses τ_0 . The second one, τ_G is due to absorption/gain of the light by the active medium (whose band gap lies around 1560 nm). While pumping the device, we are able to bleach gradually our active medium even going to a change in sign of τ_G , with inversion of carrier population, corresponding to gain and amplification of the light inside the cavity. Thanks to this tunable parameter we are able to explore the system and extract the values of the coupling and therefore Q_0 . Indeed, if we plot the transmission against the parameter τ_G ($\frac{1}{\tau_{cavity}} = -\frac{1}{\tau_G} + \frac{1}{\tau_0}$) we obtain the characteristic shape of fig.8.24.

As it can be seen, for $\tau_G < 0$ and $\tau_G \ll \tau_0$, the system behaves like as though there is no cavity. Moreover, this typical curve (fig.8.24) possesses two important features. The first one corresponds to a zero in transmission. This point corresponds to a state where the gain in the cavity τ_G exactly compensates the optical losses τ_0 . For this operation point, the only term still acting on the transmission, as a function of frequency, is then $\tau_{coupling}$. Consequently, the FWHM of the transmission, is determined at this point only by the term of coupling, and is thus $Q_{coupling}$. The second point corresponds to the divergence on the right, at this point all losses, coupling losses and cavity losses, have been compensated by

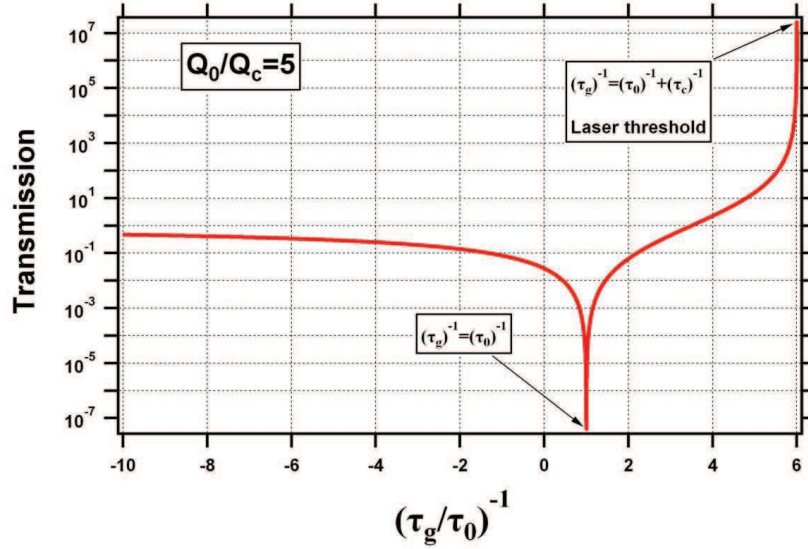


Figure 8.24: Plot of the theoretical transmission of the system depicted in fig.8.23 against τ_G expressed in fraction of τ_0 .

the gain allowing lasing operation of the cavity. Then by a fitting procedure of the S-shaped laser curve, as done previously, we should be able to deduce an approximative value of the total Q factor of the cavity. Therefore, knowing the total Q of the cavity and the $Q_{coupling}$, we will be able to retrieve the optical losses Q_0 , and, hence, the efficiency of the coupling, as defined in the next section.

8.4.3.2 Experimental study of the coupling

In order to experimentally extract these parameters we used a pump-probe experiment in order to scan the transmission spectrum for different pump powers. The system is pumped from the top using pulses of 40 ns (frequency 1 MHz) with a laser diode at 800 nm. We inject, via the silicon wire, a probe laser in the infrared that can be tuned over the gain bandwidth (1520 nm to 1620 nm) with pulses slightly shorter than the pump pulses, using a wavegenerator which is synchronized with the pump. Thus, we only probe the system when the pump is present, ie. in a controlled state. However, what we get at the output fiber is not just the probe but also the photo-luminescence emission of our sample. In order to overcome this problem we imposed an extra modulation on the probe of 400 kHz and detect using a lock-in amplifier only the signal at the probe modulation frequency, allowing us to filter the signal of interest and eliminate the PL emission of the cav-

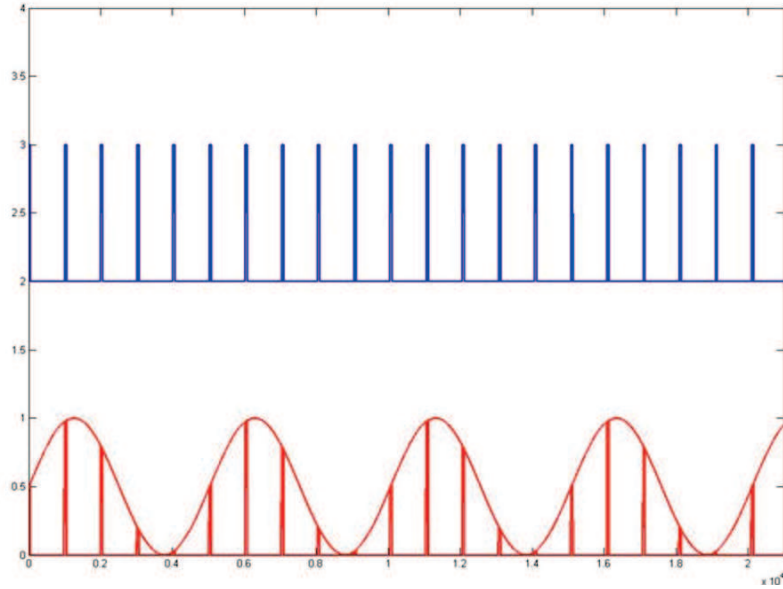


Figure 8.25: Schematic view of the pump probe experimental preparation.

ity. This processing on the pump and probe is schematically depicted in fig.8.25.

The typical results obtained are plotted on fig.8.26. First, a clear dip appears while increasing the pump power, with a minimum for a certain pump level depicted by the first red curve to the second red curve. Then from the second black curve signs of amplification already begin to show and they become pronounced as we move upwards in the fig.8.26 for increasing pump powers. We can also note the characteristic blue shift induced on the resonance for increasing carrier density in the active layer. It is also clear that the FWHM decreases with increasing pump power as absorption gets bleached reaching the value corresponding to $Q_{coupling}$ when the transmission is minimum, as explained previously. We depicted the normalized transmission on resonance measured against the pump power on fig.8.27. This curve shows the behaviour expected by analytically solving the equations (8.11), plotted on fig.8.24, ie. a starting value of the transmission equal to 1 for low pump power, a minimum reaching zero for a certain pump value and an increase beyond 1 of the measured power corresponding to amplification of the probe. From these data we measured the $Q_{coupling}$ (ie. FWHM at the minimum in transmission) which is around 2000. This measured value is slightly different from the value extracted in the previous modelling (section 8.4.1), we may attribute this difference to the phase matching condition, related to a relative uncertainty of the real index and width value for the processed InP wire.

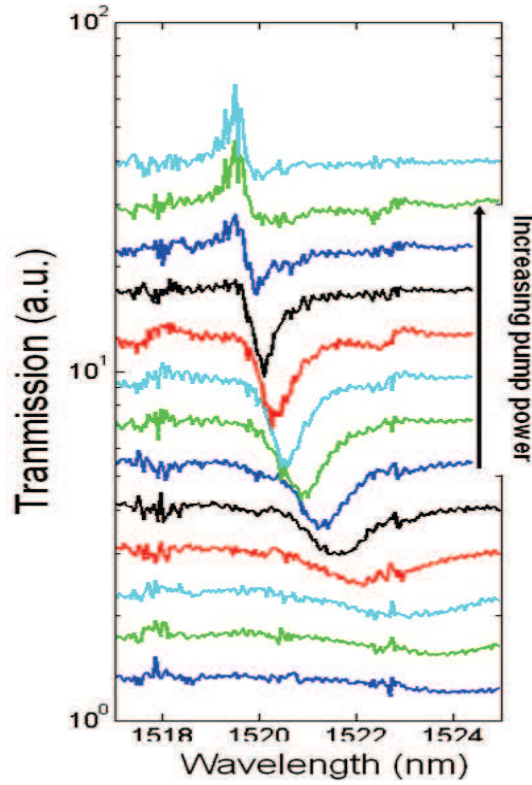


Figure 8.26: Typical transmission spectra measured for increasing pump power (from bottom to top)

Then, in order to determine the fraction of the emitted light coupled to the silicon wire, it is necessary to know the Q_0 of the cavity. The fitting procedure used previously (see chap. 8.3.2) was shown to be accurate enough to extract within a good approximation, the total Q factor of a cavity. Using a numerical fit on S – $curve$ measured on the same coupled cavity we are then able to give a value for the total Q factor corresponding to the “sum” of Q_0 and $Q_{coupling}$. The fit performed, shows that Q_0 is around 8000, coherent with the results obtained for cavity on a silicon substrate. From these values, through the following formula giving the coupling efficiency η , we deduce that 80 % of the emitted light is coupled to the silicon wire, which corresponds to a remarkably high value of collection of light emitted by a PhC structure.

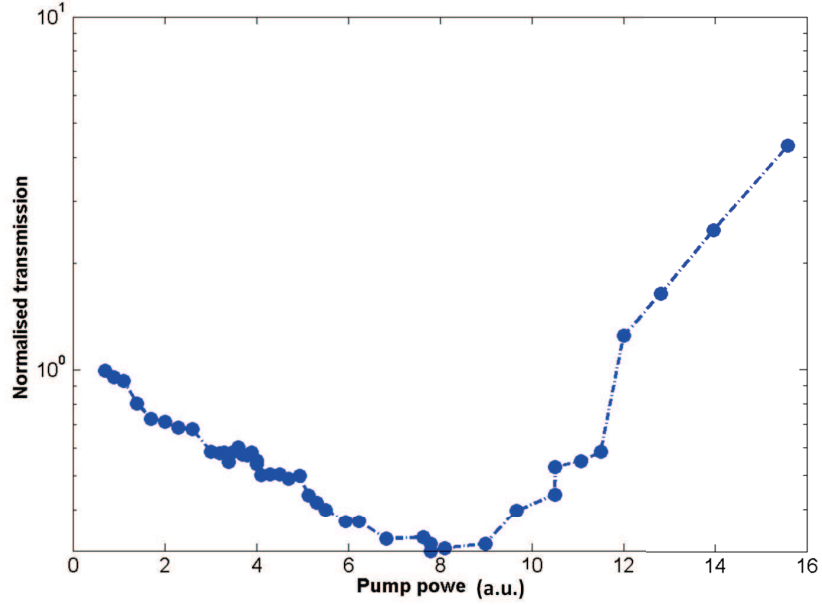


Figure 8.27: Intensity of the transmission against pump power

$$\eta = \frac{\frac{1}{Q_{coupling}}}{\frac{1}{Q_{coupling}} + \frac{1}{Q_O}} \quad (8.15)$$

In conclusion, we used and adapted a cavity design to obtain laser operation in our III-V/Si hybrid structure with fairly low threshold. This is a particularly interesting result for PhC with QWs, all the more so since we are working on a relatively high index substrate. Moreover, switching to wire cavity designs allowed us to experimentally probe and study the coupling between the two evanescently coupled levels. Latter experiments show that the extraction of light emitted in the upper level through the Si waveguide is as high as 80 % ! This value is very promising, since in the next steps, non-linear effects based on signal injection such as bistability and flip-flop operation will be studied. For these applications a high coupling efficiency will be critical in order to obtain low power switching. In the future, more experiments will have to be performed to experimentally study the coupling efficiency as a function of various parameters such as the phase matching criteria or the thickness of the intermediate layer in order to get insights concerning the tolerance of our system against these critical parameters .

8.5 Continuous wave laser operation

Last but not least, we report on results concerning the continuous laser operation, with a threshold of approximatively 6 mW. As can be seen on fig.8.28, the emission against pump power shows clearly a change of slope after a certain value of the pump power, in parallel the FWHM of the resonance decrease. We indeed obtain continuous operation by pumping the last generation of samples with a 1.18 micron diode laser, a wavelength corresponding to an energy right above the gap of the InGaAsP barriers of the quantum wells. Indeed, this decrease of the pump energy lowers the number of phonons emitted during the relaxation process of electron-holes pairs which are responsible for the device heating. Moreover, the use of an intermediate SiO_2 layer, more than just increasing the yield of bonding (see section 3.2.2), helped also to reduce the thermal resistance of the device, solving thus the problem of the poor thermal conductivity of BCB, which in the first samples was just a thin layer (90 nm) used only for bonding purposes and was increased to 400 nm in the latest batch of samples. This result opens a myriad of possibilities since achieving various optical functionalities will typically require continuous operation.

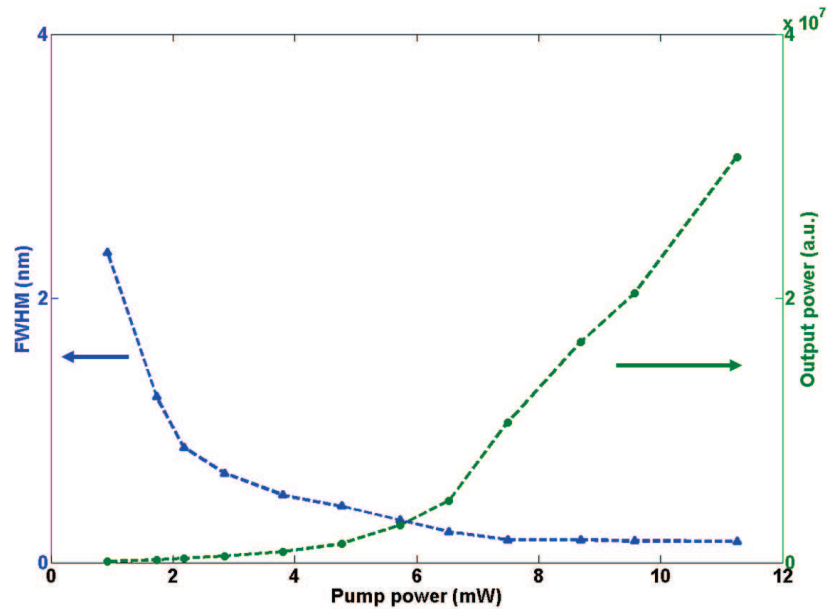


Figure 8.28: Light-in/light out curve attesting continuous laser operation under 1.18 microns pumping (blue triangles) and FWHM (green dots) against pump power.

8.6 Conclusion

The driving force behind the work presented in this chapter was to validate a design compatible with our III-V semiconductor/BCB/Silicon system, which is promising in terms of future applications. Indeed, most schemes to achieve optical functions such as flip-flops [21][bistability] are based on cavity design. It was not obvious to find a PhC based cavity structure that would possess good optical properties (high Q , small modal volume) to allow efficient non-linear operation and low power consumption light sources on a relatively high index substrate such as BCB. To overcome this difficulty, etching the underlying BCB to implement a III-V membrane would have been a solution but would have brought extra complexity in the processing, losing consequently one of the strengths of the proposed hybrid system, that is to say a relatively straight forward processing. Moreover, this would have impacted the thermal performance of the device. Fortunately, the wire cavity design has been the object of a lot of attention during the last year and turns out to be an interesting option for systems on a substrate such as SOI. Such a cavity design is therefore also very suitable for our system. Thanks to previous work, which indicated the possibilities of obtaining high Q due to the addition of a few tapering holes, the principal work on the transfer of the existing cavity design to our material system was based mainly on the application of the scaling properties of Maxwell's equations. As a result, modelling shows III-V cavities with respectably good properties, with a Q factor higher than 10^4 and modal volumes close to, or not far from, the diffraction limit (around $0.5 (\lambda/2n)^3$) with reasonable confinement factors. Experiments on stand-alone wire cavity devices show a good agreement between the expected values and the measured ones, validating modelling and processing. Laser operation has been reported for the first time initially in the pulsed regime and more recently CW operation was demonstrated. Thanks to the good control on the cavity design, little adjustments needed to be made for further integration on a silicon wire. As a result laser operation of wire cavities coupled to a silicon wire has been demonstrated. Moreover, we showed that several cascaded wire cavities can be implemented on a single silicon wire, pumped in a row resulting in an integrated multi-wavelength laser source. In subsequent experiments, the remaining and very fundamental question of the coupling efficiency has been tackled. A good understanding of the coupling scheme allowed us to experimentally extract a quantitative value for the coupling parameter, allowing to experimentally deduce a coupling efficiency as high as 80 %. Finally, by addition of a relatively thick SiO_2 layer and pumping at lower energy just above the barriers we demonstrate the possibility to obtain continuous laser operation.

This work on wire cavity can be considered as a starting point for more complex optical functions based on a photonic active cavity as will be discussed in the concluding chapter. Indeed, our latest results are showing the bistable operation of

these devices. A non-linear behaviour that can be used in order to achieve optical memory with a fast switching time (of the order of the laser build up time).

References

- [1] M. Sorel A. R. Md Zain, N. P. Johnson and R. M. De La Rue. *Ultra high quality factor one dimensional photonic crystal/photonic wire micro-cavities in silicon-on-insulator (SOI)*. Opt. Express, 16:1208412089, 2008.
- [2] I. W. Frank M. Khan P. B. Deotare, M. W. McCutcheon and M. Loncar. *High quality factor photonic crystal nanobeam cavities*. Appl. Phys. Lett., 94, 2009.
- [3] G. Shambat T. Sarmiento J. S. Harris Y. Gong, B. Ellis and J. Vuckovic. *Nanobeam photonic crystal cavity quantum dot laser*. Opt. Express, 18:87818789, 2010.
- [4] Y. Huang J.-H. Ryou P. Deotare R. Dupuis Y. Zhang, M. Khan and M. Loncar. *Photonic crystal nanobeam lasers*. Appl. Phys. Lett., 97:051104, 2010.
- [5] M.-K. Kim J.-H. Song B. Min K.-S. Kim B.-H. Ahn, J.-H. Kang and Y.-H. Lee. *One-dimensional parabolic-beam photonic crystal laser*. Opt. Express, 18:56545660, 2010.
- [6] J. Ferrera E. R. Thoen G. Steinmeyer S. Fan-J. D. Joannopoulos L. C. Kimerling Henry I. Smith E. P. Ippen J. S. Foresi, P. R. Villeneuve. *Photonic-bandgap microcavities in optical waveguides*. Nature, 390:143, 1997.
- [7] P. Lalanne J P Hugonin D Peyrade E Picard T Charvolin P Velha, J C Rodier and E Hadji. *Ultra-high-reflectivity photonic-bandgap mirrors in a ridge SOI waveguide*. New Journal of Physics, 8:204, 2006.
- [8] D. Marcuse. *Theory of dielectric optical waveguides*. Academic, New York,, 1991.
- [9] P. Lalanne and J. P. Hugonin. *Bloch-wave engineering for high Qs, small Vs microcavities*. IEEE. J. Quantum Electronic., 39:1430–1438, 2003.
- [10] T. Charvolin E. Hadji J. C. Rodier P. Lalanne P. Velha, E. Picard and D. Peyrade. *Ultra-High Q/V Fabry-Perot microcavity on SOI substrate*. OPTICS EXPRESS, Vol. 15 no. 24:16090, 2007.
- [11] P. Lalanne C. Sauvan, G. Lecamp and J.P. Hugonin. *Modal-reflectivity enhancement by geometry tuning in Photonic Crystal microcavities*. OPTICS EXPRESS,, 13, 2005.
- [12] E. Yablonovitch, K. D. Brommer T. J. Gmitter; R. D. Meade, A. M. Rappe, and J. D. Joannopoulos. *Donor and acceptor modes in photonic band structure*. Phys. Rev. Lett., 67:33803383, 1991.

- [13] Attila Mekis Steven G. Johnson, Shanhui Fan and J. D. Joannopoulos. *Multipole-cancellation mechanism for high- Q cavities in the absence of a complete photonic band gap*. Applied Physics Letters, 78-22, 2001.
- [14] www.lumerical.com.
- [15] E. Kapon. *Semiconductor Lasers*. Academic, 1999.
- [16] T. J. Karle R. Hostein R. Braive A. Beveratos I. Sagnes F. Raineri, A. Yacomotti and R. Raj. *Dynamics of bandedge photonic crystal lasers*. Opt. Express, 17:31653172, 2009.
- [17] H. Kawaguchi. *Optical bistability and chaos in a semiconductor laser with saturable absorber*,. Appl. Phys. Lett., 45(12):12641266, 1984.
- [18] P. Monnier A. Levenson R. Raj C. Seassal X. Letartre F. Raineri, C. Cojocar and P. Viktorovitch. *Ultrafast dynamics of the third-order nonlinear response in a two-dimensional InP-based photonic crystal*,. Appl. Phys. Lett., 85(11):18801882, 2004.
- [19] G. Bjork and Y. Yamamoto. *Analysis of semiconductor microcavity lasers using rate equations*. IEEE J. Quantum Electron., 27:23862396, 1991.
- [20] S. Fan P. R. Villeneuve H. A. Haus C. Manolatou, M. J. Khan and J. D. Joannopoulos. *Coupling of Modes Analysis of Resonant Channel Add-Drop Filters*. IEEE Journal of Quantum Electronics, 35:1322–1332, 1999.
- [21] John D. Joannopoulos Peter Bienstman Roel Baets Simon-Pierre Gorza Bjrñ Maes, Marin Soljacic and Marc Haelterman. *Switching through symmetry breaking in coupled nonlinear micro-cavities*. Optics Express, Vol. 14, Issue 22, pp. 10678-10683 (2006), 14:10678–10683, 2006.

9

Conclusion and perspectives

To summarize the driving forces of the work done let's take a few lines to recall first that a novel type of platform for optical interconnect has been proposed during the recent years combining III-V semiconductors and Silicon. Both materials are well known in the field of optics, with respective assets and drawbacks. Silicon is well known for being unsurpassed for any kind of passive applications but is not well suited to achieve active optical functions. III-V semiconductor alloys have shown during the last decade to be a powerful material, both in terms of light emission and dynamic optical non-linearities. Combination of those two materials is then thought to be a promising opportunity to answer to the needs in optical processing. Few works already showed results based on such composite structures, from laser emission [1] to bistability [2], and those systems are now clearly on the roadmap of the large players in this field, such as IBM, partner of the European FP7-HISTORIC project, or Intel. However, the number of groups working on this topic is still limited and consequently research on hybrid structures is at an early stage and many demonstrations are still to be done. Then, the idea behind this PhD thesis was to introduce photonic crystal based structures in this hybrid scheme. Indeed, during the last decade, PhCs have shown to offer unique possibilities to control the electromagnetic field, impacting strongly the intensity or threshold of laser emission and of plenty of non-linear effects. Gent University bonding and silicon technology and LPN knowledge on III-V semiconductors PhCs processing and properties were the starting point of the present work.

9.1 Conclusions

9.1.1 Results Review

9.1.1.1 Fabrication of the hybrid structures

The first key point to overcome was the processing of such hybrid structures. The bonding technology, based on adhesive bonding using BCB, has been developed in Gent and transferred, for a sake of simplicity, to LPN in the context of the present joint PhD. A part of the work consisted in an improvement of this bonding method, leading to a yield increase, from 50% to 100%, and a proposal to accurately control the intermediate layer thickness, critical parameter of the evanescent coupling, both by the use of an intermediate layer of SiO_2 . Moreover, this technology transfer has shown to bring added values for various works of other groups, outside the context of the hybrid structure, from phased-locked second-harmonic generation [3] to the study of the inter-band transition of InGaAs/GaAs quantum dots [4].

The second main step was the processing of the photonic crystal structure. Keeping in mind the typical scales of the periodic pattern of a PhC (around $\lambda/2n$) and that the evanescent coupling scheme used is very sensitive to phase matching, a specific technique has been developed to achieve a strict alignment fulfilling the evanescent coupling requirements. This technique, based on e-beam “semi-automatic” alignment via detection of marks pre-etched in the silicon, has given, to the best of our knowledge, a “state-of-the-art” result since the two levels, etched separately, in a CMOS line (Leti, IMEC) and further in the LPN clean room, are aligned with an accuracy better than 30 nm, far below the requirements, giving us a perfect control over the optical properties of our hybrid structures, as pointed out by the repeated strong matching between modelling and optical measurements. Last but not least, a modification, from the material point of view, resulting from the addition of the SiO_2 intermediate layer, brought a solution for a very important drawback of BCB that is to say its poor thermal conductivity. Indeed, this layer helps the spreading of the heat (thermal conductivity $\kappa_{\text{SiO}_2} = 1.4 \text{ W/mK}$, $\kappa_{\text{BCB}} = 0.29 \text{ W/mK}$) and thus its sinking to the silicon substrate. In addition we decided to pump at lower energies (1.2 microns), just above the barriers and consequently observed CW laser operation.

9.1.1.2 Modelling confronted to experimental results

Having solved these issues, all our attention was given to the upper III-V semiconductor level design. Indeed, PhC based structures offer plenty possibilities of light matter interaction enhancement through a myriad of designs. We worked on two main families of PhCs, waveguides and cavities, with specific results for each of them. We first demonstrated laser operation, using the low group velocity

modes of a photonic crystal waveguide, coupled to a silicon wire, before implementing a wire cavity design, playing this time on high Q and small modal volume V properties, which was not an obvious task due to the presence of a relatively high refractive index material such as BCB, with the same success. These results shows our ability to model our evanescently coupled hybrid system, giving tools for future works, and implement and process robustly the designed PhC structures. A first, or close to be, quite exhaustive modelling against various parameters for each design confronted with experimental study of the wire cavities was made. We gained from this exploration a better understanding of the properties of the system studied, indeed from wavelength laser emission or threshold all the experimental results are matched with modelling. Secondly, laser operation demonstration was a necessity since it is the easier and less demanding non-linear effect to observe. As will be discussed in the next section, further experiments shows a proof of the extended functionality of the cavity design through the first observation of bistability operation. Moreover, comparing the experimental and modelling results gave use insights in the coupling between the two levels, allowing us to accurately extract the coupling strength in our system, which was not an obvious task [5], showing a very efficient, around 80%, extraction of emitted light in the active level, which is very promising for further studies. It indeed corresponds to tens of nanowatts in the silicon wire allowing us to consider the possibility of implementing our hybrid structure as a unit of a larger and more complex circuitry.

9.1.1.3 Summary

Thus, this work resulted in a successful realization of active hybrid lasers, overcoming the difficulties concerning the processing, modelling and the building of a dedicated experimental setup for the study of the developed hybrid structures. The influence of various parameters were explored, matching closely the modelling, allowing a clear understanding of the lasing behaviour and allowing a qualitative and quantitative study of the coupling between the two levels.

In addition, from a general point of view, the system developed solved one of the main problems while using PhCs. Indeed, the strongest properties of PhCs are located below the light line, concern modes with a very particular impedance or cavities surrounded by strong reflectors, addressing their properties is thus a delicate task that has been simplified by the system proposed and the evanescent coupling scheme allowing to couple to PhCs without destroying their properties.

9.1.2 Bistability

A very last and promising result is the observation of a clue of bistability behaviour in the gain regime in the wire cavity hybrid devices. Indeed, under certain condi-

tions, the opening of an hysteresis cycle has been observed, in a system brought to emission via pumping, in the emission intensity as a function of the intensity injected light via the silicon wire as shown on the picture of fig.9.1.

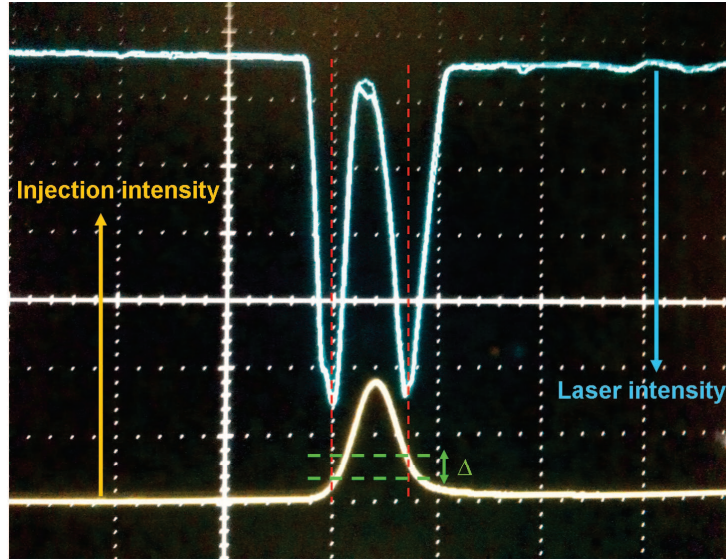


Figure 9.1: Emission intensity at λ (blue line) while injecting, at $\lambda + \delta\lambda$, the system, with various intensity, via the silicon wire (yellow line). It can be seen that the emission falls to zero for a given value of injected light and begin to recover its unperturbed emission state for a second value. The continuous variation of the injected light combined with the difference Δ (green lines) for which emission is turned off and after turned on indicate the existence of an hysteresis cycle.

The underlying physical mechanism is based on carrier depletion. Indeed, through optical pumping of the cavity we created a steady state where the conduction band is populated by carriers, corresponding, above threshold, to a certain amount of laser emission. Light injection, of a slightly detuned signal, in the system clearly impacts this state, since we offer a second path for recombination, that is stimulated emission and amplification of the injected signal, with the consequence that the number of carriers dedicated to laser emission decreases. The light emitted by the cavity is therefore a mix of spontaneous emission and stimulated emission proportional respectively to the pump power and intensity of the light injected. In order to see bistability, we play on the blue/red shift of the cavity resonance due to the carrier density change. Indeed, since we inject our signal at a red-shifted wavelength from the resonance, or laser, at steady state, a fraction of this light is amplified, and carriers depleted, and the resonance is thus red-shifted. Note the crucial fact that the amplified light, and consequently the strength of the carrier depletion, is proportional to the fraction of light injected in the cavity, so it

is proportional to the detuning between the frequency of the light injected and the cavity resonance. While increasing the intensity of the injected light we reach a point where the injected light is so close to the cavity resonance, that the resonance is pulled by the injected signal, the detuning falls to zero and the amplification is maximum, while the signal is strong enough to canalize all carriers. Note that at the same time spontaneous emission drops substantially, reaching a contrast of 100% under certain conditions. Now decreasing the signal intensity, the carrier density goes up, but since the signal remains strongly present in the cavity. Below a certain intensity the cavity decouples again from the signal and the detuning begins to increase coming back to the case where injection is low against spontaneous emission. The critical point is that the “pulling” and “releasing” of the cavity resonance does not occur for the same injection intensity, opening a hysteresis cycle.

Coming back to fig.9.1, we can give more explanations on the experimental setup used. First, in this experiment the laser intensity (blue line) is filtered, we measure only the signal at the laser frequency, thus the slightly detuned injected signal (yellow line) does not appear on the measured signal. We proceed in this way to obtain a background free measurement. So, the results show more the detuning induced on the laser than its emission intensity. However, we assume this detuning to be associated with a drastic fall in the emission intensity. As can be seen on the emission spectra while changing the injection intensity, a complementary experiment would be to show the transfer of intensity between the decreasing laser emission and the increasing signal amplification. The signature of the hysteresis loop is the two different values, while varying continuously the injection intensity, for which the laser comes back to its steady state and its initial wavelength. It has been observed that the switching intensity between the two stable states is fairly low, expected to be around few fJ, and that the contrast, if considered at a fixed wavelength can reach 100%. We expect the switching time, from the state “0” to “1”, to be driven by the build up time of the laser (expected to be of the order of tens of picoseconds [6]).

Since bistability can lead to very interesting applications, plus the fact that we can now work under continuous operation, switching time and switching energies will be the object of a quantitative study in the near future.

We conclude therefore with a promising result, demonstrating all the interest of the proposed and studied system in order to bring a solution for optical interconnect applications with fairly low switching energy, threshold and high speed operation.

9.2 Perspectives

Going beyond the presented results, PhC based hybrid structures present a tremendous playground where a lot is still to be done. In the next section we present both

opportunities to improve the current system as well as ideas to achieve far more complex optical functions.

9.2.1 Present system improvement

9.2.1.1 Design and material

First, the design of the hybrid PhC structures can be still improved. For example, in the latest modelling done, when going to smaller and smaller cavities, for the first order of the Fabry-Perot, we observe a very sharp increase of the Q factor to 10^5 (see fig.9.2). We expected this phenomenon to arise because of a mechanism called “loss recycling” [7]. This increase of the Q factor is based on the addition of a leaky mode in the system. One fraction of the losses is then due to the excitation of this leaky mode at the interface mirror/cavity. Normally, those modes would be lost for the system but a reciprocal mechanism can lead to a coupling back, arising if the second mirror on the other side is close enough, of this mode to the guided mode.

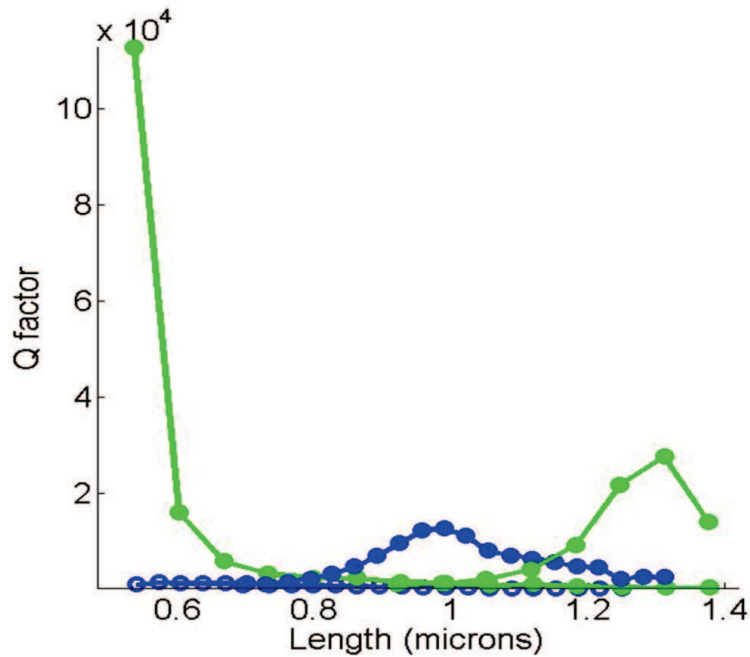


Figure 9.2: Possible signature of loss recycling. While the increase of the Q factor can be foresee for longer cavities, unexpected high Q appears for the smallest cavities modelled. Blue and Green dots correspond respectively to symmetric and anti-symmetric modes of the system.

Secondly, we can play on the active material used here. First, in section 8.5, we discussed the possibility to reduce the InP fraction in the layer stack allowing then a more efficient pumping at lower energies, above the barriers, reducing thus the heat induced. We can also think to use less embedded quantum wells, reducing the strength of the non-linear effects, but also reducing their threshold. By this way, the next generation of devices could possess increased quantum efficiency in a system where heating is reduced.

9.2.1.2 Electrical pumping

Obviously electrical pumping of our hybrid structures would be a major gain in terms of integration since we would be able to directly connect our optic level to the electrical one. In addition, the contact used for injection can also act as heat sink improving strongly the thermal properties of our system. Moreover, BCB is a well known material for electrical isolation and has shown to be suitable for high speed operation [8]. Electrical pumping is however a great concern in photonic crystal structures. To our knowledge it has been achieved only by the group of Y. H. Lee [9]. The difficulty to electrically pump such PhC based structures is mainly related to the fact that a good quality electrical pumping scheme should give a maximum of carriers recombination in the defect zone, and the PhC III-V/air holes composite structure is very resistive and increase recombinations at the edge of the structure where the contacts are located. Moreover, bringing those contacts, and thus an absorbing material, to the defect would strongly decrease the optical properties of the PhC structure. Consequently, a wise scheme and technology have to be developed to succeed in this difficult task. But we are quite optimistic in the case of the hybrid wire cavities. Indeed, wire cavities are sensibly different from “bulk” photonic crystals and should allow to overcome the problem of location of the recombination by the use of lateral contacts which would have a reduced impact on the optical properties of the cavity. Moreover, some previous realizations in another context, such as the electro-modulator based on the same type of design using carrier injection of silicon wire cavities [10], prove the potential success of this task.

9.2.2 Cascaded cavities

At the end of this work, we concluded with a wire cavity that seems to possess all the properties to go further in terms of the exploitation of non-linear effects. Indeed, starting from the existing design and structures, going to the implementation of two cascaded cavities is almost straightforward. It has been theoretically proposed to realize optical functions such as Coupled-Resonator-Induced-Transparency (CRIT) [11] [12] or switching via symmetry breaking using a struc-

tural design corresponding to two cascaded cavities coupled through a waveguide [13]. Both of these non-linear effects should allow to access interesting functionalities such as light trapping (CRIT), strong and fast modulation (CRIT) or flip-flop operation (symmetry-breaking). The process developed during this work should allow a good control on the parameters of the desired effects, for example concerning the CRIT, via our accurate alignment, phase criteria between the two cavities or matching of the resonant wavelengths of the cavities should be under control. The characteristic values and novelty in such a system will be based on the fact that, contrary to the proposed schemes, we will be able to perform those operations under gain regime resulting in a reduced threshold and a switching speed between the gain recovery time and the build up time of our lasers (tens of picoseconds).

9.2.3 Flip-flop operation

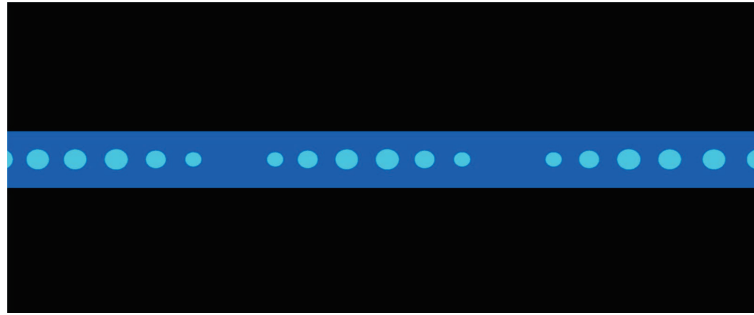


Figure 9.3: Possible scheme for the doubly resonant cavities.

Another interesting design that can be proposed for flip-flop operation is more related to the cavity design. It has been proposed [14] [15] that two lasers sharing the same gain medium, competing with each other would allow to perform flip-flop operation. Indeed, under the assumption that these two lasers possess approximately the same threshold, or same parameters such as modal volume, Q factor and confinement factor, their exist pumping parameters where the system is unstable and each of the laser mode compete for the gain medium. Leaving the system free would result in lasing operation of one or the other laser. Note that this unstable state diverge, and when one mode is lasing, this become the stable state of the system. But noticing that this competition for the gain is strongly dependent on the relative intensity of the field of each mode, it would be possible by seeding to favour laser operation on the desired mode and therefore force the system to lase under the desired configuration.

The main requirement can be fulfilled using a slight change in the wire cavity design used here. Indeed, inserting few holes in the middle of the cavity, as in the configuration proposed in fig.9.3 should result in a splitting of the cavity mode giving rise to two modes, on each side of the original resonance, at $\lambda \pm \delta\lambda$ respectively symmetric and anti-symmetric. Since, by acting on the central holes pattern, it is possible to control the strength of this splitting, it is a priori possible to obtain two modes at different wavelength sharing the same gain medium with almost the same characteristics and same threshold. Then injecting the system at a selected wavelength we should be able to control the emission wavelength of the system, with a memory effect, since the system stays stable, until a reset pulse is applied at the other laser resonance.

References

- [1] Ying-hao Kuo Richard Jones Oded Cohen Di Liang Omri Raday Matthew N. Sysak Mario J. Paniccia Alexander W. Fang, Hyundai Park and John E. Bowers. *Hybrid silicon evanescent devices*. Materials today, 10(7-8):28–35, 2007.
- [2] K. Huybrechts-T. Spuesens G. Roelkens E.-J. Geluk T. de Vries P. Regreny D. Van Thourhout R. Baets G. Morthier L. Liu, R. Kumar. *An ultra-small, low-power, all-optical flip-flop memory on a silicon chip*,. Nature Photonics, 4(3):182–187, 2010.
- [3] F. Raineri-G. D’Aguanno J. Trull Y. Halioua R. Raj I. Sagnes R. Vilaseca M. Scalora V. Roppo, C. Cojocar. *Field localization and enhancement of phase-locked second- and third-order harmonic generation in absorbing semiconductor cavities*. Phys. Rev. A, 80:043834, 2009.
- [4] S. Sauvage and al. *Homogeneous broadening of the S to P transition in InGaAs/GaAs quantum dots measured by infrared absorption imaging with nanoscale resolution*. Phys. Rev. B, 83:035302, 2011.
- [5] Kartik; Borselli-Matthew; Painter Oskar Barclay, Paul E; Srinivasan. *Efficient input and output fiber coupling to a photonic crystal waveguide*. Optics Letters, 29:697–699, 2004.
- [6] T. J. Karle R. Hostein R. Braive A. Beveratos I. Sagnes R. Raj F. Raineri, A. Yacomotti. *Dynamics of band-edge photonic crystal lasers*. Optics Express,, 17:3165, 2009.
- [7] S. Mias Ph. Lalanne and J. P. Hugonin. *Two physical mechanisms for boosting the quality factor to cavity volume ratio of photonic crystal microcavities*. Optics express, 12-3:458–467, 2004.
- [8] K. Osafune H. Yokoyama Y. Ishii T. Enoki, Y. Umeda. *Analysis of Interconnections with BCB for High Speed Digital Applications*. IEEE MTT-S Digest,, page 205, 1999.
- [9] S. H. Kwon Y. G. Ju J.K. Yang J.H. Baek S. B. Kim H. G. Park, S. H. Kim and Y. H. Lee. *Electrically driven single-cell photonic crystal laser,s*. Sciences, 305:14441447, 2004.
- [10] Jagat Shakya Sasikanth Manipatruni Bradley Schmidt, Qianfan Xu and Michal Lipson. *Compact electro-optic modulator on silicon-on-insulator substrates using cavities with ultrasmall modal volumes*. OPTICS EXPRESS, Vol. 15 no. 6:3140, 2007.

- [11] Kirk A. Fuller A. T. Rosenberger David D. Smith, Hongrok Chang and Robert W. Boyd. *Coupled-resonator-induced transparency*. Physical Review A, 69, 2004.
- [12] Andrey E. Miroshnichenko Sergei F. Mingaleev and Yuri S. Kivshar. *Coupled-resonator-induced reflection in photonic-crystal waveguide structures*. Optics Express, 16, 2008.
- [13] John D. Joannopoulos Peter Bienstman Roel Baets Simon-Pierre Gorza Bjrn Maes, Marin Soljacic and Marc Haelterman. *Switching through symmetry breaking in coupled nonlinear micro-cavities*. Optics Express, Vol. 14, Issue 22, pp. 10678-10683 (2006), 14:10678–10683, 2006.
- [14] D. N. Chigrin S. V. Zhukovsky and J. Kroha. *Bistability and mode interaction in microlasers*. Phys. Rev. A, 79:033803, 2009.
- [15] A. V. Lavrinenko S. V. Zhukovsky, D. N. Chigrin and J. Kroha. *Switchable Lasing in Multimode Microcavities*. Phys. Rev. Lett., 99:073902, 2007.



Publications and conferences

A.1 Publications

A.1.1 Related to the studies on hybrid structures

- Y. Halioua, A. Bazin, P. Monnier, T. Karle, G. Roelkens, I. Sagnes, R. Raj, F. Raineri, *Hybrid III-V semiconductor/silicon nanolaser*, Optics Express, Vol. 19, Issue 10, pp. 9221-9231 (2011).

- Y. Halioua, A. Bazin, P. Monnier, T. Karle, I. Sagnes, G. Roelkens, D. Van Thourhout, F. Raineri, R. Raj, *III-V photonic crystal wire cavity laser on silicon wafer*, Journal of the Optical Society of America B, 27(10), p.2146 (2010).

- T.J. Karle, Y. Halioua, F. Raineri, P. Monnier, R. Braive, L. Le gratiet, G. Beaudoin, I. Sagnes, G. Roelkens, F. Van Laere, D. Van Thourhout, R. Raj, *Heterogeneous integration and precise alignment of InP-based photonic crystal lasers to complementary metal-oxide semiconductor fabricated silicon-on-insulator wire waveguides*, Journal of Applied Physics, 107(6), p.8 pages (2010).

- Y. Halioua, T. Karle, F. Raineri, P. Monnier, I. Sagnes, R. Raj, G. Roelkens, D. Van Thourhout, *Hybrid InP-based photonic crystal lasers on silicon on insulator wires*, Applied Physics Letters, 95(20), p.201119 (2009).

A.1.2 Collaborations

- S. Sauvage, A. Driss, F. Reveret, P. Boucaud, A. Dazzi, R. Prazeres, F. Glotin, J.-M. Ortega, A. Miard, Y. Halioua, F. Raineri, I. Sagnes and A. Lemaitre, *Homogeneous broadening of InGaAs/GaAs quantum dots measured by infrared absorption imaging with nanoscale resolution*, Phys. Rev. B 83, 035302 (2011)

- V. Roppo, C. Cojocaru, G. D'Aguanno, F. Raineri, J. Trull, Y. Halioua, R. Vilaseca, *Phase locked second and third harmonic localization in semiconductor cavities*, J. Optoelectron. Adv. Mater. 12, 57 (2010)

- V. Roppo, C. Cojocaru, F. Raineri, G. D'Aguanno, J. Trull, Y. Halioua, R. Raj, I. Sagnes, R. Vilaseca, M. Scalora, *Field localization and enhancement of phase-locked second- and third-order harmonic generation in absorbing semiconductor cavities*, Phys. Rev. A 80, 043834 (2009)

A.2 Conferences concerning Hybrid III-V semiconductors/silicon structures

- A. Bazin, Y. Halioua, T. Karle, P. Monnier, G. Roelkens, I. Sagnes, R. Raj, F. Raineri, *Evanescent wave coupling in hybrid III-V/SOI nanolaser*, ICTON 2011 (invited), We.D2.2, Sweden-Stockholm.

- R. Raj, *A new platform for integrated optics: hybrid III-V nano-photonics crystal devices on SOI waveguides*, CMOS Emerging Technologies, Canada Whistler (2011).

- Y. Halioua, A. Bazin, T. Karle, P. Monnier, I. Sagnes, R. Raj, F. Raineri, *Optimally coupled hybrid III-V Photonics Crystal Wire cavity CW Lasers on passive SOI waveguides*, Photonic Integration - IWC4, IPR, Canada-Toronto (2011).

- F. Raineri, A. Bazin, Y. Halioua, T. Karle, P. Monnier, I. Sagnes, and R. Raj, *Hybrid III-V/Silicon on Insulator nonlinear Nanophotonics*, CLEO Europe, Germany, p.CD6.3-WED (Invited) (2011).

- A. Bazin, Y. Halioua, T. Karle, P. Monnier, F. Bordas, I. Sagnes, R. Raj, and F. Raineri, *Control of Evanescent Coupling in Hybrid III-V/SOI nanolasers*, CLEO Europe, Germany, p.CK4.3 SUN (2011).

- T. Karle, F. Raineri, F. Bordas, I. Sivan, S. Ali, Y. Halioua, G. Roelkens, R. Raj, *High temporal resolution of the ring down of SOI wire racetrack resonators*, European optical Society Annual Meeting, (2010).

- Y. Halioua, F. Raineri, A. Bazin, T. karle, P. Monnier, I. Sagnes, G. Roelkens, R. Raj, *Wire cavity photonic crystal hybrid III-V laser on silicon wire*, European Optical Society Annual Meeting, France, (2010).

- Y. Halioua, A. Bazin, T. Karle, P. Monnier, I. Sagnes, G. Roelkens, R. Raj, F. Raineri, *Hybrid III-V photonic crystal waveguide laser on silicon wire*, Integrated Photonics Research, Silicon and Nano Photonics (IPR), Photonics in Switching (PS), United States, p.IWE3.pdf (3 pages) (2010).

- A. Bazin, Y. Halioua, P. Monnier, F. Bordas, T. Karle, S. Perruchas, T. Gacoin, H. Girard, I. Sagnes, G. Roelkens, R. Raj, F. Raineri, *Thermal improvement of InP wire photonic crystal laser on silicon by addition of diamond nanoparticles in polymer bonding layer*, ECOC, Italy, p.Tu.5.E.2 (2010).

- F. Raineri, Y. Halioua, A. Bazin, T. Karle, P. Monnier, I. Sagnes, G. Roelkens, R. Raj, *Hybrid III-V photonic crystal wire cavity laser on silicon wire*, International Conference on Nanophotonics, Japan, p.O-47 (2010).

- Tim Karle, Fabrice Raineri, Frederic Bordas, Itamar Sivan, Shamyr Ali, Rama Raj, Y. Halioua, G. Roelkens, *Temporal measurements of SOI wire race-track resonators*, European Conference on Integrated Optics, United Kingdom, p.paper ThP15 (2010).

- Y. Halioua, A. Bazin, P. Monnier, T. Karle, I. Sagnes, G. Roelkens, D. Van Thourhout, F. Raineri, R. Raj, *Hybrid III-V laser on silicon wire*, InP and Related Materials, Japan, p.FrA2-2 (2010).

- Y. Halioua, T.J. Karle, F. Raineri, I. Sagnes, R. Raj, G. Roelkens, F. Van Laere, D. Van Thourhout, *InP-based 2D photonic crystal lasers heterogeneously integrated and coupled to SOI wires*, 6th IEEE International Conference on Group IV Photonics, United States, p.ThP12 (2009).

- T. Karle, Y. Halioua, F. Raineri, I. Sagnes, R. Raj, G. Roelkens, F. Van Laere, D. Van Thourhout, *III-V photonic crystal lasers heterogeneously bonded to silicon-on-insulator waveguides*, ICTON 2009 (invited), Portugal, (2009).

- Y. Halioua, T. Karle, F. Raineri, I. Sagnes, P. Monnier, R. Raj, G. Roelkens,

D. Van Thourhout, R. Baets, *Towards a new platform for integrated optics: III-V photonic crystals bonded to silicon on insulator wire waveguides*, CLEO Europe, Germany, p.JSI1.3-TuE (2009).

- Y. Halioua, T. Karle, I. Sagnes, G. Roelkens, D. Van Thourhout, R. Raj, F. Raineri, *InP 2-D Photonic Crystal lasers integrated onto SOI waveguides*, Conference on Lasers and Electro-optics (CLEO), United States, p.CMP3 (2009).

- T. Karle, Y. Halioua, F. Raineri, I. Sagnes, D. Van Thourhout, F. Van Laere, G. Roelkens, R. Raj, *Laser emission from heterogeneously integrated InP photonic crystals into SOI wires*, PECS VII, United States, (2008).